

Copyright © by

LAWRENCE CURTIS EVANS

1971

MAGNETOSPHERIC ACCESS OF SOLAR PARTICLES  
AND THE CONFIGURATION OF THE DISTANT GEOMAGNETIC FIELD

Thesis by  
Lawrence Curtis Evans

In Partial Fulfillment of the Requirements  
for the Degree of  
Doctor of Philosophy

California Institute of Technology  
Pasadena, California

1972

(Submitted 22 September 1971)

to Janet,

for her patience, cooperation, and devotion;

to Carolyn and David,

for their enthusiasm, curiosity, and interest;

to my parents,

for their motivation, counsel, and faith;

to Vernon,

for his inspiration, advice, and concern; and

to them all,

for their love is what gives meaning to the fulfillment of goals.

## ACKNOWLEDGMENTS

I am indebted to my faculty sponsor, Professor Edward C. Stone, for the time which he has taken from an increasingly busy schedule to provide guidance and encouragement throughout this research project.

I am grateful for many stimulating discussions with Dr. J. L. Faselow. Some of these discussions solved the world's fundamental problems, while most, though more mundane, were more pertinent to the study reported in this thesis. Of particular note are the fortitude he demonstrated by volunteering to read the rough drafts of this thesis, and the appropriate and helpful comments he made as a result.

It is also a pleasure to acknowledge rewarding discussions with Professor L. Davis, Jr., Dr. S. S. Murray, and Messrs. J. E. Lupton, J. W. Brown, and T. L. Garrard.

All of the design and construction and most of the calibrations of the instrument being used here were completed prior to my involvement with the project. I am most grateful to Professor J. A. Simpson, principal investigator, and the staff of the Laboratory for Astrophysics and Space Research at the University of Chicago, who, along with Professor Stone, were responsible for the successful completion of these phases of this experiment. The electron response of a detector system similar to that flown on OGO-4 was measured at California Institute of Technology



by Mr. J. E. Lupton, and the data were analyzed by Mr. J. W. Brown.

The formidable tasks of bookkeeping and routine data processing of the large number of data tapes associated with a satellite experiment have been performed admirably by Mmes. E. Aguilar and F. Pickett.

I am grateful to Professor J. A. Simpson and Messrs. J. D. Sullivan and H. J. Crawford of the University of Chicago for their help in providing some interplanetary proton data from IMP-4 for comparison with the OGO-4 data.

I am also grateful to Drs. D. H. Fairfield and N. F. Ness of the Goddard Space Flight Center for providing one hour averages of interplanetary magnetic field parameters for a period encompassing most of the lifetime of the OGO-4 satellite. These data were collected by Explorer 33, Explorer 35, and IMP-4.

I am appreciative of the fine work done by all those associated with the National Aeronautics and Space Administration OGO Project Office.

Financial aid during my graduate studies has been provided by the National Science Foundation, the State of California, and California Institute of Technology, for which I and my family are indebted. The research described in this thesis was supported by the National Aeronautics and Space Administration under contract NAS 5-3095 and grant NGL 05-002-007.

## ABSTRACT

The access of 1.2-40 MeV protons and 0.4-1.0 MeV electrons from interplanetary space to the polar cap regions has been investigated with an experiment on board a low altitude, polar orbiting satellite (OGO-4).

A total of 333 quiet time observations of the electron polar cap boundary give a mapping of the boundary between open and closed geomagnetic field lines which is an order of magnitude more comprehensive than previously available.

Persistent features (north/south asymmetries) in the polar cap proton flux, which are established as normal during solar proton events, are shown to be associated with different flux levels on open geomagnetic field lines than on closed field lines. The pole in which these persistent features are observed is strongly correlated to the sector structure of the interplanetary magnetic field and uncorrelated to the north/south component of this field. The features were observed in the north (south) pole during a negative (positive) sector 91% of the time, while the solar field had a southward component only 54% of the time. In addition, changes in the north/south component have no observable effect on the persistent features.

Observations of events associated with co-rotating regions of enhanced proton flux in interplanetary space are used to establish the

characteristics of the 1.2-40 MeV proton access windows: the access window for low polar latitudes is near the earth, that for one high polar latitude region is  $\sim 250 R_{\oplus}$  behind the earth, while that for the other high polar latitude region is  $\sim 1750 R_{\oplus}$  behind the earth. All of the access windows are of approximately the same extent ( $\sim 120 R_{\oplus}$ ). The following phenomena contribute to persistent polar cap features: limited interplanetary regions of enhanced flux propagating past the earth, radial gradients in the interplanetary flux, and anisotropies in the interplanetary flux.

These results are compared to the particle access predictions of the distant geomagnetic tail configurations proposed by Michel and Dessler, Dungey, and Frank. The data are consistent with neither the model of Michel and Dessler nor that of Dungey. The model of Frank can yield a consistent access window configuration provided the following constraints are satisfied: the merging rate for open field lines at one polar neutral point must be  $\sim 5$  times that at the other polar neutral point, related to the solar magnetic field configuration in a consistent fashion, the migration time for open field lines to move across the polar cap region must be the same in both poles, and the open field line merging rate at one of the polar neutral points must be at least as large as that required for almost all the open field lines to have merged in  $\mathcal{O}(\text{one hour})$ . The possibility of satisfying these constraints is investigated in some detail.

The role played by interplanetary anisotropies in the observation

of persistent polar cap features is discussed. Special emphasis is given to the problem of non-adiabatic particle entry through regions where the magnetic field is changing direction. The degree to which such particle entry can be assumed to be nearly adiabatic is related to the particle rigidity, the angle through which the field turns, and the rate at which the field changes direction; this relationship is established for the case of polar cap observations.

## TABLE OF CONTENTS

I. INTRODUCTION	1
II. INSTRUMENT	6
Vertical Telescope	7
Horizontal Telescope	11
Electronics and Data Formatting	14
Thresholds and Calibrations	17
III. SATELLITE	30
IV. DATA ANALYSIS	39
V. OBSERVATIONS	47
Electron Observations	47
Proton Observations	53
EDP Event of 1 December 1967	57
Solar Flare Event of 2 November 1967	70
Comparison of Electron and Proton Observations	76
VI. BACKGROUND	86
Interplanetary Environment	86
Geomagnetic Field and Magnetic Merging	92

VII. DISCUSSION	104
Electron Polar Cap	105
Access of 1.2-40 MeV Protons	107
EDP Events	114
Flare Events	120
Models of the Distant Geomagnetic Field Configuration	122
Closed Magnetospheric Configuration -- MODEL A	123
Magnetic Merging at the Sub-solar Point -- MODEL B	129
Magnetic Merging at the Polar Neutral Points -- MODEL C	132
Interplanetary Anisotropies	143
VIII. CONCLUSIONS	149
APPENDIX A: Additional Observations	154
APPENDIX B: Particle Trajectories in a Turning Magnetic Field	192
APPENDIX C: Magnetic Merging at the Polar Neutral Points	207
Assumptions	209
Assumption A	216
Assumption B	219
Assumption C	220
Derivation of Merging Rates -- General	221
Assumption A	228
Assumption B	235
Assumption C	240
Results	244
REFERENCES	256

## I. INTRODUCTION

An investigation of the physical processes involved in the access of low energy particles from interplanetary space into the interior of the earth's magnetic field is of special significance to several geophysical and astrophysical questions. Such an investigation bears directly on the question of the configuration of the distant geomagnetic field and the relation between this field and the polar cap region. A definition of this configuration is perhaps the only means available for the determination of the degree to which magnetic field merging plays a rôle in the interaction between solar and terrestrial plasmas and magnetic fields. Constraints placed on the extent of magnetic merging in this interaction would have far-reaching implications for other phenomena involving solar magnetic fields and for some phenomena involving galactic magnetic fields.

Since the discovery, in 1964 [1], that the solar wind distorts the geomagnetic field to the extent of forming a "tail" in the anti-solar direction, there has been a good deal of speculation concerning the configuration of the magnetic field in this tail at large distances from the earth. The models which have been presented for this configuration by Dungey (1961) [2], Dessler (1964) [3], and Frank (1971) [4] differ in their estimates of the length of the tail by one or two orders of magnitude. As Dessler pointed out, charged particle observations in the polar

caps constitute one of the most efficient and appropriate means of determining the structure of the distant geomagnetic field, since it is not practical to use satellite-born magnetometers to map this structure in detail.

Since the fundamental theoretical difference between the three models of the distant geomagnetic field is the assumption made about the extent and/or mechanism by which the solar and terrestrial fields merge, a resolution of questions concerning the configuration of the distant field can have a direct bearing, through these models, on the question of whether magnetic field merging is a significant process in the interaction between the solar wind and the geomagnetic field. Since it has been suggested that magnetic field merging may play an important role in, for instance, the generation of solar [5] and/or galactic [6] flares, a determination of the possibility or impossibility of magnetic merging in astrophysical plasmas, even over a limited range of plasma parameters, would be quite significant. The interaction between the solar wind plasma and the geomagnetic field is the only readily available system for which this can be determined.

Although charged particle measurements cannot determine the extent of magnetic merging directly, they can lead to the establishment of constraints to be placed on magnetospheric models. Several studies have been conducted with this goal in mind. Observations of  $>50$  keV and  $>20$  keV electrons in the magnetotail have been interpreted by Van Allen [7,8] and Anderson and Lin [9] as evidence that these electrons gain access to the magnetotail along geomagnetic field lines which are



connected to the interplanetary field. These results have, however, been interpreted differently by Michel and Dessler [10], who have modified the closed field configuration model (e.g. no merging) to account for these electron observations. In any case, the mode of access for  $>1$  MeV protons may be quite different than that for  $>50$  keV electrons, owing to the large differences in magnetic rigidity ( $\sim 0.05$  MV for the electrons *vs.*  $\sim 100$  MV for the protons) and velocity ( $0.43c$  (electrons) *vs.*  $0.046c$  (protons)). The observation by Evans and Stone [11] of a large north/south difference in the proton polar cap flux lasting for more than twenty hours showed that the question of proton access was still unresolved.

Prior to the observations reported by Evans and Stone [11], some evidence of structure in observed polar cap proton fluxes was available [12-21], but the observations were too sparse to lead to comprehensive analysis. Since this preliminary report, several observations of persistent north/south asymmetries have been reported [22-26], and several of the most recent (Englemann, *et al.* [24], Van Allen, *et al.* [25], and Morfill and Quenby [26]) have been interpreted in the context of the Dungey open field configuration, relating the north/south polar cap flux differences to interplanetary flux anisotropies. Van Allen, *et al.* [25], for instance, report observations which seem to follow this relationship closely, but only for a period of about six hours during one solar flare event. This emphasizes a limitation which is common to all the previous observations cited above: none of these studies deal with observations from more than two events. Results obtained from the analysis of only one or two flare events are subject to the severe limitation that the

solar and interplanetary parameters which determine the behavior of the particle flux near the earth can vary significantly from one solar flare event to the next. Thus, although it is now well established that large scale structure in the polar cap flux of low energy protons is not uncommon, aside from the indications that interplanetary flux anisotropies play a role in the observations of north/south asymmetries, the relationship between polar cap fluxes and interplanetary particle fluxes is still unresolved.

The high time, energy, and flux resolution of the data presented in this thesis make them particularly appropriate to an investigation of low energy charged particle access to the polar caps. As suggested by Vampola [27], low rigidity electron observations can be used to map the geomagnetic tail field lines onto the polar caps in order to determine the polar cap boundary between open and closed geomagnetic field lines; the 333 observations of this boundary reported here will result in a much more comprehensive mapping than the 25 such observations previously available [27]. The proton observations reported herein differ from the observations cited above in at least two important aspects: (1) the availability of data throughout an eighteen month period has resulted in the compilation and analysis of fifty-four solar proton events rather than one or two, and (2) some of these events represent the first polar cap observations of fluxes associated with regions of enhanced flux in interplanetary space which are co-rotating past the earth. These observations will be interpreted in terms of the locations of the access windows for 1.2-40 MeV protons for the different regions of the polar

caps. The configuration of these access windows will then be related to the magnetospheric models mentioned above, and hence to the question of magnetic field merging.

## II. INSTRUMENT

The detector system used in this study consists of two independent particle telescopes, each designed (a) to optimize charge and energy resolution within a range of incident particle energies, and (b) to be sensitive and operable over a wide range of incident particle fluxes. Because of their orientations on the spacecraft (see Section III), these telescopes are referred to as the vertical telescope and the horizontal telescope. Measurements consist of the counting rates, energy loss, and range of incident particles [28].

The rapid motion of a polar orbiting satellite with respect to the geomagnetic field subjects a detector system on board to rapid fluctuations in incident fluxes, due to changing geomagnetic cutoffs and trapped particles. This tends to place an upper limit on the sampling period for the various rates monitored by the system. In order to obtain adequate resolution of these fluctuations, the rates for this experiment were averaged over a maximum of 288 msec, during which time the spacecraft will have moved, typically, 1.1 minutes in latitude. Although this averaging rate represents the situation for the bulk of the data reported here (data which were collected on the on-board tape recorder), when the spacecraft telemetry was in the real time mode the averaging time is either 72 msec or 18 msec, depending on the exact telemetry configuration. Data collected in the real time mode are particularly

suitable to the study of phenomena closely related to the geomagnetic field, such as cutoffs.

### *Vertical Telescope*

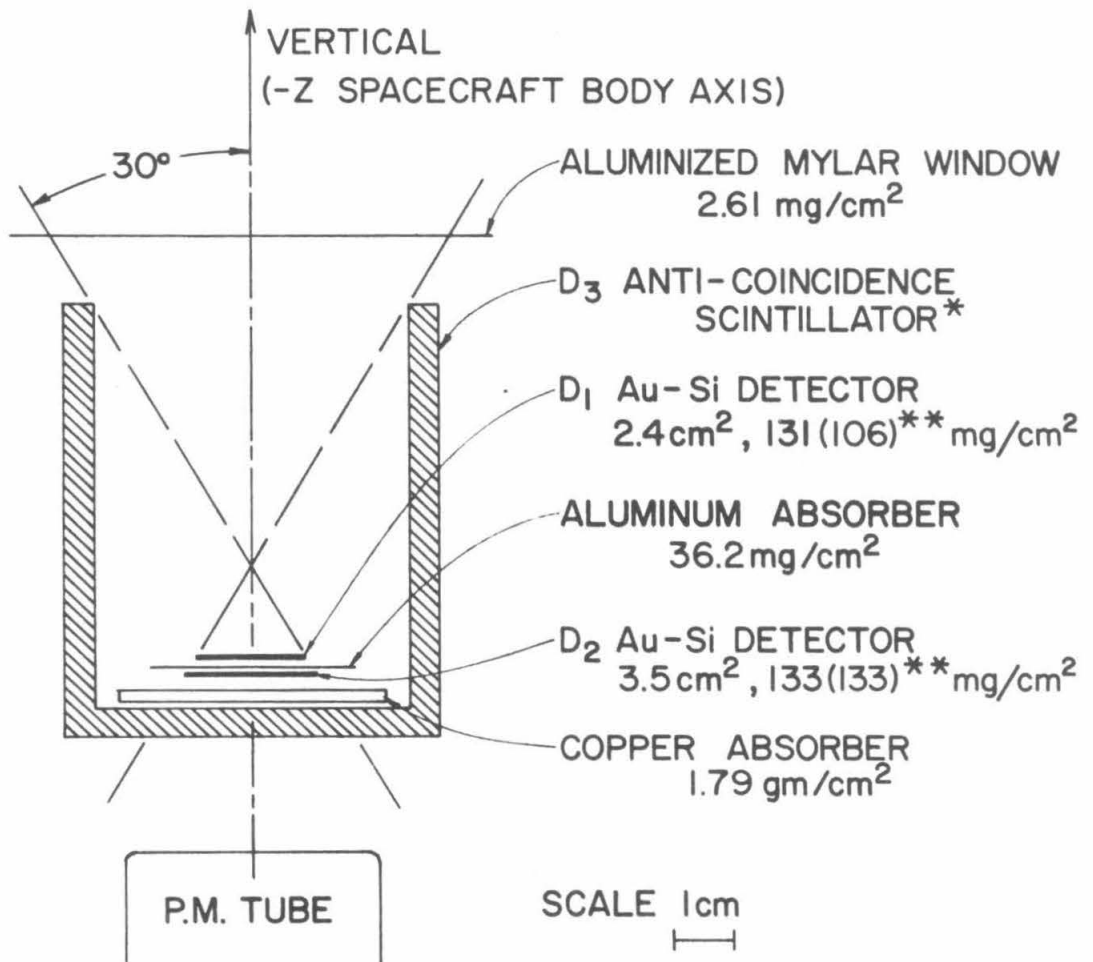
Figure II-1 shows a schematic cross sectional view of the vertical telescope, which consists of a stack of circular detectors and absorbers. From top to bottom, they are: a gold-silicon surface barrier detector, an aluminum absorber, another gold-silicon surface barrier detector, and a copper absorber. Such solid state detectors measure the energy lost by a charged particle passing through the sensitive region of the detector; the physical characteristics of these detectors and absorbers are given in table II-1. The detector stack is completely surrounded, except for the entrance aperture, by a cylindrical plastic scintillator cup, which serves to (1) collimate the response of the telescope, (2) help discriminate against side showers and nuclear interactions within the stack, and (3) determine the high energy analysis limit ( $\sim 40$  MeV/nucleon) for the system. The entrance aperture is covered by a  $3/4$  mil (0.00075 in) aluminized mylar light baffle; the thickness of this baffle contributes significantly to the low energy threshold (1.21 MeV/nucleon) of the telescope.

Incident particles are analyzed only if not registered in the anti-coincidence detector  $D_3$ . The number of particles with energy losses above an electronically determined threshold in  $D_1$  and  $D_2$  are recorded, along with the number of  $D_1D_2$  coincidences. In addition, the energy

Figure II-1

Schematic cross section of vertical telescope.

# OGO-II, IV VERTICAL PARTICLE TELESCOPE



\* SCINTILLATOR IS SURROUNDED BY 138  
mg/cm<sup>2</sup> OF MAGNESIUM.

\*\* VALUES FOR OGO-IV ARE IN PARENTHESES.

D<sub>1</sub> AND D<sub>2</sub> BOTH HAVE DEPLETION  
DEPTHS OF 56 mg/cm<sup>2</sup>.

Table II-1

Physical Properties of Detectors and Absorbers  
in the Vertical and Horizontal Telescopes

Detector/Absorber	Material	Thickness (mg/cm <sup>2</sup> )	Sensitive Area (cm <sup>2</sup> )
Window (Vertical)	Mylar	2.6 ± 0.2	-
D <sub>1</sub> (Total) (Depletion region)	Silicon	106 ± 2 56 ± 5	2.4 (nom.)
Absorber	Aluminum	36 ± 4	-
D <sub>2</sub> (Total) (Depletion region)	Silicon	133 (nom.) 56 (est.)	3.5 (nom.)
Absorber	Copper	1790 ± 45	-
Inner housing	Magnesium	138 ± 9	-
D <sub>3</sub>	Plastic Scintillator	505 ± 27	-
Window (Horizontal)	Mylar	1.22 (nom.)	
H <sub>1</sub> (Total) (Depletion region)	Silicon	11.7 (nom.) 5.8 (nom.)	0.079 (nom.)



lost in  $D_1$  is measured for one event during each sample period. The number of particles measured by  $D_3$  are also recorded. The electronic configuration and the geometrical factors for the various rates are discussed in more detail below.

As noted in table II-1, the detectors used in this experiment are not fully depleted; fully depleted detectors with such large sensitive areas were not available when this experiment was designed. As will be noted below, the non-uniformity of the depletion depth over the sensitive area of the detector was one of the principle factors which limited the resolution of the pulse height analysis of the output from  $D_1$ .

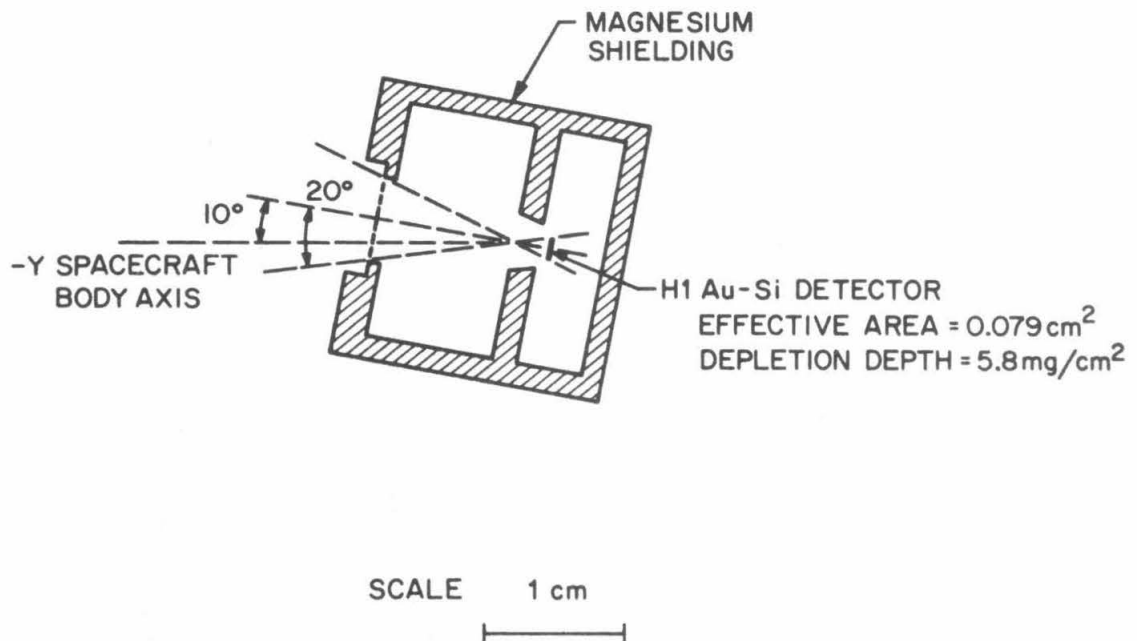
#### *Horizontal Telescope*

A schematic cross section of the horizontal telescope is shown in figure II-2. This telescope, which is considerably smaller than the vertical telescope, consists of a single gold-silicon surface barrier detector completely surrounded, except for the entrance aperture, by a magnesium shield. As in the vertical telescope, the entrance aperture is covered by a 0.00035 in. aluminumized mylar light baffle. The physical characteristics of the horizontal detector and window are included in table II-1. It should be noted that the collimation for this telescope is passive, in contrast to the active collimator available for the vertical telescope. The effect of this difference on the response of these two telescopes is indicated below in connection with the energy dependent geometrical factors. All charged particles losing more energy

Figure II-2

Schematic cross section of horizontal telescope. Note that the scale used here is different than that used in figure II-1.

## OGO-II, IV HORIZONTAL PARTICLE TELESCOPE



in the sensitive region of the detector than the electronically determined threshold are counted.

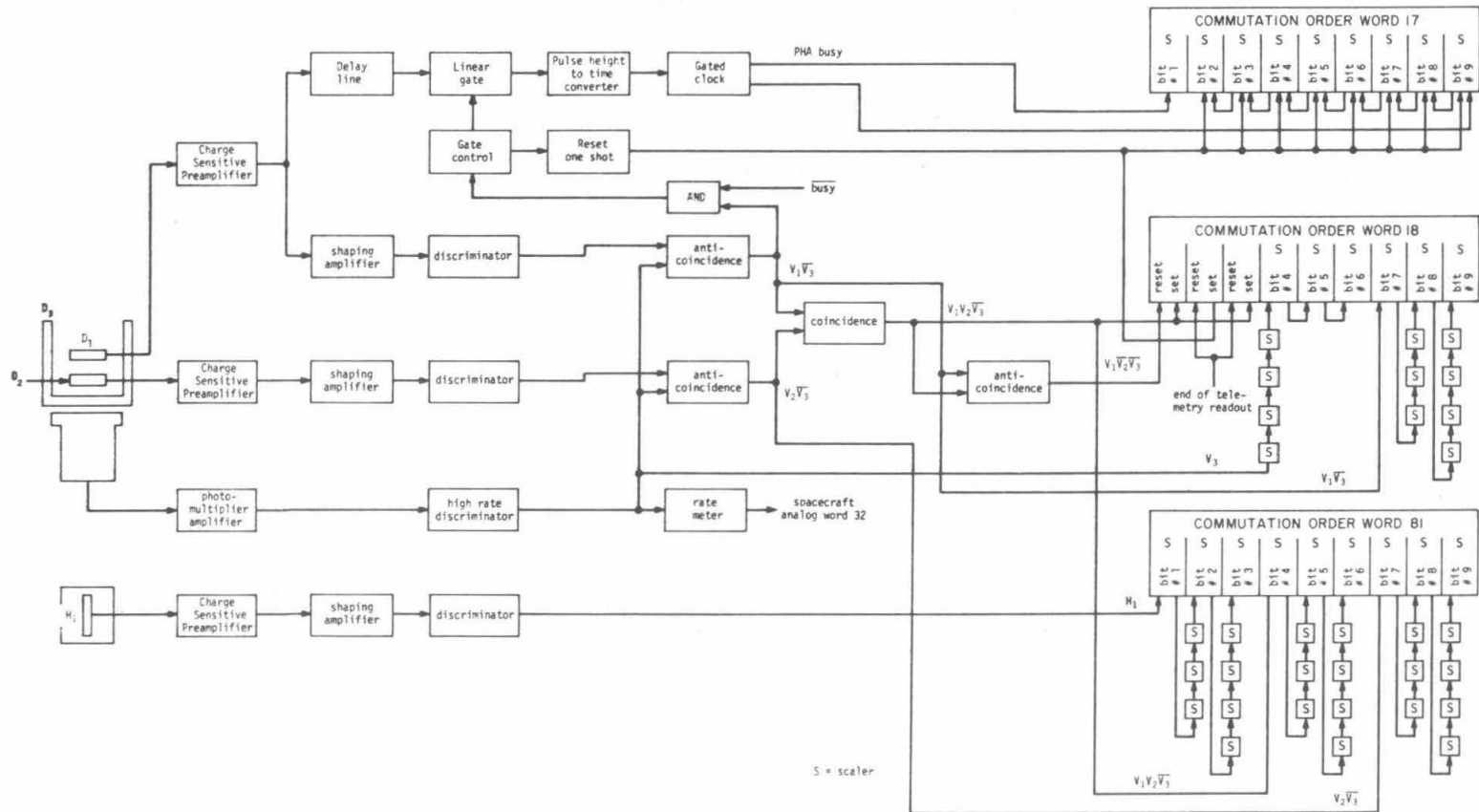
### *Electronics and Data Formatting*

The block diagram in figure II-3 illustrates the logic configuration of the electronics system associated with the two charged particle telescopes and the format in which the data are stored in the spacecraft. The details of the electronic components are similar to those for Experiment F-20 on OGO-6 which were specified in a paper presented to the Fourteenth Nuclear Science Symposium of the IEEE in 1967 [29]. As indicated on this figure, the following information is stored by this experiment:

1. The  $2^0$ ,  $2^4$ , and  $2^9$  bits of the recycling scalars corresponding to the number of counts from the following four logic configurations:  $V_1\overline{V_3}$ ,  $V_2\overline{V_3}$ ,  $V_1V_2\overline{V_3}$ , and  $H_1$  ( $V_1 \equiv D_1$ ,  $V_2 \equiv D_2$ ,  $V_3 \equiv D_3$ ).
2. The  $2^4$ ,  $2^5$ , and  $2^6$  bits of a recycling scalar associated with the number of  $V_3$  counts.
3. A 256-channel pulse height analysis of the amount of energy deposited in  $D_1$ . Only one such analysis can be stored; the contents of word 17 are erased prior to storing a new event analysis. Thus only the last event analyzed before each readout is available.
4. Flags indicating whether the pulse height analyzed event is a new event (since the last telemetry readout) and whether the threshold of  $D_2$  was exceeded on the event analyzed.

Figure II-3

Functional block diagram of electronics system.



5. A digitization of an analog rate meter connected to the output of the  $V_3$  discriminator.

The spacecraft telemetry will be discussed in Section III.

### *Thresholds and Calibrations*

The electronic thresholds associated with the discriminators of the four detectors were set so as to minimize the contamination due to background noise. The values of these thresholds in terms of detector output and of incident particle energy were determined by electronic and particle calibrations. The electronic calibrations give a precise determination of the discriminator thresholds and pulse height analyzer response as a function of charge at the input to the charge sensitive pre-amplifier, while the particle calibrations enable a determination of the response and resolution of the detectors.

In order to interpret these calibrations in terms of the response of the telescope, interpolations were made in the range-energy loss tables given by Janni [30] wherever necessary. These tables were generated by integrating a semi-empirical expression for the energy loss of a charged particle passing through a homogeneous material. The calibrations are described in more detail in a Space Radiation Laboratory Internal Report [31].

The results of the electronic calibrations of the detector thresholds are given in table II-2.

Table II-2  
Energy loss thresholds for OGO-4 detectors

Detector	Threshold (25 °C)	Temperature Coefficient
D <sub>1</sub>	424±22 keV	0.0 keV/°C
D <sub>2</sub>	253±23 keV	0.3 keV/°C
D <sub>3</sub>	53±3 mV	-0.1 mV/°C
H <sub>1</sub>	377±14 keV	0.6 keV/°C



By using the range-energy loss tables mentioned above, the correspondence between the pulse height analyzer channel thresholds and incident proton energy can be determined. This is shown in figure II-4. An important facet of the correspondence shown in this figure is that for channel numbers greater than 29 (and less than 72) two incident proton energies can be associated with each channel threshold. Below channel 29, the availability of the range information provided by  $D_2$  makes the association between incident proton energy and channel threshold unique. The effect of these *double-valued* pulse height analyzer channels on the analysis of the data will be discussed in Section IV.

The proton response of the vertical telescope was determined by exposing the assembled telescope to a series of proton beams using the Caltech Tandem Van de Graff accelerator [31].

The electron response of the detectors in the vertical telescope was determined by exposing nearly identical detectors to the beam of a magnetic spectrometer [32]. Electron geometrical factors as a function of energy for  $D_1$  and  $D_2$  determined in this manner are given in figure II-5. It is clear from these results that the electron sensitivity of the  $V_1V_2\overline{V_3}$  rate is negligible. The thin depletion depth and high electronic threshold of the  $H_1$  detector insure that the electron sensitivity of the  $H_1$  rate is  $< 10^{-4}$  [33].

The incident energy ranges corresponding to the rates measured by this experiment are summarized in table II-3. In addition to the average geometrical factors included in table II-3, energy dependent proton

Figure II-4

Correspondence between pulse height analyzer channel thresholds and incident proton energy (incident in mylar window). The  $D_1$  discriminator level is indicated, along with the energies corresponding to the triggering of  $D_2$  and  $D_3$ . The alpha particle response is also shown. Note the set of channels for which there is no one-to-one correspondence between channel threshold and incident proton energy. These channels are referred to as *double-valued*.

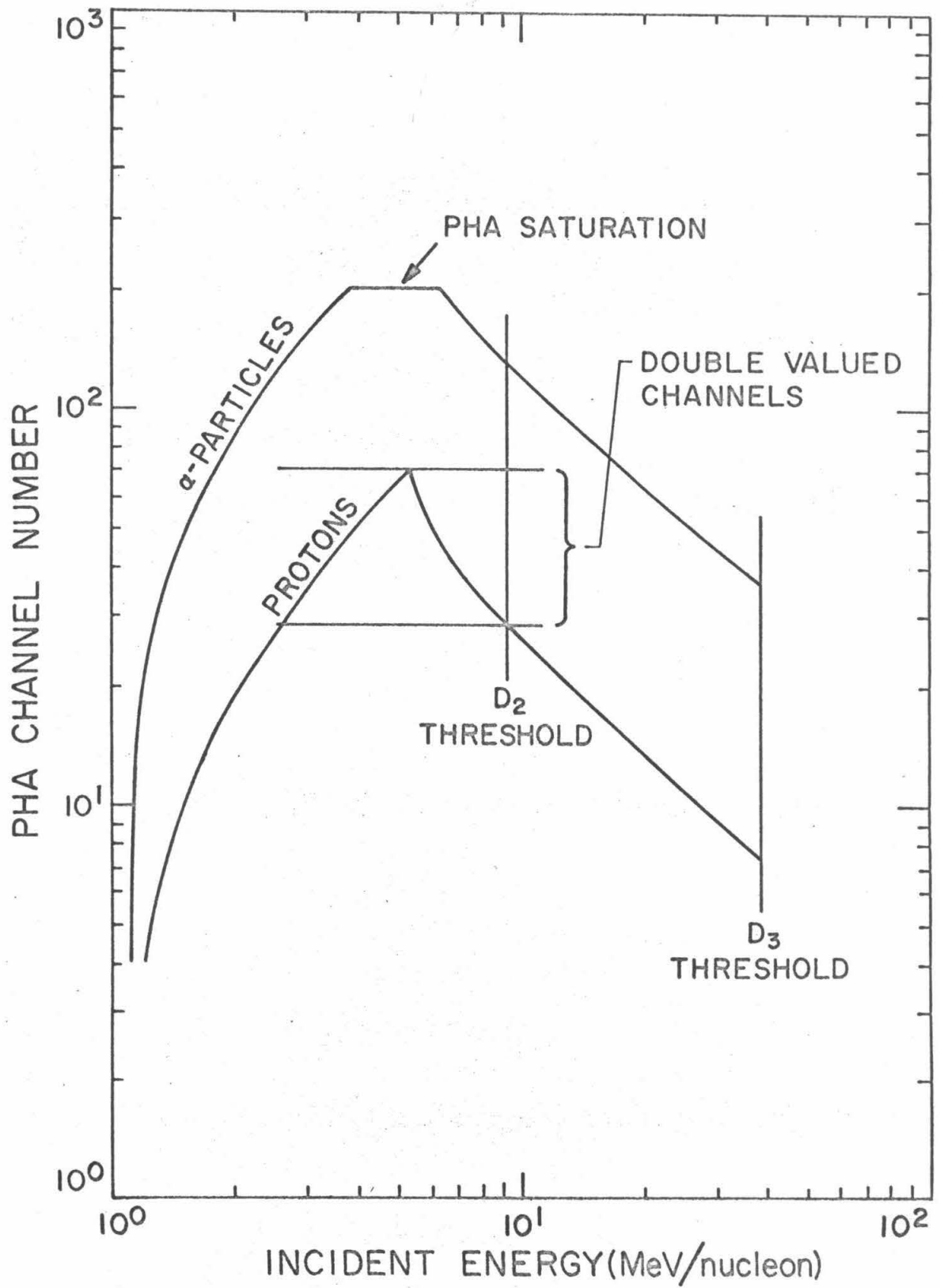


Figure II-5

Electron geometrical factors for  $V_1\overline{V}_3$  and  $V_2\overline{V}_3$  rates.

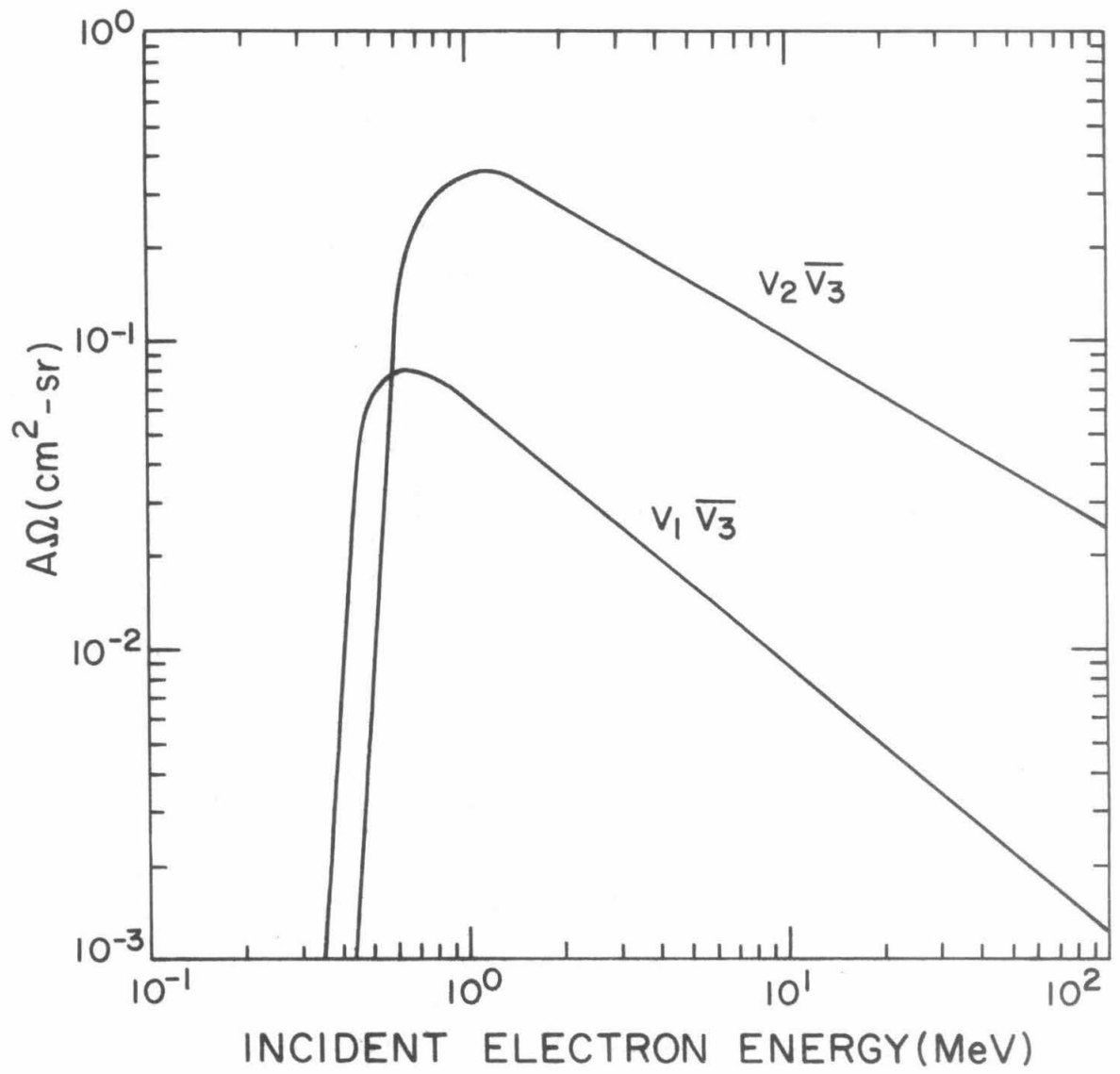


Table II-3  
Incident Energy Ranges Corresponding to  
Electronic Rate Configurations

Rate Configuration	Incident Energy Range		Approximate Geometrical Factors ( $A\Omega$ ) ( $\text{cm}^2\text{-sr}$ )	
	Electrons (MeV)	Nuclei (MeV/nucleon)	Electrons	Nuclei
$V_1\overline{V_3}$	0.45-1.8	1.24-40.4	0.08	1.06
$V_2\overline{V_3}$	0.67-2.5	9.3-40.4	0.36	1.42
$V_1V_2\overline{V_3}$	0.67-1.8	9.3-40.4	$10^{-3}$	1.16
$H_1$	---	0.88-~4.5	$10^{-4}$	0.013
$V_3$	0.53	37.	?	?

geometrical factors have been calculated for all rates but  $V_3$  using a Monte Carlo technique. These are shown in figures II-6 and II-7. Comparing these two figures, the effect of the passive collimation in the horizontal telescope is clear: the high energy response of the  $H_1$  rate is quite complex.

Figure II-6

Energy dependent geometrical factors for the  $V_1\overline{V}_3$ ,  $V_2\overline{V}_3$ , and  $V_1V_2\overline{V}_3$  rates.



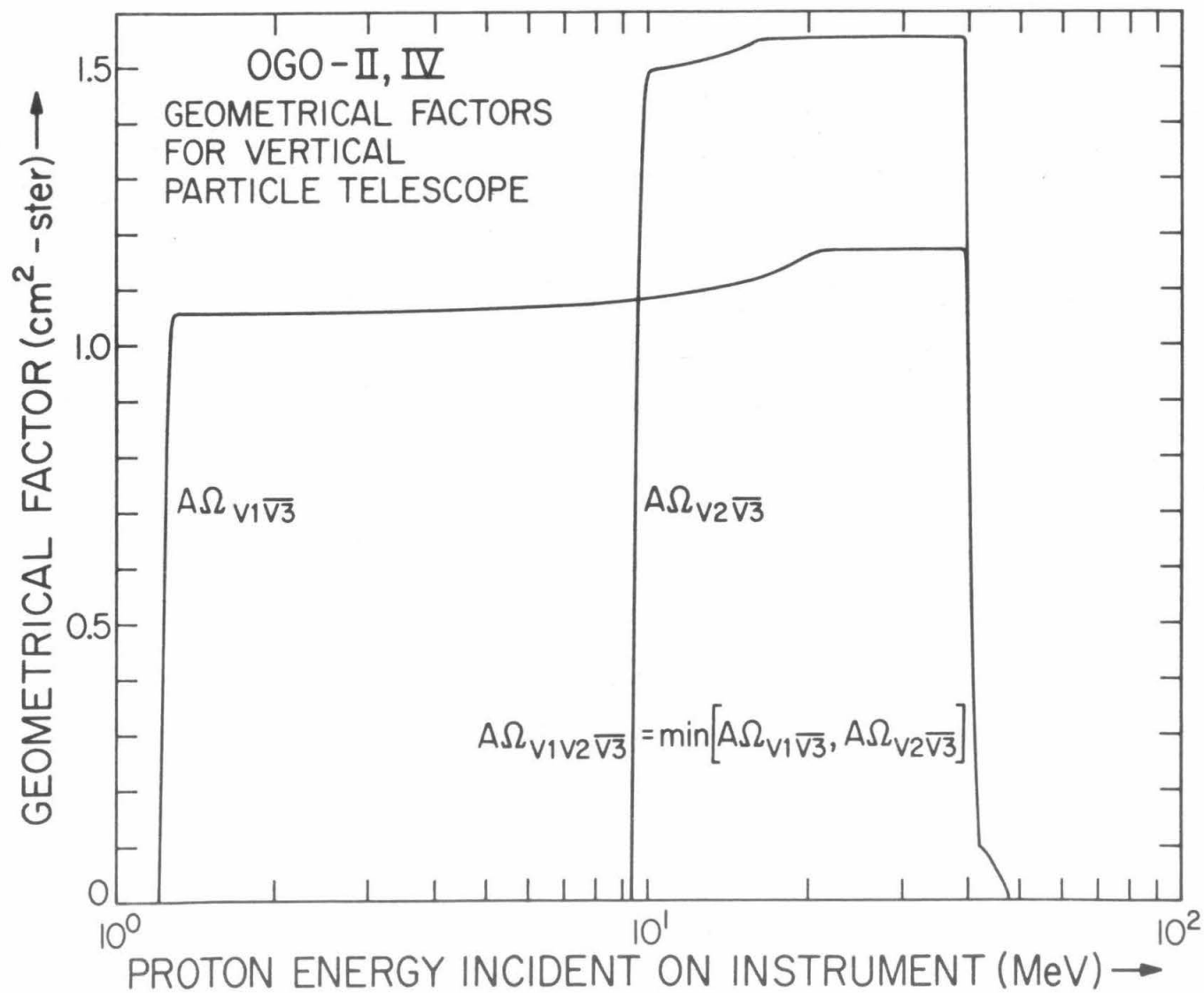
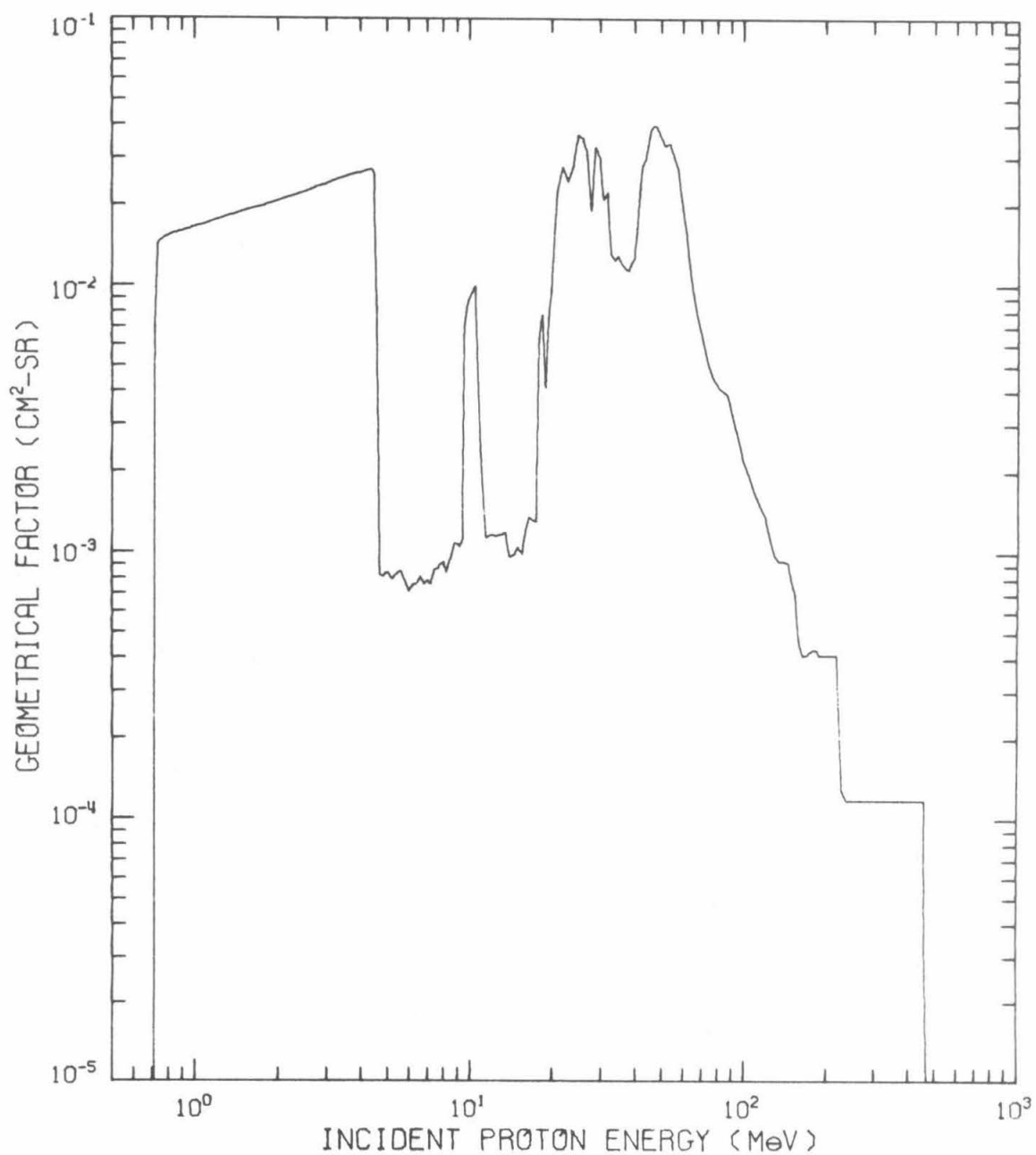


Figure II-7

Energy dependent geometrical factor for the  $H_1$  rate.

OGO-IV HORIZONTAL TELESCOPE  
GEOMETRICAL FACTOR

### III. SATELLITE

OGO-4 is the fourth in the series of six Orbiting Geophysical Observatory satellites sponsored by the National Aeronautics and Space Administration. This satellite was launched from the Pacific Missile Range on 28 July 1967 into an orbit with an initial inclination of  $86^\circ$ , apogee of 908 kilometers, perigee of 412 kilometers, and orbital period of 98 minutes [34].

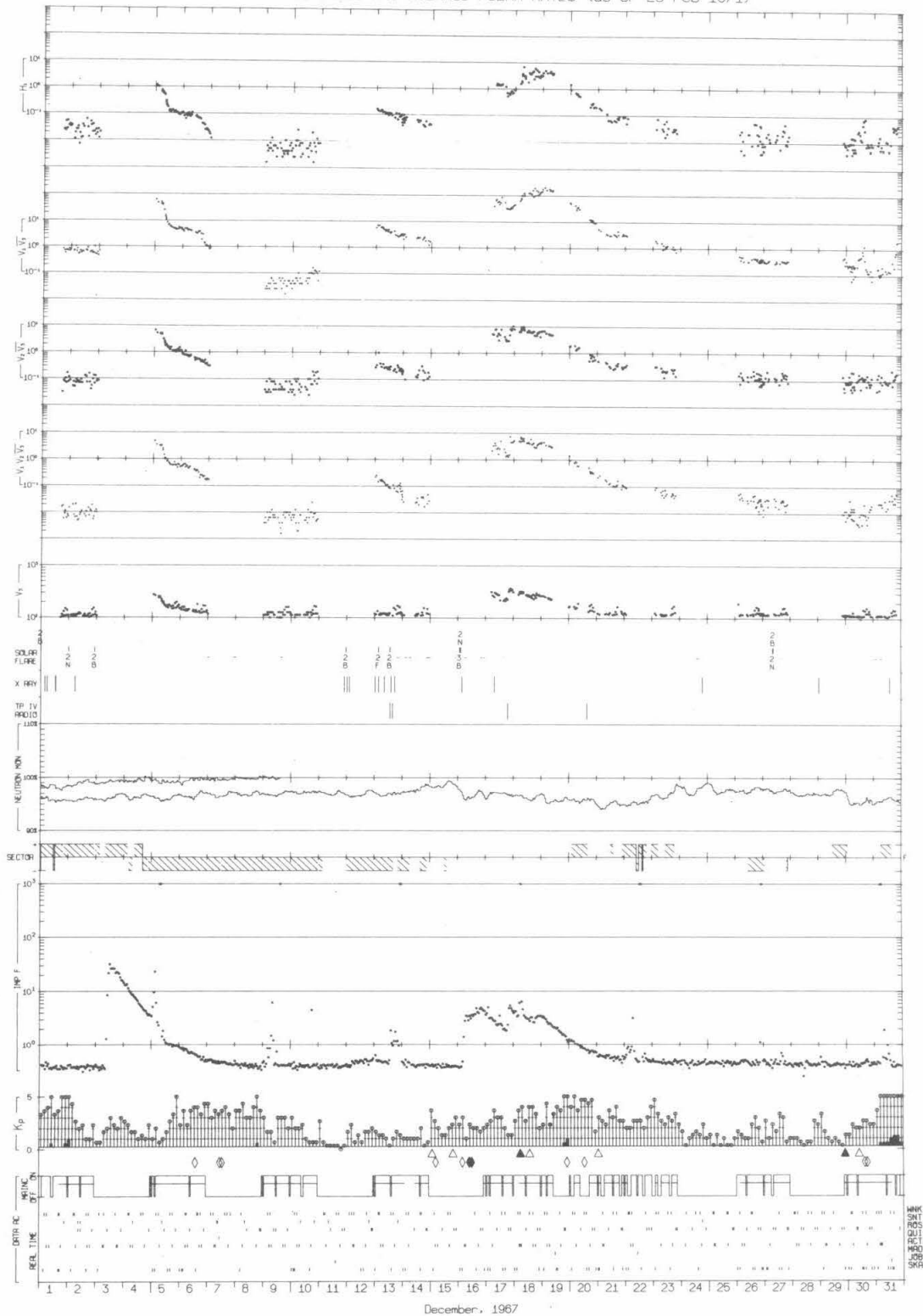
The instrument described in Section II was mounted on the spacecraft so that only particles incident on the vertical telescope from directions within  $30^\circ$  of the zenith do not trigger the anti-coincidence counter,  $D_3$ , prior to passing through the solid state detectors,  $D_1$  and  $D_2$  (see figure II-1). Similarly, the horizontal telescope was mounted so that collimated particles represent particles incident from directions nearly perpendicular to the zenith.

Because of a need to time-share the spacecraft telemetry facilities between two sets of experiments, the data collected by this experiment were only available about 50% of the time: often in two day periods separated by two day gaps in the data. The effect of this telemetry configuration on the data from this experiment is illustrated in the OGO-4 Data Coverage Plots [35]; figure III-1 is a typical example of these plots.

Figure III-1

A typical example of the OGO-4 Data Coverage Plots. An explanation of the information displayed on this figure is given by Evans [35], where a complete set of these plots covering the entire period during which at least one of the OGO-4 tape recorders was operable will also be found. These plots are designed to fulfill the dual purpose of indicating the availability of the data from this experiment and of comparing these data to other geophysical, interplanetary, and solar data of interest.

## OGO-4 DATA COVERAGE AND AVERAGE POLAR RATES (as of 28 Feb 1971)



December, 1967

The spacecraft was deactivated on 23 October 1969, but the failure of the second of the two on-board tape recorders on 19 January 1969 represented, at least for this study, the practical limit of the period for which useful data are available.

The trajectories of OGO-4 during several typical orbits mapped onto a polar representation of geocentric latitude *vs.* geocentric longitude are shown in figure III-2. As the plane of the satellite orbit remains relatively stationary in space, the earth rotates under the satellite, causing the apparent shift in the trajectories. Contours of constant invariant latitude ( $\Lambda$ ) [36] are also projected into this coordinate system for reference; it should be noted that some of the orbits reach a much lower maximum invariant latitude than others, especially in the south.

Since many of the charged particle effects which can be measured by this experiment are closely related to the geomagnetic field and the sun-earth-satellite orientation, the data observed with OGO-4 can be more efficiently organized in a coordinate system reflecting the position of the satellite in the geomagnetic field and the sun-earth-satellite orientation. Of several coordinate systems reflecting these parameters, one of the most effective and widely used is that consisting of invariant geomagnetic latitude ( $\Lambda$ ) *vs.* magnetic local time (MLT) [37]. The trajectories shown in figure III-2, mapped into this system, are shown in figure III-3. It is clear that in this coordinate system the effects of the rotation of the earth are minimized, and the differences in maximum

Figure III-2

A projection of typical OGO-4 trajectories onto a polar representation of geocentric latitude *vs.* geocentric longitude. Projections of these trajectories onto both geographic poles are shown for comparison, and contours of constant invariant geomagnetic latitude ( $\Lambda$ ) are indicated.



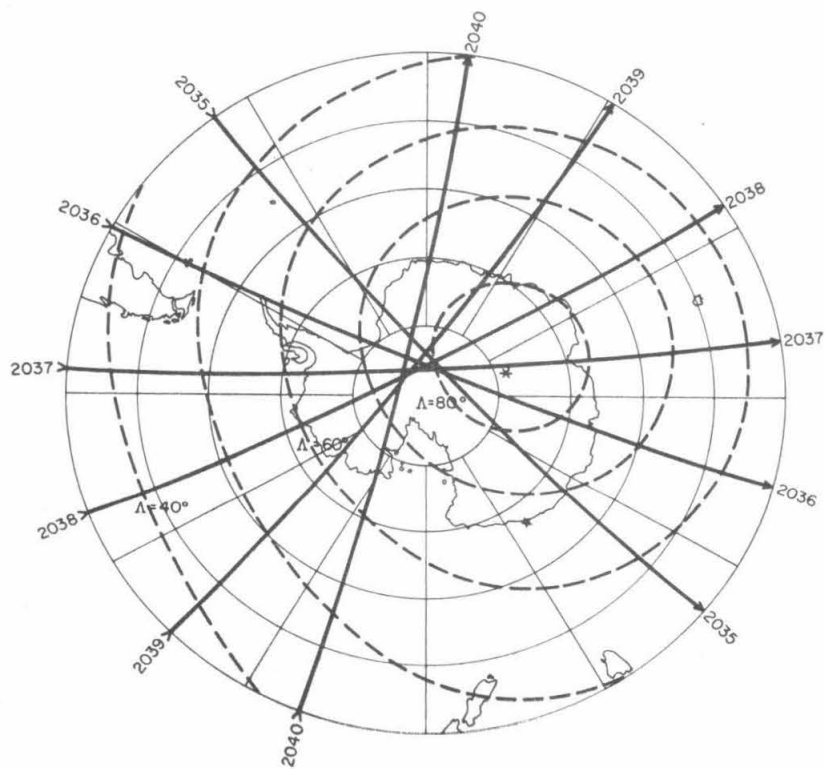
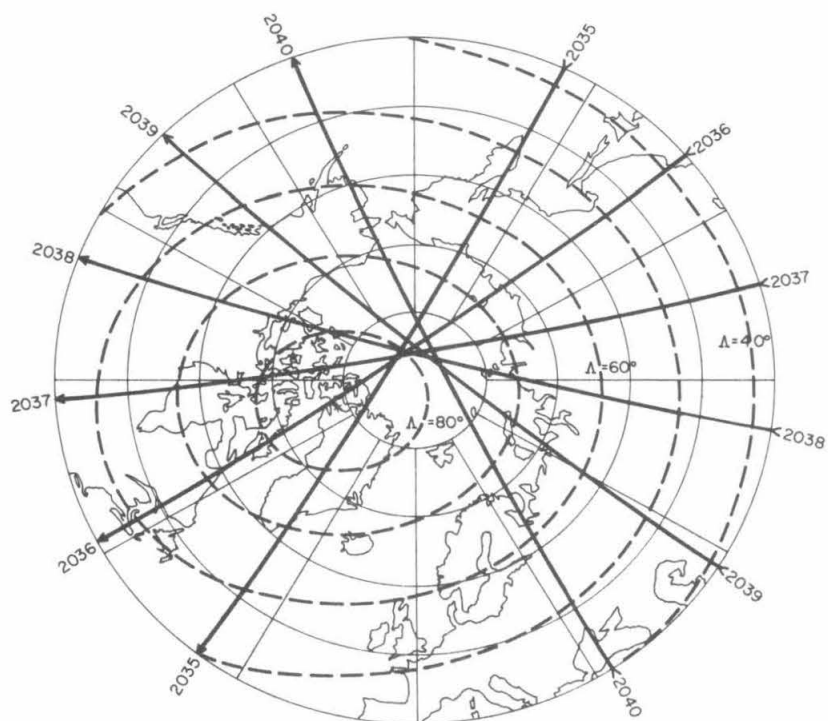
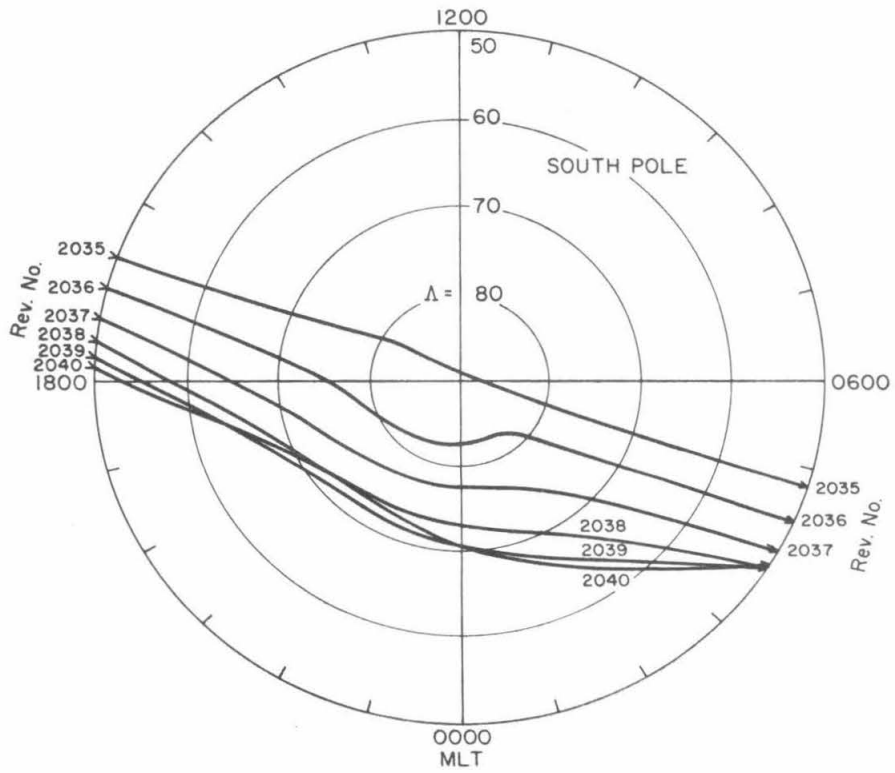
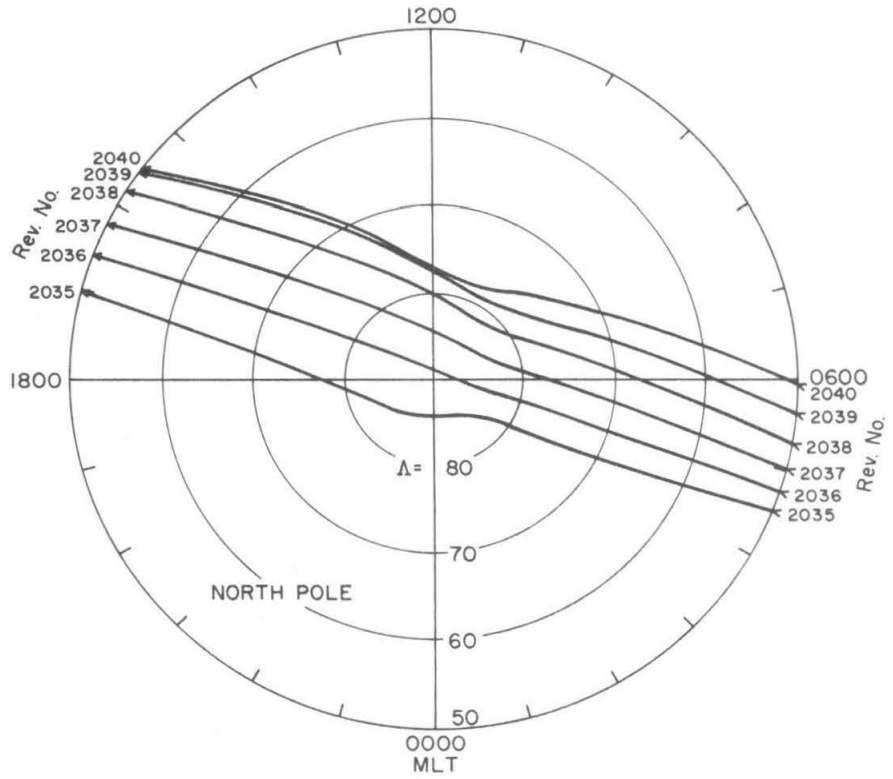


Figure III-3

A projection of the sameOGO-4 trajectories shown in figure III-2 into a geomagnetic coordinate system: invariant latitude ( $\Lambda$ ) *vs.* magnetic local time (MLT). The field coefficients given by Cain,*et al.* [38] were used to calculate  $\Lambda$ .



invariant latitude are depicted more explicitly.

Since for the bulk of the observations reported here a critical distinction will be made between data collected at low and high polar geomagnetic latitudes (see section V), the data collected during polar passes such as 2039 and 2040 in the north and 2038, 2039 and 2040 in the south may be seriously degraded due to the limited degree to which the satellite penetrates to high geomagnetic latitudes.

#### IV. DATA ANALYSIS

The processing scheme used for the data from this experiment is illustrated by the block diagram shown in figure IV-1. The data came to Caltech stored on two classes of magnetic tapes: experimenter tapes and attitude-orbit tapes. The former contained the decommutated data for this experiment, while the latter provided the position and orientation of the spacecraft as a function of time (one point per minute) calculated from data collected by tracking stations. The information from these two classes of tapes was interleaved, time ordered and stored on a third class of magnetic tape, referred to as an abstract tape. The study being reported here has involved the processing of data from a total of 931 magnetic tapes, representing almost 300,000 minutes ( $\sim 62 \times 10^6$  read-outs) of playback data. The format of the data on these tapes is described elsewhere [39].

A complete collection of plots showing the detector rates as a function of time [28] serve as a catalogue of these data from which one can evaluate the performance of the experiment and specify the periods of data most suitable for a particular study. With this information any of the other programs indicated on figure IV-1 can be employed.

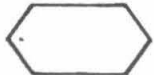
The calculation of rates for the output of the solid state detectors is complicated somewhat by the fact that only the  $2^0$ ,  $2^4$  and  $2^9$

Figure IV-1

Block diagram representation of the procedure developed to process OG0-4 data at Caltech. The symbolism used is as follows:



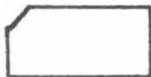
= magnetic tape



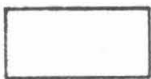
= computer program (program names are given in capital letters.)



= branch (decision)

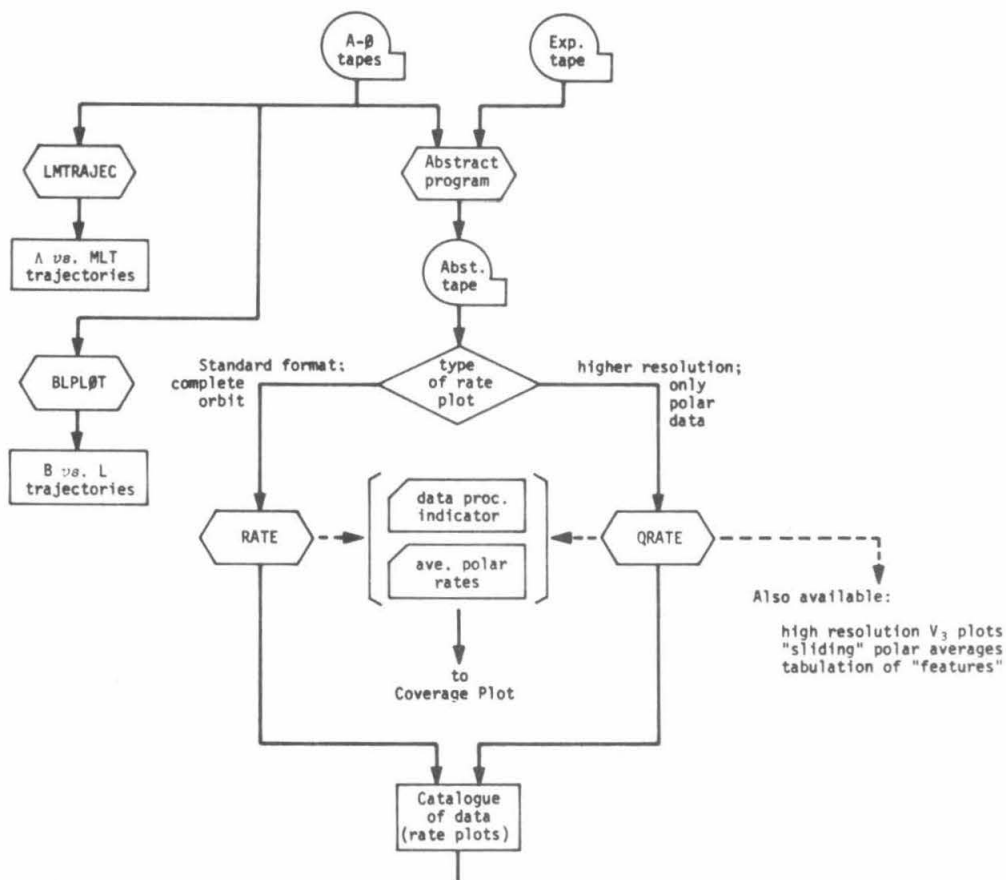


= cards punched



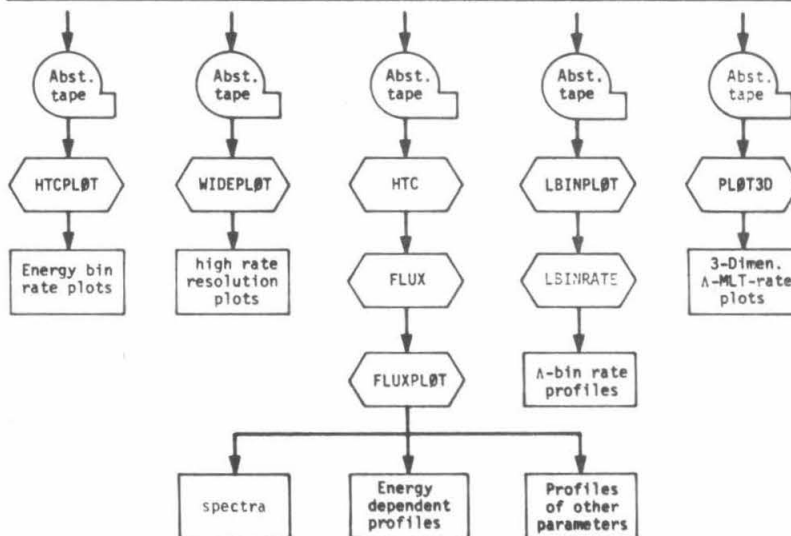
= results (only the resultant plots are shown on this diagram; each program has the option of tabulating results as well.)

The rate plots, which constitute the data catalogue, are discussed by Evans, *et al.* [28].



The decision at this point depends in the type of problem being studied and the available data as indicated on the rate plots and OGO-4 Data Coverage Plots.

Some of the choices currently available are indicated.



bits of the rate scalers are recorded. Figure IV-2 illustrates that special care must be exercised in the calculation of rates in some ranges, and that for detection rates above  $\sim 500$  counts per read-out ( $\sim 1740$  counts per second for playback data) an unambiguous determination of these rates can be made only in special circumstances.

Using the accumulation of many pulse height analyzed events along with the response curve shown in figure II-4 and the energy dependent geometrical factor illustrated in figure II-6, differential flux spectra can be calculated. However, as pointed out in connection with the  $D_1$  response curve (figure II-4), for a range of pulse height analyzer channels the correspondence between channel threshold and incident proton energy is not one-to-one. As a consequence, the spectra presented in Section V have been calculated using the iterative technique illustrated in figure IV-3.



Figure IV-2

Probabilities of a change occurring in the  $2^0$ ,  $2^4$  and  $2^9$ -bits of a detector scaler during one read-out as a function of the event rate expressed in counts/read-out.

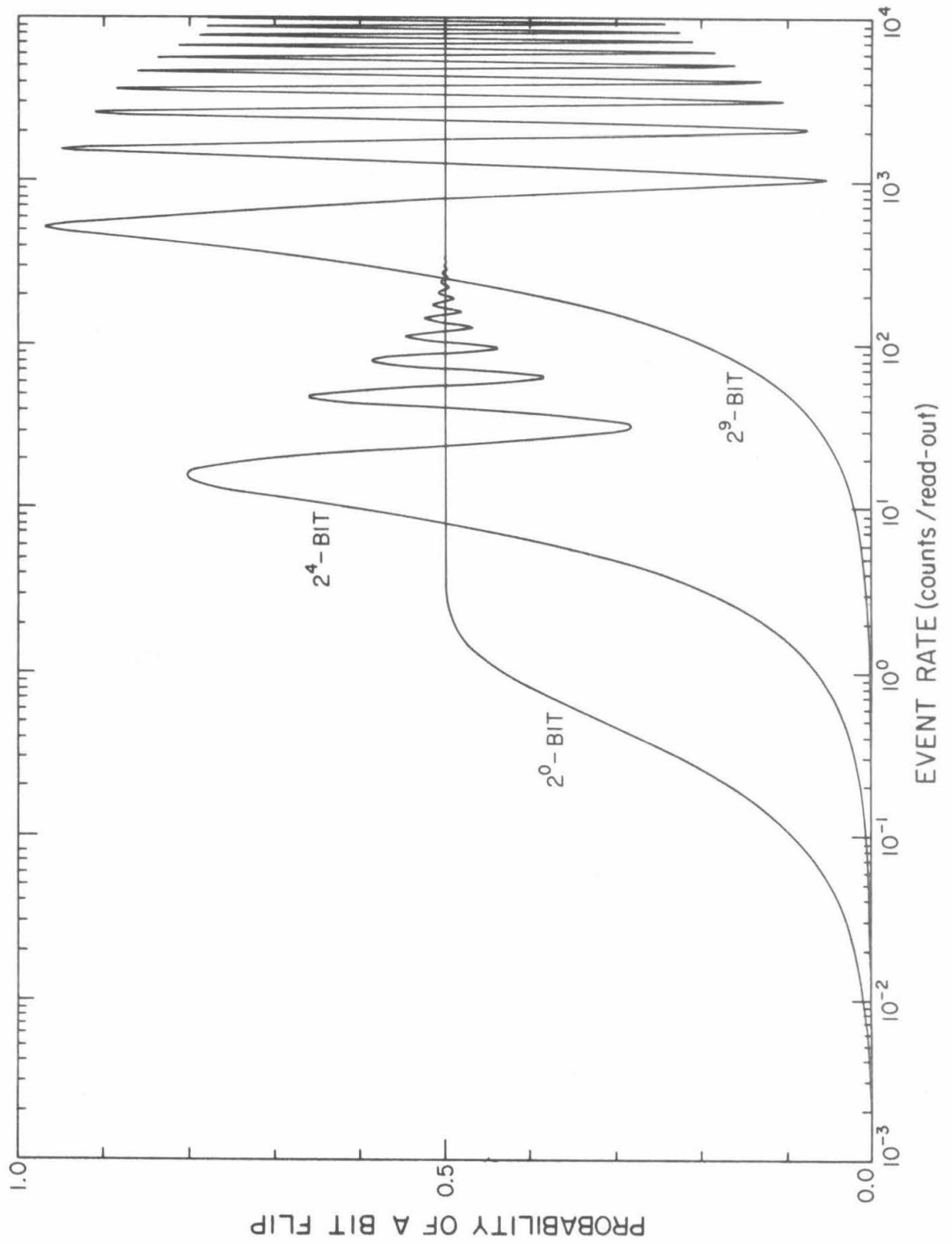


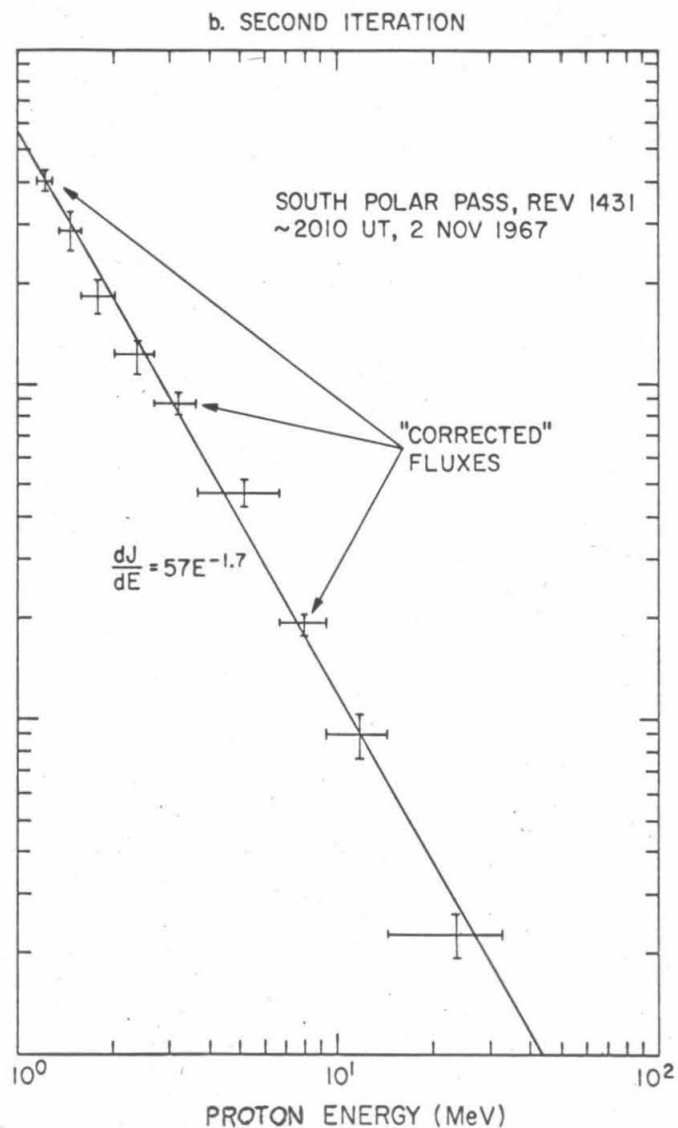
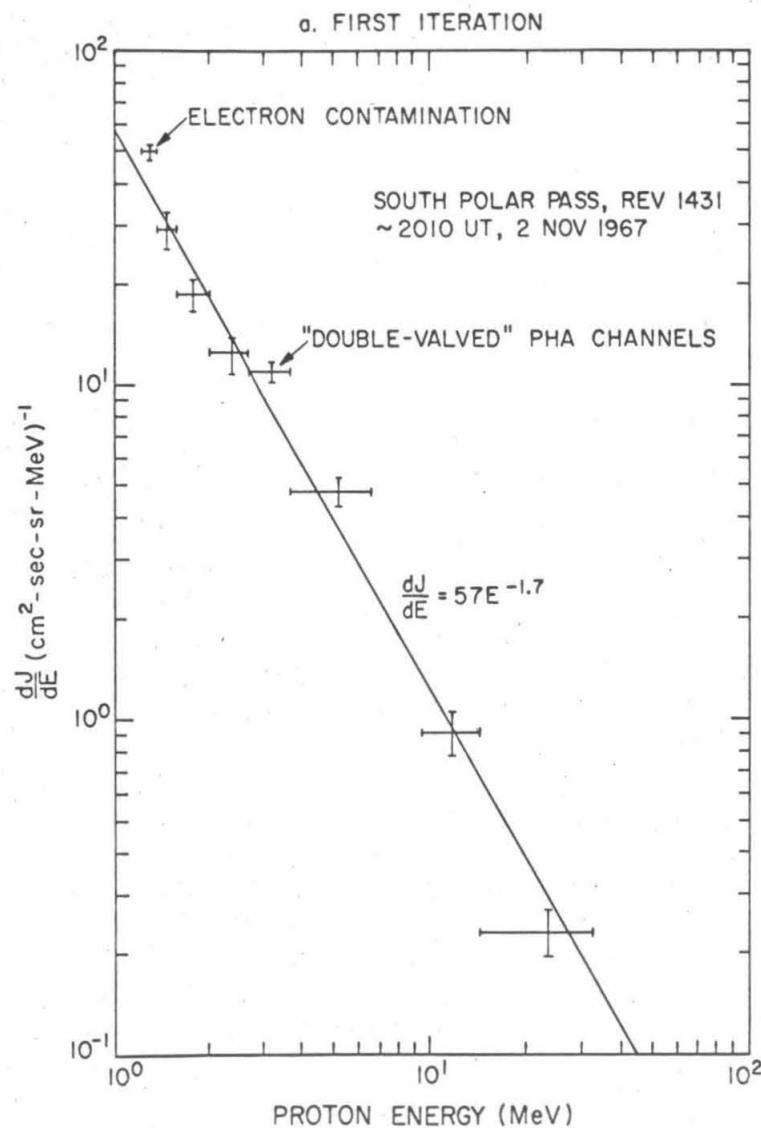
Figure IV-3

Iterative technique used to calculate differential energy spectra.

A spectrum is first calculated in a straightforward manner, and standard regression techniques are used to determine the "best" fit to

$$\frac{dJ}{dE} = AE^{-\gamma}$$

using only the points for which the energy identification is unique (figure IV-3a). This function is then used to determine the proportion of events in a double valued energy bin to be assigned to each energy interval corresponding to the group of pulse height analyzer channels involved. The flux for this group of channels is then recalculated. The results of this procedure (figure IV-3b) are valid (for the affected points) only to the extent that the actual spectrum agrees with the function used to approximate it.



## V. OBSERVATIONS

Utilizing the data processing procedure outlined in Section IV, many of the available data from OGO-4 have been processed. The OGO-4 Data Coverage Plots [35] indicate the periods during which data were available, and also indicate for which of these periods the data have been processed. These data are particularly appropriate to the study of the entry of solar particles into the earth's magnetosphere, and several periods have proven to be instructive. In addition to electron observations, two examples of proton observations will be presented as illustrative of the type of observations available. A more complete compilation of pertinent data, including those events presented here, is given in Appendix A.

### *Electron Observations*

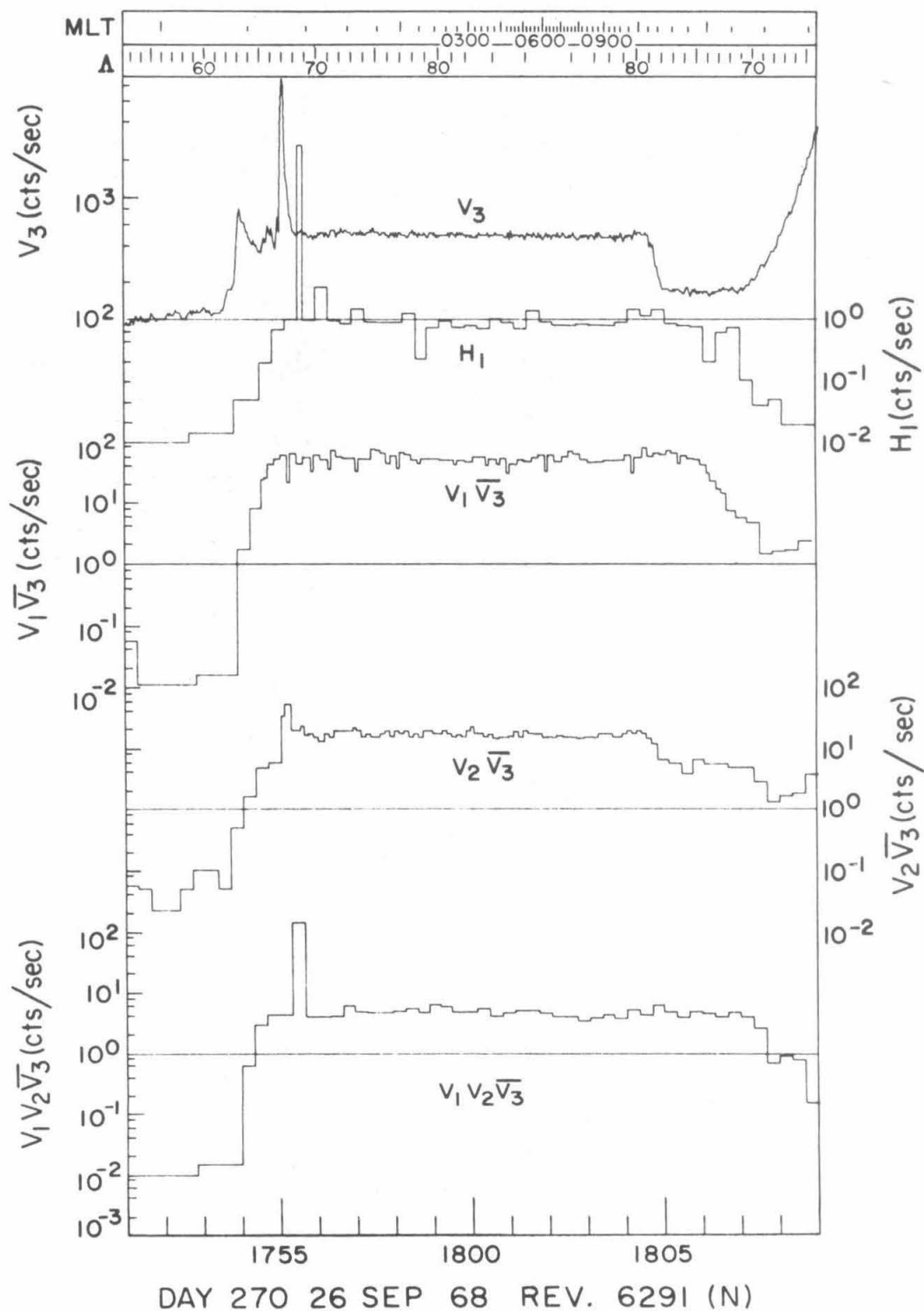
Although the instrument described in Section II was not designed primarily to detect electrons, several periods of high electron fluxes were observed in the polar cap regions on board OGO-4. Some of the characteristics of electron polar cap observations have previously been reported [27,40,41], but the data presented here provide, for the first time, a comprehensive mapping of the boundary of the electron polar cap region. As discussed in Section VII, this boundary represents the boundary between open and closed geomagnetic field lines.

As mentioned in Section II, the  $V_1\overline{V_3}$  and  $V_2\overline{V_3}$  rates are much less sensitive to electrons than to protons. Although the contribution of electrons to the observed rates varies considerably, it is typically  $\leq 15\%$  for the  $V_1\overline{V_3}$  rate and  $\leq 35\%$  for the  $V_2\overline{V_3}$  rate. In addition, we recall that the OGO-4 anti-coincidence scintillator,  $V_3$ , is sensitive to electrons above a threshold energy of  $\sim 530$  keV. Normally, then, electrons constitute a rather minor constituent of the observed rates. There are periods, however, when the electron flux is sufficiently high relative to the proton flux that electrons become an identifiable constituent of the  $V_1\overline{V_3}$ ,  $V_2\overline{V_3}$  and  $V_3$  rates. The identification of these periods and the identification of the rates as predominantly due to electrons is illustrated in figure V-1. The rates from this polar pass show a uniform electron polar cap flux between 1750:40 UT and 1805:40 UT; beyond 1806:00 the spacecraft had moved to invariant latitudes where the electrons did not have free access. That this enhancement can be associated strictly with electrons can be seen clearly by comparing the  $V_2\overline{V_3}$  rate (electrons and protons) with the  $V_1V_2\overline{V_3}$  rate (protons only). In order to improve the precision with which the electron polar cap boundary could be specified, the  $V_3$  rate was plotted on an expanded scale, shown in figure V-2a.

Figure V-2b illustrates that the edge of the electron polar cap was normally associated with an electron spike near magnetic local midnight (MLT  $\approx$  2100-0211). Figure V-2c is an example of an electron polar cap observation showing a particularly striking feature (i.e. the sharp depression at 0233:40 UT). These features were rarely observed and normally occurred only late during the recovery phase of a magnetic

## Figure V-1

Rates observed during a typical OGO-4 polar pass ( $\Lambda \geq 50^\circ$ ) illustrating an enhanced electron polar cap flux. These data are from the north polar pass of Rev. 6291 on 26 September 1968.





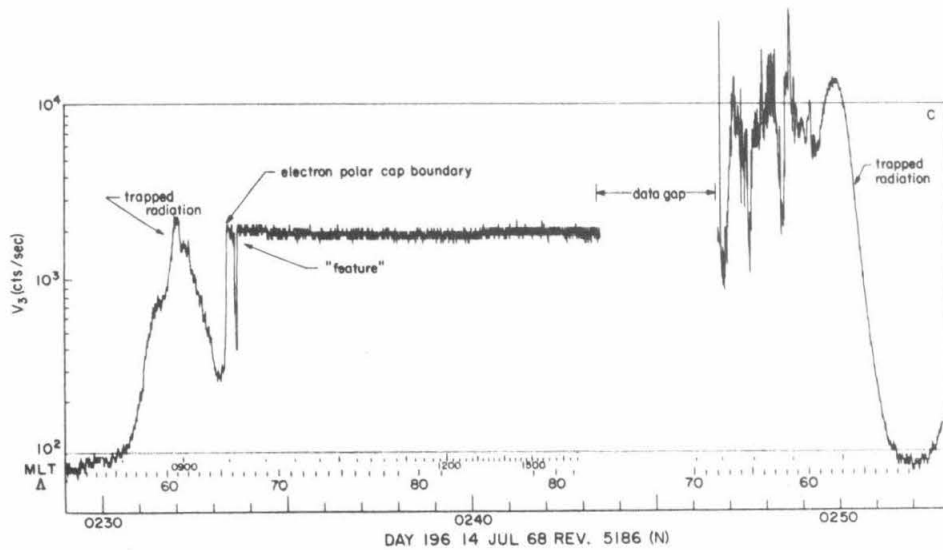
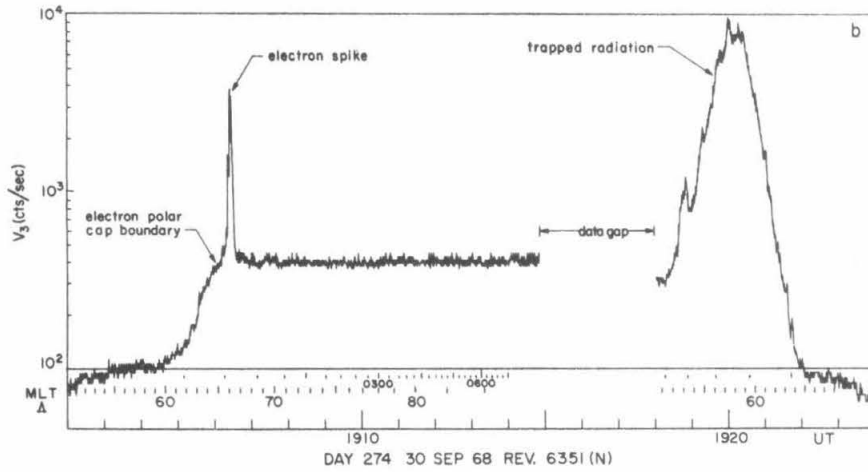
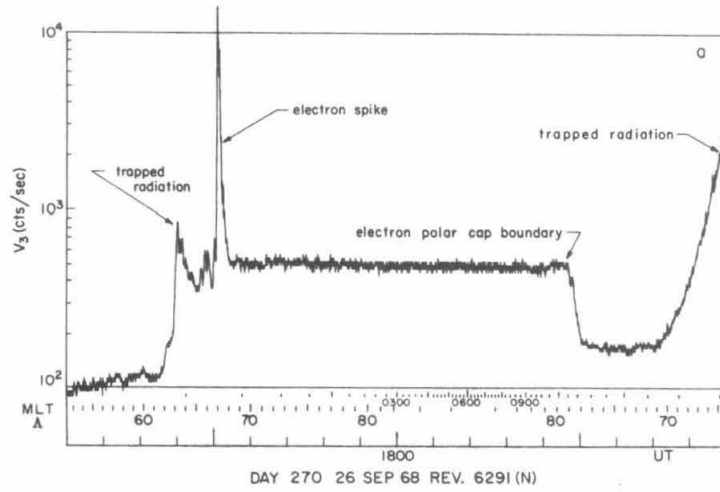
## Figure V-2

High resolution plots of the  $V_3$  rate, showing characteristic electron polar cap observations:

V-2a:  $V_3$  rate shown in figure V-1.

V-2b: An example of the type of electron spike associated with the edge of the electron polar cap between MLT  $\sim$  2100 and MLT  $\sim$  0200.

V-2c: An example of a well-defined feature in the electron polar cap flux. Such features were rarely observed.



storm.

A total of 333 such observations were made during magnetically quiet periods, and the resultant map of the electron polar cap boundary is shown in figure V-3. Here the geomagnetic coordinates (invariant latitude and magnetic local time) of each observation of the boundary are indicated by a symbol. The apparent dependence on geomagnetic activity will not be discussed here. The values reported by Vampola [27], which he extrapolated to magnetically quiet conditions, are shown for comparison.

We can now define the following terms with respect to the electron results from this experiment: *high polar latitudes (HPL)* and *low polar latitudes (LPL)*. High polar latitudes will refer to the invariant latitudes between the electron polar cap boundary and the geomagnetic pole; low polar latitudes will refer to the invariant latitudes between geomagnetic cutoff for 1.2-40 MeV protons (below which polar proton fluxes cannot be observed due to the Earth's magnetic field) and the electron polar cap boundary. These definitions will be useful in organizing the proton observations.

### *Proton Observations*

Most of the data collected by this instrument are by design dominated by proton fluxes. Since we are interested in studying those periods during which the proton counting rate changes significantly during a time scale of several hours, the proton data can be effectively

Figure V-3

Observed electron polar cap boundary data in an invariant latitude-magnetic local time coordinate system.

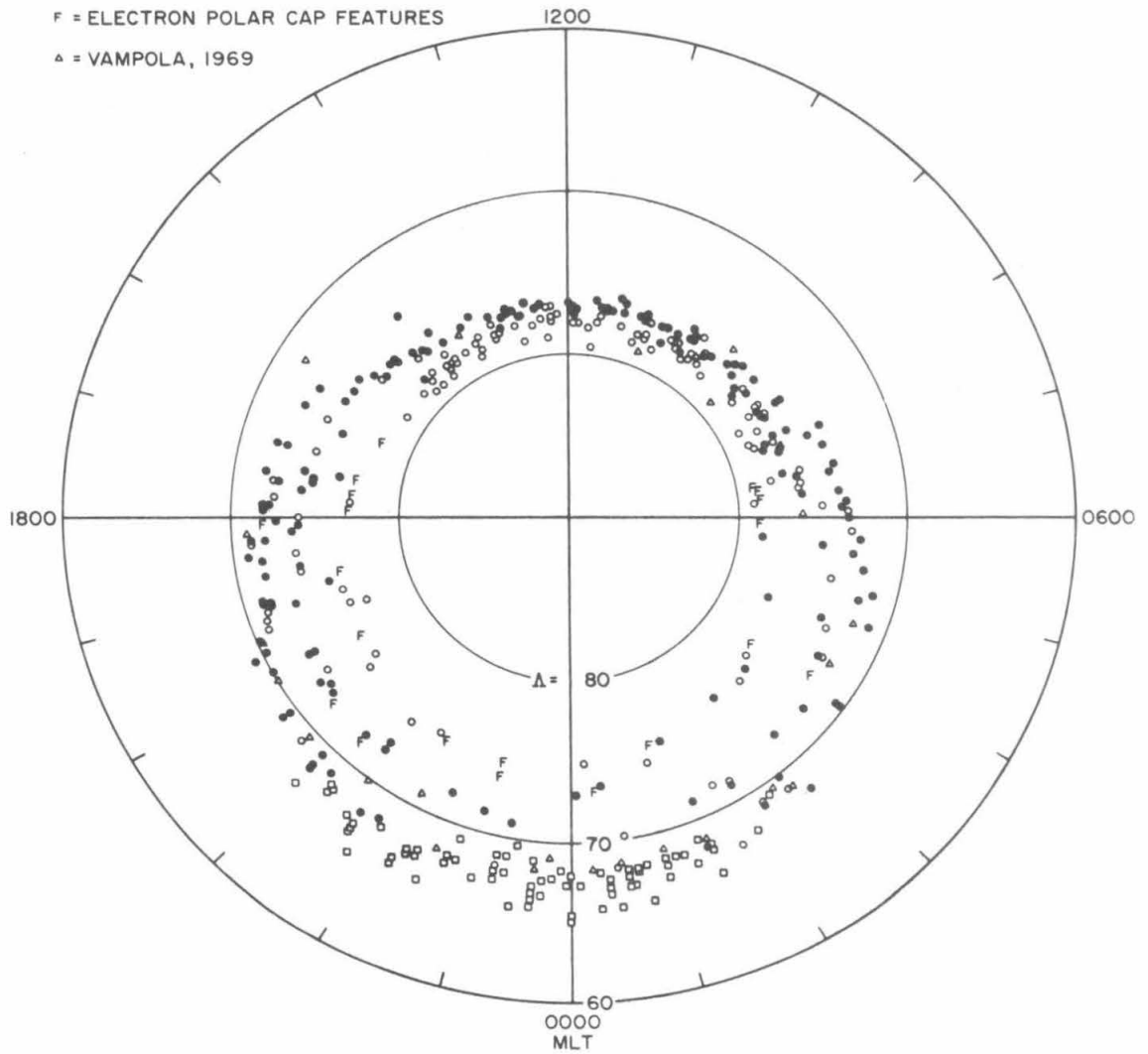
○ =  $K_p < 2^-$

● =  $2^- \leq K_p < 4^-$

□ = ELECTRON SPIKES

F = ELECTRON POLAR CAP FEATURES

△ = VAMPOLA, 1969



displayed on a plot of proton counting rate (or flux) as a function of time, which is referred to as a *profile*. In particular, we will be interested in comparing the profiles of fluxes measured at low polar latitudes and at high polar latitudes. As discussed in Section VII, the north and south low polar latitude regions are most likely connected by closed field lines, while the north and south high polar latitudes are not. Therefore, no distinction will be made between data collected in the north and south low polar latitude regions, whereas the data from the two high polar latitude regions will be kept separate.

The temporal variations observed in the proton flux can normally be divided into two main types: those events associated with and having the characteristics of solar flare events, and those events which have been variously referred to as Energetic Storm Particles (Bryant, *et al.* [42,43] and Rao, *et al.* [44]), Delayed Particle Events (Lin and Anderson [45]), and Protons Associated with Centers of Solar Activity (Fan, *et al.* [46]). We will follow the lead of Anderson [47] and try to avoid any semantics problem by referring to these events as *EDP* (*E*nergetic *D*elayed *P*articles) events. Although treated in more detail in Section VI, a brief description of the essential differences between these two classes of events may indicate why the distinction between them is made. Flare events are characterized by impulsive ejection of particles by the sun followed by their propagation through interplanetary space. This typically results in a rapid rise ( $\sim$ few hours) to a maximum proton flux, followed by a long, nearly exponential decay with a time constant of about one day. EDP events, on the other hand, are characterized by a region of

limited radial extent and enhanced low energy particle flux being convected outward by the solar wind plasma (expanding solar corona). For our purposes here, EDP events are phenomenologically characterized by the following (after Anderson [47]):



1. Fluxes occur predominately at low energies.
2. Profiles show much more rapid rise and fall than flare event profiles and often exhibit large fluctuations during the event.
3. The duration of the event is normally between  $O(1 \text{ hour})$  and  $O(1 \text{ day})$ .
4. Events are often associated with a "weak depression" in the sea level neutron monitor rates.
5. Events are sometimes associated with one or more geomagnetic sudden commencements or sudden impulses.

Presented below are typical examples of the observations of both of these classes of particle events.

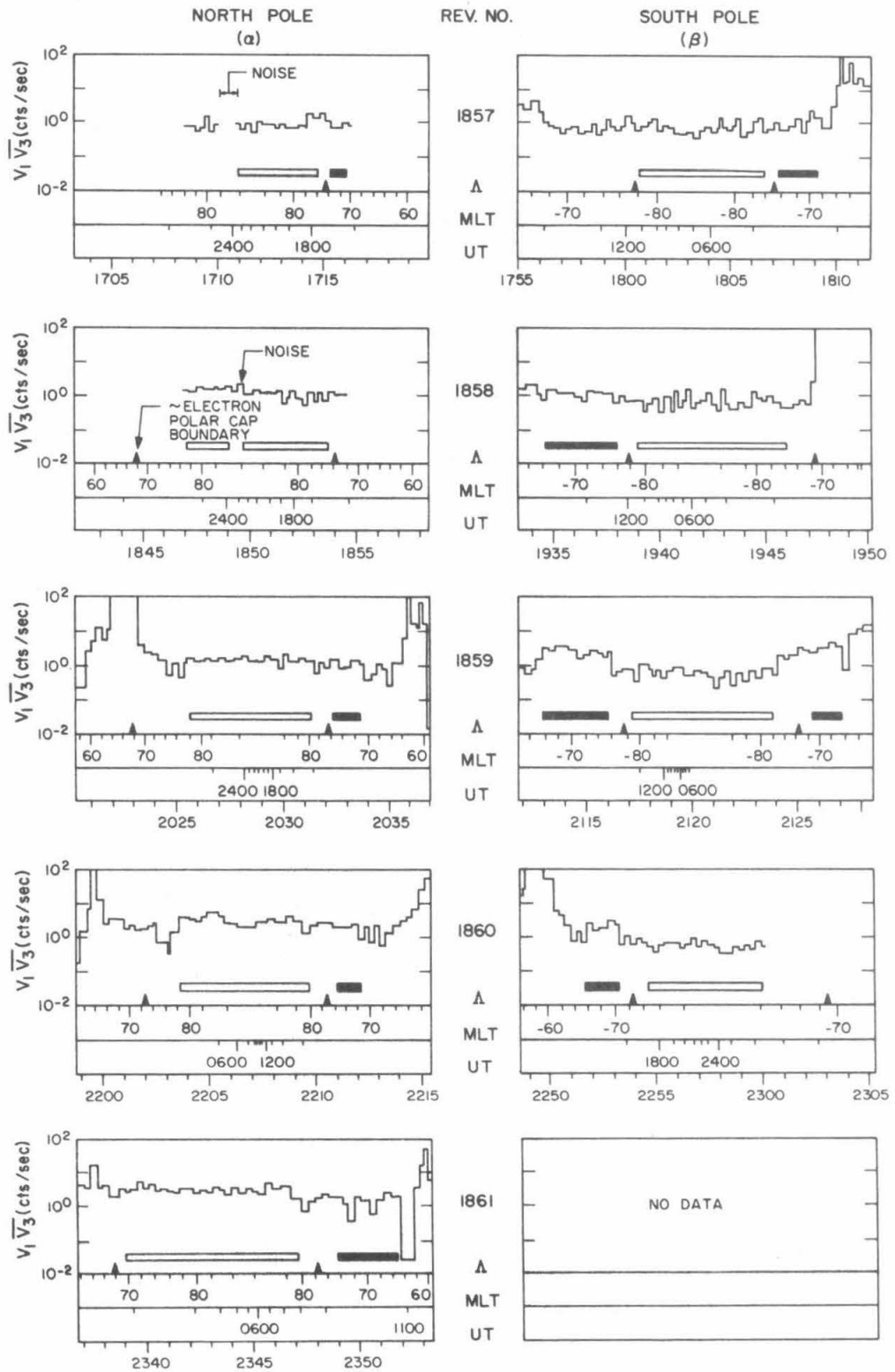
*EDP event of 1 December 1967*

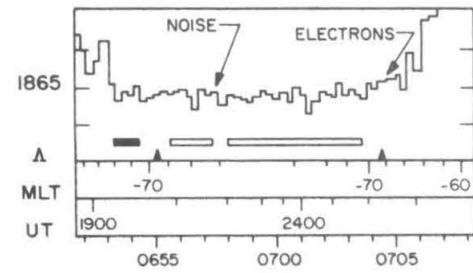
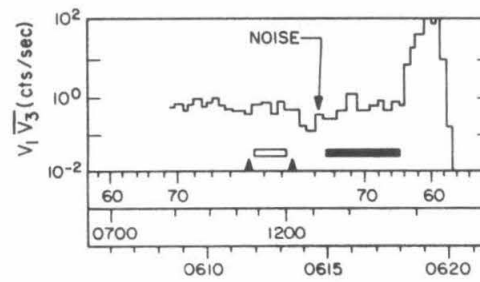
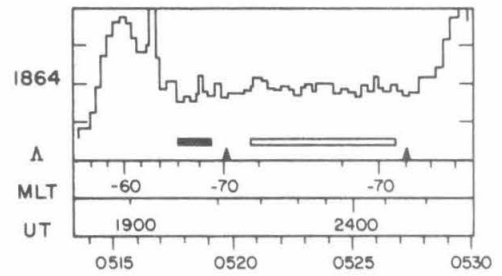
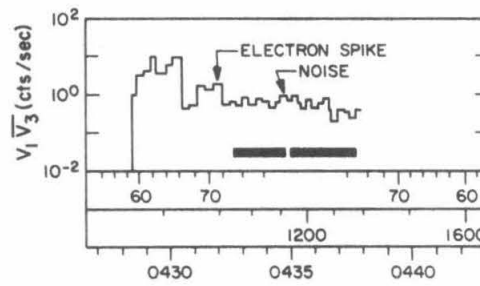
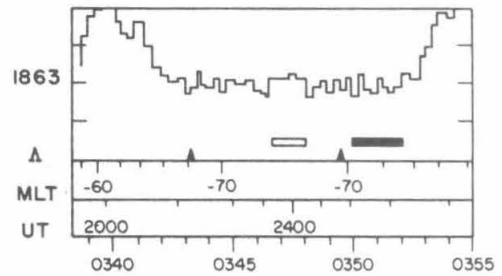
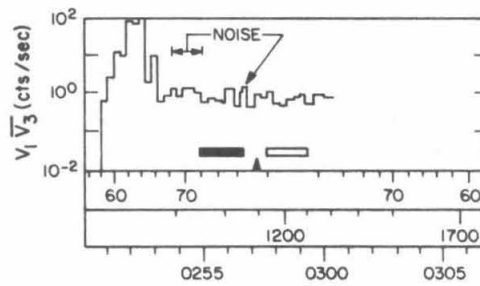
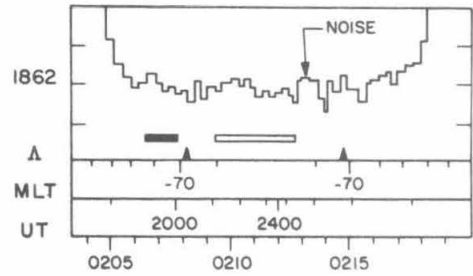
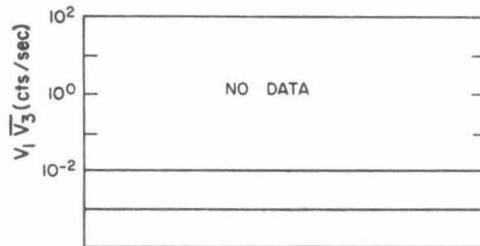
Figure V-4 shows the  $V_1 \overline{V_3}$  rate as a function of time for each available polar pass from 1700 UT on 1 December 1967 to 0700 UT on 2 December. This figure illustrates the averaging intervals used to obtain average counting rates for each of the polar cap regions (LPL and HPL), and the relation between these averaging intervals and the electron polar cap boundary data presented in figure V-3. The profiles of the flux measured in the low polar latitude (LPL) region and in the

Figure V-4

$V_1\overline{V_3}$  counting rate ( $\sim 15$  second averages) during all of the available polar passes from 1700 on 1 December 1967 to 0700 on 2 December. The averaging intervals used to obtain average rates for low polar latitude (  ) and high polar latitudes (  ) are shown and compared to the approximate location of the electron polar cap boundary ( $\blacktriangle$ ) as shown in figure V-3. In addition to universal time, geomagnetic coordinates ( $\Lambda$  and MLT) are also indicated.







north and south high polar latitude (HPL) regions are in figure V-5. All data points shown in this figure have errors comparable to those of the four points with explicit error bars. The arrows near the top of the figure indicate a gap in the data, which included both a south and a north polar pass (see Section III). The time resolution of the LPL profile is twice that of the other two profiles because the north and south LPL regions are considered equivalent.

The identification of this event as an EDP event is supported by the extremely fast "decay" of the flux, the predominantly low energy nature of the event (see discussion of spectra below), and the presence of a weak depression in the Alert Neutron Monitor [48]. In addition, figure V-6 shows a direct comparison between the data in figure V-5 and the interplanetary flux of 0.79-9.6 MeV protons and 0.17-1.00 MeV electrons measured by the University of Chicago experiment on board IMP-F [49]. The correlation between these interplanetary data and the LPL profile is notable.

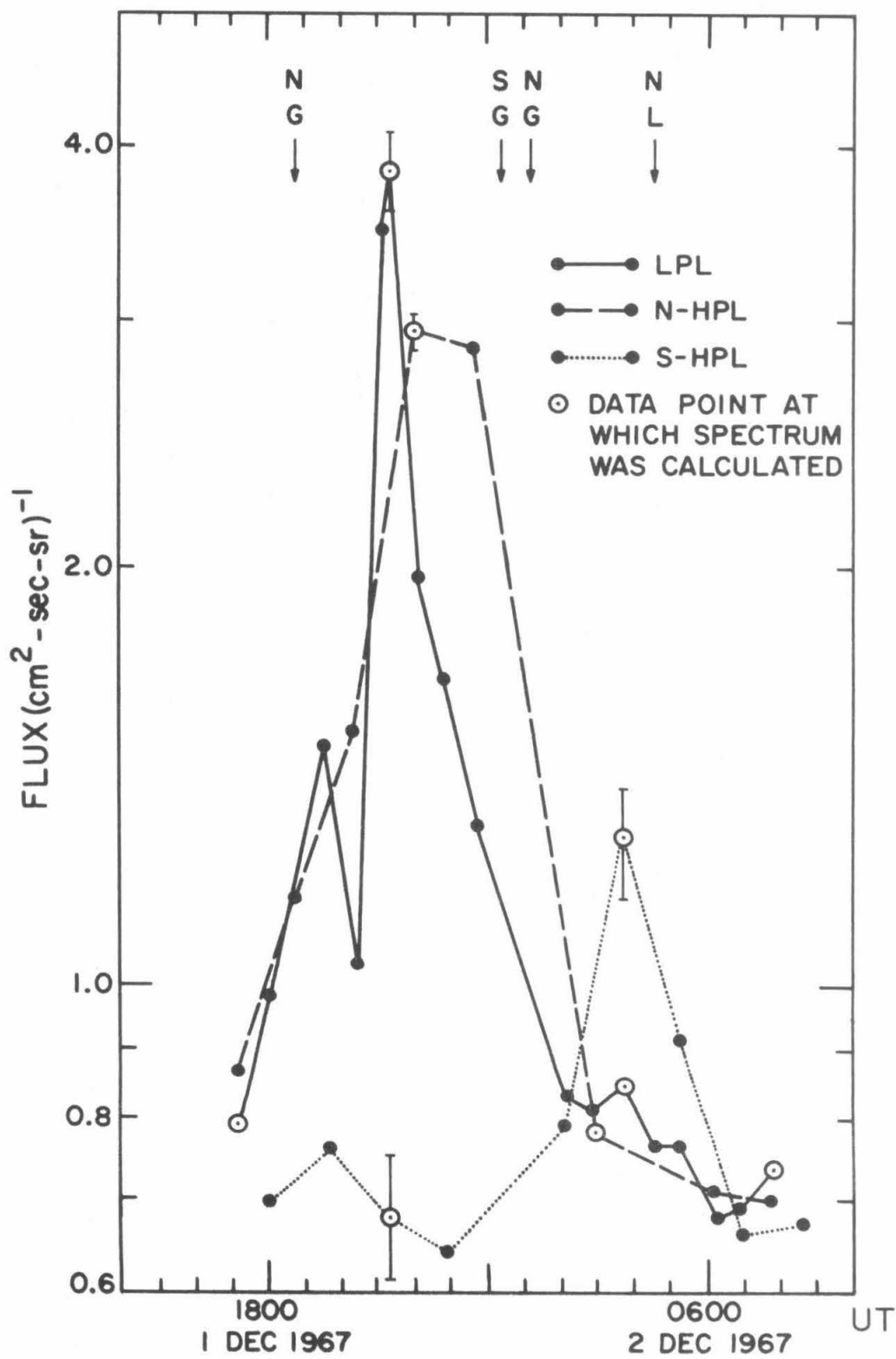
The most obvious features of these profiles are that (1) all three profiles are different (a peak occurs first at LPL, next at northern HPL, and last at southern HPL) and (2) only the LPL peak occurs at the same time as the peak seen in the IMP-F data.

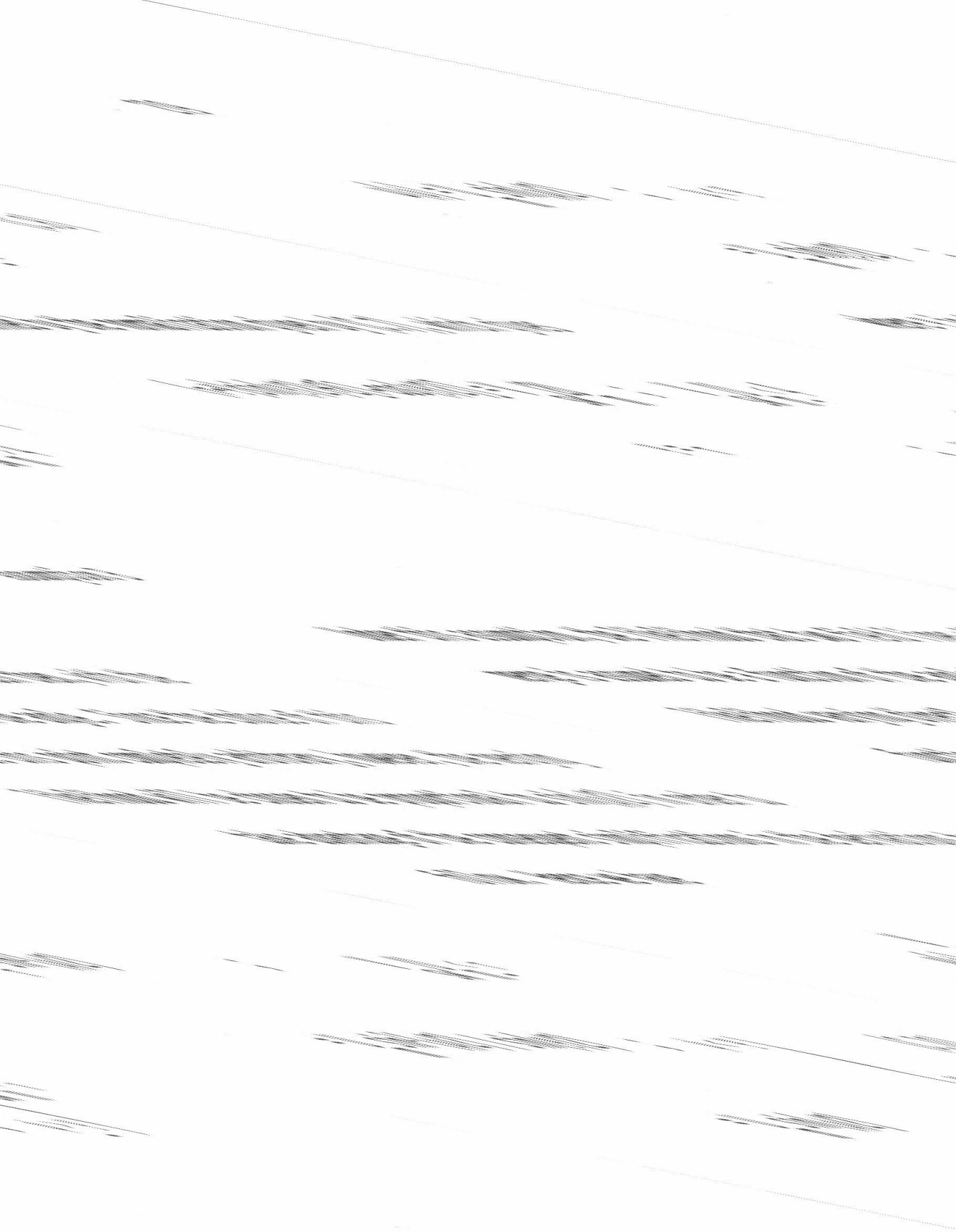
In order to determine the relationship among these peaks, spectra were calculated at eight times during this event; the data for which spectra were calculated are indicated by the circled points on figure V-5. These spectra are shown in figure V-7. The data upon which the spectra

Figure V-5

Flux profiles for EDP event of 1 December 1967. The profile for each region is distinguished from the other profiles according to the following code:

- low polar latitudes
- north high polar latitudes
- .....● south high polar latitudes





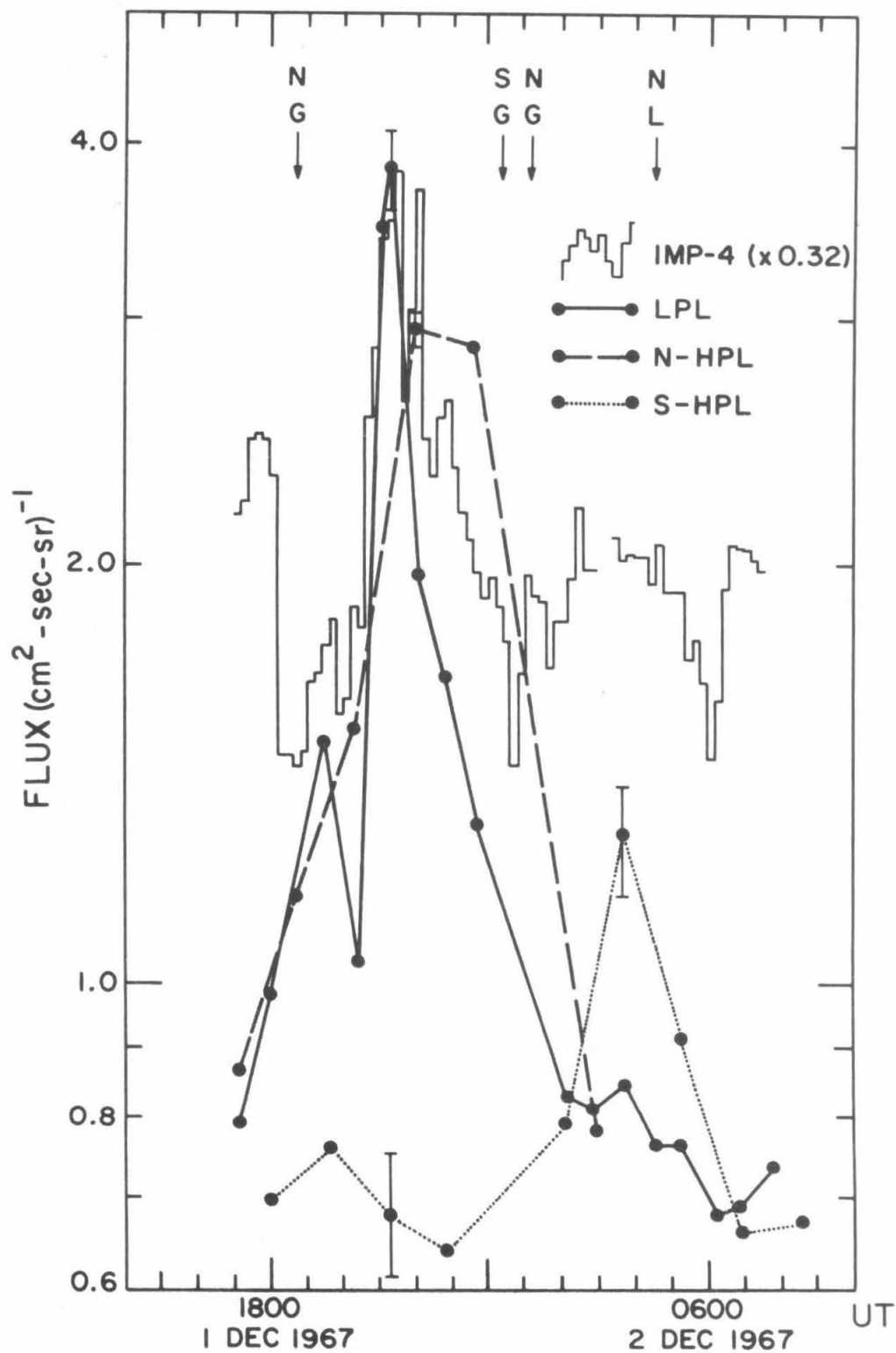


Figure V-7

Differential energy spectra of the following fluxes calculated from data collected during the 1 December 1967 EDP event:

V-7a: Low polar latitudes prior to the beginning of the event.

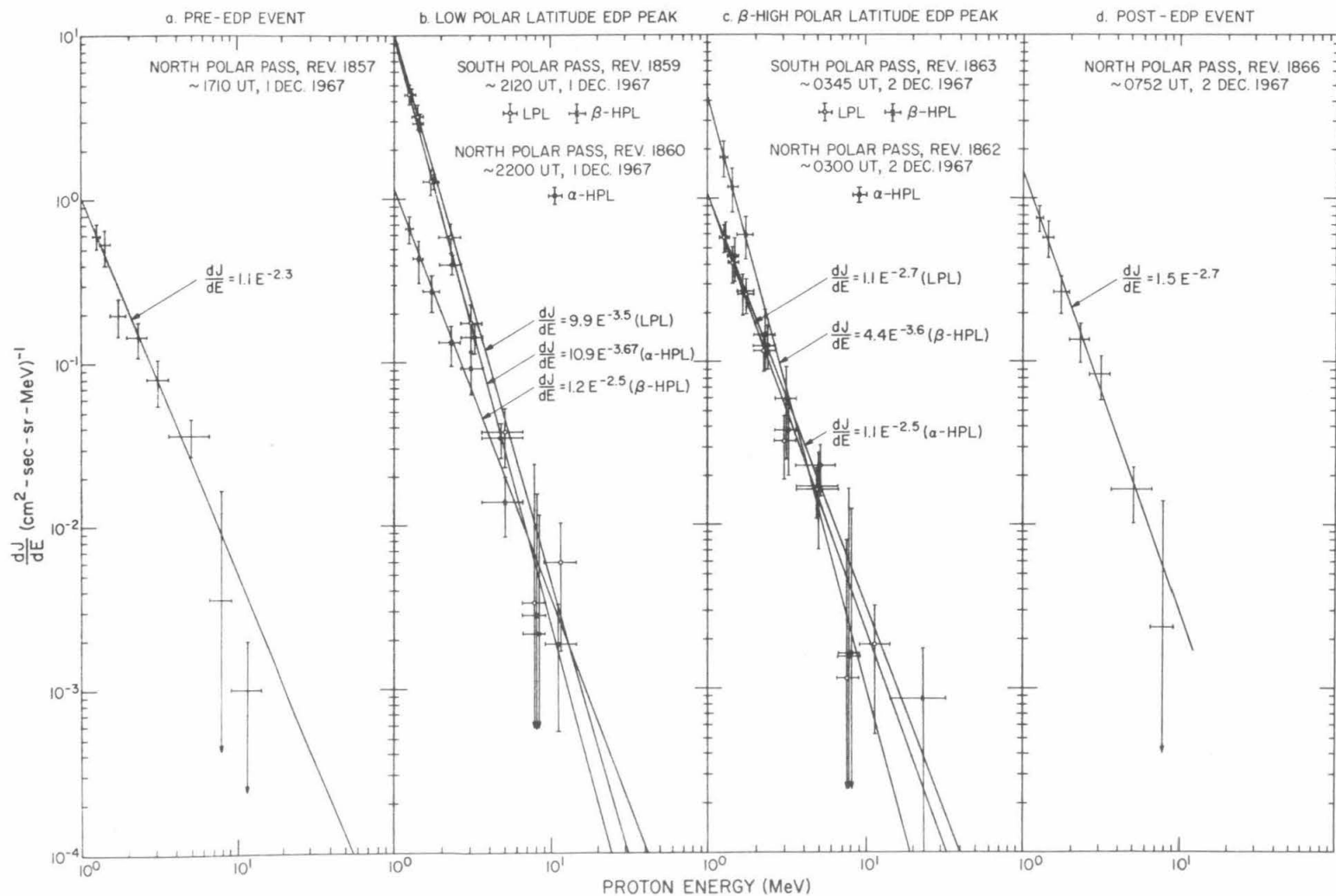
V-7b: Low polar latitude peak, northern high polar latitude peak, and southern high polar latitude data from the same time.

V-7c: Flux from each of the three regions collected at or near the southern high polar latitude peak.

V-7d: Low polar latitudes after the end of the event.

In all four cases, LPL data points are indicated by an open circle ( $\circ$ ), northern HPL by a closed circle ( $\bullet$ ) and southern HPL by a cross ( $\times$ ).





in figure V-7b were based were collected during consecutive polar passes in order to minimize any differences due to temporal effects; the same is true of the data in figure V-7c. We note the striking interchange in rôles from figure V-7b to figure V-7c between the southern HPL region and the LPL and northern HPL regions.

These eight spectra are summarized in table V-1, which gives the coefficient and exponent of the best fit for each spectrum to an equation of the form

$$\frac{dJ}{dE} = AE^{-\gamma}$$

where  $J$  is the flux in particles/cm<sup>2</sup>-sec-sr, and  $\gamma$  is referred to as the spectral index. One standard deviation errors for  $A$  and  $\gamma$ , as well as the  $\chi^2$  "goodness of fit" parameter, are also indicated on this table.

The spectra observed at each of the peaks indicate the following:

(a) compared to the spectra observed before and after the event, each of the peaks consisted of a larger proportion of low energy protons and exhibited spectral indices typical of those observed for EDP events in interplanetary space [50], and (b) the spectral index of the flux was essentially the same at each peak. The first point supports the identification of these peaks as due to EDP fluxes, while point (b) is consistent with the interpretation that all of the peaks represent a sampling of the same particle population. This interpretation is aided by the observations that the magnitude and spectrum of the ambient flux change very little throughout the event and that the spectral indices for the peak fluxes are significantly different than the index for the *ambient flux*.

TABLE V-1

1 Dec. 1967 EDP Event Spectra (see figure V-7)

Best Fit to  $\frac{dJ}{dE} = AE^{-\gamma}$ 

Relationship to Event	Coefficient "A" (cm <sup>2</sup> -sec-sr-MeV) <sup>-1</sup>	Spectral Index "γ"	χ <sup>2</sup>	P(>χ <sup>2</sup> )
Pre-event LPL	1.07 ± 0.18	2.31 ± 0.23	9.33	0.316
LPL peak	9.90 ± 0.15	3.52 ± 0.22	0.96	0.995
Northern HPL peak	10.90 ± 0.11	3.67 ± 0.17	2.52	0.961
Southern HPL at LPL peak	1.21 ± 0.21	2.53 ± 0.29	1.47	0.983
LPL at Southern HPL peak	1.13 ± 0.19	2.66 ± 0.24	2.19	0.974
North. HPL at S. HPL peak	1.10 ± 0.23	2.52 ± 0.32	1.95	0.962
Southern HPL peak	4.43 ± 0.26	3.62 ± 0.41	1.28	0.989
Post-event LPL	1.47 ± 0.21	2.69 ± 0.29	1.08	0.993

These observations lead to the following description of the 1 December 1967 event. The interplanetary region of enhanced flux arrives at the earth and is observed almost simultaneously by IMP-F and at LPL. About 1.2 hours later, by which time the LPL flux has decreased significantly, this flux is observed to reach a maximum at northern HPL. Finally, after these two fluxes have definitely returned to ambient flux levels, the EDP flux is observed at southern HPL.

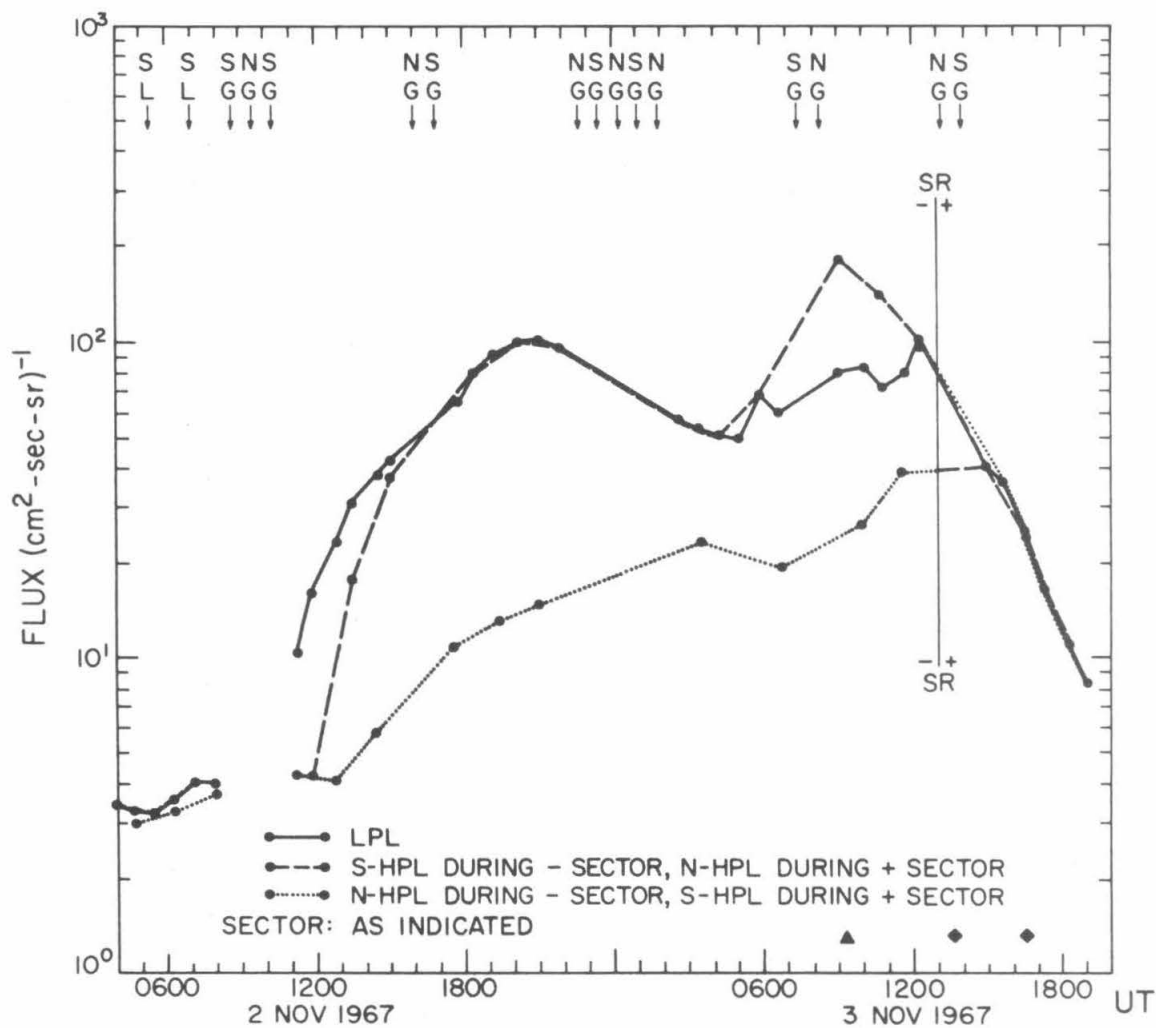
*Solar Flare Event of 2 November 1967*

The second of the two classes of solar particle events of interest here consists of those events associated with solar flares. As with EDP events, we will compare the profiles of the flux at low polar latitudes and the flux at north and south high polar latitudes. Many flare events have been used in this study; most of these are subject to the limitation imposed by the time-sharing nature of the OGO-4 telemetry: in general, data are available for two day periods separated by two day gaps. This limitation is more critical for flare events, which might last 6-8 days, than for EDP events, which have typical durations between one hour and one day.

Typical of the observations which, in spite of this limitation, have features of interest are the profiles of the 2 November 1967 flare event in figure V-8. Preliminary results of the study of this event have been previously reported [11]. Typical errors are indicated for arbitrarily selected data points.

## Figure V-8

Profiles of the 2 November 1967 solar flare event. The symbols in this figure are explained in Appendix A (see table A-3). A 2B flare occurred on the sun at 0852 UT on 2 November 1967, accompanied by 2-12 Å X-ray emission that peaked at 0858 UT.



This is a particularly good example of a prolonged difference between the flux observed in one high polar latitude region and the flux observed in the other two polar regions. The north high polar latitude flux is consistently lower than the other two fluxes for a period of  $\sim 25$  hours. This type of profile configuration, where one high polar latitude profile is markedly different than the other high polar latitude profile has been referred to as a North-South (N/S) asymmetry [11,25].

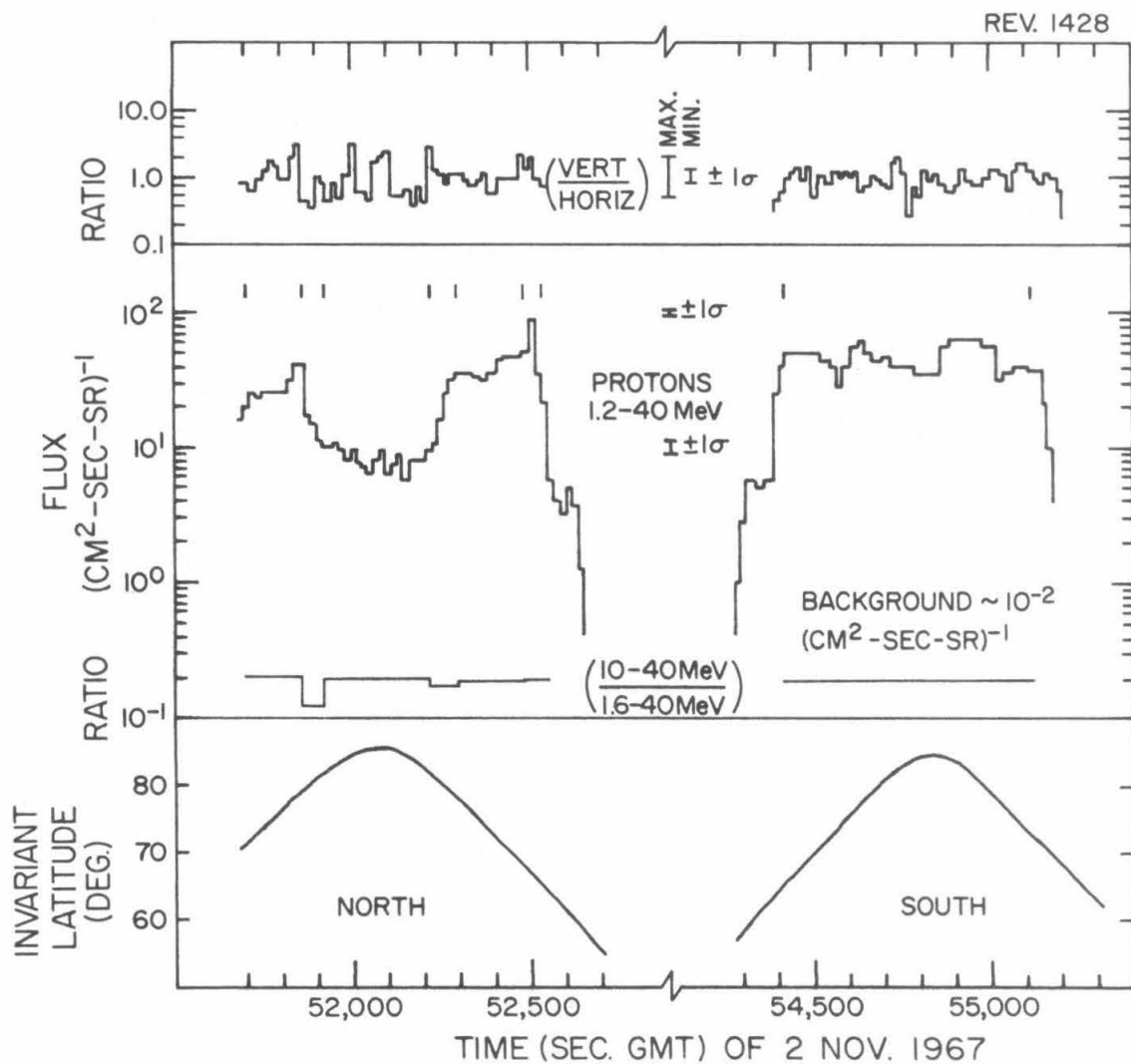
The appearance of such a N/S asymmetry during a single polar pass is illustrated by figure V-9. This figure shows the  $V_1\overline{V_3}$  rate for the north and south polar passes of one orbit early during the 2 November 1967 event. Southern polar passes from later in the event show even less structure. The ratio of the flux of 10-40 MeV protons to the flux of 1.6-40 MeV protons is an indication that the same ratio of minimum to maximum flux occurred over the entire measured energy range from 1.2 to 40 MeV. As is discussed below, pulse height analysis gives the same indication. Figure V-9 also contains the ratio of the vertically incident to the horizontally incident flux, normalized so that unity corresponds to an isotropic flux. There is no evidence of a large anisotropy in conjunction with the intensity variations, ruling out a pitch-angle dependent cut-off effect.

The manner in which the feature in the north polar proton flux illustrated in figure V-9 is repeated consistently for a long period as shown in figure V-8 suggests the possibility of referring to these observations as persistent features. A feature in the proton polar cap flux will be termed *persistent* if it is observed during two or more

Figure V-9

Selected north and south polar passes observed early during the 2 November 1967 solar flare event. Isotropy is indicated by a vertical/horizontal ratio of unity. Any spectral change would be indicated by a change in the 10-40 MeV/1.6-40 MeV proton ratio, which has a statistical error of  $\leq 1\%$ . Invariant latitude is included for reference.





consecutive orbits (excluding orbits for which appropriate data are unavailable).

The mapping of the regions of maximum and minimum intensity into the invariant latitude-magnetic local time ( $\Lambda$ -MLT) coordinate system is shown in figure V-10, along with the low latitude rigidity cutoff previously determined for 1.5 MeV protons during a magnetically quiet period in 1961 [51].

Spectra were calculated throughout this event, and figure V-11 shows a typical example of the spectrum from the northern high polar latitude region compared to the spectrum from the low polar latitude region observed at the same time. The shapes of these spectra are remarkably similar and differ only by a constant multiplicative factor. Although there are some variations early in the event, as shown on figure V-12, no prolonged energy dependent effects can be observed.

#### *Comparison of Electron and Proton Observations*

During the 28 September 1968 event, a comparison between electron polar cap observations and the features which occur in the polar proton intensities was possible, and it is shown in figure V-13. During this event the persistent proton feature took the form of a depression. The observations of the electron polar cap boundary are mapped into an invariant latitude-magnetic local time coordinant system and represented by solid circles; the high latitude limits of the enhanced flux region associated with low polar latitudes appear as open circles. It is clear that the

Figure V-10

A mapping of the north polar passes of OGO-4 into invariant latitude-magnetic local time coordinates for the period of the 2 November 1967 flare event. The locations of the regions of maximum and minimum proton fluxes are shown. Observed geomagnetic cutoffs are indicated and compared to cutoffs reported for a quiet geomagnetic field in September, 1961 [51]. The extent of data coverage is indicated where it is less than a complete polar pass.

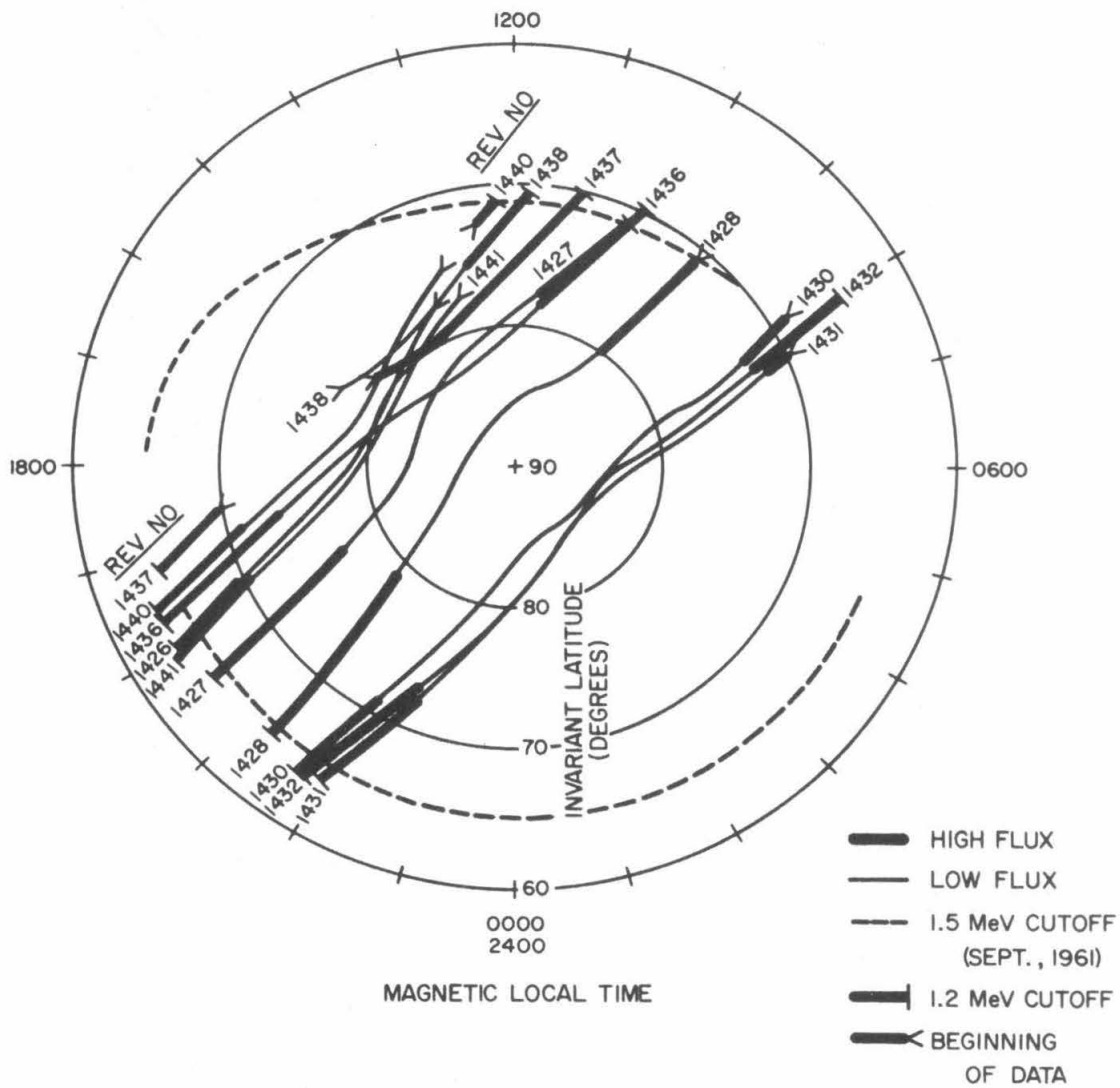


Figure V-11

Typical proton differential energy spectra observed during the 2 November 1967 solar flare event. Open circles represent the spectrum observed at low polar latitudes, and crosses represent the spectrum observed at the same time at northern polar latitudes.

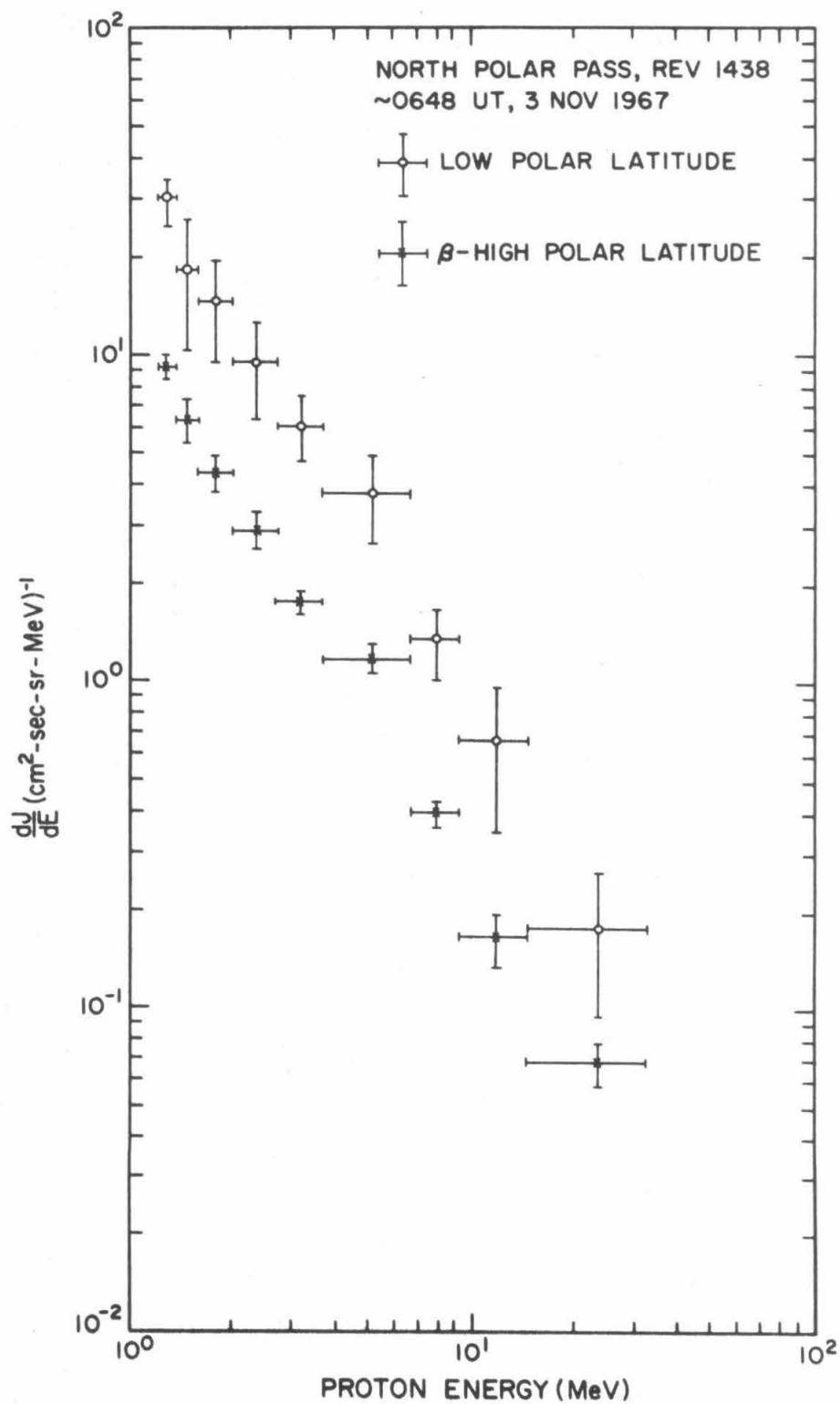


Figure V-12

Ratio of low polar latitude flux to northern high polar latitude flux as a function of energy for the period of the 2 November 1967 solar flare event. Each symbol consistently represents the ratio for a specific range of energies. The longer horizontal lines indicate the  $\pm 1\sigma$  limits of the ratio of the low polar latitude  $V_1\overline{V_3}$  rate (1.2-40 MeV protons) to the northern high polar latitude  $V_1\overline{V_3}$  rate.

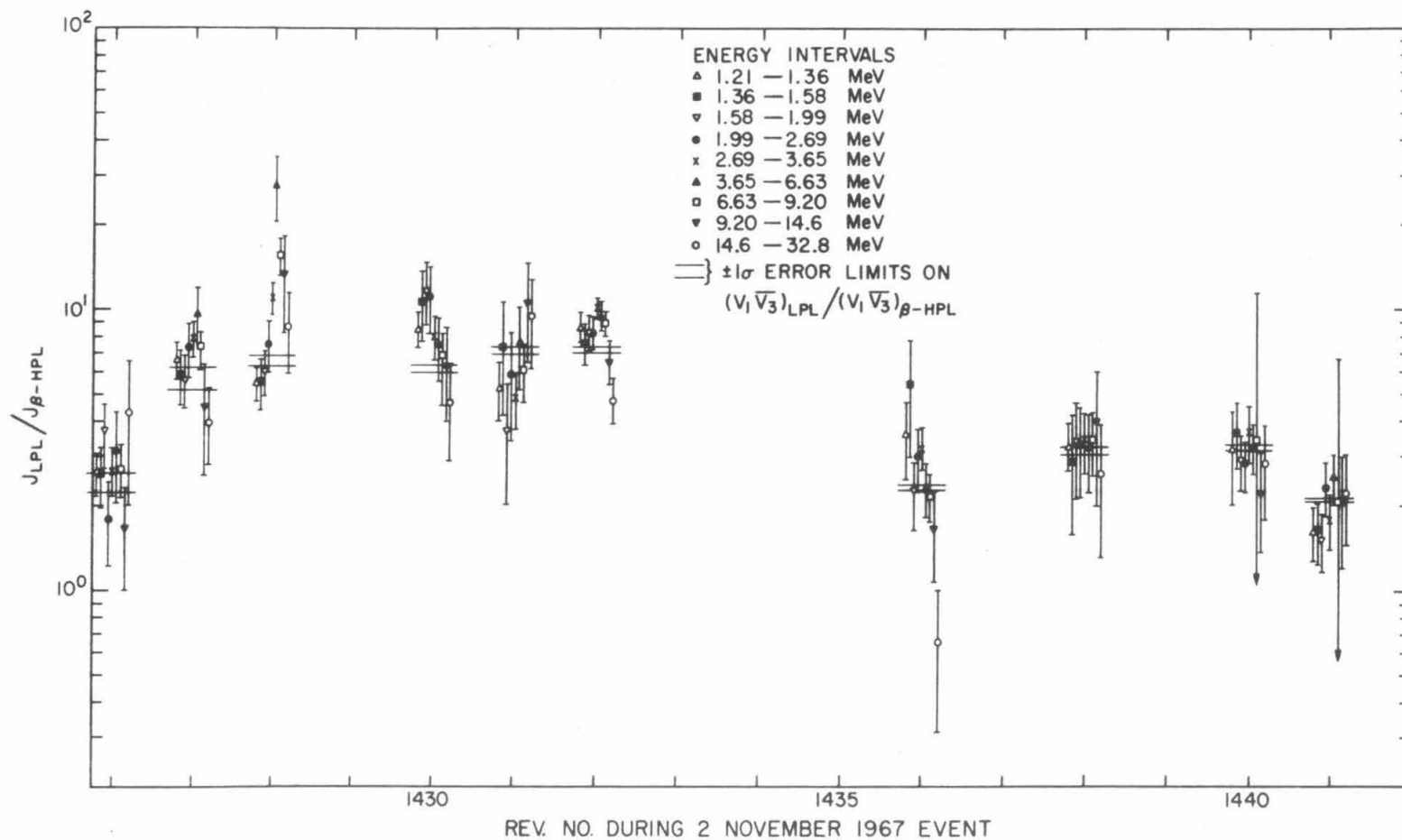


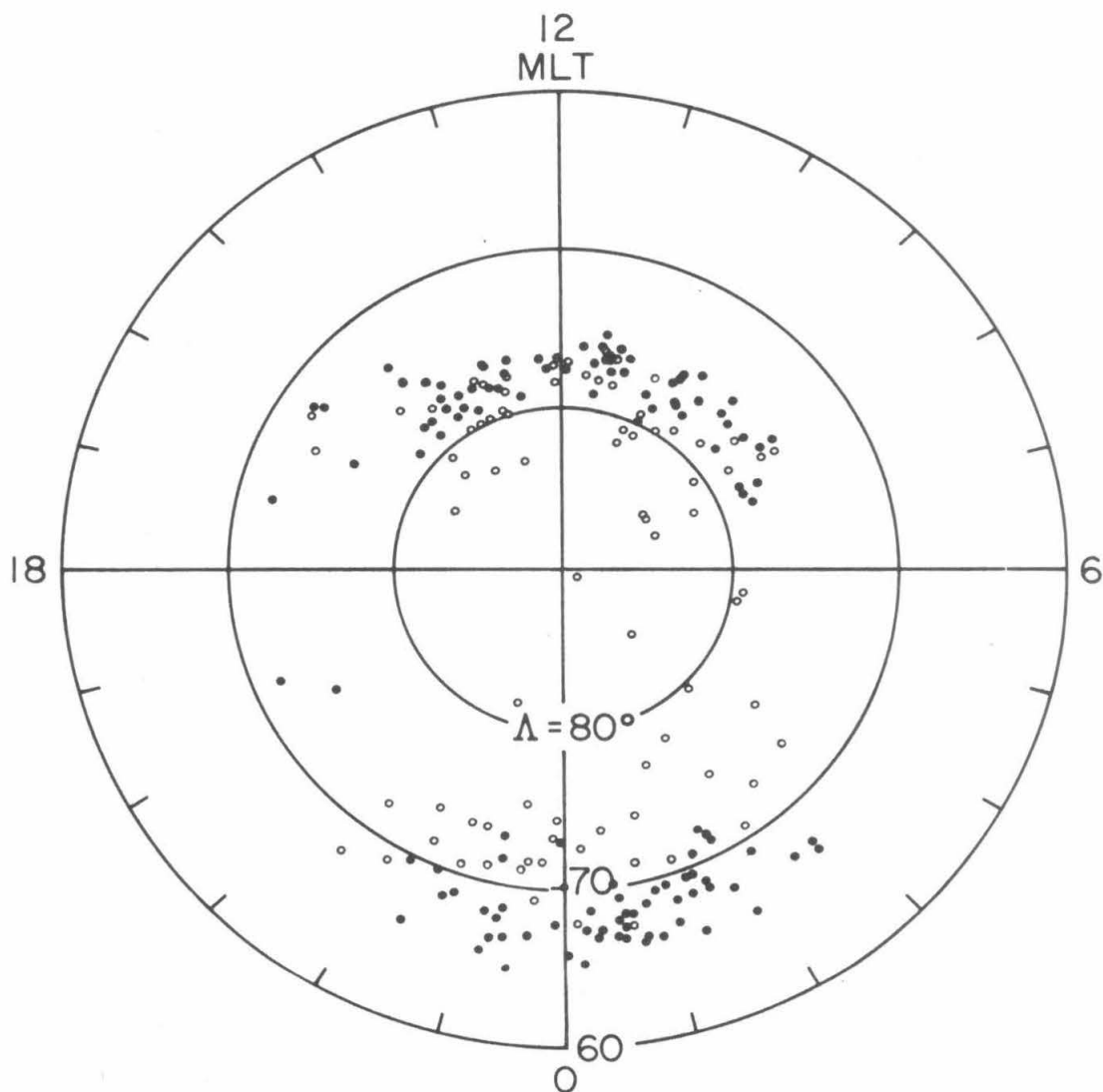


Figure V-13

Comparison in invariant latitude-magnetic local time coordinates of observed electron polar cap boundaries with observed high latitude limits of regions with enhanced proton fluxes. During the event shown, these enhanced fluxes were observed at low polar latitudes.

SEPT. 28, 1968

- ELECTRON
- PROTON



latitudes of the proton limits are  $\geq$  the latitudes of the electron polar cap boundary. This comparison indicates that the region where electrons have rapid access is the region where the proton access is delayed.

## VI. BACKGROUND

The significance of the data presented in Section V can be most effectively investigated in the proper context. As will be pointed out in Section VII, these data are particularly relevant to questions concerning the configuration of the distant geomagnetic field. Since charged particles observed in the polar regions propagate through interplanetary space, a brief description of this environment and the behavior of energetic solar particles therein is appropriate. In order to establish the context for the discussions to follow, the distorted configuration of the near-earth geomagnetic field will be presented, along with the significance and difficulties of studying the distant geomagnetic field.

### *Interplanetary Environment*

The model which we will use here is the one which was first proposed by Parker [52]. In this model the solar corona plasma continues to expand radially outward from the sun to form a super-Alfvenic solar wind. The solar magnetic field is "frozen into" the solar wind plasma [53] and is thus convected outward from the sun. In the presence of a homogeneous, uniform solar wind flow, the combination of the radial solar wind flow and the rotation of the sun would cause the solar magnetic field to be pulled into an Archimedian spiral configuration, such that near the earth

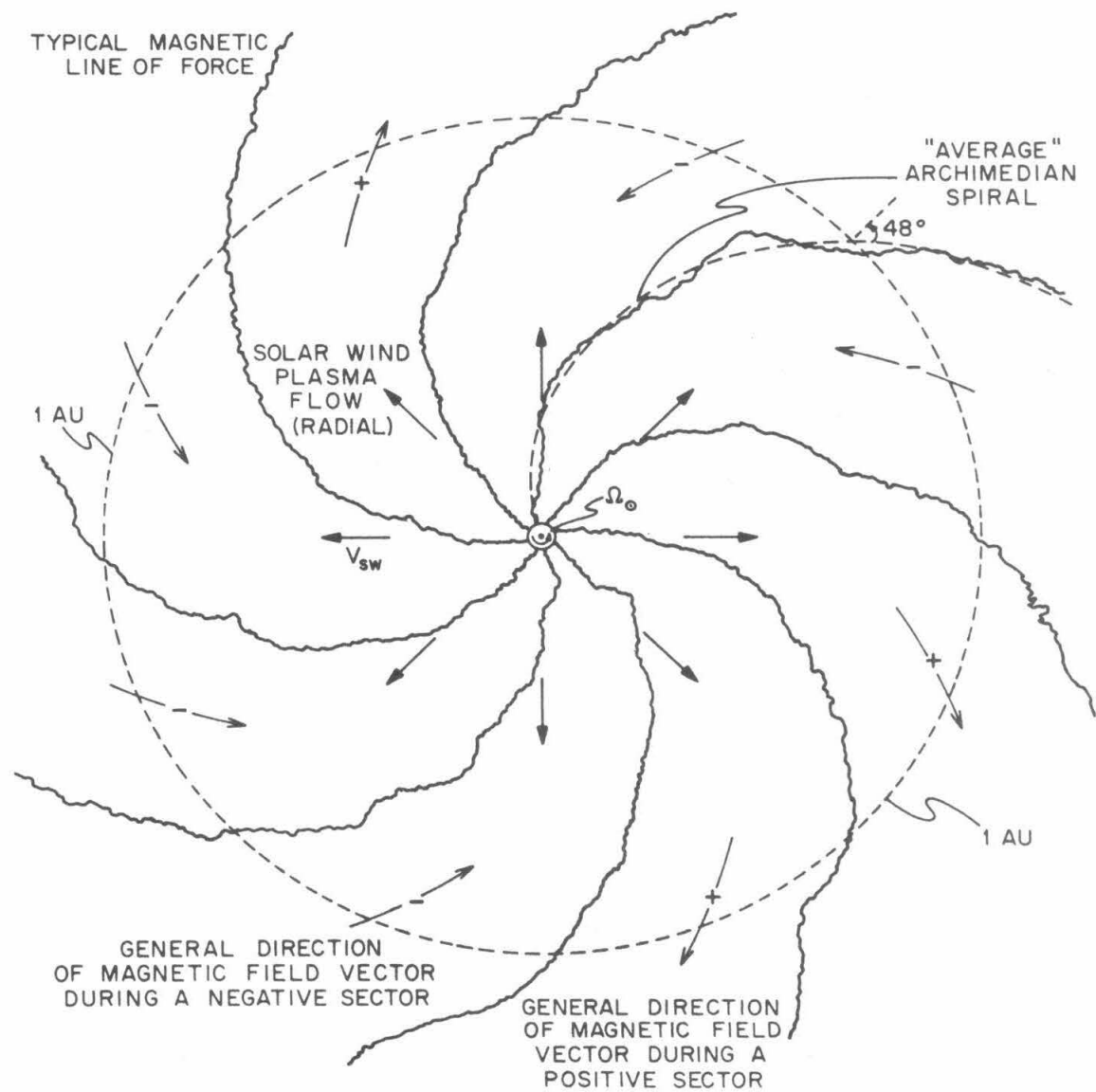
the angle between the magnetic field and a radial vector would be about  $48^\circ$ , measured in the ecliptic plane [54]. Neither the source of the magnetic field nor the medium in which it is being convected is either homogeneous or uniform, however. As a consequence, the configuration of the interplanetary magnetic field fluctuates considerably from this ideal position (*cf.* [55]), and the actual configuration is more like that depicted schematically in figure VI-1. An important parameter of the solar magnetic field is the mean direction of the field, designated as positive (negative) if the field direction is predominately away from (toward) the sun along the average spiral direction. Most of the time this mean direction is observed to be divided into sectors [56], also shown in figure VI-1. The history of this sector structure during the lifetime of the OGO-4 data acquisition [57,58] is indicated on the OGO-4 Data Coverage Plots (an example is shown in figure IV-1; the complete set is given by Evans [35]).

As indicated in Section V, solar cosmic ray events can be divided into two different phenomenological classes: (a) the prompt event, or solar flare event, in which particles arrive within a few hours of the parent flare, and (b) delayed events, or EDP (Energetic Delayed Particle) events, in which particles arrive a day or more after the parent flare [59]. Since each of these classes of events has been observed with OGO-4, it is appropriate to briefly discuss some of the phenomenological aspects of each.

Solar flare particles are thought to be injected into interplanetary space impulsively at the sun more or less coincident with a relatively

Figure VI-1

Schematic representation of the configuration of the solar magnetic field near the ecliptic plane.



NOT TO SCALE

large release of energy (e.g. optical, X-rays, synchrotron radiation from energetic electrons). After injection, the propagation of these particles from the sun to the point of observation is determined by the characteristics of interplanetary space. The results of this propagation are normally an increase in the interplanetary flux to a maximum over a time scale of about five to fifteen hours [59], followed by a decay which becomes more or less exponential after a few hours with a decay time constant on the order of a day. The radial gradient in the flare flux is normally negative at 1 AU early in the event, but may become positive during the decay phase. Such a positive gradient has been observed by O'Gallagher  $\left( \frac{1}{J} \frac{dJ}{dR} \approx 2.0 \times 10^{-3} \% / R_{\oplus} \right)$  [60]. Current models for the propagation of solar flare protons in interplanetary space [61,33] give  $\frac{1}{J} \frac{dJ}{dR} \approx 1.5-11.0 \times 10^{-3} \% / R_{\oplus}$  as typical for gradients near 1 AU for late times ( $t > 140$  hours). Early during the decay phase, interplanetary gradients could be as high as  $40-50 \times 10^{-3} \% / R_{\oplus}$ , depending on the position of the flare on the sun [33].

Anisotropies in the interplanetary proton fluxes associated with prompt events are observed throughout most events [59,62]. The degree and direction of the anisotropy varies greatly, however, during each event and also from one event to another. During the early phase of a prompt event, particles are normally observed streaming out from the sun along the direction of the interplanetary magnetic field [63,64]. This field aligned anisotropy decays rapidly and is usually not dominant shortly after the maximum flux is observed (5 to 15 hours after onset) [59,63]. After this time the anisotropy direction is independent of the magnetic



field direction and is inferred to be parallel to the solar wind velocity for a period of a few days [59]. The magnitude of the anisotropy during this phase is energy dependent and is normally between 5% and 20% [63]. Late in the decay phase of the event (more than four days after onset) the anisotropy is directed more or less perpendicularly to the magnetic field direction and its magnitude is  $\leq 5\%$  [65]. The general duration and magnitude of interplanetary anisotropies during these three phases will be referred to in Section VII when the effect of these anisotropies on polar cap observations is discussed.

Another aspect of interplanetary anisotropies which will be of significance in Section VII is that, in general, the magnitude of the maximum anisotropy is inversely dependent upon the solar longitudinal separation between the parent flare and the foot of the interplanetary line of force passing through the point of observation [59]. Although this is generally true, large ( $\geq 3:1$ ) anisotropies have been observed at lower proton energies during the initial phases of some flare events which are time correlated to east limb optical flares [66].

The other class of solar particle events consists of the delayed events, or EDP events, which have been observed many times in interplanetary space (e.g., as cited in Section V, [42-47,50]). Most of the phenomenological aspects of these events are mentioned in Section V, so we will confine our attention here to their source, with one exception: these events are usually associated with large field directed anisotropies in interplanetary space [44]. These EDP phenomena are normally associated

with the so-called "active" regions of the sun; the enhanced flow of plasma from such a region sets up an interplanetary configuration such as that illustrated in figure VI-2 [*cf.* 42,46,47], which co-rotates with the sun. The effect of simultaneous observations at radially separated points in space would be to observe an abrupt and short-lived enhancement at the most sunward observation point first and at the point furthest from the sun last. The importance of this class of events to our study is that such events are associated with spatially well-defined interplanetary features which sweep past the earth and down the geomagnetic tail (see below) at a nearly constant velocity, that of the solar wind. Polar cap observations of EDP events will provide the basis for determining approximately where the particles observed in a given region of the polar cap gained access to the geomagnetic field.

#### *Geomagnetic Field and Magnetic Merging*

An important consequence of the existence of the solar wind is the resultant configuration of the earth's magnetic field. The result of this plasma-magnetic field interaction is the confinement of the geomagnetic field to a cavity, called the magnetosphere, whose size and shape are determined by a balancing of the various magnetic and plasma pressures involved [67-70]. The current picture of the near-earth configuration of the magnetosphere is illustrated in figure VI-3 (*cf.* [71]). As a matter of definition, those geomagnetic field lines on which some charged particles are capable of completing at least one bounce period (i.e., mirroring in both hemispheres) will be termed *closed* field lines. Those on

Figure VI-2

Schematic representation of an interplanetary region of enhanced low energy flux co-rotating with the sun [42,46,47]. As the region co-rotates past the earth, radially separated observation points would record different event "arrival" and "departure" times. The difference between these times would depend only upon the solar wind velocity and the radial separation between the points.

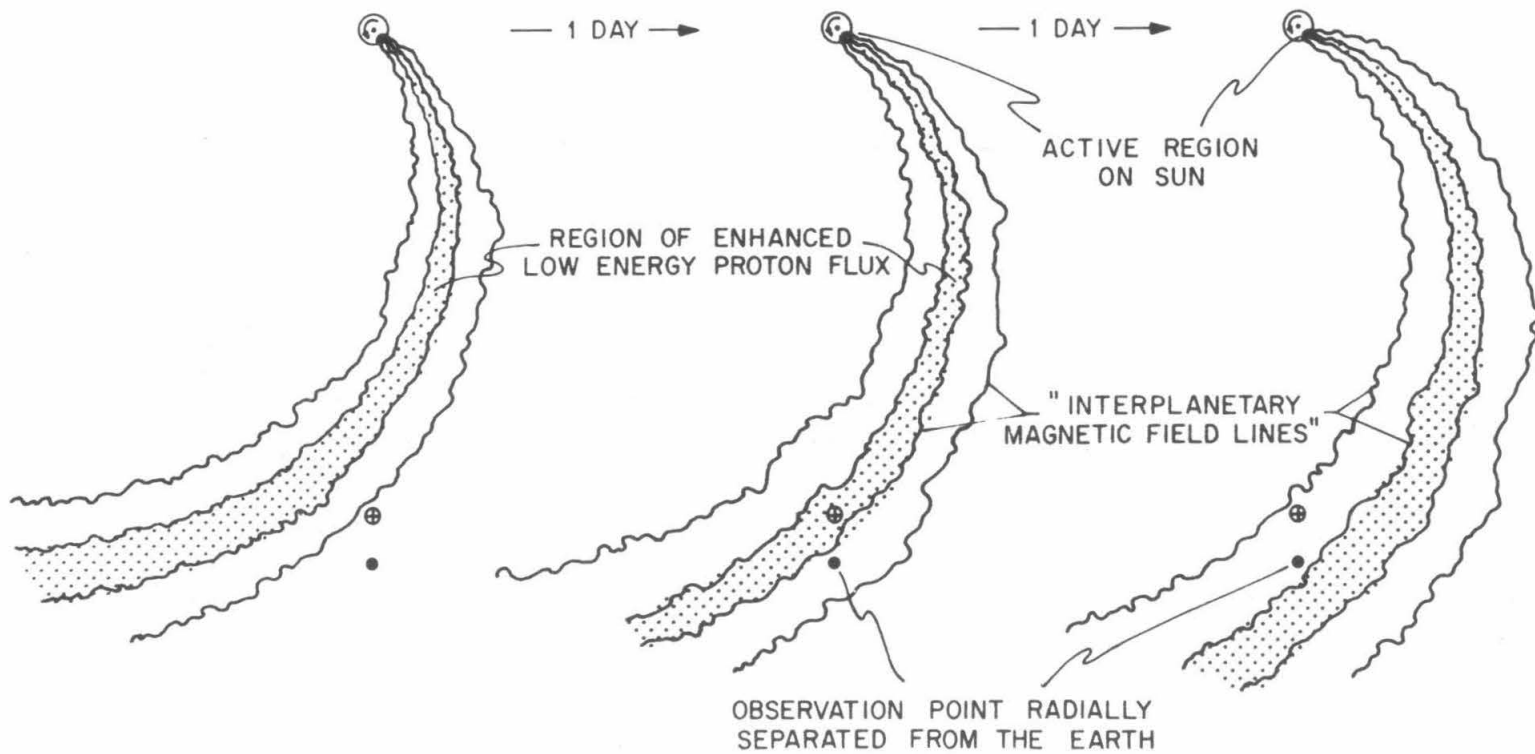
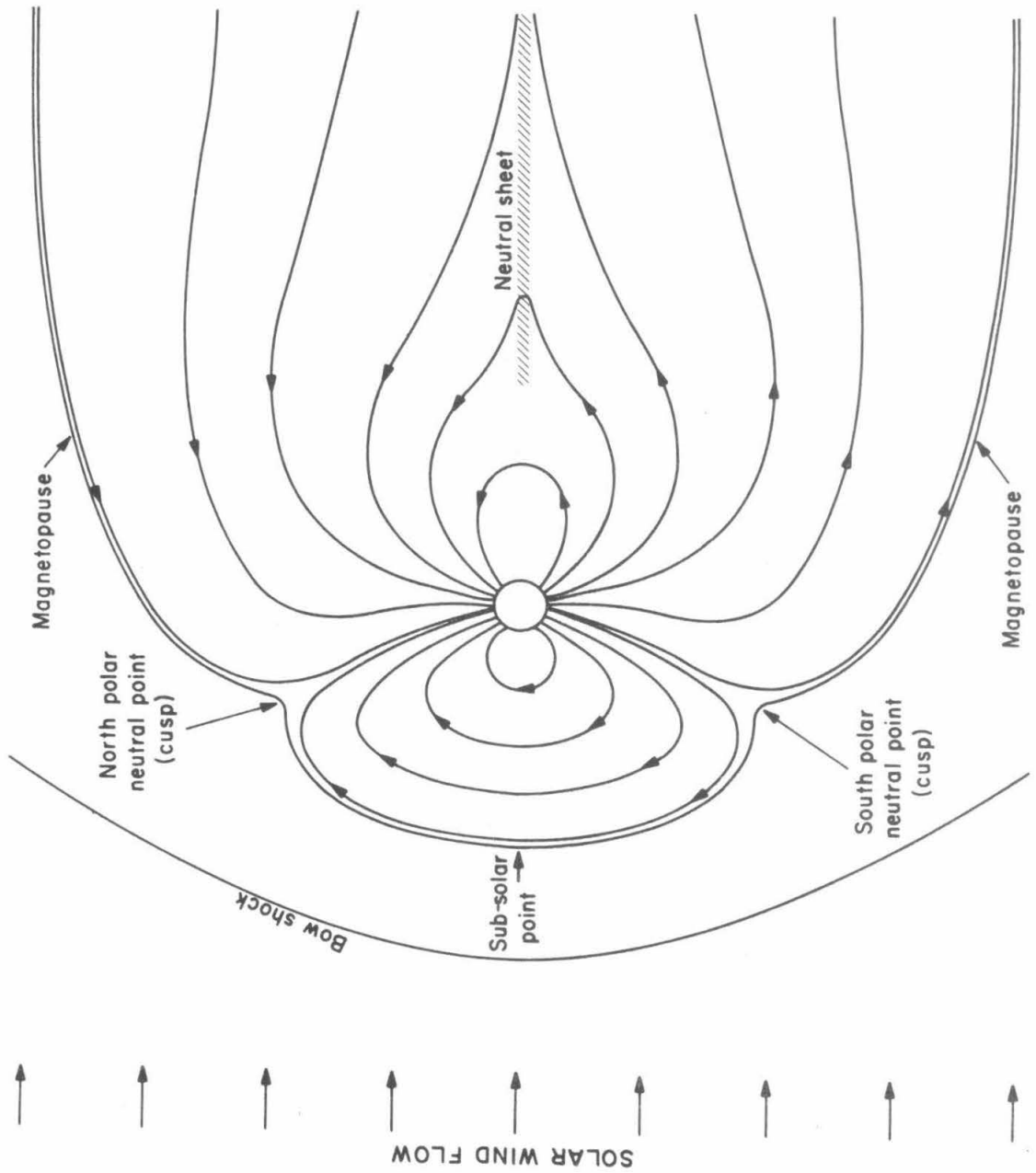


Figure VI-3

Schematic representation of the near-earth configuration of the earth's magnetosphere.



which such trajectories are impossible for any charged particles will be termed *open* field lines. In general, the open field lines constitute the field in the distant geomagnetic tail (see, for instance, [72,73]). The configuration of the geomagnetic tail has been mapped rather completely at least as far behind the earth as about  $80 R_{\oplus}$  (somewhat beyond the orbit of the moon) [71,72,74-76]. There is some indication that at least a geomagnetic wake may extend as far as  $500 R_{\oplus}$  [77,78] or  $1000 R_{\oplus}$  [79-81] behind the earth. These observations are, however, complicated by the motion of the tail [80], and the detailed structure at these distances has not been measured directly.

A concept which will be of importance later should be defined at this time: that of an *access window* for the entry of particles into the magnetosphere. For a given location in the interior of the magnetosphere, the access window for particles of a given rigidity will be defined as the set of all points on the "surface" of the magnetosphere where particles of that rigidity can gain access to the interior and be subsequently observed at the given location. Since a surface *per se* may be well-defined neither in the distant tail nor in a region where the two fields are directly connected, the use of the term "surface" is meant to imply (a) the interface between the geomagnetic field and the interplanetary magnetic field and/or (b) the extension of this interface through a region where the fields are directly connected, if such a region exists. This definition is similar to, but more formal than, that given by Gall, *et al.* for what they refer to variously as "penetration regions" [82] and "windows" [83].

In the absence of direct measurements of the distant geomagnetic tail (beyond  $80 R_{\oplus}$ ), one of the currently unresolved questions concerning the geomagnetic field is whether or not this field merges (i.e. reconnects) with the interplanetary magnetic field. The rôle of charged particle observations in the resolution of this question is that they can act as "probes" of a magnetic field where direct measurements of the field are infeasible. Assuming either the presence or absence of magnetic field merging between the solar and terrestrial fields, it is possible to postulate what the resultant magnetic field configuration might be. An analysis of a configuration so obtained will then yield implications concerning the characteristics of charged particle access from interplanetary space to the interior of the magnetosphere and the relationship between interplanetary particle fluxes and fluxes observed in the polar cap regions. Comparisons of polar cap observations with the predictions concerning these observations arising from such a magnetic field configuration will yield constraints to be incorporated in the model.

The implications of merging between the solar and terrestrial magnetic fields are not, however, restricted to questions of particle access into the magnetosphere. It is generally thought, for instance, that magnetic field merging may play a rôle in the formation of solar flares [5], and might even be involved in galactic phenomena [6]. An investigation of these possibilities is hampered, though, by the lack of concrete evidence concerning the conditions under which merging could take place.

The basic mechanism for the reconnection of magnetic fields is

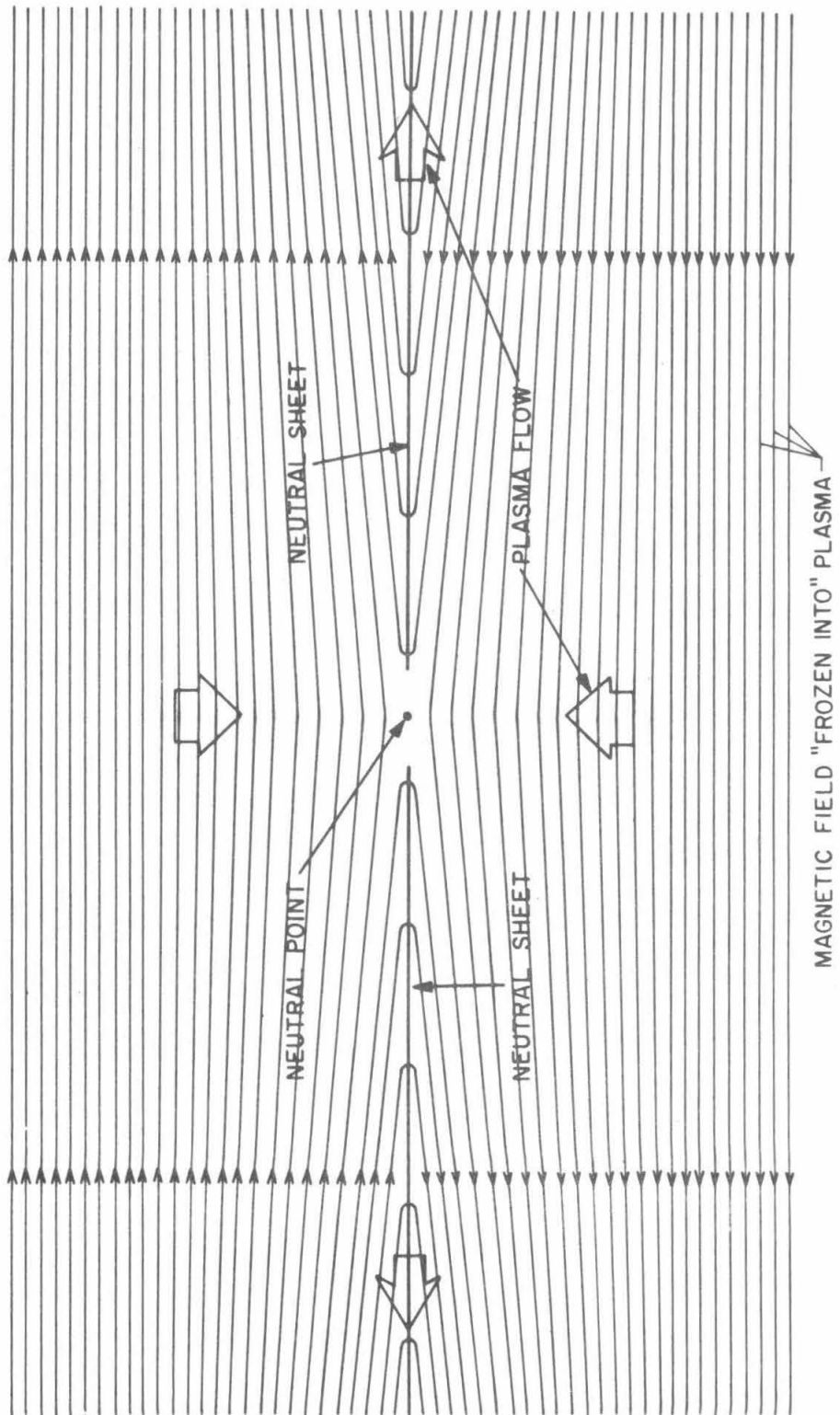


provided by the finite conductivity of the plasma. In 1956, Sweet [84] pointed out that the diffusion rate for magnetic fields in the vicinity of a *neutral point* (at which  $\vec{B}$  vanishes) will be much faster than in other regions of a plasma. Since the magnetic forces vanish at such a point, the magnetic field will tend to form a sheet near which  $\vec{B}$  reverses direction on a relatively small length scale; such a sheet is termed a *neutral sheet*. A neutral point also tends to be a stagnation point of the plasma flow, in which case the magnetic field is convected toward the neutral point, where the field lines are "broken" and "reconnected" as the direction of the plasma flow changes by  $90^\circ$ . Since the field vanishes at the neutral point, however, the process is more accurately thought of as one in which the field being carried to the neutral point disappears and reappears in a different configuration, as determined by the fluid flow. Figure VI-4 illustrates this process, which is referred to as Sweet's mechanism; its astrophysical implications have been investigated by Parker [85].

In order to provide a mechanism whereby higher merging rates than those associated with Sweet's mechanism could be attained, Petschek [86] has suggested that while diffusion may be presumed to dominate the magnetic merging in the immediate vicinity of the neutral point, the plasma which is convecting the field away from the neutral point (after merging) may be moving at the Alfvén velocity,  $V_A$ . Petschek finds that the maximum incoming plasma velocity which can be supported by such a scheme is given by the following recursive relation:

Figure VI-4

Schematic depiction of a neutral point, at which the magnetic field is shown undergoing merging *via* Sweet's mechanism. The angle between the two fields near the neutral sheet has been exaggerated.



$$U_m = \frac{\pi V_A}{4 \ln \left( \frac{16 U_m^2 \pi \sigma L}{V_A c^2} \right)} \quad (6.1)$$

where  $\sigma$  is the conductivity of the plasma at the neutral point, and  $L$  is the scale size of the diffusion region. Sonnerup [87] has recently refined this approach somewhat, and has reported the following relationship for determining the maximum plasma velocity at which the fields may merge:

$$U_m = V_A (1 + \sqrt{2}) \quad (6.2)$$

By treating the basic field equations involved, Yeh and Axford [88] conclude that in general there is no maximum merging velocity, although they show that Sonnerup's solution is a special case of their solution -- the only non-singular case, according to Sonnerup. Considering the scarcity of observational information concerning magnetic merging, it is virtually impossible to determine which, if any, of these solutions is more nearly correct. Even establishing the absence of merging between the solar and terrestrial magnetic fields would be significant.

As a matter of terminology, geomagnetic field configurations arising from the assumption of the absence of magnetic merging between the solar and terrestrial fields are referred to as *closed* magnetospheric models, while those configurations based on the presence of merging are termed *open* magnetospheric models. In the next Section, after a discussion of

the general implications of the electron and proton observations, examples of each of these types of magnetospheric models will be presented and compared to the OGO-4 results presented in Section V and Appendix A.

## VII. DISCUSSION

The information in Section VI provides the basic framework into which the data presented in Section V can be placed. The OGO-4 electron observations provide a comprehensive determination of the boundary between low polar latitudes (closed field lines) and high polar latitudes (open field lines). After this interpretation of the electron data has been established, the proton observations can be used to investigate the characteristics of the "windows" where these charged particles can gain access to the geomagnetic field. The observations of EDP events will be of particular interest in this regard, especially with respect to characterizing the positions and extents of these access windows. These EDP data represent the first reported observations of clearly identifiable interplanetary features, which are propagating down the tail, appearing at different times in different regions of the polar cap. With the particle access configuration established, the three major models of the distant geomagnetic field will be presented, noting the relationship of each to the fundamental question of magnetic merging. The pertinent predictions and extrapolations of the field configuration resulting from each model will be compared with the OGO-4 data with the result that severe constraints can be placed on each model.

*Electron Polar Cap*

The low magnetic rigidity and high velocity of the 0.4-1.0 MeV electrons observed by this experiment make these electron observations of particular importance in defining the transition between the region of open field lines and the region of closed field lines in the magnetosphere [7-9,27,41,89,90]. The identification of the electron polar cap with open geomagnetic field lines can be established as follows. The origin of 50 keV polar cap electrons has been shown to be beyond about  $64 R_E$  behind the earth by moon shadowing experiments conducted with a lunar orbiter by Van Allen and Ness [89], Van Allen [7,8], Anderson and Lin [9], and Anderson [90]. In addition, Van Allen and Ness [89] observe a diffusion rate perpendicular to the magnetic field less than 100 km/sec between the moon and the earth. These observations, coupled with the low rigidity of the electrons, imply that the edge of the electron polar cap plateau should reflect the boundary of open field lines closely. The high electron velocities mean that differences in mode or position of access which might cause large variations in proton fluxes are not significant in electron observations. For instance, Van Allen [8] reports transit times for electrons travelling from interplanetary space to inside the magnetotail of  $\leq 100$  seconds, which were interpreted by Van Allen as indicating that electrons can gain direct access to the geomagnetic tail. As a result of the high velocities and rapid access, the electron flux over the polar caps is relatively homogeneous above the electron polar cap boundary (see figures V-1 and V-2, also Vampola [27] and West and Vampola [41]). The relative uniformity of the electron flux

inside the boundary makes the specification of the location of this boundary rather unambiguous. We therefore interpret the data presented in figure V-3 as a definition of the region of the polar cap which is associated with open field lines in the geomagnetic tail. Whereas Vampola [27] has reported 25 observations of this boundary which he has extrapolated to geomagnetically quiet conditions (indicated on figure V-3), the 333 boundary observations made withOGO-4 during magnetically quiet periods constitute a much more comprehensive mapping of the open field line region than has previously been possible.

For the purpose of clarifying the proton observations, it is clear that the region defined as the high polar latitude (HPL) region in Section V is associated with the geomagnetic field lines which constitute the geomagnetic tail. Likewise, the low polar latitude (LPL) region is associated with closed geomagnetic field lines, which never extend far from the earth ( $< 30 R_{\oplus}$ ). In order to avoid the complications associated with any transition region, data associated with high polar latitudes have been collected at invariant latitudes well above the boundary indicated on figure V-3. Low polar latitude data similarly avoid the region close to the boundary of open field lines. As shown by figure V-18, persistent proton features can be identified consistently with the region of open field lines. With this in mind, we turn now to the proton observations.



*Access of 1.2-40 MeV Protons*

While electrons are able to define the edge of the open field line region with some precision, the much lower velocities and higher rigidities of the 1.2-40 MeV protons make them more sensitive to the effects of interplanetary gradients and anisotropies, different access modes and access window positions. Consequently, they can be used as "probes" to investigate the characteristics of the access windows.

Prior to the report of preliminary results from this experiment for the 2 November 1967 event [11], some evidence of polar cap features was available [12-20], but the observations were too sparse to lead to comprehensive analysis. Although since the report of the persistent feature observed during the 2 November 1967 event several observations of persistent features have been reported [21-26], the conclusions drawn from these observations still suffer from a paucity of data: only Bostrom [21] and Morfill and Quenby [26] have reported observations from more than one event (two events in both cases).

A summary of all of the proton events observed to date in the OGO-4 data is presented in figure VII-1. As indicated in this figure, there is a strong correlation between the pole in which a persistent feature was observed on OGO-4 and the interplanetary sector structure. With notable exceptions, the persistent features were observed in the north pole during negative sectors and in the south pole during positive sectors. This correlation is consistent with other reported studies in which the interplanetary sector structure has been considered [13,24-26,91-93 (the

Figure VII-1

Summary of OGO-4 observations of solar events. The information indicated on this figure is as follows:


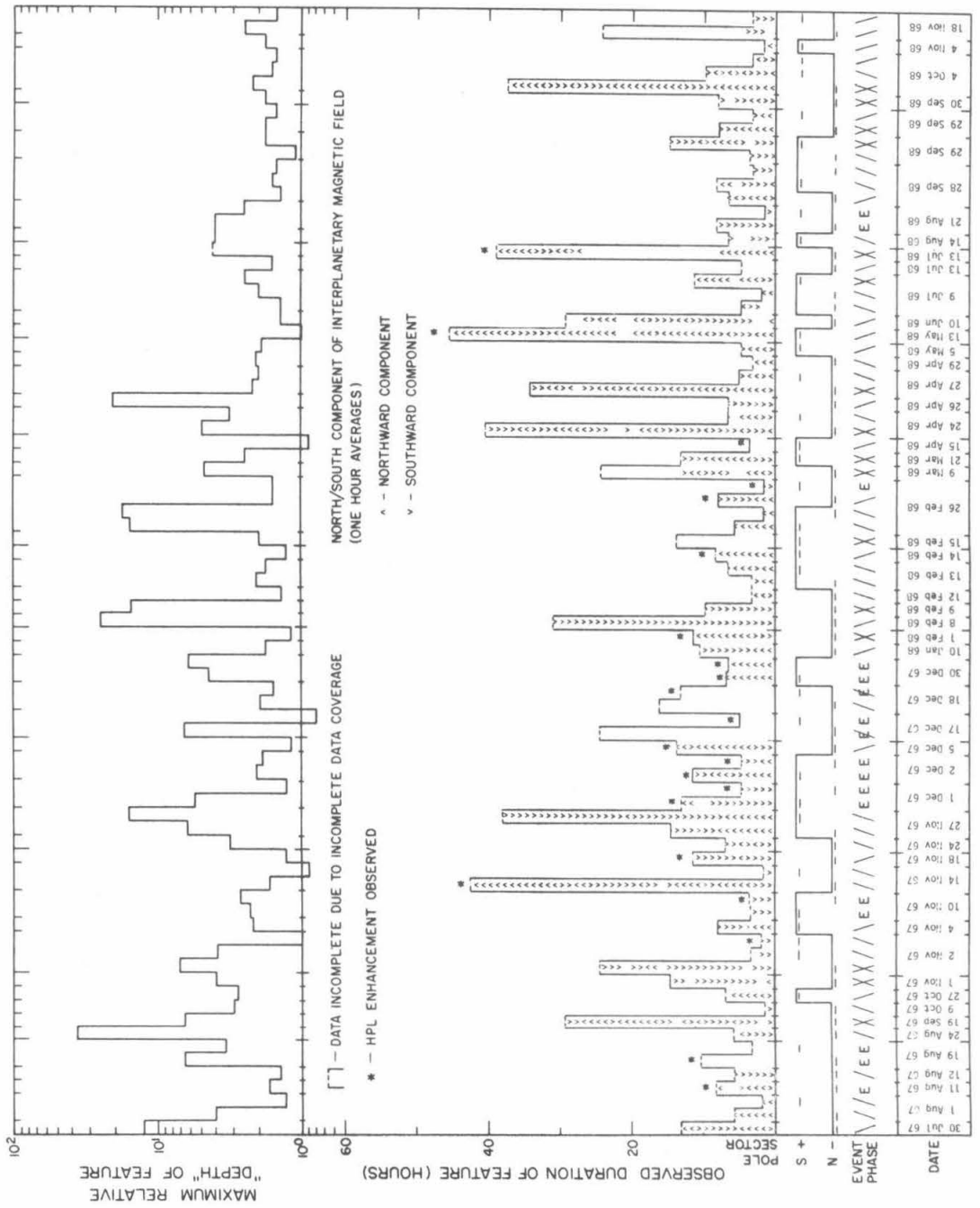
1. Each event is identified by date.
2. The phase of the flare during which a persistent feature was observed is indicated:
  - / = observation during the rise of flare
  - \ = observation during the decay of flare
  - E = EDP event observation
3. The pole in which the persistent feature was observed is indicated ( \_ \_ ^ \_ ) and compared to the interplanetary magnetic field sector (  ).
4. The duration (in hours) of the feature is indicated. In 75% of these observations the actual duration of the event was not measurable due to incomplete data coverage.
5. The history of the north/south component of the solar magnetic field is represented by a vertical sequence of " ^ "s (northward component) and " v "s (southward component). Each symbol represents the average sense of this component during one hour [94]; the lowest symbol indicates the status of this component at the beginning of the observations.

Figure VII-1 (continued)

6. Those events during which an enhancement was observed at high polar latitudes are indicated (\*).
7. For each polar pass of the indicated pole during the event, the ratio of the LPL  $V_1\overline{V_3}$  rate to the HPL  $V_1\overline{V_3}$  rate was calculated. The maximum of these ratios is plotted as the "maximum relative 'depth' of the feature."



last three do not involve satellite proton polar cap observations)]. In accordance with this correlation and for the sake of clarity, the following terms will now be introduced:  $\alpha$ -pole and  $\beta$ -pole. These terms have been carefully selected in an attempt to avoid any terms which might connote any feature of any model. The correspondence between the north and south geomagnetic poles and the  $\alpha$ -pole and  $\beta$ -pole is dependent upon the interplanetary sector and is given in table VII-1. With this definition, the field lines in the geomagnetic tail associated with the  $\alpha$ -pole are usually more nearly antiparallel to the interplanetary magnetic field lines than those field lines in the geomagnetic tail associated with the  $\beta$ -pole. We can now restate the sector correlation noted above as: "With notable exceptions, the persistent features were observed in the  $\beta$ -pole." The persistent flare event features were correlated with the interplanetary sector structure in this manner 91% of the time, while they appeared to be completely uncorrelated with the north-south component of the interplanetary field. The interplanetary field had a southward component only 54% of the time, and figure VII-1 shows that during several events this component changed direction several times with no notable effects.

The data in table VII-2 tend to strengthen the correlation between the interplanetary sector structure and the observations of persistent features considerably. This table lists all of the instances when a sector reversal was observed in interplanetary space [94] while a persistent polar cap feature was being observed. Within the constraints imposed by the inherent time resolution of the observations and the frequent gaps in the data, the following is implied by these data: persistent features

TABLE VII-1

Correspondence Between  $\alpha$ -pole/ $\beta$ -pole  
North/South Geomagnetic Poles

	North Pole	South Pole
Positive Interplanetary Sector	$\alpha$ -pole	$\beta$ -pole
Negative Interplanetary Sector	$\beta$ -pole	$\alpha$ -pole

TABLE VII-2

Time Correlation of Sector Reversals [94] with Persistent Features

Date	Last Feature Obs.			Sector Reversal Univ. Time (HHMM)	1st Pass after SR in Same HPL		Figure Showing Profile
	Hours Before SR	$\sqrt{V_1 V_3}$ (cts/sec) LPL	HPL		Hours after SR	$\sqrt{V_1 V_3}$ (cts/ sec)	
11 Aug 67	0.2	28.	40.	1600	1.5	26.	
28 Oct 67	0.6	0.8	0.4	1200	1.0	0.55	
3 Nov 67	1.3	89.	28.	1300	1.8	45.	E-3
10 Nov 67	0.9	3.4	2.2	2300	4.0	2.8	E-4
10 Feb 68	3.9	2.45	1.09	0500	0.9	2.3	E-10
10 Feb 68	1.4	4.3	11.6	1300	0.3	3.3	
12 Feb 68	1.9	0.94	0.65	1100	0.6	1.85	E-11
10 Jun 68	1.2	525.	398.	1230	0.3	501.	
10 Jul 68	0.8	141.	252.	0300	0.8	112.	
2 Sep 68	0.6	3.84	1.26	1200	1.0	3.02	
28 Sep 68	0.8	67.	57.	0800	0.8	75.	
28 Sep 68	0.6	162.	119.	2000	1.0	163.	
30 Sep 68	1.2	350.	305.	2100	0.3	316.	
30 Sep 68	1.2	285.	213.	1400	0.4	282.	
30 Sep 68	0.8	390.	253.	1600	0.8	385.	

observed prior to a reversal in the interplanetary magnetic field are not present in the data within  $O(1 \text{ hour})$  after the reversal. Additionally, there appears to be no distinction in this regard between persistent HPL depressions and persistent HPL enhancements.

This strong correlation between the interplanetary sector and the persistent features, embodied in the  $\alpha$ -pole/ $\beta$ -pole terminology, can now be used to help organize and interpret additional aspects of the proton observations.

#### *EDP Events*

The observations of EDP events are of particular interest because these events can be associated with an interplanetary region of limited spatial extent which is propagating radially away from the sun (and thus down the length of the geomagnetic tail) at a reasonably constant and well defined velocity: that of the solar wind. As a consequence, time delays between the appearance of the event in different polar cap regions must be directly related to the time required for the region of enhanced flux in interplanetary space to propagate from one access window to the next.

A total of eleven EDP events and possible EDP events have been observed with this experiment. These are tabulated in table VII-3, which includes an indication of some of the factors leading to the identification of each event as an EDP event. In every case the event was observed first at low polar latitudes, which recent work [26,95] involving the



TABLE VII-3

## OGO-4 Observations of EDP Events

Date	Univ. Time of LPL Peak (HHMM)	Delay (hrs. UT) between LPL Peak and:		<del>Alert</del> Neutron Monitor Indi- cation? <sup>a</sup>	SC/SI within 4 hrs. of LPL Peak?	Unam- biguous Ident. as EDP Event? <sup>b</sup>	Figure Showing Profile
		$\alpha$ -HPL Peak	$\beta$ -HPL Peak				
11 Aug 67	0400	0.0	2.0	FD	YES	NO <sup>b</sup>	A-1
19 Aug 67	0548	1.2	13.9 <sup>c</sup>	WD	YES	YES	A-2
10 Nov 67	2145	1.1	--- <sup>d</sup>	NO	NO	YES	A-4
15 Nov 67	0400	--- <sup>e</sup>	6.0	NO	NO	YES	
15 Nov 67	0830	--- <sup>e</sup>	5.1	NO	NO	NO	
1 Dec 67	2130	1.2	7.0	WD	NO	YES	A-5
2 Dec 67	1300	1.3 <sup>c</sup>	3.8 <sup>c</sup>	NO	NO	YES	A-6
17 Dec 67	0600	0.0	21.2	NO	NO	NO	
30 Dec 67	1135	1.4	5.9	FD	YES	YES	A-7
30 Dec 67	1420	2.2	--- <sup>e</sup>	FD	YES	YES	A-7
27 Aug 68	1515	0.4	1.3	NO	NO	NO	
1 Oct 68	0130	--- <sup>e</sup>	5.0	FD	YES	YES	
Average delays:		1.4 $\pm$ 0.4	6.9 $\pm$ 3.3				

<sup>a</sup>. FD = Forbush Decrease; WD = weak depression

<sup>b</sup>. All events in this table exhibit most of the phenomenological characteristics of EDP events (e.g. only observed at low energies, rapid variations in counting rate, short duration), but those indicated by "NO" in this column have some facet which is not completely consistent with EDP observations (*cf.* discussion in Appendix A concerning the 11 August 1967 event).

<sup>c</sup>. Observation is uncertain or impossible due to a data gap.

<sup>d</sup>. Sector reversal occurs before  $\beta$ -HPL EDP peak would be expected.

<sup>e</sup>. Observation impossible due to orbit which did not penetrate to HPL.

calculation of proton trajectories in a model magnetosphere has indicated corresponds to an access window in the vicinity of the earth (within about  $20 R_{\oplus}$ ). After a short delay, which averaged  $1.4 \pm 0.4$  hours, the event was observed at  $\alpha$ -high polar latitudes. After a much longer time delay ( $6.9 \pm 3.3$  hours) the event was observed at  $\beta$ -high polar latitudes. The following conclusions can be made and are illustrated in figure VII-2 (an average solar wind velocity of 400 km/sec is assumed in calculating the access window "positions"):

1. THE ACCESS WINDOW FOR 1.2-40 MeV PROTONS OBSERVED AT  $\alpha$ -HIGH POLAR LATITUDES IS SOMEWHAT FURTHER FROM THE SUN THAN THE ACCESS WINDOW FOR THOSE PROTONS OBSERVED AT LOW POLAR LATITUDES. ( $\alpha$ -high polar latitude access window is located approximately  $320 \pm 90 R_{\oplus}$  behind the earth.)

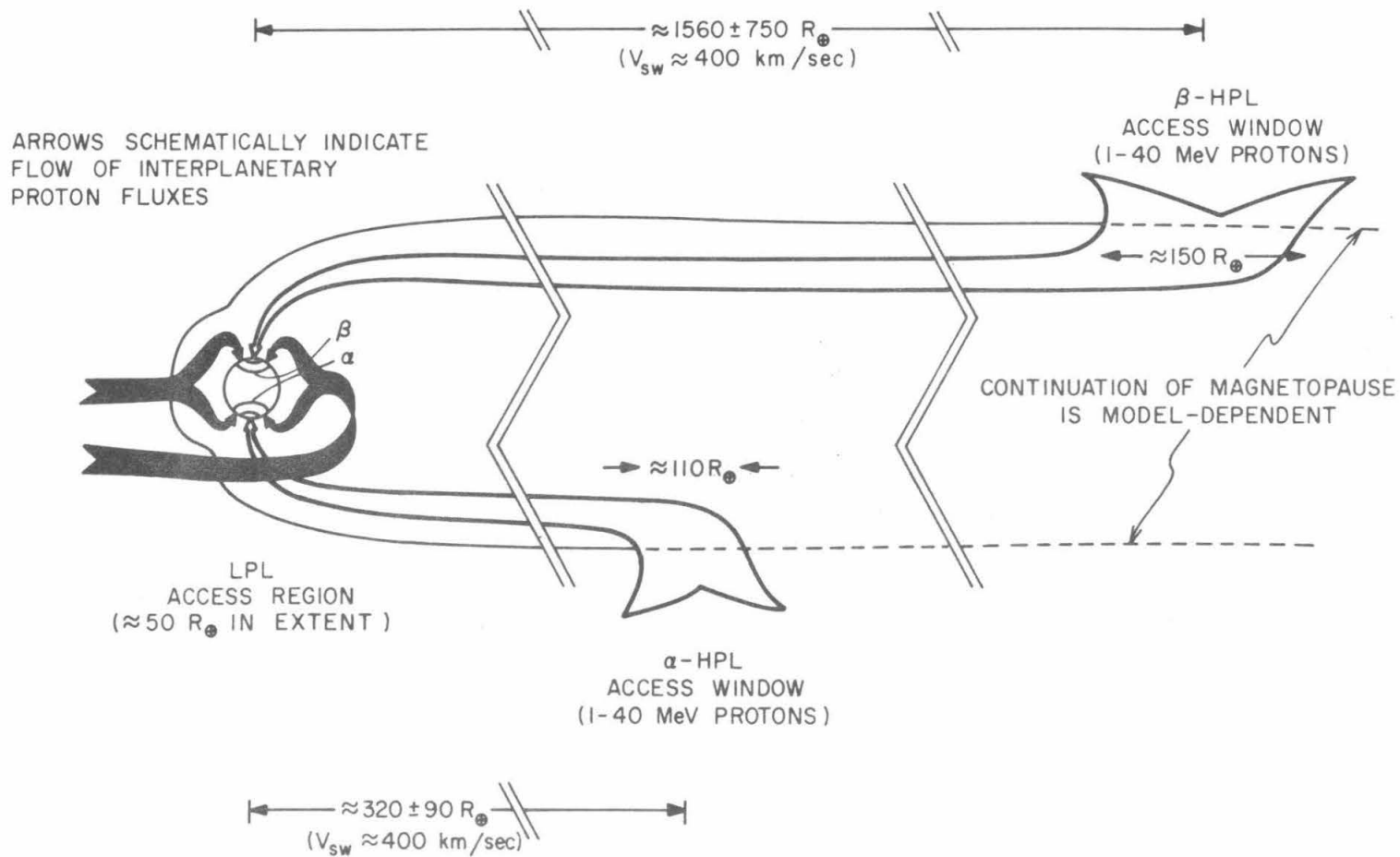
2. THE ACCESS WINDOW FOR 1.2-40 MeV PROTONS OBSERVED AT  $\beta$ -HIGH POLAR LATITUDES IS SIGNIFICANTLY FURTHER FROM THE SUN THAN THE ACCESS WINDOW FOR THOSE PROTONS OBSERVED AT LOW POLAR LATITUDES. ( $\beta$ -high polar latitude access window is located approximately  $1560 \pm 750 R_{\oplus}$  behind the earth.)

Examples of these EDP observations are given in figures A-1, A-2, A-4 through A-7, and V-4.

In addition to the location of the access windows, estimates of the extent of the windows can also be inferred from these data. Although in general the polar cap flux is related to the interplanetary flux by a

Figure VII-2

Schematic representation of the configuration of the magnetospheric access windows for 1.2-40 MeV protons. This configuration is referred to as the  $L_{\alpha\beta}$  configuration in the text. This diagram is intended to be completely model-independent; magnetic fields are not indicated, nor are details concerning the method by which protons gain access.



convolution integral, all that is needed at this point is an estimate. For this purpose, the "width" of the feature,  $\Delta T$ , as shown on a profile, may be related to the spatial extent of the feature in interplanetary space,  $L_{ip}$ , and the spatial extent of the access window,  $L_w$ , by the approximation

$$\frac{L_{ip} + L_{w,reg}}{V_{sw}} \approx \Delta T_{reg} \quad (7.1)$$

where  $V_{sw}$  is the solar wind velocity, and "reg" represents one of "LPL", " $\alpha$ -HPL", or " $\beta$ -HPL". Using  $\sim 1$  hr. as a typical value for  $L_{ip}$  (indicated by the data presented by McCracken, *et al.* [66] and Anderson [47]), theOGO-4 EDP observations give the following estimates for the extent of the access windows:

$$\begin{aligned} L_{LPL} &\sim 50 R_{\oplus} \\ L_{\alpha-HPL} &\sim 110 R_{\oplus} \\ L_{\beta-HPL} &\sim 140 R_{\oplus} \end{aligned} \quad (7.2)$$

These numbers are very rough estimates due to the sparcity of well defined data and the assumptions made above, but the ratio between any two of these values can be considered accurate to within a factor of 2.

Questions relating to the details of the magnetic field configuration in the vicinity of the access windows and the method by which this access is achieved will be discussed below, after considering the extent to which the solar flare event observations support the  $L\alpha\beta$  access window configuration illustrated in figure VII-2.

*Flare Events*

The interpretation of the EDP event observations was aided in no small degree by the availability of several events for which the data coverage was virtually continuous and almost uninterrupted. Because of the much longer duration of solar flare particle events, conclusions drawn from observations of flare events are, in contrast, subject to the following two limitations: (1) the time-sharing nature of the OGO-4 telemetry made it virtually impossible to obtain a profile of a complete flare event (see Section III), and (2) the interplanetary configuration of proton fluxes during solar flare events is highly dependent on non-uniform interplanetary parameters and parameters related to the parent flare. The first point implies that several flare events must be observed to construct a comprehensive picture of particle access. The second point, on the other hand, implies that this is a limitation not confined to data from OGO-4. Indeed, any conclusions drawn from observations of a single flare event are subject to the limitation that only one set of solar flare and interplanetary parameters are represented. As the basis for the conclusions presented here, though, more than twenty-five solar flare events were investigated, representing a wide range of these parameters; these observations are summarized in table A-1.

Although interpretations of the proton flare event observations are complicated by the effects of interplanetary propagation, at least four aspects of these observations imply an  $L\alpha\beta$  configuration for the access regions:

1. Flare onsets consistently occur later at  $\beta$ -high polar latitudes than at either low polar latitudes or  $\alpha$ -high polar latitudes. The 2 November 1967 event (figures V-7 and A-3) is a particularly good example of this: there are two  $\beta$ -pole observations after the beginning of the flare is seen at LPL, showing a flux comparable to the pre-event flux at  $\beta$ -HPL. The 13 July 1968 event, shown in figure A-12, is another example of this delayed onset phenomenon.

2. Flare onsets are sometimes observed to occur later at  $\alpha$ -HPL than at LPL. Once again, the 2 November 1967 event (figures V-7 and A-3) is a good example of this type of observation.

3. The "shape" of the  $\beta$ -HPL profile relative to the LPL profile consistently exhibits the characteristics expected in observations taken further from the sun: in all cases the  $\beta$ -HPL peak (a) is broader, (b) represents a smaller maximum flux, and (c) occurs at a later time. The 13 July 1968 event (figure A-12) is a perfect example of this phenomenon. Note that the  $\beta$ -HPL peak is clearly broader, lower, and later than the LPL peak. Other complete examples are scarce due to the data acquisition problem, but the 1 February 1968 event (figure A-8) is notable.

4. Occasionally the peak  $\beta$ -HPL flux is greater than the LPL flux measured at the same time. This results in the persistent feature being an enhancement, normally during the decay phase of the event. The 1 February 1968 (figure A-8) and 13 July 1968 (figure A-12) events

are graphic examples of this type of observation, but the 13 May 1968 event (figure A-11) is particularly notable: a significant  $\beta$ -HPL enhancement lasting for more than forty hours. An access window configuration of the  $L_{\alpha\beta}$  type discussed above would mean that a  $\beta$ -HPL enhancement should be observed whenever the interplanetary flux gradient is positive and large enough:

$$\frac{1}{J} \frac{dJ}{dR} \geq 5 \times 10^{-3} \% / R_{\oplus} \text{ for a } V_1 \overline{V_3} \text{ rate of } \sim 10 \text{ cts/sec.}$$

The consistency with which all four of these phenomena are observed is strong evidence for the existence of the  $L_{\alpha\beta}$  access window configuration illustrated in figure VII-2.

Thus, the OGO-4 proton observations consistently imply that the 1.2-40 MeV proton access windows are often related in the manner illustrated in figure VII-2, which we are referring to as the  $L_{\alpha\beta}$  configuration. This configuration and other aspects of these data are quite relevant to the problem of placing constraints on the possible configurations of the distant geomagnetic tail.

#### *Models of the Distant Geomagnetic Field Configuration*

As mentioned above, one of the important and currently unresolved questions concerning the geomagnetic field is the degree to which the solar and terrestrial magnetic fields merge. Although charged particle observations cannot answer this question directly, a great deal of insight can be gained by analyzing the implications of such observations in the context of possible configurations of the geomagnetic field. Several such



configurations can be postulated, of course, but we will deal here with three fundamentally different models: a closed configuration (i.e., no merging), referred to as *model A*, an open configuration involving merging near the sub-solar point on the front of the magnetosphere (*model B*), and an open configuration involving merging at the polar neutral points (*model C*). Each of these models will be dealt with in turn: after a brief description of the major facets of a model, some of the consequences with respect to charged particle observations in the polar caps will be investigated. Following the discussion of the model, the pertinent OGO-4 data will be compared to these predictions. The results of this comparison between the model predictions and the OGO-4 results are listed in table VII-4. In this table, the predictions which are not attributable to one or more of the proponents of a given model and are thus the responsibility of this paper are indicated by italics; these extrapolations will be discussed below.

#### *Closed Magnetospheric Configuration -- MODEL A*

In the absence of merging, there will be no direct link between the geomagnetic field and the interplanetary magnetic field. Michel and Dessler have dealt with this picture extensively [3,10,96-100]. The most striking characteristic of this model is a very long tail, extending as far as an astronomical unit or more behind the earth [3]. As one moves away from the earth along the tail, the tail is pictured as being gradually flattened by the anisotropic pressure of the interplanetary magnetic field looping over the tail. It is postulated that somewhere between 1.1 and

TABLE VII-4

## Correlation of Magnetic Field Configuration Predictions with OGO-4 Data

	Conse- quence of model A? <sup>1</sup>	Conse- quence of model B? <sup>2</sup>	Conse- quence of model C? <sup>3</sup>	Conclu- sion from OGO-4 Data?	References to OGO-4 Data
1. Persistent features are correlated with interplanetary sector measured at 1 AU.	NO	YES	YES	YES	Tables VII-2 and A-1 Figures VII-1, A-3, A-4, and A-9
2. Persistent features are correlated with N/S component of solar magnetic field.	NO	YES	NO	NO	Table A-1 Figure VII-1
3. Disappearance of persistent feature correlated with sector reversal at 1 AU within 0(1 hour).	NO	?	YES <sup>4</sup>	YES	Table VII-2 Figures A-1, A-3, A-4, and A-9
4. Delay between LPL EDP peak and $\alpha$ -HPL EDP peak is 0(1 hr).	NO	YES	YES <sup>4</sup>	YES	Table VII-3 Figures A-1, A-2, A-4 thru A-7, and V-4
5. Delay between LPL EDP peak and $\beta$ -HPL EDP peak is 0(7 hrs).	?	NO	YES <sup>4</sup>	YES	Table VII-3 Figures A-1, A-2, A-5 thru A-7, and V-4
6. $\beta$ -HPL flux should always be $\leq \alpha$ -HPL flux.	YES	NO	NO <sup>4</sup>	NO <sup>5</sup>	Figures A-8, A-11, and A-12

TABLE VII-4 (continued)

(Correlation of Magnetic Field Configuration Predictions with OGO-4 Data)

	Conse- quence of model A? <sup>1</sup>	Conse- quence of model B? <sup>2</sup>	Conse- quence of model C? <sup>3</sup>	Conclu- sion from OGO-4 Data?	References to OGO-4 Data
7. Interplanetary flux gradients contribute to persistent features and N/S asymmetries.	<i>YES</i>	NO	<i>YES</i>	YES	Consequence of $L_{\alpha\beta}$ access window configuration
8. Interplanetary anisotropies contribute to persistent features and N/S asymmetries.	?	YES	<i>YES</i>	YES?	Discussed in text
9. Persistent features or N/S asymmetries in the absence of interplanetary anisotropies.	<i>YES</i>	NO	<i>YES</i>	YES	Indirect evidence: east limb flares, flare decays, & long duration features
10. Persistent $\beta$ -HPL > $\alpha$ -HPL in absence of interplanetary solar-directed anisotropies.	<i>NO</i>	NO	<i>YES</i>	YES	EDP events
11. $\beta$ -HPL access window is about five times further behind the earth than $\alpha$ -HPL access window.	NO	NO	<i>YES</i>	YES	Consequence of $L_{\alpha\beta}$ access window configuration

TABLE VII-4 (notes)

<sup>1</sup>Michel and Dessler [10]: Extended geomagnetic tail, flattened by interplanetary magnetic field, becoming filamentary beyond 1.1-1.5 AU. Diffusive access from the earth to the filamentary region; rapid access to filaments for  $\alpha$ -pole.

<sup>2</sup>Dungey [2], Axford, *et al.* [104], Reid and Sauer [13], Van Allen, *et al.* [25], and others: merging near the subsolar point on the magnetopause; implies north and south geomagnetic tails are both of the same length. Rapid access along field lines; interplanetary anisotropies may cause different HPL fluxes in the two poles.

<sup>3</sup>Frank [4]: Merging at the polar neutral points; implies north and south geomagnetic tails may be of different lengths. Rapid access along field lines; interplanetary gradients as well as anisotropies may affect polar cap observations.

<sup>4</sup>Answer depends upon the satisfaction of the constraints specified in the text. See also Appendix C.

<sup>5</sup> $\beta$ -HPL flux to  $\alpha$ -HPL flux ratios as great as 2 have been observed during the decay phase of solar flare events; figure A-11 is a good example of a period during which the  $\beta$ -HPL flux was about 30-40% higher than the  $\alpha$ -HPL flux; this implies a gradient of  $\sim 2 \times 10^{-3} \% / R_{\oplus}$ . See also figures A-8 and A-12. This degree of enhancement is greater than would be expected from a solar-directed interplanetary anisotropy, the magnitude of which is typically between 5% and 20%.

1.5 AU the tail has become so drastically flattened ( $\sim 10^3 R_{\oplus}$  wide by  $\sim 10 R_{\oplus}$  thick at about  $10^4 R_{\oplus}$  behind the earth) that the field becomes filamentary [10]. It is questionable, however, whether such a degree of flattening is supportable [101].

The primary mode of access for charged particles is by diffusion through the sides of the tail [10,97-99]. Michel and Dessler also postulate that charged particles may be able to rapidly gain access to the geomagnetic field in the filaments (i.e., beyond 1.1-1.5 AU) [10]. Michel and Dessler further point out that such a mechanism will probably be more effective for one pole than the other, depending on the orientation of the interplanetary field near the pertinent filaments in such a way that particles should be able to enter the filaments of the  $\alpha$ -tail (defined in terms of the sector at 1.1-1.5 AU) more readily than those of the  $\beta$ -tail. This could lead to north/south differences in the fluxes observed at high polar latitudes, which would be correlated with the configuration of the interplanetary field at 1.1-1.5 AU (cf. A1 and A3 in table VII-4). The north/south component of the field does not appear to be pertinent to these access mechanisms (cf. A2). Although these mechanisms appear to be independent of the presence of interplanetary anisotropies (cf. A8, A9 and A10), it would seem that interplanetary flux gradients between 1 AU (LPL access window) and 1.1-1.5 AU could result in the observation of persistent features in the polar caps (cf. A7).

It is instructive to cast these access mechanisms in the framework of access windows. Both poles are said to have a window for slow, diffusive

access extending from  $\geq 1$  AU to  $\approx 1.1-1.5$  AU, in which the rate of access is postulated to be independent of the orientation of the interplanetary field, and hence the same in both windows. Beyond these access windows, in the filamentary portion of the tail (*cf.* A11), is the rapid access window, which is postulated to be effective only for the  $\alpha$ -pole. This access window configuration implies that the  $\beta$ -HPL flux can never exceed the  $\alpha$ -HPL flux, since any flux gaining access to the  $\beta$ -tail would gain access to the  $\alpha$ -tail at the same rate through the diffusive windows (*cf.* A6). The predictions of this model with respect to the observation of EDP events also follow from this picture of the access windows. The EDP peak would, of course, be observed at LPL coincident with the arrival at 1 AU of the interplanetary region of enhanced flux. After a delay of 10-50 hours (approximate solar wind propagation time for 0.1-0.5 AU), a peak would be observed at  $\alpha$ -HPL. If the diffusion rate in the diffusive access windows were sufficiently rapid, an additional  $\alpha$ -HPL EDP peak might be observed, coincident with a  $\beta$ -HPL peak and before the  $\alpha$ -HPL peak due to access through the rapid access window. Whether or not the diffusion rate is rapid, however, it is clear that in either case the EDP observations would be phenomenologically quite different than those observed with OGO-4 (*cf.* A4 and A5).

As indicated in table VII-4 these predictions are inconsistent with the OGO-4 data. With the severe constraints which these data place on this model, it is questionable whether it can remain supportable in its present form. This does not imply, however, that no other closed magnetospheric configuration could be developed which would meet these constraints.

*Magnetic Merging at the Sub-solar Point -- MODEL B*

In contrast to the situation in model A, significant merging between the geomagnetic field and the interplanetary magnetic field will result in a configuration in which the high polar latitude regions are directly connected to interplanetary space. In 1961, Dungey [2] pointed out that in the presence of a southward component in the interplanetary magnetic field there might be two magnetic neutral points in the geomagnetic-interplanetary magnetic field system: one on the solar side of the magnetosphere, perhaps near the sub-solar point on the magnetopause, and the other behind the earth. As he and others have pointed out [102-107], if conditions at the neutral points were such as to allow magnetic field merging, then a configuration could be postulated wherein geomagnetic field lines merge with interplanetary field lines on the solar side of the magnetosphere, are pulled back across the polar caps as the solar field continues to propagate with the solar wind, and eventually reconnect at the anti-solar neutral point, after which the lines migrate back around the polar caps to the front of the magnetosphere again. Since the length of the tail in this configuration would be the product of the "age" of the tail (average time from merging at the neutral point on the solar side of the magnetopause to reconnection at the anti-solar neutral point) and the average propagation velocity, near the magnetopause, of the plasma in which the interplanetary field line is imbedded, the north and south geomagnetic tails would necessarily be the same length. Although both are the same length, as Dungey [106], Reid and Sauer [13], Van Allen, *et al.* [25], and others have pointed out, one tail may be connected to portions of the

interplanetary field which are solar-directed, while the other is connected to an anti-solar-directed field. This effect depends on the orientation of the solar field in the ecliptic plane (e.g. the sector of the solar field) near the earth (*cf.* B1 and B3 in table VII-4), and the entire process is dependent on the presence of a southward component in the solar field (*cf.* B2).

The access mechanism for low rigidity particles in this model is rather simple: the direct connection between the polar cap magnetic field and the interplanetary magnetic field allows interplanetary fluxes to gain access to the polar cap regions directly, although the trajectories involved may be non-adiabatic. Reid and Sauer [13], Van Allen, *et al.* [25], and others [24,26,108] have pointed out that interplanetary anisotropies may contribute to features observed in the polar cap regions (*cf.* B8), especially if adiabatic motion is invoked to imply that the only particles seen at  $\alpha$ -HPL will be those having interplanetary pitch angle within a few degrees of zero, while the only particles seen at  $\beta$ -HPL will be those having interplanetary pitch angles within a few degrees of  $180^\circ$ . The validity of this assumption is discussed below and in Appendix B.

Several consequences for polar cap charged particle observations can be extrapolated from this model; most of these are consequences of the implied access window configuration: both HPL access windows located the same distance (the most recent estimates being a few hundred earth radii [25]) behind the LPL access window, which is, again, within  $\sim 20 R_\oplus$  of the earth (*cf.* B11). Although interplanetary flux gradients could not, of course,



cause north/south asymmetries, they might cause persistent features if large enough  $\left( \left| \frac{1}{J} \frac{dJ}{dR} \right| \gtrsim 3 \times 10^{-2} \% / R_{\oplus} \right)$  to cause discernible differences between the LPL flux and the HPL flux (Cf. B7). Clearly, then, with that one possible exception, persistent features and north/south asymmetries would not be expected except in the presence of interplanetary anisotropies (Cf. B9 and B10). Also, if the interplanetary anisotropy were solar-directed, one would expect to observe a larger flux at  $\beta$ -HPL than at  $\alpha$ -HPL (Cf. B6). This access window configuration also implies that during EDP events both HPL peaks would be observed at the same time: on the order of an hour after the LPL peak (Cf. B4 and B5).

The disappearance of persistent features may or may not be correlated to sector reversals, depending on the effect a given reversal has on the magnitude of the interplanetary anisotropy. If the anisotropy disappears coincident with the sector reversal, then so also will the persistent feature. If the anisotropy is unaffected by the sector reversal, then the feature should be seen to change from one pole to the other, staying in the  $\beta$ -pole (or  $\alpha$ -pole) (Cf. B3).

The extent to which the OGO-4 data agree with these predictions is illustrated in table VII-4. The net result of the observations is the implication that although interplanetary anisotropies may contribute to the features observed at the polar caps, other causes are clearly important as well. In particular, the EDP event observations are somewhat difficult to interpret in the context of an open field configuration in which the north and south HPL access windows are the same distance from the earth.

*Magnetic Merging at the Polar Neutral Points -- MODEL C*

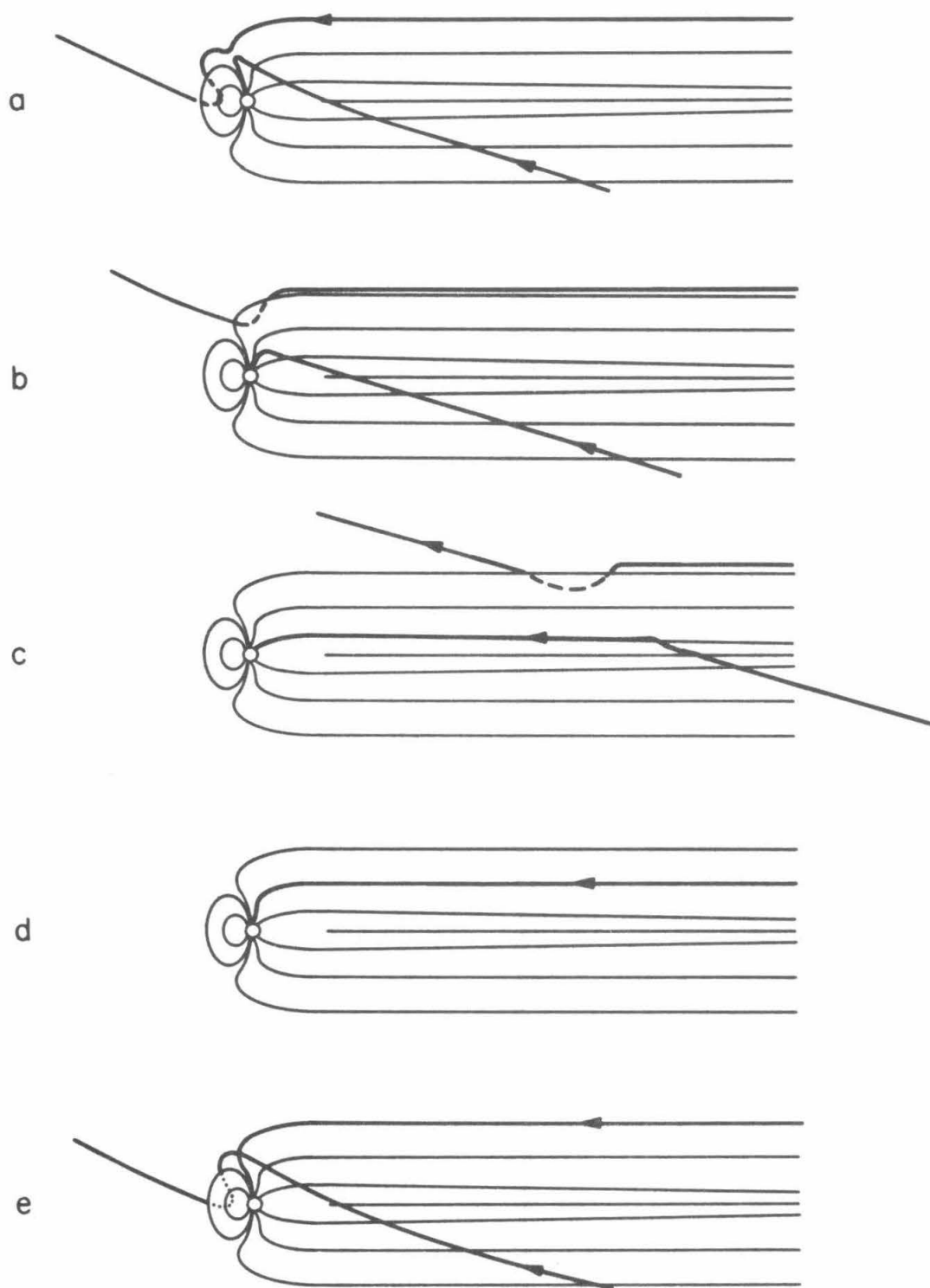
Frank has recently proposed a new variation of the open geomagnetic field configuration in connection with his studies of the relationship among the polar cusp region, the neutral sheet region, and auroras [4,109, 110]. Although this model was originally intended to explain other phenomena, its relevance to the problem of particle access into the magnetosphere is unique: it is an open configuration in which widely separated access windows might be a natural consequence. It is important, therefore, to investigate what constraints must be placed on the model to yield the sector-dependent  $L\alpha\beta$  access window configuration prior to discussing the consequences of the model with respect to charged particle access. First, though, a brief description of the model is necessary.

All merging which takes place between the geomagnetic field and the interplanetary field is assumed to take place only at the polar neutral points (see figures VI-3 and VII-3). After a geomagnetic line of force merges with an interplanetary line of force, the foot of the line of force is pulled back along the boundary of the high polar latitude region. The intersection of the line of force and the magnetopause travels along an extension of the polar "cusp" region along the flank of the magnetosphere until the neutral sheet region is reached. At this point one of two things occurs, depending on the pre-merging configuration of the geomagnetic field line:

- A. The geomagnetic field line was originally a closed field line. The other end of the original line, which connects to the other

Figure VII-3

Schematic representation of the "history" of an open geomagnetic field line which merges with an interplanetary magnetic field line at the northern polar neutral point. The geomagnetic line of force merges at the neutral point (a), is pulled back along the cusp region (b) and into the neutral sheet region (c). The line eventually begins to migrate across the polar cap (d), until it once again passes near the polar neutral point (e).



pole, has been following a similar path along the "cusp" region in the other hemisphere. In the neutral sheet the lines again merge, re-connecting the two ends of the original interplanetary field line. The reconnected geomagnetic field line is eventually convected back to the front of the magnetosphere to undergo the process again.

B. The geomagnetic field line was originally an open field line. The other end of the original geomagnetic field line is no longer connected to the earth, and consequently appears to play no further part in the process of particle access. The line of force connected to the earth eventually begins to migrate across the tail until it is passing near the neutral point again, at which time the process can start again. The migration takes place to replenish open field lines which are being removed from the neutral point by the merging process (see figure VII-3).

Since only the open field lines are involved in the definition of access into the high polar latitude regions, we will confine our attention to the second process.

Since the interplanetary lines of force continue to be convected away from the earth by the solar wind, the length of the geomagnetic tail would be proportional to its "age": i.e., the time required for a line to complete an entire cycle, from merging to merging again. This time, in turn, is in some sense inversely proportional to the rate at which open field lines merge at the neutral point. It is immediately obvious, of course, that if the open field line merging rate were different at the two neutral points,

then the north and south geomagnetic tails would be of different lengths. There is, therefore, a mechanism whereby an  $L\alpha\beta$  configuration could be established. It remains, however, to investigate what conditions must be met to achieve the configuration of figure VII-2, which the OGO-4 data have established. There are at least three features which are pertinent in this regard:

- (1) the relative locations of the access windows,
- (2) the extent of the access windows, and
- (3) the time correlation between the disappearance of persistent features and sector reversals in the interplanetary field.

(1). The observational evidence which was discussed in relation to the  $L\alpha\beta$  access window configuration illustrated in figure VII-2 indicates that the position of the  $\beta$ -HPL access window can be between 3 and 10 times as far behind the earth as the  $\alpha$ -HPL access window. For this to occur, the rate at which open field lines merge at the  $\alpha$ -polar neutral point must be 3-10 times the rate at the  $\beta$ -polar neutral point. The theoretical investigation of this point is rather complex and is considered in detail in Appendix C. One of the major difficulties encountered in trying to deal with magnetic merging in this configuration is the applicability of earlier studies, all of which have concentrated on a configuration like that shown in figure VI-4: two exactly antiparallel fields considered in a plane parallel to the fields and perpendicular to the interface between them. The work of Sweet [84], Petschek [86], Sonnerup [87], and Yeh and Axford [88], discussed above, can be generalized to treat two non-antiparallel fields by the superposition of a constant field perpendicular

to the plane in which they analyze the antiparallel field configuration and by making the suitable minor readjustments of their results (see (6.1) and (6.2)). The configuration of the fields at the geomagnetic neutral points, however, involves, as shown in figure C-2, the interaction between a region where the field is homogeneous and a region where the orientation of the field is a strong function of position. Assumptions must consequently be made concerning the merging likelihood for two fields as a function of the angle between them in the presence of fields at all such angles. The implications of three such assumptions, chosen as representative of a wide range of possible assumptions, are investigated in Appendix C.

The main conclusions to be drawn from the results of Appendix C are that (a) such differences in polar merging rates are well within the limits of reasonable parameters if certain assumptions are made concerning the angular dependence of the merging rate, and (b) if the sector is redefined in terms of the earth-sun line and the interplanetary field direction near the polar neutral point instead of the average spiral angle and the field direction far from the earth, the correct sector correlation follows.

That the critical interplanetary field configuration is that of the portion of the field near the polar neutral points complicates matters considerably. It is not clear how this configuration depends in detail on the field configuration in interplanetary space and on the solar wind parameters [cf. 111,112]. Nor is it clear that for a given set of interplanetary parameters the interplanetary field will make the same angle with the

earth-sun line at one neutral point as it does at the other. Until this question is resolved, it will not be possible to determine whether there is an exact, detailed correlation between the access window positions inferred from the data and those inferred from this model.

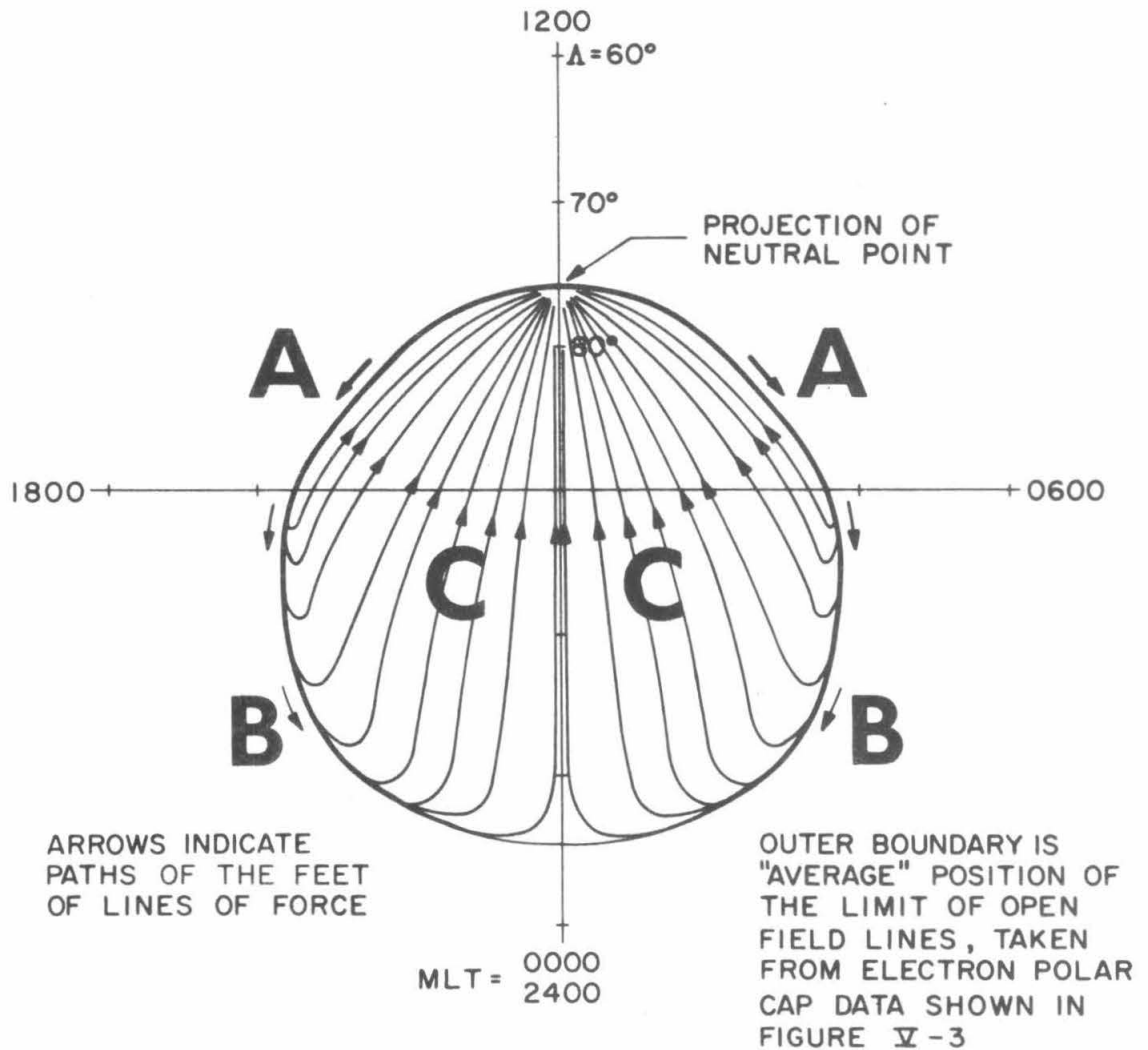
(2). The size of the HPL access windows relative to their positions places constraints on the way in which the geomagnetic field lines migrate from the neutral point to the neutral sheet region and back to the neutral point. Figure VII-4 shows a tentative migration pattern, wherein the paths followed by the feet of the open lines of force are shown projected into an invariant latitude-magnetic local time coordinate system. After merging at the neutral point a line is pulled down the cusp region (paths A), into the neutral sheet region (paths B), and finally migrates back to the neutral point (one of paths C). As soon as the foot of a line of force enters the central region of the polar cap (C), the intersection of that line with the magnetopause becomes part of the HPL access window for that pole. It remains part of the access region until the magnetopause intersection is no longer connected to the polar region (i.e., until the line merges again at the neutral point). The length of the access window (measured parallel to the axis of the tail) is therefore proportional to the time required for the lines to migrate from the neutral sheet region (B) across the polar cap (C) to the neutral point.

The data presented in Section V indicate the parameters given in (7.2) as "typical" for the  $L\alpha\beta$  access window configuration. In contrast to the case for the positions of the access windows, the length of the windows does not seem to depend heavily on the interplanetary sector. This



Figure VII-4

Tentative sketch of the migration pattern for polar geomagnetic field lines in Frank's magnetospheric model (model C). Examples of the "paths" followed by the feet of the polar field lines are projected into a  $\Lambda$ -MLT coordinate system.



would imply that the time spent by a line migrating across region C would need to be more or less independent of the total migration time for a complete cycle. This is a clear constraint which the experimental data place on this configuration.

(3). The data shown in table VII-2 indicate that persistent  $\beta$ -HPL features disappear within about one hour after a reversal in the interplanetary sector. This means that within one hour after a sector reversal from, for instance, negative to positive the northern high polar latitude access region has changed from a  $\beta$ -HPL configuration to an  $\alpha$ -HPL configuration. This establishes a lower limit for the merging rate at the  $\alpha$ -polar neutral point: it must be at least as large as that necessary for almost every high polar latitude field line to have merged with the interplanetary field at least once in less than one hour; i.e., an open field merging rate not less than  $\sim 1.3 \times 10^5 \mu\text{G-R}_{\oplus}^2/\text{hr}$ .

This rate is not inconsistent with the following estimate for the maximum rate at which the interplanetary magnetic field impinges on the polar neutral points. If all of the  $\sim 50 \mu\text{G}$  interplanetary magnetic field which impinges on the front of the magnetosphere is thought of as being swept up past the neutral point by the  $\sim 225 R_{\oplus}/\text{hr}$  (400 km/sec) solar wind, then the "rate" at which the interplanetary field would impinge on each neutral point would be  $\sim 1.4 \times 10^5 \mu\text{G-R}_{\oplus}^2/\text{hr}$ .

These rates are also consistent with at least two of the theoretical maximum merging rates discussed in Section VI: those predicted by Sonnerup [87] and by Yeh and Axford [88]. The consistency with the latter predic-

tion is self-evident, since they predict that there will be no upper limit on the merging rate. In order to check the consistency of these merging rates with the prediction of Sonnerup, given by (6.2), we must estimate the solar wind conditions near the polar neutral points. According to Spreiter, *et al.* [111],

$$V_{np}/V_{sw} \sim 0.7$$

and

$$\rho_{np}/\rho_{sw} \sim 1.8$$

Also, according to Alksne [113],

$$B_{np}/B_{sw} \sim 4$$

This means that

$$V_{A,np}/V_{A,sw} \sim 3$$

and the Alfvénic Mach number of the solar wind plasma near the polar neutral point is therefore

$$\begin{aligned} (M_A)_{np} &= (M_A)_{sw} \frac{V_{np}/V_{sw}}{V_{A,np}/V_{A,sw}} \\ &\sim 1.9 \end{aligned}$$

Thus the idea of the interplanetary magnetic field merging as fast as it impinges on the neutral point is not inconsistent with (6.2), which specifies

$$M_A \leq 2.4$$

Assuming these constraints to be satisfied, the degree to which the OGO-4 data agree with the resultant predictions of this model is indicated in table VII-4, although the *a priori* assumption that the constraints discussed above were satisfied was begging the question somewhat. It is interesting that this model is the only type discussed here which even qualitatively provides a mechanism for generating an  $L_{\alpha\beta}$  access window configuration. Although the data presented here cannot provide a conclusive test of the validity of the model in its present form, they do provide three major constraints within which more refined versions of the model will have to be developed.

#### *Interplanetary Anisotropies*

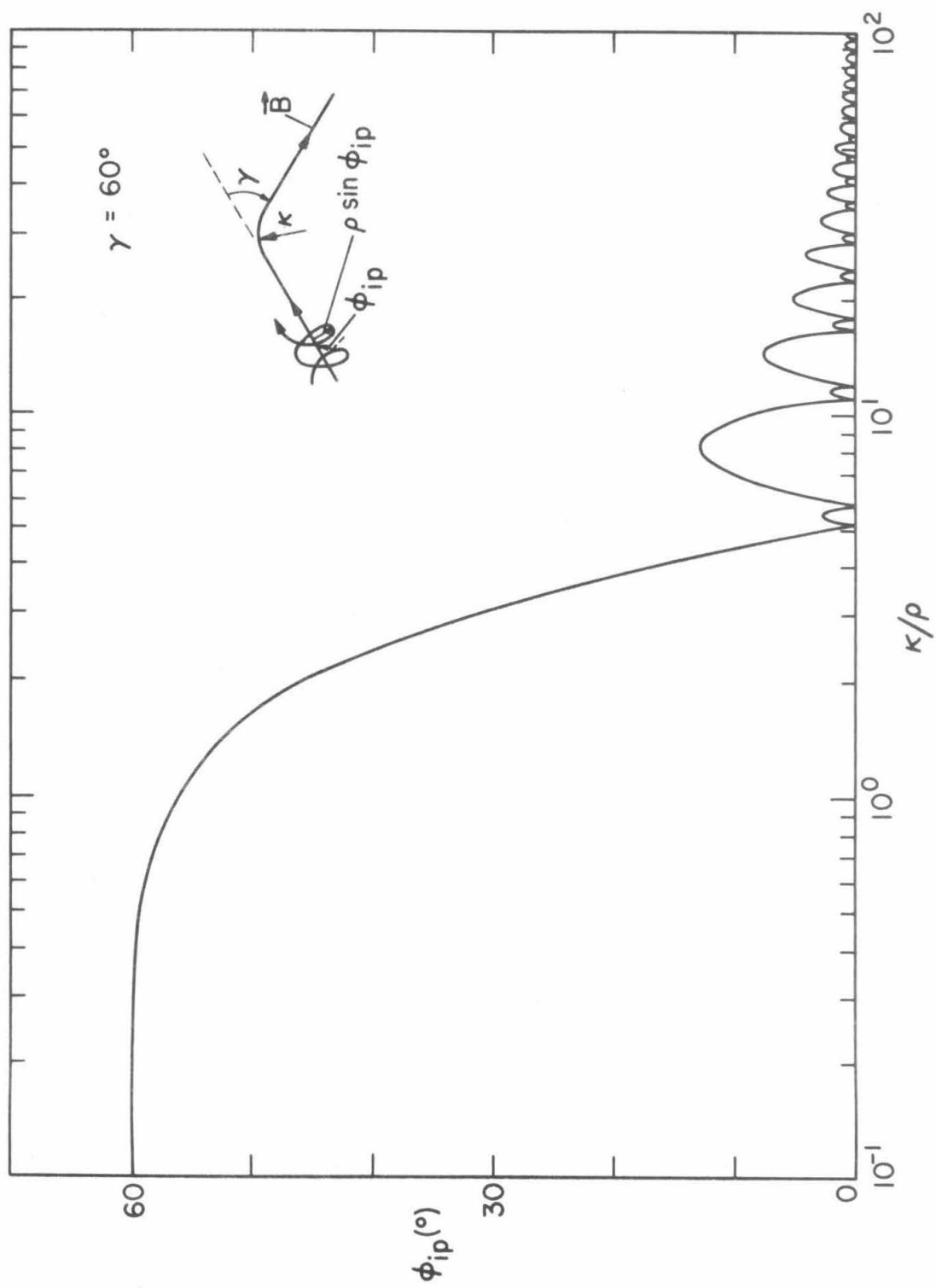
Although not directly supportable from the OGO-4 data due to a lack of interplanetary measurements, it is certainly not unreasonable to suppose that interplanetary anisotropies may have some affect on polar cap observations and may contribute to persistent features (*Cf.* #8 in table VII-4). The entire role of interplanetary anisotropies in the formation of polar cap features in an open geomagnetic configuration is not at all as straightforward as it may appear at first, however. The assumption of adiabatic motion in the propagation of particles from interplanetary space to the polar regions means that the magnetic moment is conserved and that therefore the only particles observable at the altitude of OGO-4 are those with interplanetary pitch angles  $\leq 1^\circ$  or  $\geq 179^\circ$ . Since the geomagnetic tail field and the interplanetary field are almost never parallel, the propagation of particles from interplanetary space to the geomagnetic tail

will involve the passage through a region where the magnetic field is changing direction. Since the propagation of particles in the tail between the transition region (access window) and the polar caps can be considered adiabatic, only those particles with pitch angles near zero (or  $180^\circ$ ) in the tail will be observed at the altitude of OGO-4. If the "curvature" of the magnetic field in the transition region is sufficiently large compared to the gyroradius of the particle, then adiabatic motion might indeed be expected.

Appendix B treats this problem in some detail, dealing with the configuration of two magnetic fields equal in magnitude separated by a region in which the field changes direction with a constant radius of curvature (*cf.* figure B-1). Figure VII-5 shows typical results for the magnetic fields at an angle of  $60^\circ$ . In this figure,  $\phi_{ip}$  is the interplanetary pitch angle giving a pitch angle of  $0^\circ$  after traversing the transition region;  $\phi_{ip}$  is shown as a function of  $\kappa/\rho$ , where  $\rho$  is the particle's gyroradius and  $\kappa$  is the constant radius of curvature of the field in the transition region. Other values of  $\gamma$  give comparable results (see Appendix B). These results show that, for  $\gamma=60^\circ$ , unless  $\kappa/\rho \geq 50$ , the interplanetary pitch angle ultimately being observed at the polar caps varies drastically as a function of particle energy and as a function of the instantaneous interplanetary field configuration. One would not expect, for instance, that 3 MeV protons, which have a gyroradius of about  $9.8 R_\oplus$  in a  $60 \mu\text{G}$  interplanetary field, with pitch angles  $\leq 1^\circ$  in interplanetary space would be observed at the polar caps, except transiently, unless  $\kappa$  were greater than about  $490 R_\oplus$ . Since the cross sectional

Figure VII-5

Interplanetary pitch angle ( $\phi_{ip}$ ) giving a pitch angle of  $0^\circ$  after passing through a region in which the magnetic field changes direction through an angle  $\gamma=60^\circ$ . The direction change is assumed to take place at a constant radius of curvature,  $\kappa$ . The gyro-radius of the particle in the magnetic field, whose magnitude does not change, is represented by  $\rho$ . See Appendix B for a more detailed explanation of these results.





radius of the entire tail at about  $200 R_{\odot}$  is about  $25 R_{\odot}$ , it is hard to visualize a transition region which is at least  $490 R_{\odot}$  wide. These pitch angle mapping results are, of course, relevant only in the presence of an interplanetary anisotropy; if the interplanetary flux is isotropic, it does not matter *which* interplanetary pitch angles are observed over the polar caps.

Although direct observational evidence for interplanetary anisotropies is not available from the OGO-4 data, there are three pieces of pertinent indirect evidence indicating the observation of persistent north/south differences in the absence of interplanetary anisotropies (Cf. #10 in table VII-4):

- (a): A number of the flare events observed with OGO-4 either were associated with east limb optical flares or were possibly associated with optical flares on the other side of the solar disc. Although interplanetary anisotropies have been observed at low proton energies during *some* east limb flares, it is suggestive that persistent features (and hence north/south flux differences) were observed during all flare event observations made with OGO-4.
- (b): Persistent features are consistently observed during the decay phase of flare events, whereas anti-solar directed field aligned interplanetary anisotropies normally disappear shortly after the peak of a flare event. Interplanetary anisotropies observed during the decay phase of flare events are normally anti-solar directed and solar wind aligned. Examples of persistent  $\beta$ -HPL depressions are shown in fig-

ures A-3 and A-9. The  $\beta$ -HPL flux was as much as a factor of 10 below the LPL and  $\alpha$ -HPL fluxes during the 8 February 1968 event (figure A-9).

- (c): Several features are observed to persist for very long periods, exceeding 40 hours in at least two of the cases shown in Appendix A. This is a much longer duration than that expected for large interplanetary anisotropies (5-15 hours, depending on the time between onset and the peak). Figure A-3 shows a persistent feature which lasted for more than 24 hours. The best example, though is probably that in figure A-9, showing a very large feature  $((V_1\sqrt{V_3})_{\text{LPL}} : (V_1\sqrt{V_3})_{\beta\text{-HPL}} \text{ as large as } 25:1)$  persisting for at least 31 hours *during the decay* phase of the flare event.

### VIII. CONCLUSIONS

Observations of polar cap fluxes of low energy solar protons (1.2-40 MeV) and electrons (0.4-1.0 MeV) made with an experiment on board the OGO-4 satellite lead to the following conclusions.

1. Extensive observations of electron polar cap fluxes during geomagnetically quiet periods have resulted in a comprehensive mapping of the boundary between open and closed geomagnetic field lines onto the polar cap. This mapping, shown in figure V-3, is an order of magnitude more comprehensive than previously available.
2. Observations during 54 solar proton events have established that the presence of persistent features in the polar cap proton flux is the norm rather than the exception (see table A-1 and figure VII-1).
3. A comparison between the electron polar cap boundary (see conclusion #1) and persistent features in the proton polar cap flux indicate that, in general, these features represent different flux levels in the open field line region (high polar latitudes -- HPL) than in the closed field line region (low polar latitudes -- LPL).
4. There is a strong correlation between the observation of persistent polar cap features and the sector structure of the interplanetary magnetic field: in general, persistent features are observed in the south

pole during a positive sector and in the north pole during a negative sector. On the basis of this correlation, the term " $\beta$ -pole" is defined in such a manner as to refer to the south pole during a positive sector and in the north pole during a negative sector; in both cases the opposite pole is referred to as the  $\alpha$ -pole. The OGO-4 observations reported here are correlated in this fashion 91% of the time.

5. The observation that persistent features disappear within  $\mathcal{O}$ (one hour) of a reversal in the interplanetary sector is also consistent with this sector correlation.

6. There appears to be little or no correlation between the presence of persistent features in the proton polar cap flux and the orientation of the north/south component of the interplanetary magnetic field: during the observations of persistent features this component was southward only 54% of the time and changed orientation several times with no noticeable effect.

7. Observations of solar proton events, especially those associated with co-rotating regions of enhanced flux in interplanetary space, have been used to establish the  $L_{\alpha\beta}$  access window configuration illustrated in figure VII-2, in which the LPL access window is near the earth, the  $\alpha$ -HPL access window is a few hundred earth radii behind the earth (in the anti-solar direction), and the  $\beta$ -HPL access window is located  $\mathcal{O}(2000 R_{\oplus})$  behind the earth.

8. The widths of the HPL peaks observed on the EDP event profiles

imply that the extent of the  $\alpha$ -HPL access window is about the same as that of the  $\beta$ -HPL access window. A comparison with the LPL peaks further implies that neither of the HPL access windows is much larger than the LPL access window (see figure VII-2).

9. Although direct interplanetary measurements are not available from the OGO-4 data, it is concluded that the following contribute to persistent polar cap features (north/south asymmetries):

- A. limited interplanetary regions of enhanced flux propagating past the earth,
- B. radial gradients in the interplanetary flux, and
- C. anisotropies in the interplanetary flux.

10. The OGO-4 observations are not consistent with the particle access mechanisms proposed by Michel and Dessler [3].

11. The access window configuration deduced from EDP event observations (conclusion #7) is not consistent with an access window configuration in which both HPL access windows are the same distance from the earth, as would be expected in an open magnetospheric configuration involving magnetic merging near the sub-solar point (*cf.* Dungey [2]).

12. An  $L\alpha\beta$  access window configuration (conclusion #7) may be a consequence of an open magnetospheric model involving magnetic merging at the polar neutral points (*cf.* Frank [4]). To achieve this configuration, however, it is necessary that the model satisfies at least the following constraints:

A. The merging rate for open geomagnetic field lines at one polar neutral point ( $\alpha$ ) must be  $\sim 5$  times that at the other polar neutral point ( $\beta$ ). This difference between the open field line merging rates must be related to the orientation of the interplanetary magnetic field, as measured far from the neutral point, in such a way as to be consistent with the observed correlation with the interplanetary sector structure (conclusion #4) and lack of correlation with the north/south component of the interplanetary field (conclusion #6).

B. The time required for open field lines to migrate from the neutral sheet region across the polar cap to the vicinity of the neutral point must be about the same in both tails, so as to account for both HPL access windows being about the same size (conclusion #8).

C. The rate at which open field lines merge with the interplanetary field at the  $\alpha$ -polar neutral point must be at least as large as that required for almost all of the open field lines to have merged in  $O(\text{one hour})$ , since  $\beta$ -HPL features disappear within  $O(\text{one hour})$  after a sector reversal (conclusion #5).

In addition to these observational conclusions, the following conclusions are implied by the results of the theoretical investigations presented in Appendices B and C.

Appendix B: The assumption of adiabatic motion for the access of 1.2-40 MeV protons from interplanetary space to the interior of the

magnetosphere is not a good approximation. If the extent to which an interplanetary pitch angle distribution maps onto the polar cap region were to be determined from appropriate data, figure B-4 would indicate the constraints thus imposed on the configuration of the magnetic field in the vicinity of the access windows.

Appendix C: The satisfaction of constraint A mentioned above in conclusion #12 is possible if the proper assumptions are made concerning angular dependence of the probability that two field lines will merge. This can be seen by comparing figures C-8, C-9 and C-10.

Although the results outlined above are most consistent with a field configuration involving magnetic merging at the polar neutral points, the question of whether there is a significant degree of merging between the geomagnetic and interplanetary magnetic fields cannot be unambiguously determined by charged particle measurements. These observations do, however, provide a suitable platform upon which to base theoretical investigations of this question.

## APPENDIX A

### Additional Observations



This appendix provides a summary of all proton events observed with OGO-4 and observed flux profiles for several events which can be referred to in the context of the discussion in Section VII. Due to the time-sharing nature of the OGO-4 telemetry, it is not possible to obtain a single profile which illustrates all of the features necessary for Section VII. Table A-1 tabulates all of the proton events observed with OGO-4 and indicates pertinent data relating to the orientation of the interplanetary magnetic field. Most of the data in this table are also depicted in figure V-5.

The events whose profiles are presented here are divided into three classes: EDP events (normally associated with co-rotating features), solar flare events, and events having characteristics of both EDP events and flare events (class C events). A description of these classes of events and the criteria used to distinguish between EDP events and flare events are discussed in Sections V and VI. In addition, the 1 December 1967 EDP event and the 2 November 1967 solar flare event are discussed in some detail in Section V. Accompanying the profiles of each event here is a brief list of the more notable observational features of the event. Events are presented chronologically to facilitate finding any specific one.

All presentations of profiles in this thesis conform to the following conventions (the assignment of the terms  $\alpha$ -pole and  $\beta$ -pole is

Table A-1

OGO-4 -- Observed Persistent Polar Cap Features: 1-40 MeV Protons

First Observation		Total Elpsd. Time (hrs.)	$\left(\frac{\text{LPL}}{\text{HPL}}\right)$ max	Pole Sector	% Southern Solar Field	Event Phase R=Rise D=Decay E=EDP	Obsrvd?	Enhancements	
Date	Univ. Time (HHMM)							$\left(\frac{\text{HPL}}{\text{LPL}}\right)$ max	Duration (hrs.)
30 Jul 67	1820*	>13.2	12.5	N -	58%	D	N		
1 Aug 67	1745	> 5.7 <sup>†</sup>	4.0	N -	0%	R	N		
	2140	> 1.8 <sup>†</sup>	1.3	S -	0%	R	N		
11 Aug 67	0155*	> 8.2	1.7	N -	33%	E	Y	1.3	3.5
12 Aug 67	1620*	> 5.7	1.4	N -	100%	R	N		
19 Aug 67	0320*	>10.4 <sup>†</sup>	6.8	N -	44%	E	Y	1.7	>2.0 <sup>†</sup>
	0410*	> 3.1	3.4	S -	44%	E	N		
24 Aug 67	1345	> 5.8 <sup>†</sup>	37.0	N -	75%	R	N		
19 Sep 67	0305*	>29.2 <sup>†</sup>	6.6	N -	47%	R D	N		
9 Oct 67	0040	> 1.2 <sup>†</sup>	3.0	N -	100%	R	N		
27 Oct 67	1730*	> 6.8	2.8	S +	15%	D	N		
1 Nov 67	1540	14.7	4.0	N -	97%	R D	N		
2 Nov 67	1115*	>24.4 <sup>†</sup>	7.2	N -	90%	R D	N		
	1150*	> 3.2 <sup>†</sup>	3.9	S -	100%	R	N		
	3305*	> 1.9	1.0	S -	100%	R	Y	2.3	>1.9
4 Nov 67	2200	8.8	2.2	S +	66%	D	N		
10 Nov 67	2025	3.2	2.3	S +	100%	E	N		
	2110	> 3.3 <sup>†</sup>	2.7	N +	100%	E	Y	1.3	>1.4 <sup>†</sup>
14 Nov 67	0330*	>42.5 <sup>†</sup>	1.7	N -	37%	R	Y	1.1	>1.6 <sup>†</sup>
	1210	> 1.6 <sup>†</sup>	0.9	S -	50%	R	N		
18 Nov 67	0200*	>11.5	1.3	N -	87%	D	Y	1.3	1.6
24 Nov 67	1730	> 6.5 <sup>†</sup>	3.2	N -	69%	R	N		

Table A-1 (continued)

First Observation		Total Elpsd. Time (hrs.)	$\max \left( \frac{LPL}{HPL} \right)$	Pole Sector	% Southern Solar Field	Event Phase R=Rise D=Decay E=EDP	Enhancements	Duration (hrs.)
Date	Univ. Time (HHMM)						Obsrvd? $\max \left( \frac{HPL}{LPL} \right)$	
27 Nov 67	0900	14.7	6.3	N +	46%	R		
	0950	>38.0 <sup>+</sup>	15.9	S +	73%	R D	N	
1 Dec 67	1800*	>13.0	5.6	S +	82%	E	Y	1.4
	1850	> 4.7 <sup>+</sup>	1.3	N +	100%	E	Y	>3.7 <sup>+</sup>
2 Dec 67	0700	11.5	2.1	S +	46%	E	Y	>1.0 <sup>+</sup>
	0935	> 4.7 <sup>+</sup>	1.9	N +	43%	E	Y	>1.0 <sup>+</sup>
5 Dec 67	0015	>13.8	1.2	N -	27%	D	Y	4.9
17 Dec 67	0105*	>24.5	6.6	N -	--	RE	N	
	0825	5.0	0.8	S -	--	E	Y	5.0
18 Dec 67	1610	>16.2 <sup>+</sup>	2.0	N -	--	R	N	
	0715	>13.2 <sup>+</sup>	1.6	S -	--	RE	Y	8.1
30 Dec 67	1045	6.8	4.5	S +	0%	E	Y	>1.0
	1130	6.5	6.2	N +	0%	E	Y	1.6
10 Jan 68	2150*	>10.5 <sup>+</sup>	1.8	N -	60%	D	N	
1 Feb 68	2010	11.4	1.2	N -	26%	R D	Y	3.3
8 Feb 68	1805*	>31.0 <sup>+</sup>	25.2	N -	100%	D	N	
9 Feb 68	1515*	>11.2 <sup>+</sup>	15.8	N -	100%	R D	N	
12 Feb 68	0640	3.2	1.4	N -	38%	R	N	
13 Feb 68	1335	> 3.2 <sup>+</sup>	2.1	N +	53%	R	N	
	0930*	> 6.6 <sup>+</sup>	1.8	S +	24%	R	N	
14 Feb 68	0630*	> 8.3 <sup>+</sup>	1.3	S +	0%	D	Y	>1.6 <sup>+</sup>
15 Feb 68	1015	>13.8 <sup>+</sup>	2.0	S +	--	R D	N	
26 Feb 68	1120	5.7	15.8	S +	0%	R	N	
	1210	1.6	17.8	N +	0%	R	N	
	1700	8.0	1.6	N -	62%	D	Y	7.4
	2415	1.5	1.6	S -	100%	E?	Y	1.5

Table A-1 (continued)

First Observation		Total Elpsd. Time (hrs.)	$\max \left( \frac{\text{LPL}}{\text{HPL}} \right)$	Pole Sector	% Southern Solar Field	Event Phase R=Rise D=Decay E=EDP	Obsrvd?	Enhancements $\max \left( \frac{\text{HPL}}{\text{LPL}} \right)$	Duration (hrs.)
9 Mar 68	2305*	>24.4 <sup>+</sup>	4.8	N -	45%	R D	N		
21 Mar 68	2330	>13.2 <sup>+</sup>	2.5	S +	43%	R D	N		
15 Apr 68	0010*	> 3.4	0.9	S +	--	D	Y	1.5	>3.4
24 Apr 68	0730*	>40.5 <sup>+</sup>	5.0	N -	67%	R D	N		
	2115	> 6.6	3.2	S -	46%	R	N		
26 Apr 68	1930*	> 6.5	21.0	N -	85%	D	N		
27 Apr 68	1330	34.2	2.2	N -	36%	R D	N		
	2400	5.0	1.5	S -	50%	R	N		
29 Apr 68	1725	> 3.2 <sup>+</sup>	1.6	N -	9%	R	N		
5 May 68	2200*	> 4.8 <sup>+</sup>	1.4	S +	38%	D	N		
13 May 68	2130*	>45.5 <sup>+</sup>	≈1.0	S +	--	D	Y	1.6	>45.5 <sup>+</sup>
10 Jun 68	1720*	>29.2	1.4	N -	63%	D	N		
9 Jul 68	0415	4.8	1.4	N +	67%	R	N		
	1210	1.9	2.0	N +	0%	R	N		
	1000*	>11.3 <sup>+</sup>	2.5	S +	18%	R D	N		
13 Jul 68	0215*	> 4.8	1.6	N -	--	D	N		
13 Jul 68	1025	>38.9 <sup>+</sup>	>4.2	N -	20%	R D	Y	1.2	>27.6 <sup>+</sup>
14 Aug 68	1645	> 6.5 <sup>+</sup>	4.0	S +	85%	R	N		
21 Aug 68	1315	> 8.2 <sup>+</sup>	4.0	N -	100%	E	N		
	1545	1.5	2.5	S -	100%	E	N		
28 Sep 68	0220	> 6.5 <sup>+</sup>	1.4	N -	39%	D	N		
	1120	> 8.2 <sup>+</sup>	1.6	S +	56%	R	N		
	1345*	> 3.2	1.5	N +	100%	R	N		
29 Sep 68	0415	> 3.5 <sup>+</sup>	1.1	N +	100%	R	N		
	0500	>14.8 <sup>+</sup>	1.8	S +	64%	R D	N		

Table A-1 (continued)

First Observation		Total Elpsd. Time (hrs.)	$\frac{LPL}{HPL}$ max	Pole Sector	% Southern Solar Field	Event Phase R=Rise D=Decay E=EDP	Obsrvd?	Enhancements $\frac{HPL}{LPL}$ max	Duration (hrs.)
Date	Univ. Time (HHMM)								
29 Sep 68	2345	8.0	1.8	N -	25%	R D	N		
	2745	> 3.2	1.5	S -	31%	D	N		
30 Sep 68	1420*	> 8.1 <sup>†</sup>	1.8	N -	72%	R D	N		
4 Oct 68	0400	> 37.5 <sup>†</sup>	2.2	N -	32%	R D	N		
	0815	> 9.8	1.6	S -	51%	R	N		
	3410	3.3	1.5	S -	62%	D	N		
4 Nov 68	2340*	> 1.6 <sup>†</sup>	1.8	S +	0%	D	N		
18 Nov 68	2330*	> 24.2	2.5	N -	--	D	N		
	2600*	> 3.2 <sup>†</sup>	1.5	S -	100%	D	N		

---

\*Observation of the beginning of the event was prevented by the unavailability of the pertinent data.

<sup>†</sup>Persistent feature was observed in the last appropriate polar pass prior to a period during which the pertinent data were unavailable.

reproduced from table VII-1 in table A-2):

1. The horizontal axis is always time, expressed in terms of hours of universal time. Tick marks are placed every hour, and are labelled every six hours, consistent with clarity.
2. The vertical axis is always observed flux of 1.2-40 MeV protons ( $V_1\overline{V}_3$ ) expressed in units of  $(\text{cm}^2\text{-sec-sr})^{-1}$ .
3. Error bars are indicated for representative points for flux levels below  $10 (\text{cm}^2\text{-sec-sr})^{-1}$ , and all other points of comparable flux can be assumed to have comparable precision. If no error bars are indicated, they may be assumed to be smaller than the size of the dot used to indicate the observation, which is the case for all flux levels greater than  $10 (\text{cm}^2\text{-sec-sr})^{-1}$ .
4. The region in which a profile was observed is indicated by the type of line connecting the data points:
  - solid line    ---    low polar latitudes (LPL)
  - dashed line    ---     $\alpha$ -pole high polar latitudes ( $\alpha$ -HPL)
  - dotted line    ---     $\beta$ -pole high polar latitudes ( $\beta$ -HPL)
5. Separate observations of  $\alpha$ -HPL fluxes are not indicated unless significantly different than the flux at LPL.
6. Interplanetary sector structure (positive, negative, or uncertain) is indicated at each sector reversal or change (indicated by long vertical lines). If no sector changes occur during the period covered by the profiles, the predominant sector for the period is stated in the legend.
7. The roles of  $\alpha$ -pole and  $\beta$ -pole are assumed to change coincident

TABLE A-2

Correspondence Between  $\alpha$ -pole/ $\beta$ -pole  
North/South Geomagnetic Poles

	North Pole	South Pole
Positive Interplanetary Sector	$\alpha$ -pole	$\beta$ -pole
Negative Interplanetary Sector	$\beta$ -pole	$\alpha$ -pole

with a sector reversal. If a period of uncertain sector is encountered, the previous assignment of  $\alpha$ -pole and  $\beta$ -pole rôles is maintained until the sector becomes definable.

8. Missing data are indicated by arrows pointing downward near the top of the figure. The arrows are labelled to indicate the pole for which data are missing due to a gap in the available data ( $G$ ), or due to a pass which does not reach a sufficiently high invariant latitude to penetrate the high polar latitude region ( $L$ ). In the latter case, of course, only HPL data should be missing; LPL observations should not be effected. The occasional exception to this is the south polar pass which does not reach a high enough invariant latitude to be above the rigidity cutoff latitude at any time. Such missing data are labelled  $V$  (very low pass) to indicate that LPL data are also unavailable. If the data are available but are contaminated by telemetry noise, the label  $N$  is used.
9. Sudden commencements and sudden impulses are indicated in the same manner as on the OGO-4 Data Coverage Plots: sudden commencements are represented by a triangle, sudden impulses by a diamond. Confirmed observations are represented by solid symbols, unconfirmed by open symbols.

Table A-3 lists all symbols and abbreviations used on the profiles.



Table A-3a

## Standard Symbols Used on Event Profiles

<u>Symbol</u>	<u>Meaning</u>
$\alpha$	$\alpha$ -pole (See Table E-2)
$\beta$	$\beta$ -pole (See Table E-2)
•——•	Low polar latitude profile
• — — •	$\alpha$ -pole high polar latitude profile
•.....•	$\beta$ -pole high polar latitude profile
↓	Data not available
▲	Confirmed sudden commencement
△	Unconfirmed sudden commencement
◆	Confirmed sudden impulse
◇	Unconfirmed sudden impulse
I	Representative $\pm 1\sigma$ error bars
+	Positive interplanetary magnetic field sector
-	Negative interplanetary magnetic field sector
0	Indeterminate interplanetary magnetic field sector

Table A-3b

## Standard Abbreviations Used on Event Profiles

<u>Abbreviation</u>	<u>Meaning</u>
G	Data gap
HPL	High polar latitude
L	Low pass (HPL data unavailable)
LPL	Low polar latitude
N	Data degraded by noise
SR	Sector reversal in interplanetary magnetic field
UT	Universal time
V	Very low pass (HPL and LPL data unavailable)

## Figure A-1

*11 August 1967 -- Class C Event*

1. Very high fluxes: statistical errors are much smaller than dots used to represent data points.
2. The extremely rapid decay is a strong indication that this is not a flare event. The sudden commencement at 0555 UT and the weak depression in the sea level neutron monitor [48] tend to confirm that this is an EDP event. The absence of a feature in the  $\alpha$ -HPL profile is, however, inconsistent with normal appearance of an EDP event. In addition, the delay between the LPL peak and the  $\beta$ -HPL peak ( $\sim 2.0$  hours) is much smaller than that normally associated with EDP events ( $\sim 6.6$  hours).

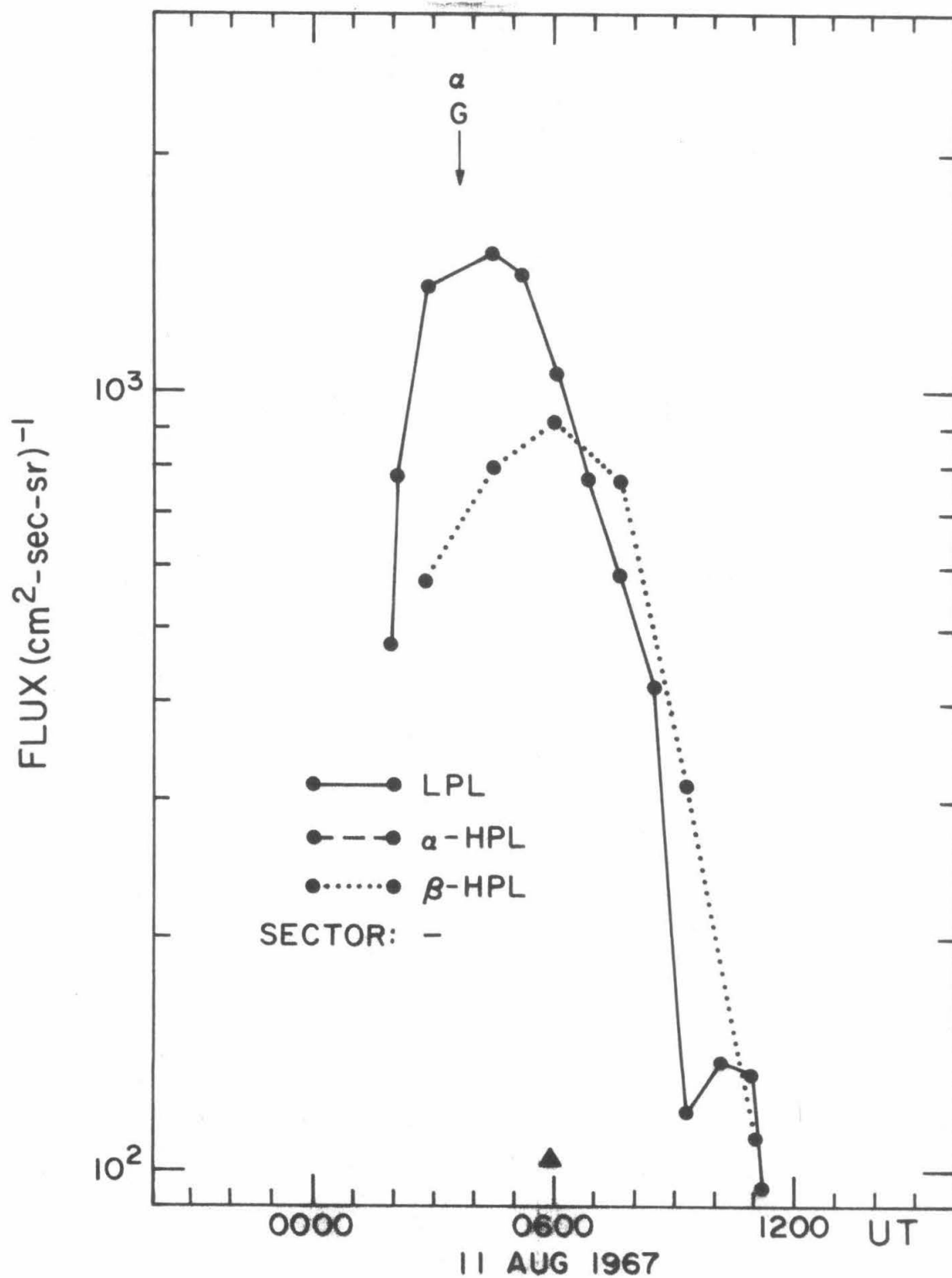


Figure A-2

*19 August 1967 -- EDP Event*

1. This event is superimposed on the decay phase of an earlier flare event.
2. The LPL peak and  $\alpha$ -HPL peak are clearly delineated.
3. The  $\beta$ -HPL flux continues to decay normally during the period of peak flux in the other two regions.
4. The data gap at  $\sim 2200$  UT prevents the observation of the complete  $\beta$ -HPL peak, although the beginning of this peak is observed at  $\sim 1940$  UT. Because of the low rates, the probability that this flux is a statistical variation from the LPL flux is  $\leq 4.2 \times 10^{-8}$ . Although this is not as statistically significant as most observations of features, and although there is only the one point, it is nonetheless consistent that the  $\beta$ -HPL flux at  $\sim 1940$  UT is part of the  $\beta$ -HPL EDP peak.

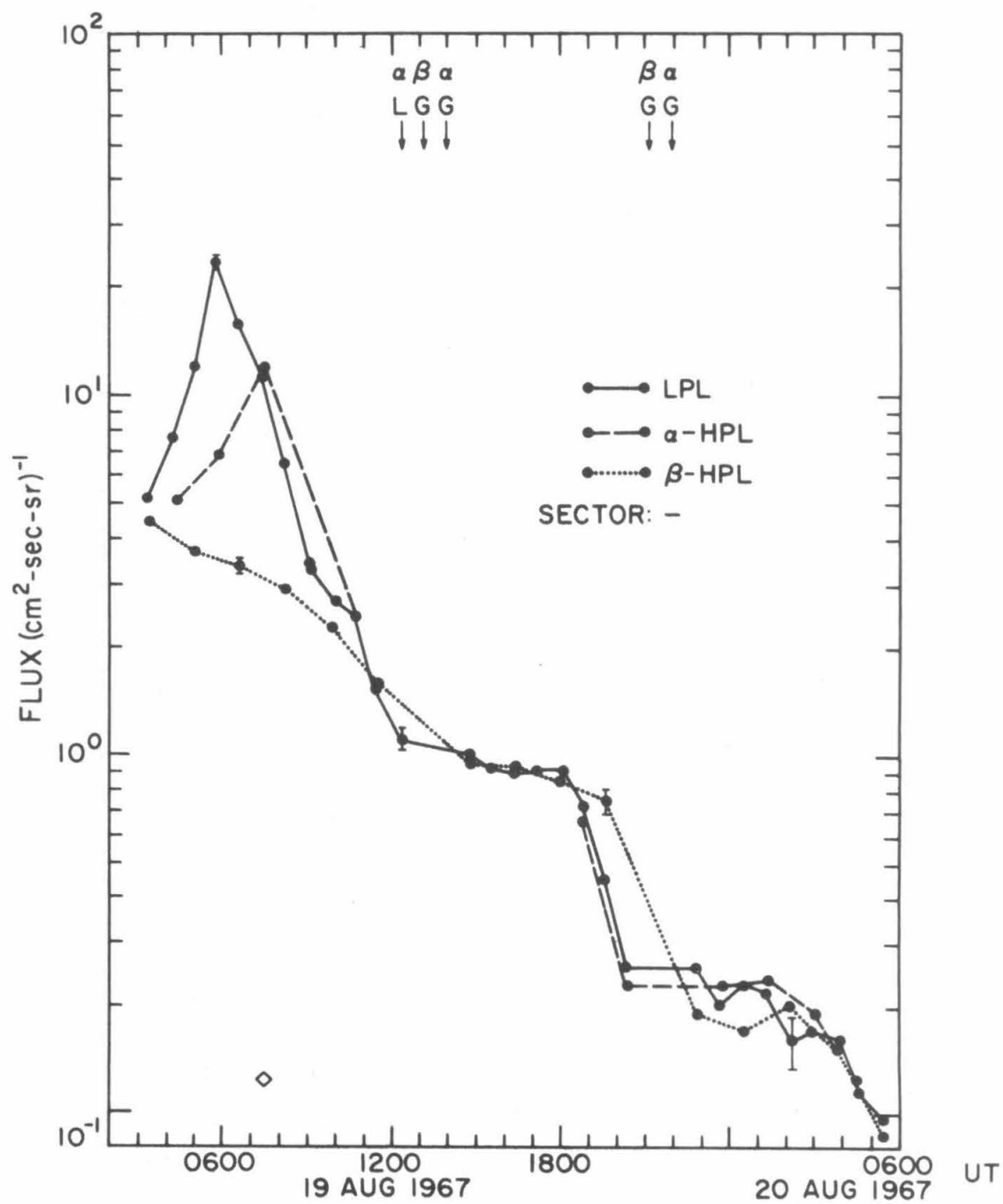
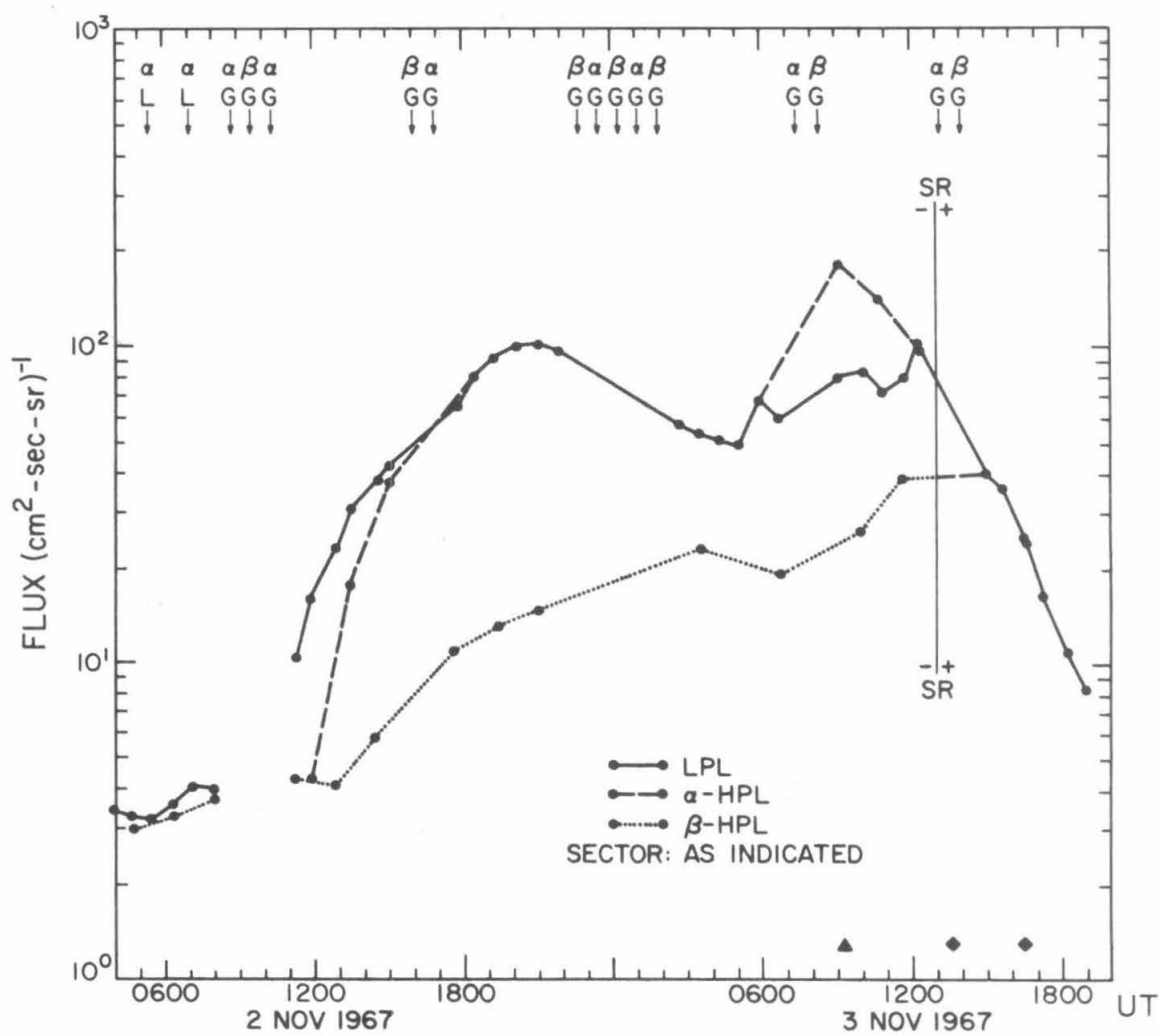


Figure A-3

*2 November 1967 -- Flare Event (see also Section V)*

1. This is an excellent example of a persistent feature. The feature in the  $\beta$ -pole is observed to last for the entire period from  $\sim 1120$  UT on 2 November to  $\sim 1140$  UT on 3 November (24+ hours). The data suggest that, but for the data gaps before and after this period, the feature might have been observed for a slightly longer period.
2. While the last north pole ( $\beta$ -pole) observation prior to the sector reversal at  $\sim 1300$  UT on 3 November contained the feature, the first north pole observation after this sector reversal did not show the feature.
3. A significant persistent feature is observed in the  $\alpha$ -pole lasting for  $\sim 3$  hours starting with the observation at  $\sim 1200$  UT on 2 November.
4. The onset of the flare event is delayed in both HPL regions.



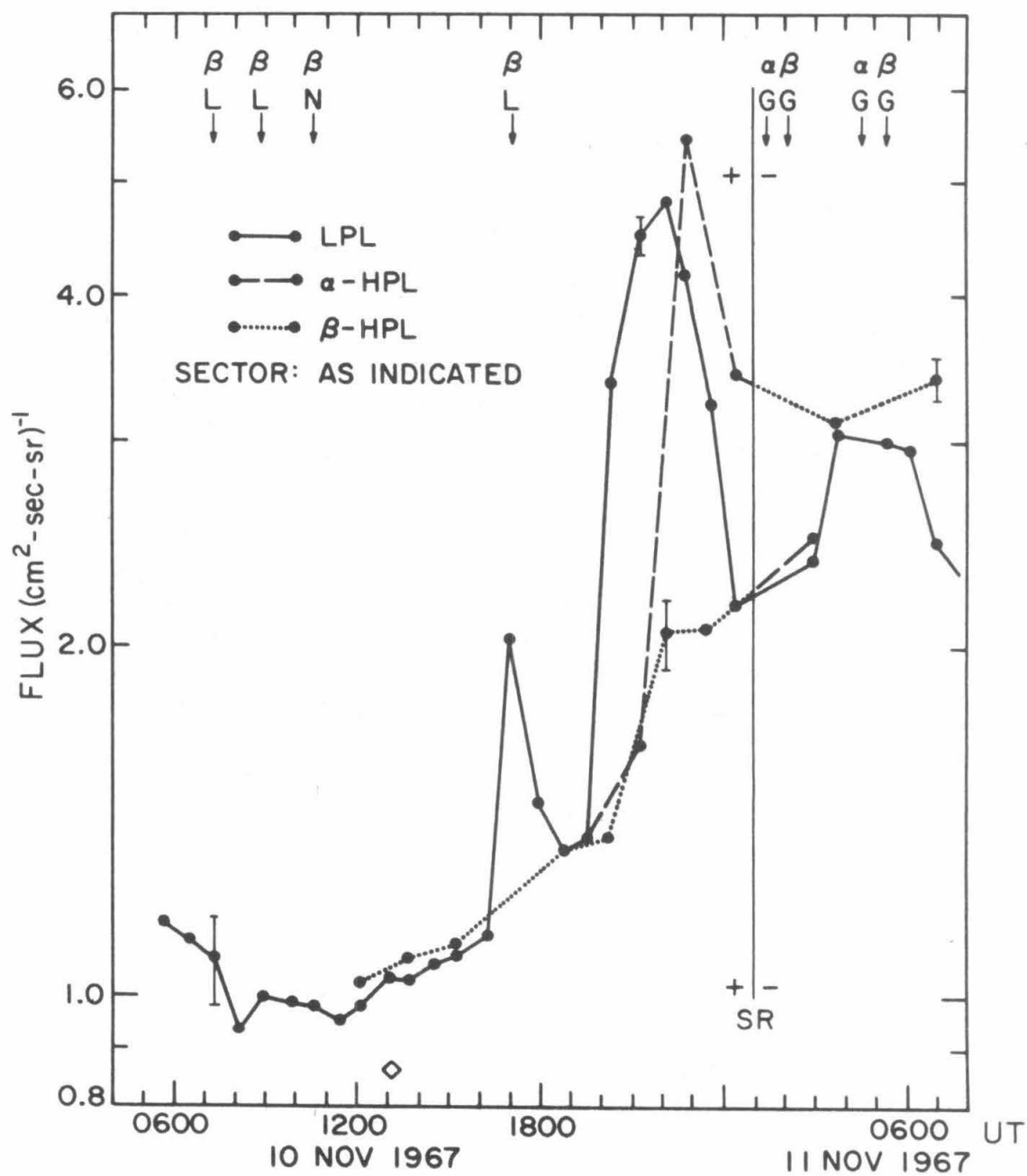


## Figure A-4

*10 November 1967 -- EDP Event*

1. This EDP gives a good resolution of the LPL flux peak and the  $\alpha$ -HPL flux peak. The appearance of a higher value for the  $\alpha$ -HPL flux peak may be somewhat misleading: the actual maximum LPL flux may not have been observed due to the mechanics of the satellite orbit.
2. The  $\beta$ -HPL flux peak is not observed for this event. It should, of course, be noted that a sector reversal occurs before ( $\sim 0100$  UT on 11 November) one might expect to observe a peak in this region (perhaps  $\sim 0300$  to  $\sim 0600$  UT on 11 November). Any conclusion drawn here should, however, be tempered somewhat by the degradation of the observations caused by the two data gaps following the sector reversal: 50% of the observations pertinent to this point are missing.
3. It is interesting that the flux in the post-sector reversal  $\beta$ -HPL region does not fluctuate in the same manner as that in the LPL region, but instead remains rather constant. This is consistent with a picture in which, immediately after a sector reversal, the access region associated with the new  $\beta$ -HPL region propagates with the solar wind, thus continuing to sample the same interplanetary flux, for the time necessary for the solar wind to carry the access region to a position consistent with the newly-established field

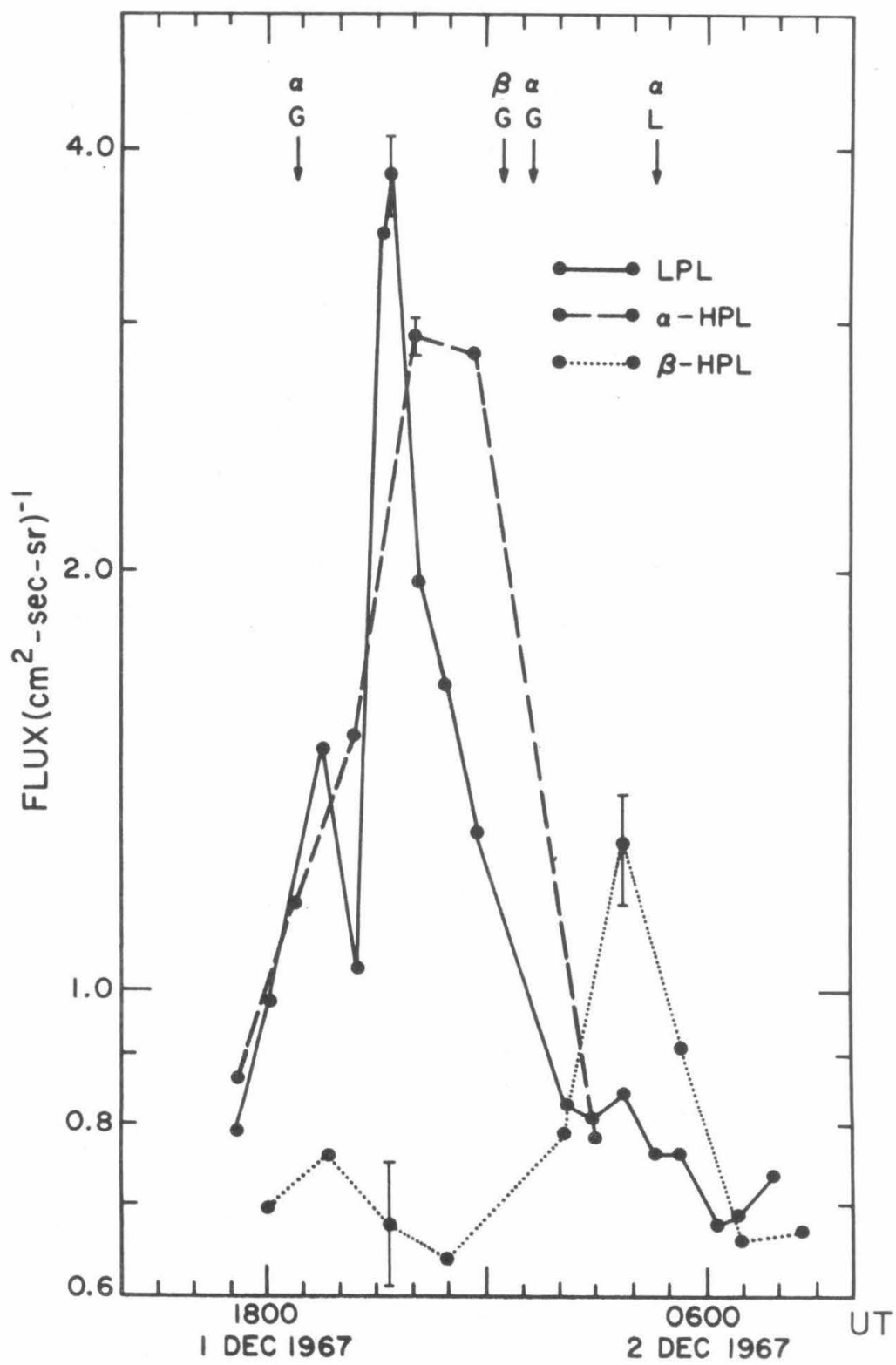
configuration (4-8 hours for a position  $1000-2000 R_{\oplus}$  behind the previous position). Again, this observation must be tempered by the precaution mentioned above.



## Figure A-5

*1 December 1967 -- EDP Event (see also Section V)*

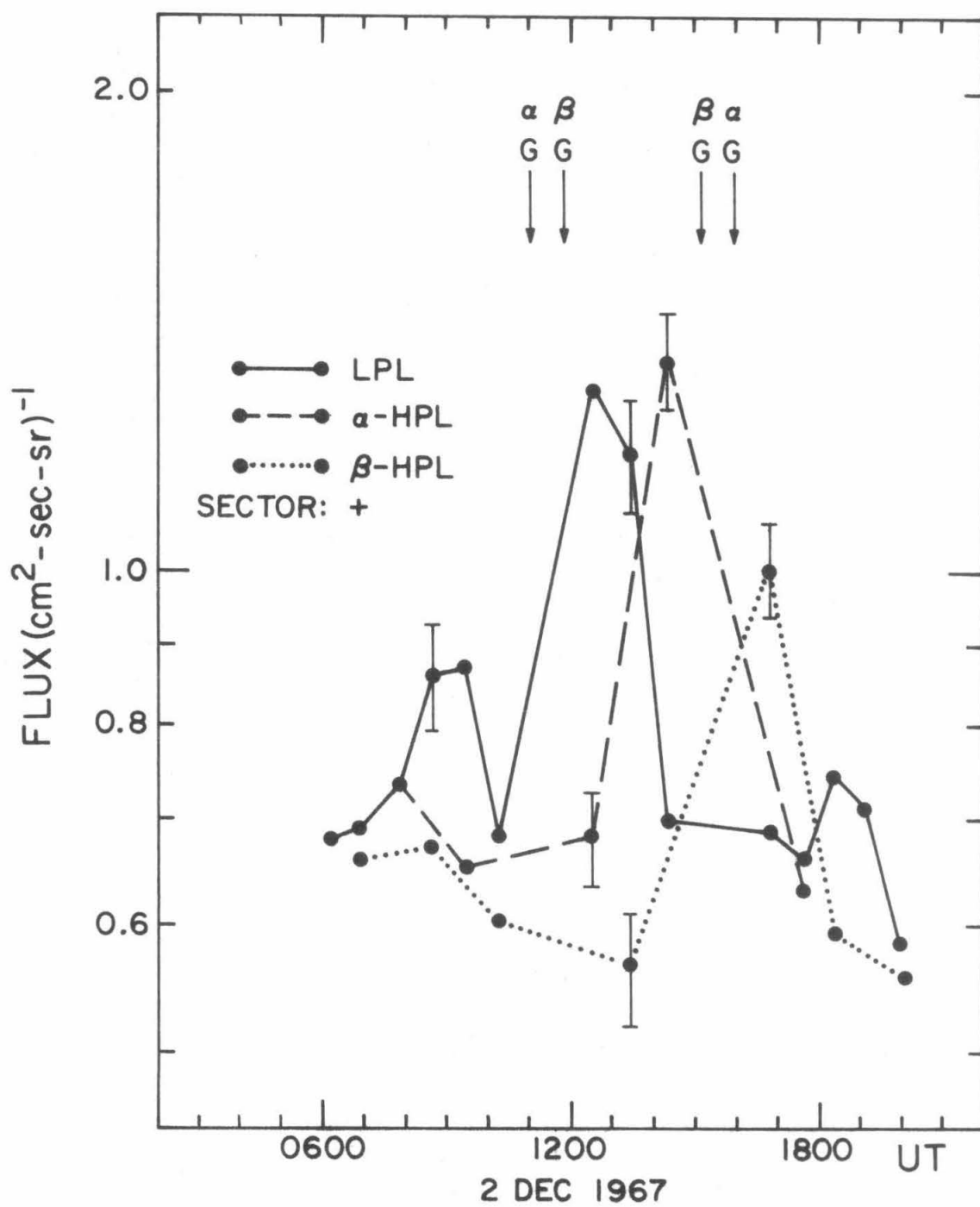
1. This profile is a definitive illustration of an EDP event being observed first on the LPL region, shortly thereafter in the  $\alpha$ -HPL region, and finally, after a delay of  $\sim 6\frac{1}{2}$  hours, in the  $\beta$ -HPL region.
2. The flux observed in the  $\beta$ -HPL region gives every sign of being independent of variations in the fluxes observed in the other two regions. The reverse also appears to be true.
3. Indications of the independence of the fluxes in the LPL region and the  $\alpha$ -HPL region with respect to each other are also clear.
4. The width of the  $\alpha$ -HPL flux peak as presented in figure A-5 is misleading: an inherently poor time resolution ( $\sim 100$  minutes between points) is compounded by the ubiquitous spectre of a data gap.
5. Poor time resolution may also be partly responsible for the much lower peak flux observed in the  $\beta$ -HPL region.



## Figure A-6

*2 December 1967 -- EDP Event*

1. All of the expected three peaks (LPL,  $\alpha$ -HPL, and  $\beta$ -HPL) are resolved and appear in the expected order. The observation of the precise temporal relationships among these flux peaks is seriously degraded, however, by the two data gaps at  $\sim 1100$ - $1200$  UT and  $\sim 1500$ - $1600$  UT. In spite of this expected degradation, at least the following two observations are clear:
  - a. Both HPL flux peaks begin after the beginning of the LPL flux peak.
  - b. The LPL flux peak ends before, or at least coincident with, both of the HPL flux peaks.



## Figure A-7

*30 December 1967 -- EDP Event*

1. Profiles of LPL flux and  $\alpha$ -HPL latitude flux both show a double-peaked structure.
2. The observation of the second  $\beta$ -HPL flux peak may have been prevented by the configuration of the satellite orbit: during the  $\beta$ -pole (south pole) passes at  $\sim 2030$  UT and  $\sim 2210$  UT, the satellite orbit did not reach a maximum invariant latitude large enough for penetration of the HPL region.



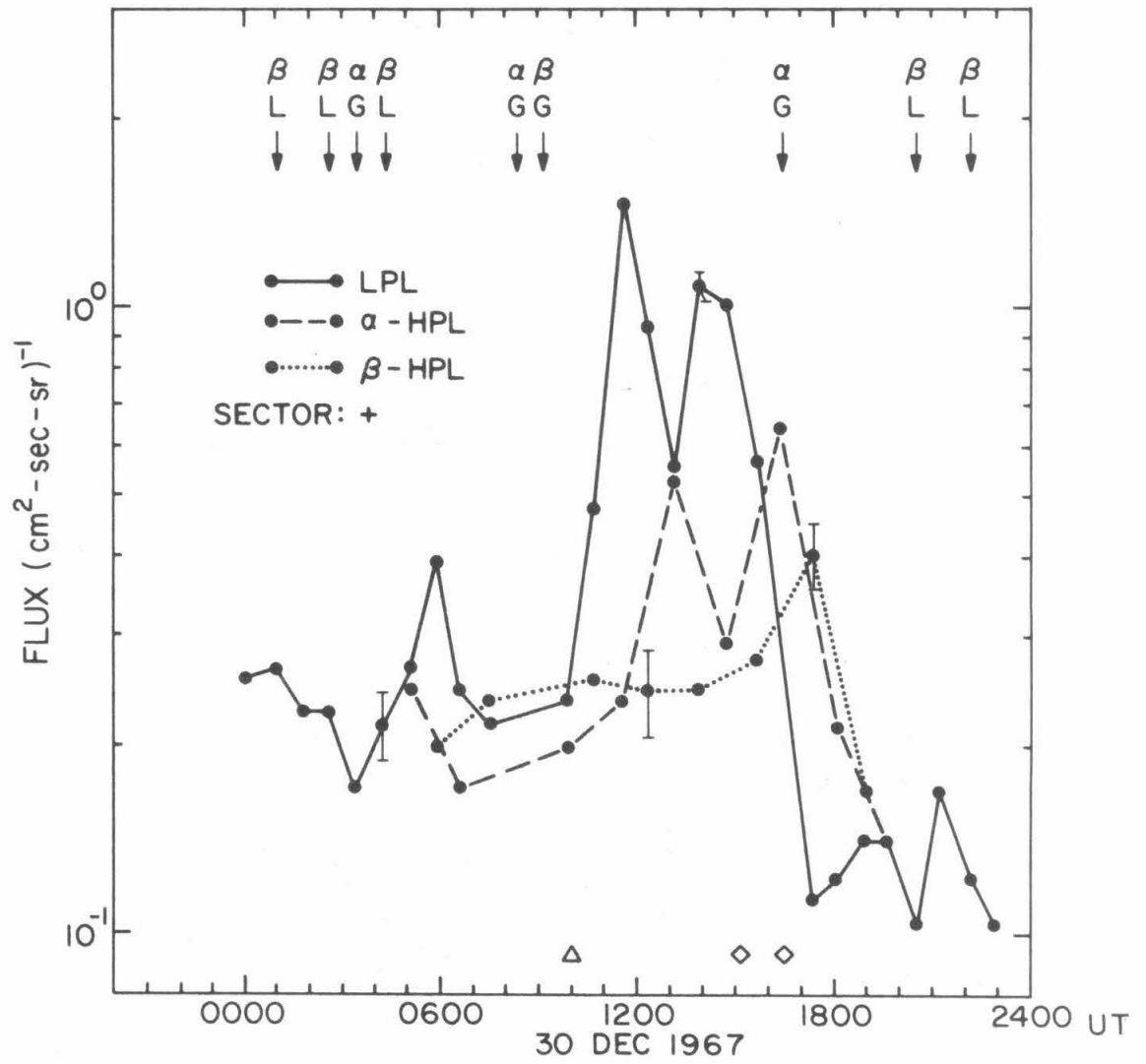


Figure A-8

*1 February 1968 -- Solar Flare Event*

1. This is a particularly good example of a flare event in which the  $\beta$ -HPL flux "crosses over" the LPL and  $\alpha$ -HPL flux (at  $\sim 0220$  on 2 February). Unfortunately, the omnipresent data gap nearly destroys observations of the event. Nevertheless, there are indications that the  $\beta$ -HPL flux remained at a higher level than the LPL flux until the small LPL enhancement at  $\sim 0640$  on 2 February. This higher  $\beta$ -HPL flux is, of course, observed as an enhancement in the high latitude region of the  $\beta$ -pole.

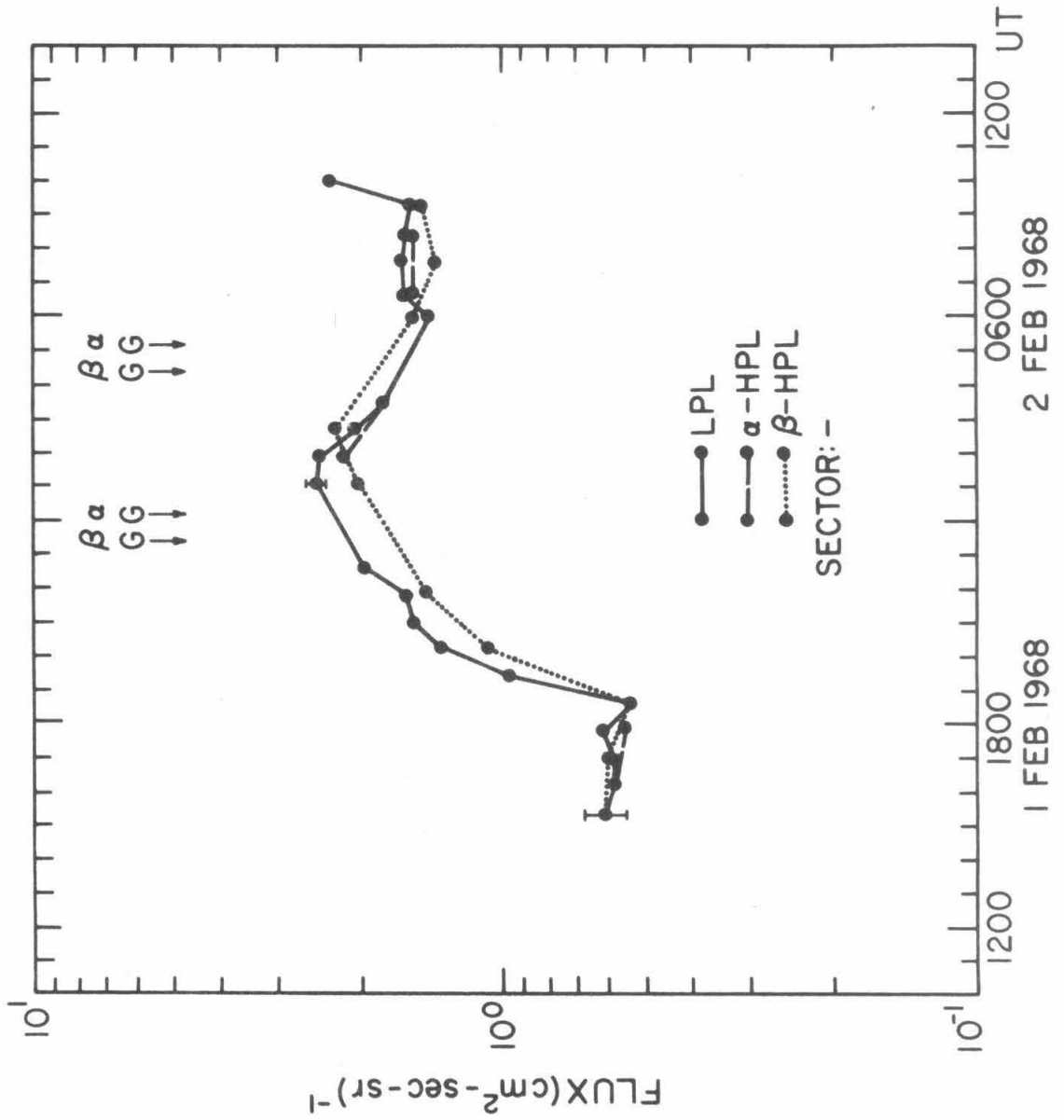
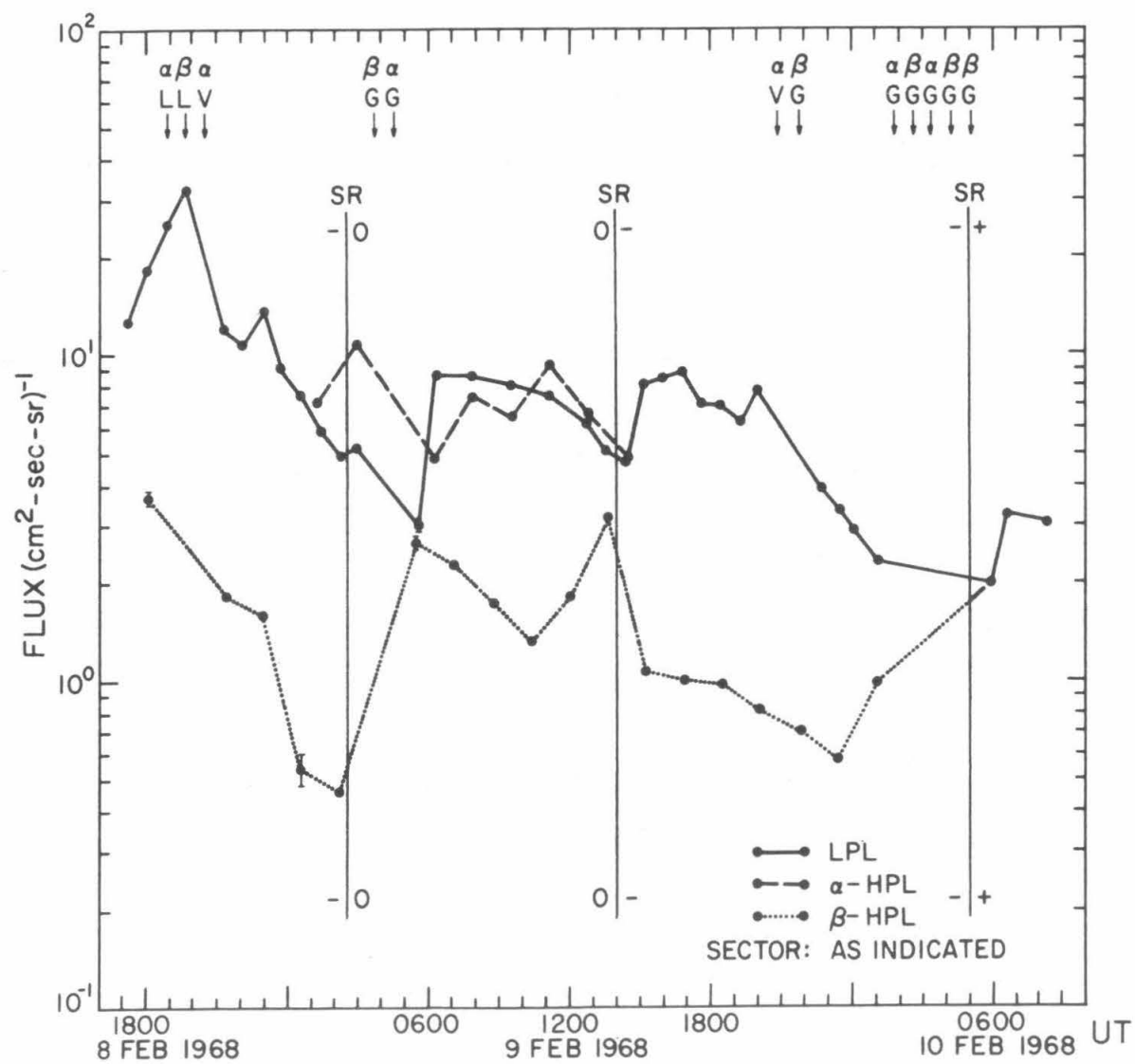


Figure A-9

*8 February 1968 -- Solar Flare Event*

1. This profile illustrates a long period observation of a persistent feature which is, with a few exceptions, quite large. The ratio of the LPL flux to  $\beta$ -HPL flux reaches a maximum in excess of 25:1. The feature persists from the beginning of the profile at  $\sim 1720$  UT on 8 February to  $\geq 0100$  UT on 10 February, a period of  $\geq 31\frac{1}{2}$  hours (see no. 2, below).
2. The duration of this persistent feature is interrupted by the period of uncertain sector structure from  $\sim 0230$  UT to  $\sim 1400$  UT on 9 February. During this "uncertain" period there would appear to be times ( $\leq 0530$  UT and, perhaps,  $\sim 1200$  UT to  $\sim 1400$  UT on 9 February) when the  $\beta$ -HPL flux tends to approach the LPL flux more closely. Unfortunately, the behavior of the  $\beta$ -HPL flux *vis-à-vis* the LPL flux from  $\sim 0230$  UT to  $\sim 0530$  UT on 9 February is somewhat less definitive due to the data gap. The  $\beta$ -HPL peak at  $\sim 1400$  UT on 9 February is possibly a flux enhancement, considering the continuous appearance of the  $\beta$ -HPL decay from  $\sim 0530$  UT to  $\sim 2330$  UT on 9 February if the observations at  $\sim 1200$  UT and  $\sim 1330$  UT are omitted.
3. A sector reversal occurs at  $\sim 0550$  on 10 February, and, although it is significant that the first north polar observation after the

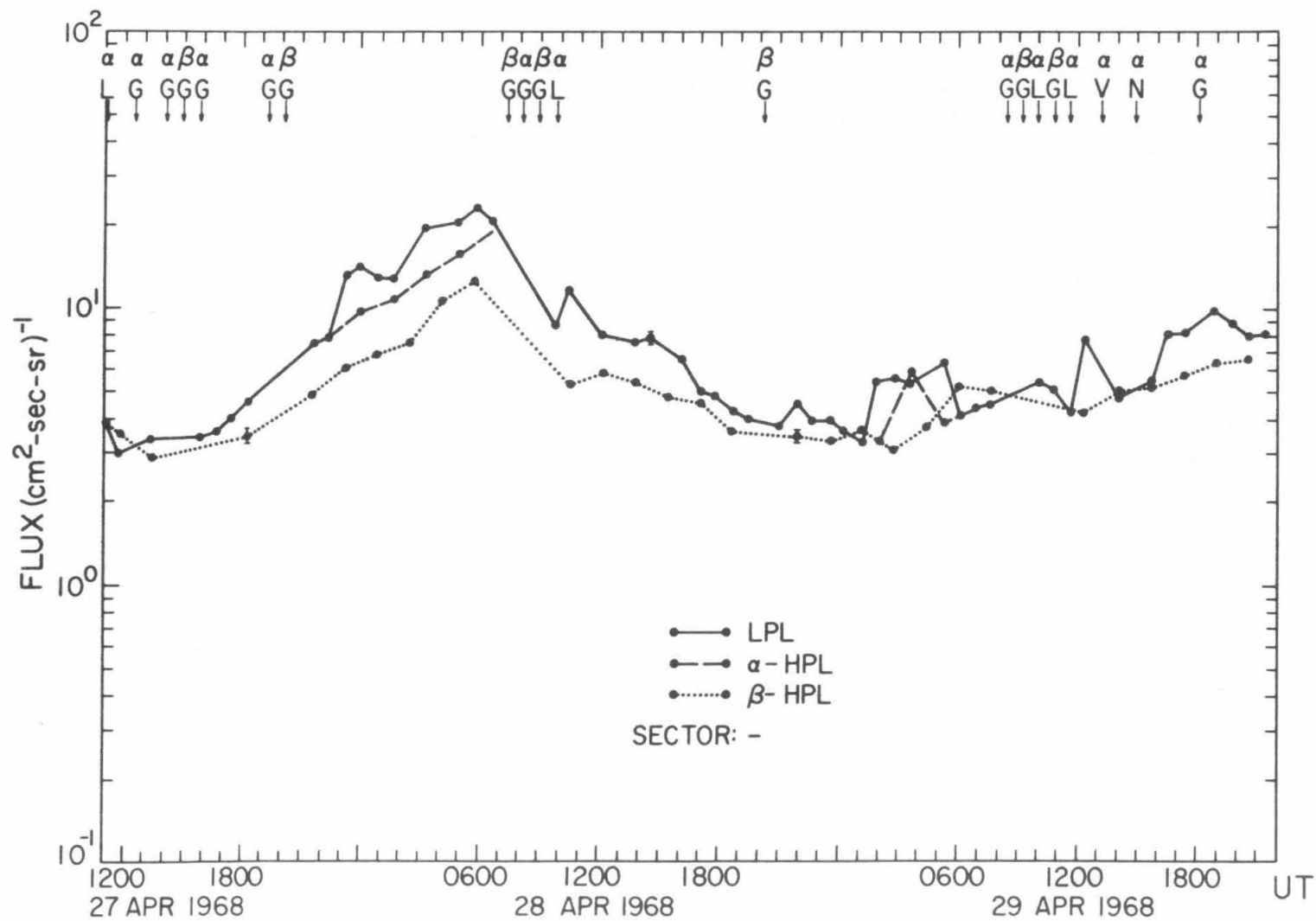
sector reversal shows no feature, the period of missing data immediately preceding the sector reversal (includes two  $\beta$ -HPL passes) somewhat clouds the question of the simultaneity of the feature disappearance and sector reversal.



## Figure A-10

*27 April 1968 -- Class C Event*

1. A  $\beta$ -HPL feature (depression) is observed for a period of  $\sim 34$  hours during the rise and decay of this event.
2. A  $\alpha$ -HPL depression is observed for  $\sim 6\frac{1}{2}$  hours beginning at  $\sim 0000$  on 28 April.
3. The flux increase observed at  $\sim 0130$  UT on 29 April at LPL is not observed at  $\alpha$ -HPL until 0200-0340 UT, and not at  $\beta$ -HPL until later still.
4. The beginning of another persistent  $\beta$ -HPL feature is observed at  $\sim 1600$  UT on 29 April, but no data are available past  $\sim 2200$  UT.





## Figure A-11

*13 May 1968 -- Solar Flare Event*

1. An example of a persistent  $\beta$ -HPL enhancement. This feature lasts for  $\sim 40$  hours. A small increase (probably an EDP event) is superimposed on the LPL flux and  $\alpha$ -HPL flux near the beginning of the profile.

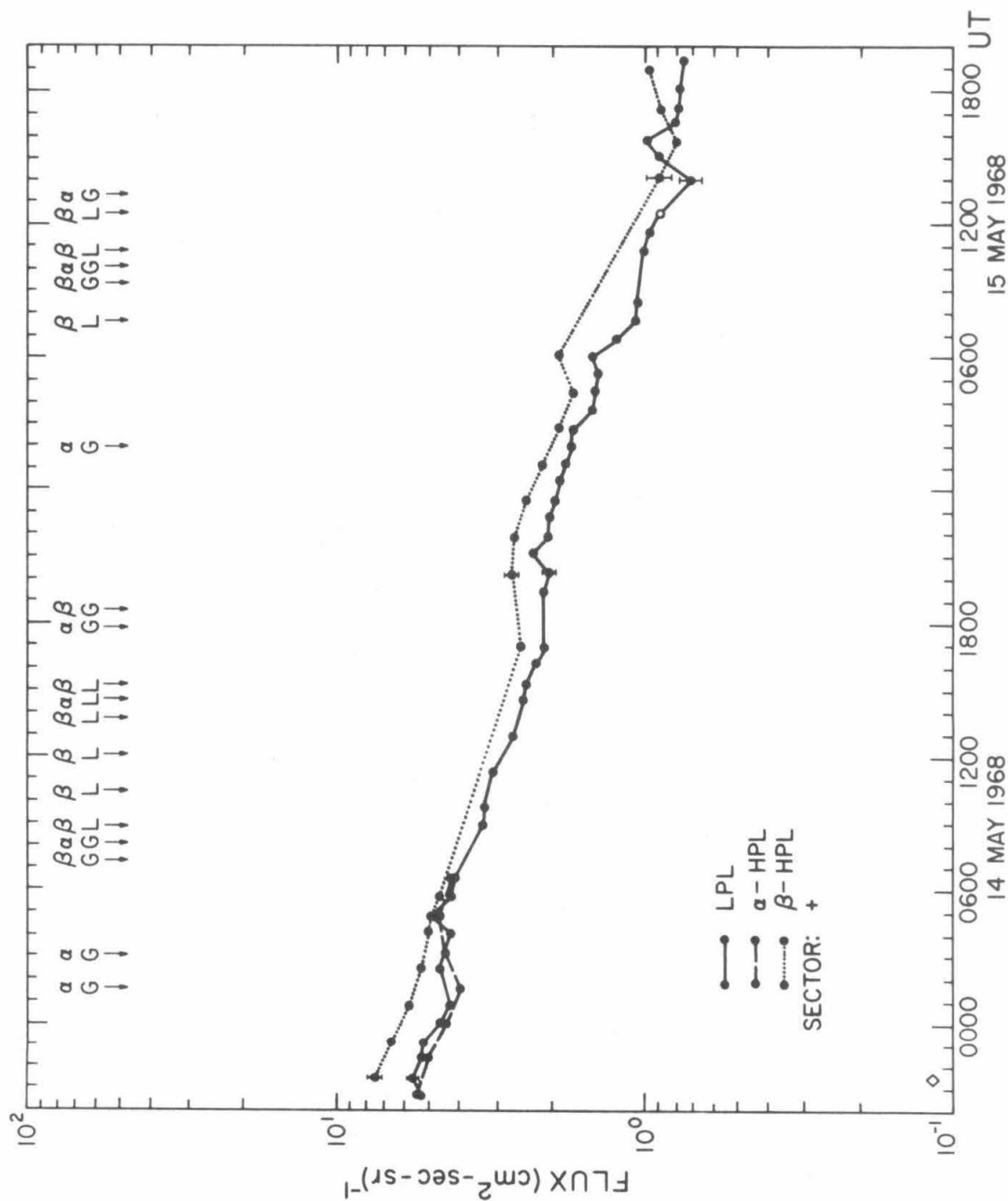


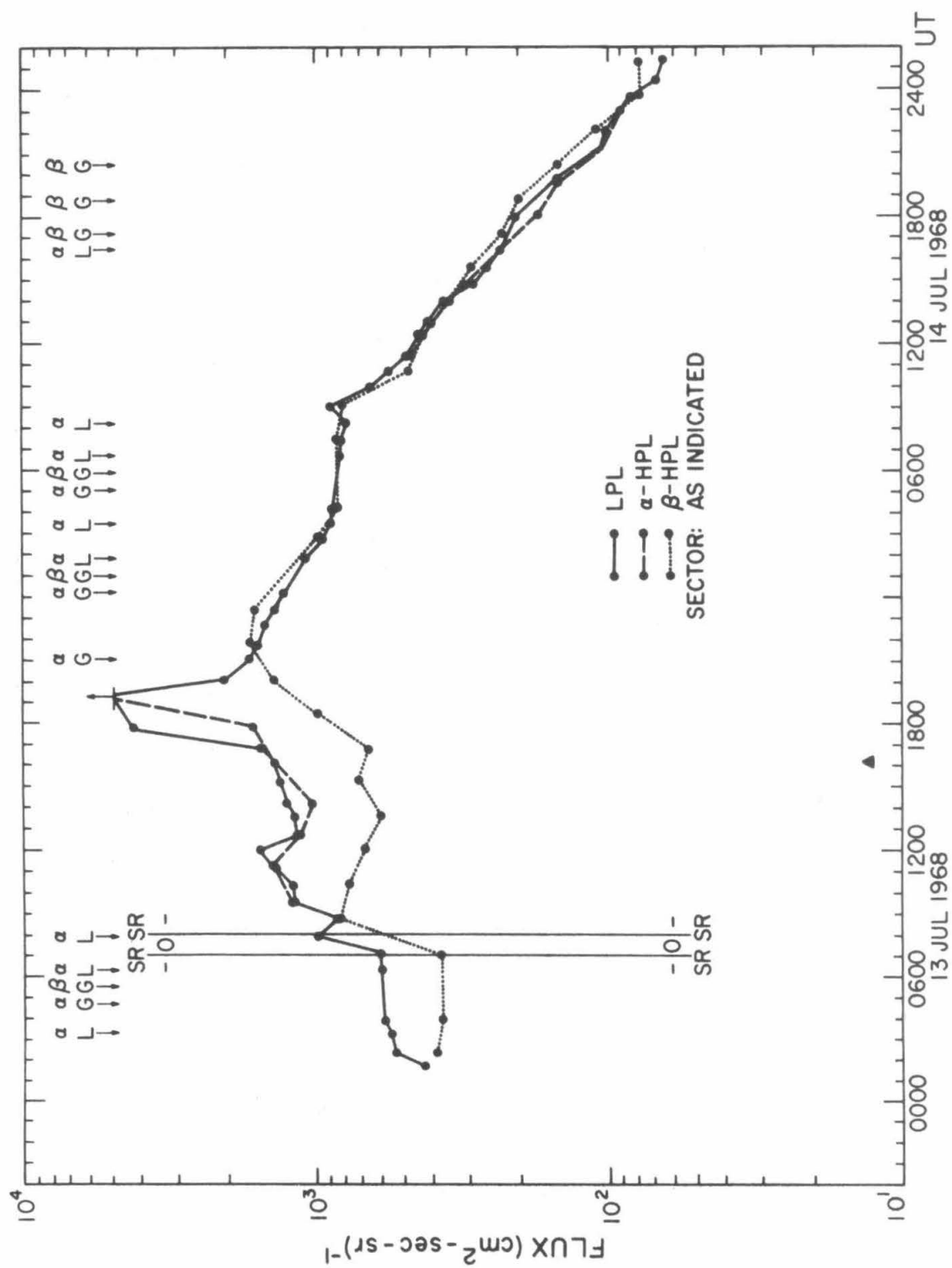
Figure A-12

*13 July 1968 -- Solar Flare Event*

1. Flux levels are very high on these rates, and errors are consequently very small.
2. The temporary disappearance of the persistent  $\beta$ -HPL feature between  $\sim 0700$  UT and  $\sim 0840$  UT on 13 July is probably related to the period of uncertain sector structure near  $\sim 0730$  UT.
3. After  $\sim 0840$  UT on 13 July the  $\beta$ -HPL flux decayed for  $\geq 5$  hours while the LPL and  $\alpha$ -HPL fluxes were increasing.
4. The small increase in the  $\beta$ -HPL flux at  $\sim 1500$  UT on 13 July might be associated with the increase seen at LPL at  $\sim 1100$  UT.
5. The most notable feature of this profile is the event which reaches a maximum flux at  $\sim 1800$  UT on 13 July at LPL. The following observations can be made about this event:
  - a. The gap in the LPL and  $\alpha$ -HPL fluxes at  $\sim 1900$  UT is due to overscaling (see Section IV).
  - b. The event reaches a maximum at  $\beta$ -HPL  $\sim 3$  hours later than at LPL. The maximum flux is lower, and the "width" of the peak is much greater.
  - c. The transition from  $\beta$ -HPL depression to  $\beta$ -HPL enhancement

occurs prior to the  $\beta$ -HPL peak.

- d. During the decay of this event the  $\beta$ -HPL flux remains greater than the LPL and  $\alpha$ -HPL fluxes, with the exception of the broad feature (EDP?) superimposed on the decay from  $\sim 0400$  UT to  $\sim 1400$  UT on 14 July.



## APPENDIX B

### Particle Trajectories in a Turning Magnetic Field

The configuration of the geomagnetic field in the presence of significant merging between the geomagnetic and interplanetary magnetic fields has been the subject of a good deal of effort on the part of several investigators (see Sections VI and VII and the pertinent references cited therein). The access of charged particles into the magnetosphere with such a configuration is rather straightforward: the direct connection between the fields implies that trajectories probably exist whereby particles in interplanetary space can more or less "follow" the field lines into the geomagnetic tail. The assumption which is normally made is that these interplanetary particles gain access to the geomagnetic tail adiabatically, which means that the magnetic moment is conserved and that consequently the pitch angle of the particle in the tail,  $\phi_{gt}$ , is related to that in interplanetary space,  $\phi_{ip}$ , by

$$\sin^2(\phi_{gt}) = \frac{B_{gt}}{B_{ip}} \sin^2(\phi_{ip}) \quad (B.1)$$

where  $B_{gt}$  and  $B_{ip}$  represent the magnitude of the geomagnetic field and the interplanetary magnetic field, respectively.

One of the implications of the assumption summarized in (B.1) is that the particles observed over one polar cap will be those whose interplanetary pitch angles were  $\leq 1^\circ$ , while the particles observed over the other polar cap will be those whose pitch angles in interplanetary space

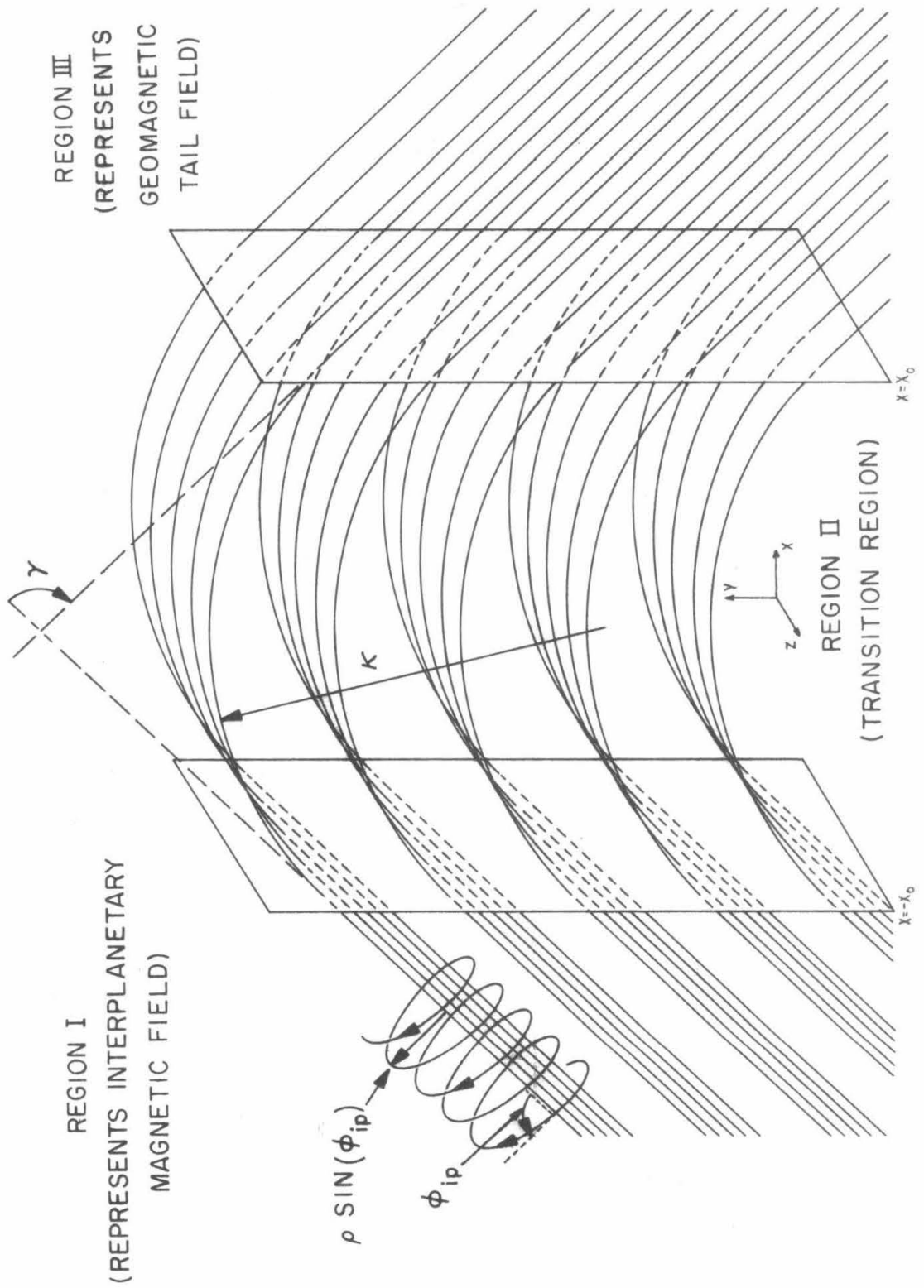
were  $\geq 179^\circ$ . The interplanetary pitch angles observed at a given pole would be dependent on the sector of the interplanetary field: a detector in the northern polar region would observe  $\phi_{ip} \approx 0^\circ$  particles during a positive sector and  $\phi_{ip} \approx 180^\circ$  particles during a negative sector. Although unimportant if the interplanetary flux is isotropic, the implications of the assumption of adiabatic motion are very significant in the presence of large interplanetary anisotropies: one would expect the differences between the fluxes observed in the two polar regions to follow a field-directed interplanetary anisotropy rather closely.

The mapping of interplanetary pitch angles onto the polar caps will be altered, however, if the assumption of adiabatic motion is relaxed. In order to simplify the following discussion, we will refer to the scale over which the magnetic field is changing direction in terms of the radius of curvature of a typical line of force for this field: i.e., the more rapidly the field changes direction the smaller the radius of curvature would be. In the limit of a minimum radius of curvature which is much larger than the gyroradius of the particles, one would expect adiabatic motion to be a rather good approximation. The gyroradius of a 1 MeV proton in a  $50 \mu\text{G}$  interplanetary field is, however,  $6.8 R_\oplus$ , while that for a 10 MeV proton is  $21.5 R_\oplus$ . Since the geomagnetic tail itself has a radius of about  $20\text{--}30 R_\oplus$ , adiabatic motion may require a transition region between the interplanetary field and the geomagnetic field of  $70\text{--}220 R_\oplus$ . In order to place constraints on the size of this transition region based on particle observations in the polar cap regions and in interplanetary space in the presence of large interplanetary anisotropies,



Figure B-1

Schematic representation of a "turning" magnetic field.



it is necessary to investigate this problem in more detail.

A good deal of insight into the pitch angle mapping problem can be gained by analyzing the behavior of particles in the field configuration illustrated in figure B-1: two regions, each containing a uniform, homogeneous magnetic field of the same magnitude, separated by a transition region in which the constant magnitude field changes direction (in the plane of the two fields only) at a constant rate (i.e., the radius of curvature,  $\kappa$ , of a line of force in this region is a constant throughout the region). The total angle through which the field turns is designated by  $\gamma$ . The equation of motion of a proton in such a field is given by the Lorentz force:

$$\frac{d\vec{v}}{dt} = \frac{e}{mc}(\vec{v} \times \vec{B}) \quad (\text{B.2})$$

The solutions of this equation in Regions I and III are helices whose axes are parallel to the magnetic field. In region III this is given by

$$\begin{aligned} x &= [v \cos(\phi)\cos(\beta)]t + \rho \sin(\phi)\sin(\beta)\cos(\omega t + \delta) \\ &\quad + [x_0 - \rho \sin(\phi)\cos(\delta)\sin(\beta)] \\ y &= \rho \sin(\phi)[\cos(\omega t + \delta) - \cos(\delta)]\cos(\beta) - [v \cos(\phi)\sin(\beta)]t + y_0 \\ z &= \rho \sin(\phi)[\sin(\omega t + \delta) - \sin(\delta)] + z_0 \end{aligned} \quad (\text{B.3})$$

and

$$\begin{aligned}
 v_x &= v[\cos(\phi)\cos(\beta)+\sin(\phi)\sin(\beta)\sin(\omega t+\delta)] \\
 v_y &= v[\sin(\phi)\cos(\beta)\sin(\omega t+\delta)-\cos(\phi)\sin(\beta)] \\
 v_z &= v \sin(\phi)\cos(\omega t+\delta)
 \end{aligned}
 \tag{B.4}$$

where  $\beta$  is the angle between the field and the  $x$ -axis,  $\phi$  is the pitch angle of the particle,  $\rho$  is the gyroradius of the particle, and  $x_0$ ,  $y_0$ ,  $z_0$  and  $\delta$  specify the initial position of the particle and phase of its motion. An almost identical set of equations can be written for the solution in region I. These equations can be used to determine whether a proton which is leaving region II will re-enter region II and, if so, where and with what velocity. The situation within region II is, on the other hand, completely different: (B.2) is no longer amenable to an analytic solution, but the computational simplicity of (B.2) makes the use of a digital computer natural.

Using the techniques outlined above, a digital computer was programmed to determine charged particle trajectories in the magnetic field configuration shown in figure B-1. Since the motion of the particles after they have gained access to the geomagnetic tail is assumed to be adiabatic, the particles observed at the orbit of a low altitude, polar orbiting satellite will have had pitch angles very near  $0^\circ$  (north pole) or  $180^\circ$  (south pole) in the geomagnetic tail near the access windows. The problem was therefore delimited to one of finding the interplanetary

(region I) pitch angle,  $\phi_{ip}$ , which would result in a  $0^\circ$  pitch angle in the northern geomagnetic tail (region III) for various values of the pertinent parameters. Solutions for the southern geomagnetic pole can be obtained by taking the supplement of the pitch angle found for the northern tail.

Figures B-2 and B-3 show typical results from these calculations. Figure B-2 shows  $\phi_{ip}$  as a function of  $\kappa/\rho$  for five values of  $\gamma$ , where  $\kappa$  is the radius of curvature of the field, and  $\rho$  is the gyroradius of the particle. Figure B-3 shows  $\phi_{ip}$  as a function of  $\gamma$  for six values of  $\kappa/\rho$ . It is interesting that for a configuration in which the field is turning too sharply ( $\kappa/\rho$  small), no interplanetary particles are seen at the polar caps if  $\gamma \gtrsim 90^\circ$ .

It is immediately obvious from figures B-2 and B-3 that the mapping of interplanetary pitch angle distributions into particles observed over the polar caps is by no means a simple one. From these data one can generate contours of the minimum  $\kappa/\rho$  and the maximum  $\gamma$  which insure that a given interplanetary pitch angle will be observable over the polar caps. Such contours are presented in figure B-4. Contours such as these can be used in conjunction with polar cap and interplanetary pitch angle distribution observations to place constraints on the magnetic field configuration in the access window region. Suppose, for instance, that it were established from observations that only those protons with interplanetary pitch angles  $\leq 4^\circ$  were observed in one polar cap, while only those with interplanetary pitch angles  $\geq 176^\circ$  were observed in the other polar cap.

Figure B-2

Interplanetary pitch angles giving a  $0^\circ$  pitch angle in the northern geomagnetic tail as a function of the radius of curvature,  $\kappa$ , of the field in the transition region (see figure B-1) and the gyroradius,  $\rho$ , of the particle. Results are shown for five different field configurations, represented by different angles,  $\gamma$ , through which the field turns.

$$U_m = \frac{\pi V_A}{4 \ln \left( \frac{16 U_m^2 \pi \sigma L}{V_A c^2} \right)} \quad (6.1)$$

where  $\sigma$  is the conductivity of the plasma at the neutral point, and  $L$  is the scale size of the diffusion region. Sonnerup [87] has recently refined this approach somewhat, and has reported the following relationship for determining the maximum plasma velocity at which the fields may merge:

$$U_m = V_A (1 + \sqrt{2}) \quad (6.2)$$

By treating the basic field equations involved, Yeh and Axford [88] conclude that in general there is no maximum merging velocity, although they show that Sonnerup's solution is a special case of their solution -- the only non-singular case, according to Sonnerup. Considering the scarcity of observational information concerning magnetic merging, it is virtually impossible to determine which, if any, of these solutions is more nearly correct. Even establishing the absence of merging between the solar and terrestrial magnetic fields would be significant.

As a matter of terminology, geomagnetic field configurations arising from the assumption of the absence of magnetic merging between the solar and terrestrial fields are referred to as *closed* magnetospheric models, while those configurations based on the presence of merging are termed *open* magnetospheric models. In the next Section, after a discussion of

Figure B-3

Interplanetary pitch angles giving a  $0^\circ$  pitch angle in the northern geomagnetic tail as a function of the angle,  $\gamma$ , through which the magnetic field turns (see figure B-1). Results are shown for six values of  $\kappa/\rho$ .



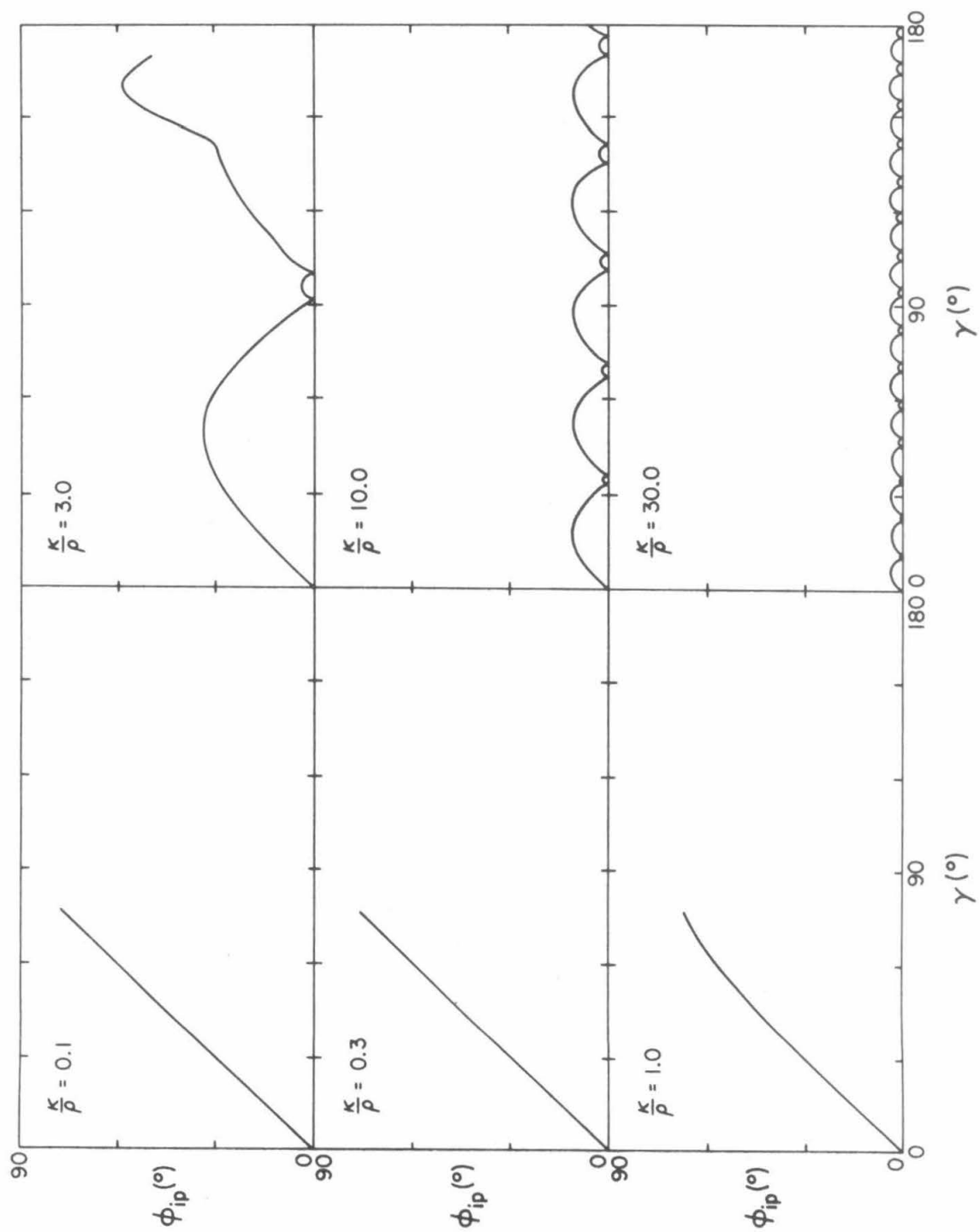
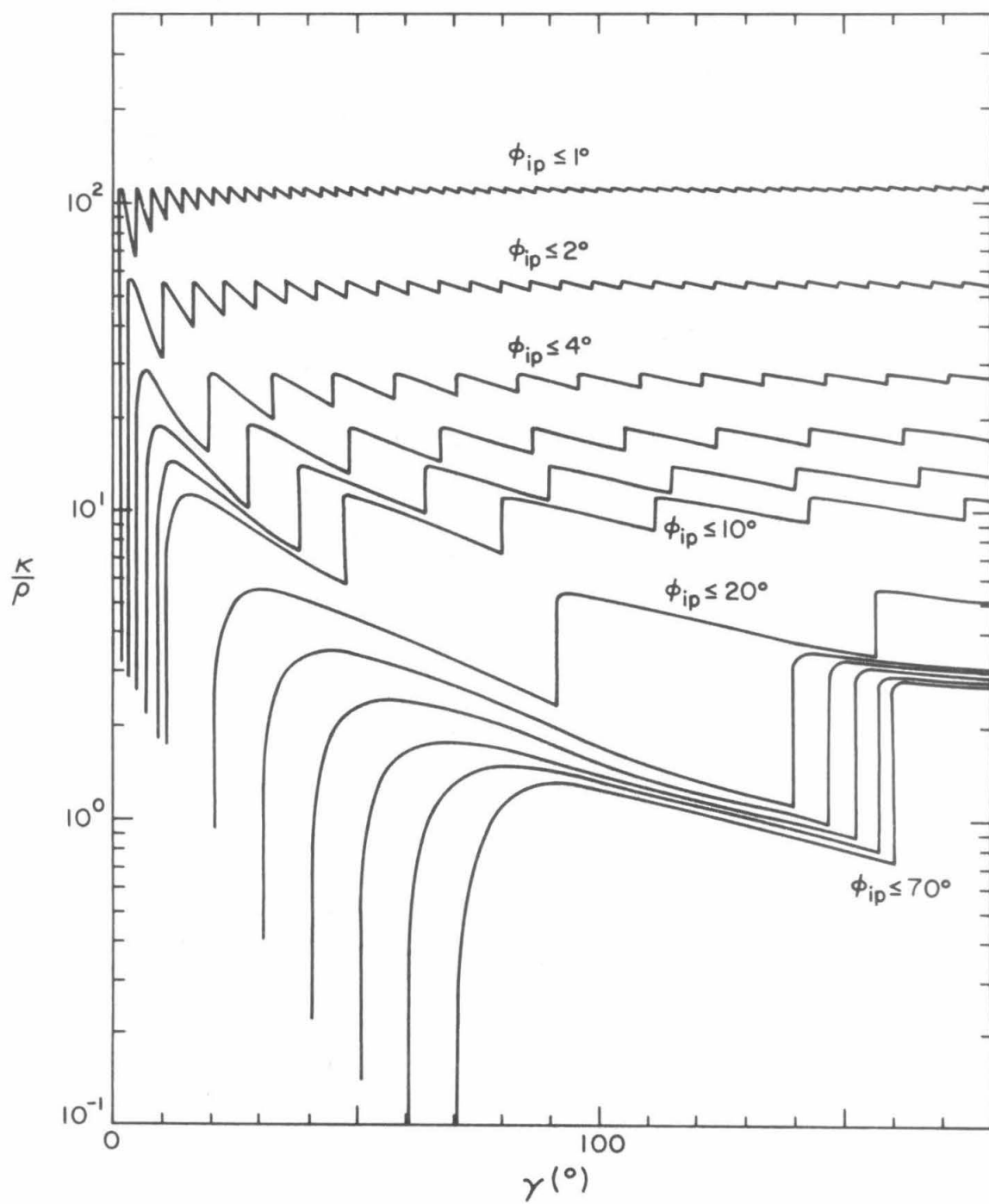


Figure B-4

Contours of the minimum  $\kappa/\rho$  for a given value of  $\gamma$  (or maximum  $\gamma$  for a given value of  $\kappa/\rho$ ) which will insure that the particles observed in the polar cap region represent interplanetary pitch angles no greater than the specified values.



Considering that the field will "turn" through an average angle of either  $48^\circ$  or  $132^\circ$  ( $48^\circ$  is the average Archimedian spiral angle at 1 AU, while the geomagnetic tail field is either parallel or antiparallel to the solar wind, which flows radially away from the sun), then the  $\phi_{ip} \leq 4^\circ$  contour on figure B-4 would imply that we must have  $\kappa \geq 27$  for the transition regions for both poles. For 1 MeV protons, this means  $\kappa \geq 184 R_\oplus$  ( $1.17 \times 10^6$  km), while for 10 MeV protons this means  $\kappa \geq 580 R_\oplus$  ( $3.7 \times 10^6$  km). For comparison, the tail, itself, is probably 40-60  $R_\oplus$  in diameter (see the discussion by Evans [101] for a more detailed consideration of the tail size and shape).

## APPENDIX C

### Magnetic Merging at the Polar Neutral Points

Frank [4] has recently proposed a magnetospheric model (see Section VII) which is of special interest to the study of low rigidity particle access to the polar regions: a direct consequence of the model is the possible formation of geomagnetic tails of different lengths for the two polar regions. It is the purpose of the study presented in this appendix to investigate the mechanisms which give rise to this consequence with a view toward determining what constraints must be placed on the model in order to yield the  $L_{\alpha\beta}$  access window configuration discussed in Section VII.

The major assumption of this model is the postulation that all merging between the geomagnetic field and the interplanetary magnetic field occurs at the polar neutral points. The location of these neutral points with respect to the magnetosphere is indicated in figure VI-5. Both open and closed geomagnetic field lines are assumed to merge with the interplanetary field at the neutral points, but the lines which were originally closed subsequently remerge in the neutral sheet. Since the interplanetary field lines with which open geomagnetic field lines merge are convected away from the earth with the solar wind, the length of the geomagnetic tail is proportional to its "age" (i.e., the time required for these open field lines to complete one cycle from merging to merging again). This age is, in turn, inversely proportional to the rate at which open field lines merge at the appropriate polar neutral point. In order to evaluate this model with respect to observational results, it

is necessary to investigate this merging process and the relative open field line merging rates at the two poles in some detail.

### *Assumptions*

The field configuration at the polar neutral point is represented in figure C-1, which shows the geomagnetic field at the northern neutral point, over which the interplanetary magnetic field has been pulled by the solar wind. The geometry of the field clearly contributes greatly to the complexity of the problem in this configuration. It is sufficient at this point, though, to consider the plane configuration shown in figure C-2, which may be related to the more complex geometry by considering the situation in the immediate vicinity of the neutral point in figure C-1. These figures can be transformed into a representation of the southern polar neutral point by reversing the sense of the geomagnetic field.

Figure C-2 also illustrates two of the parameters which will be used in this study:

$\phi$ : the angle between a field line and the projection of the earth-sun line in the plane of the field interface, measured from the anti-solar direction.

$\psi$ : the angle between a given geomagnetic field line and the direction of the interplanetary magnetic field.

This study is predicated on the following assumptions:

1. The boundary between open and closed geomagnetic field lines

Figure C-1

Schematic representation of the field configuration at the northern polar neutral point. A possible configuration for the interplanetary magnetic field near the neutral point is indicated by the heavier lines.



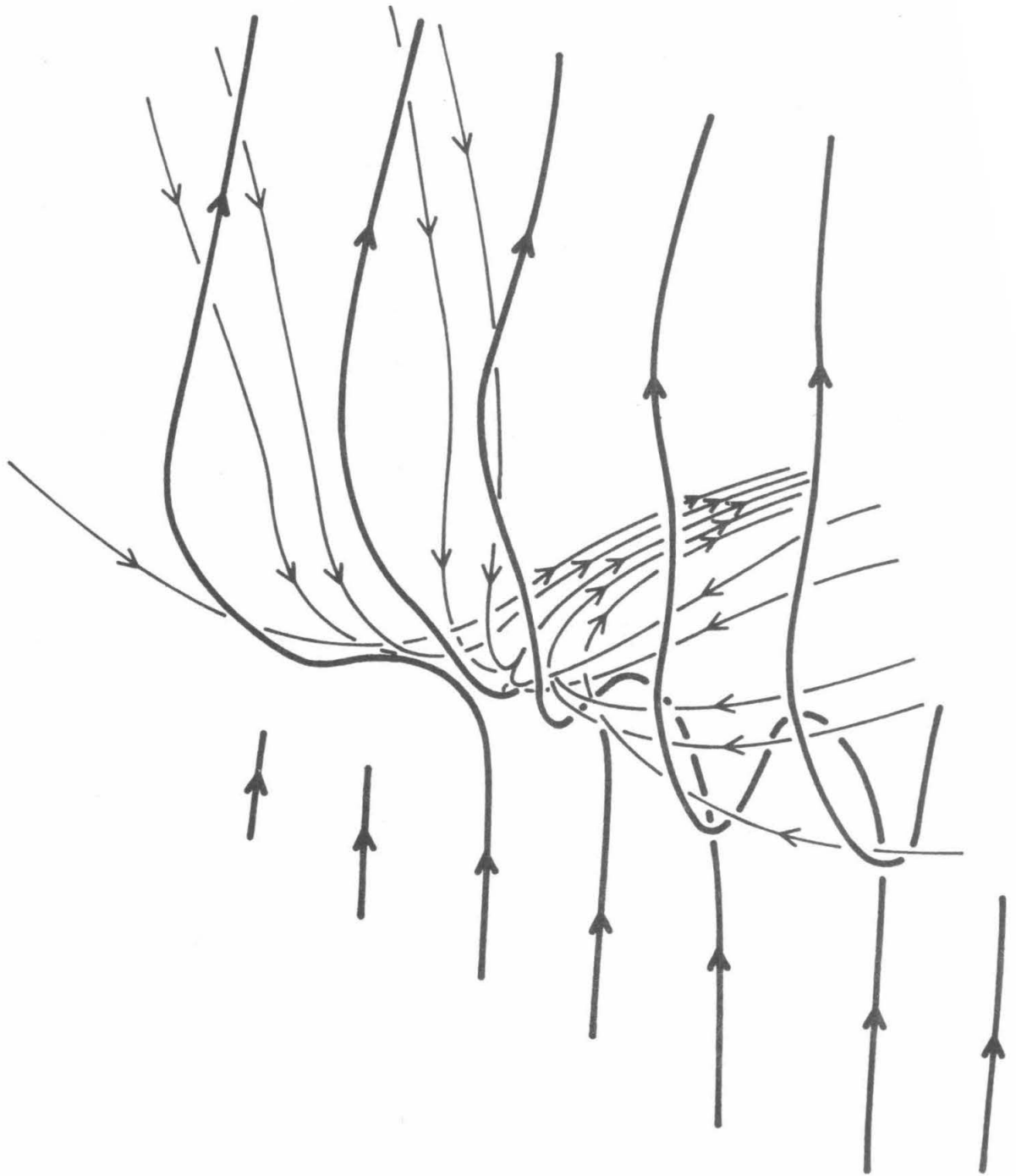
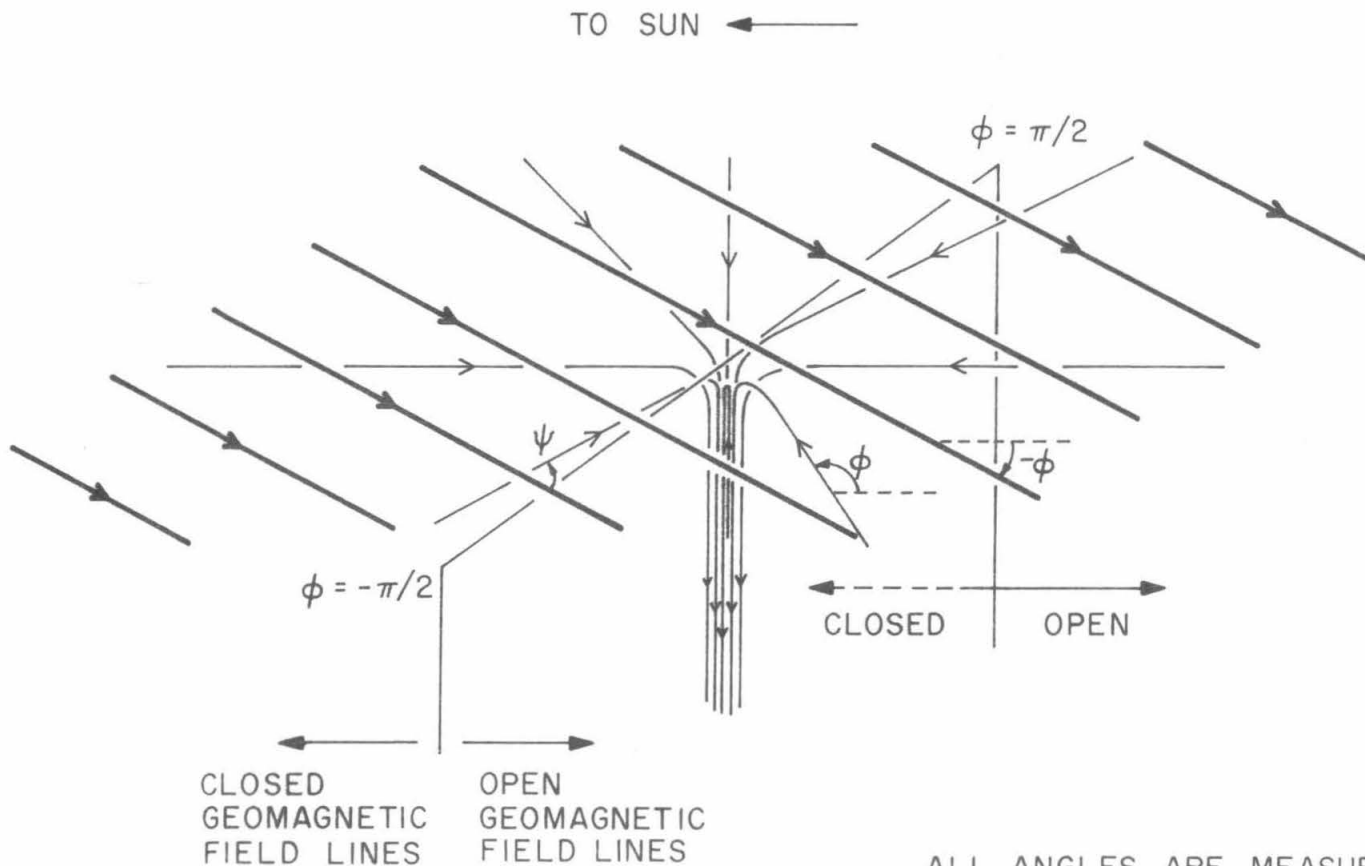


Figure C-2

Schematic representation of a plane interface between a uniform magnetic field and a magnetic field with a neutral point. This field configuration is essentially the same as that shown in figure C-1, while the geometry is greatly simplified.



ALL ANGLES ARE MEASURED  
IN A PLANE PARALLEL  
TO PLANE OF INTERFACE  
BETWEEN THE TWO FIELDS

is assumed to be perpendicular to the earth-sun line, with open field lines being those lines with  $\phi$  in the interval  $[-\pi/2, \pi/2)$ .

2. The angular configuration of the interplanetary magnetic field in the plane of the interface between the two fields is assumed to vary randomly, over a period of a few hours, according to a Gaussian-like distribution:

$$P(\phi) = \frac{C}{\sigma\sqrt{2\pi}} e^{-(\phi-\Phi)^2/2\sigma^2} \quad (C.1)$$

where  $C$  is defined by normalization:

$$\int_{-\pi}^{\pi} d\phi P(\phi) = 1 \quad (C.2)$$

which implies

$$C = \left[ \operatorname{erf}\left(\frac{\pi}{\sigma\sqrt{2}}\right) \right]^{-1} \quad (C.3)$$

3. The rate at which a given geomagnetic field line merges with the interplanetary magnetic field is dependent only on the solar wind velocity, the maximum merging rate for *any* two field lines based on plasma parameters, and the angle,  $\psi$ , between the geomagnetic field line in question and the direction of the interplanetary field.

4. The rate at which plasma is supplied for the merging process is limited by the solar wind velocity in the vicinity of the neutral point.

5. The rate at which the interplanetary field merges is the same at both polar neutral points.

Since the interplanetary field is "frozen into" the solar wind plasma, magnetic merging rates can be expressed in terms of equivalent plasma velocities. This equivalence conforms to the nomenclature used by Petschek [e.g. 86], Sonnerup [87], and Yeh and Axford [88]. One of the results of these previous studies which is of most significance here is the determination of the maximum equivalent plasma velocity,  $U_m$ . There is some disagreement, however, as to the proper dependence of  $U_m$  on plasma parameters:

$$U_m = \frac{V_A \pi}{4 \ln \left( \frac{16 U_m^2 \pi \sigma L}{V_A c^2} \right)} \quad (\text{Petschek})$$

$$U_m = V_A [1 + \sqrt{2}] \quad (\text{Sonnerup}) \quad (\text{C.4})$$

$$U_m < \infty \quad (\text{Yeh and Axford})$$

Without attempting to choose among these, we will express our results relative to  $U_m$ . Although all of these studies have dealt with the configuration of exactly anti-parallel fields, the results are applicable to the present configuration if the fields which are at an angle  $\psi$  to each other are resolved into parallel and anti-parallel components. Since the superposition of a constant magnetic field perpendicular to the antiparallel fields considered in the above studies has no essential effect on their derivations, we can write the maximum possible merging rate for fields at an angle  $\psi$  as

$$U_{\max}(\psi) = U_m \sin(\psi/2) \quad (C.5)$$

so that the actual merging rate for these fields obeys

$$u(\psi) \in [0, U_{\max}(\psi)] \quad (C.6)$$

The only other information available about the form of  $u(\psi)$  is the normalization implied by the fourth assumption above:

$$2 \int_0^\pi d\psi \, u(\psi) \leq V_{sw} \quad (C.7)$$

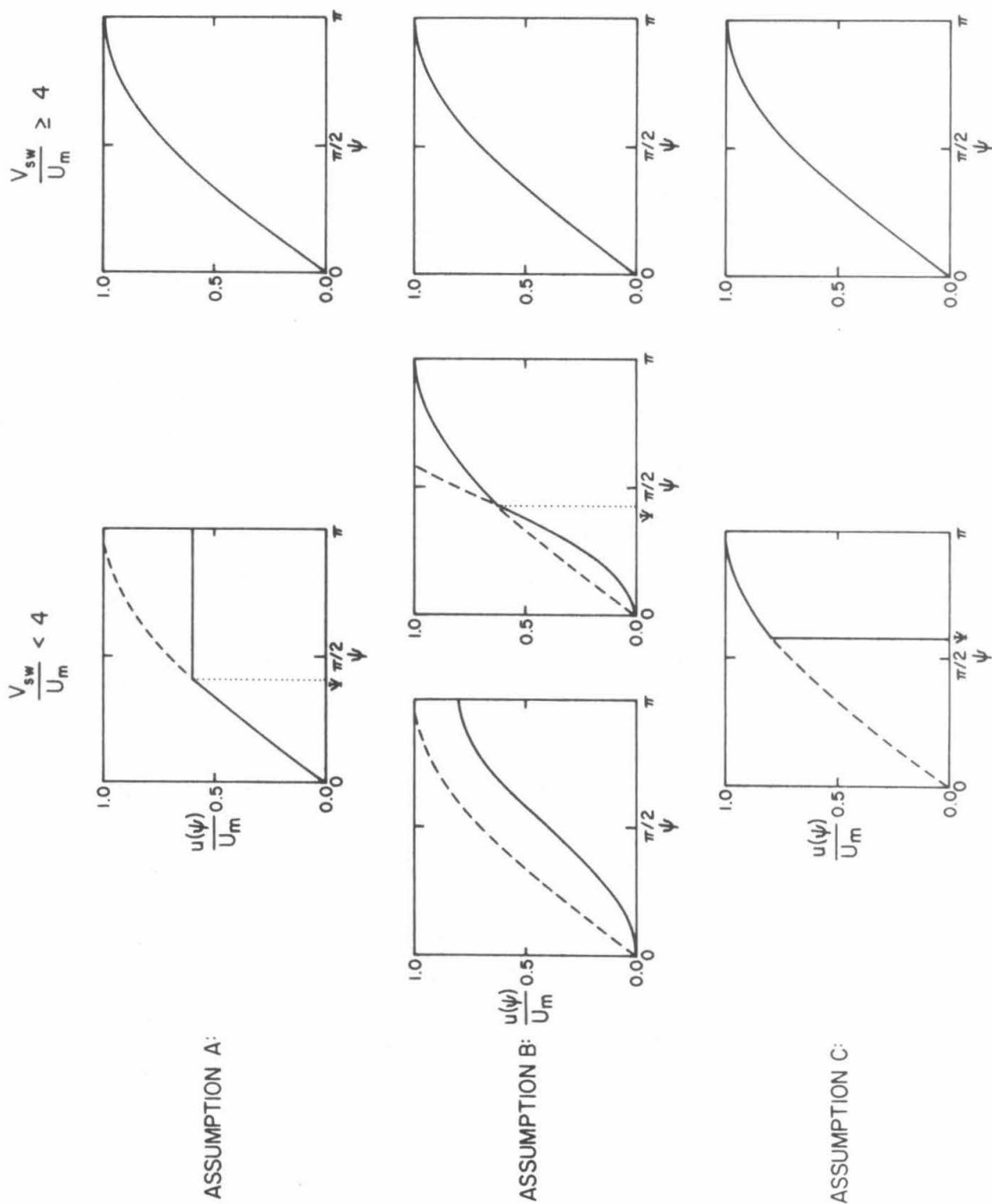
As a consequence, the specification of an exact form for  $u(\psi)$  in the case of  $V_{sw}/U_m$  sufficiently small is somewhat arbitrary. The question, of course, is whether the interplanetary magnetic field merges preferentially with more nearly antiparallel geomagnetic field lines. Since the answer to this is not clear, three assumptions will be made about the angular dependence of the merging rate, each of which will, of course, lead to different results. Figure C-3 illustrates the general form taken by  $u(\psi)$  under each of these assumptions.

#### *Assumption A*

The probability that two field lines will merge is taken to be independent of the angle between them. This means

Figure C-3

General behavior of  $u(\psi)$  for each of the three assumptions made in the text.





$$\begin{aligned}
 u(\psi) &= U_m \sin(\psi/2) & ; & \quad \psi < \Psi \\
 &= U_m \sin(\Psi/2) & ; & \quad \psi \geq \Psi
 \end{aligned} \tag{C.8}$$

where  $\Psi$  is determined by the normalization given by (C.7), which gives

$$\begin{aligned}
 (\pi - \Psi) \sin(\Psi/2) + 2[1 - \cos(\Psi/2)] &= V_{sw}/2U_m & ; & \quad V_{sw}/U_m \leq 4 \\
 \Psi &= \pi & ; & \quad V_{sw}/U_m > 4
 \end{aligned} \tag{C.9}$$

#### *Assumption B*

Under this assumption, the likelihood that two field lines will merge is assumed to be a function of the angle between them, with the likelihood varying directly with the angle. Since the choice of this function is at this point completely arbitrary, however, the merging likelihood will be chosen to be proportional to  $\sin(\psi/2)$  in order to take advantage of the consequent simplifications in the derivations to follow. Hence we have

$$\begin{aligned}
 u(\psi) &= \frac{V_{sw}}{\pi} \sin^2(\psi/2) & ; & \quad V_{sw}/U_m \leq \pi \\
 &= U_m \sin^2(\psi/2) / \sin(\Psi/2) & ; & \quad \psi < \Psi \\
 &= U_m \sin(\psi/2) & ; & \quad \psi \geq \Psi
 \end{aligned} \left. \vphantom{\begin{aligned} u(\psi) &= \frac{V_{sw}}{\pi} \sin^2(\psi/2) \\ &= U_m \sin^2(\psi/2) / \sin(\Psi/2) \\ &= U_m \sin(\psi/2) \end{aligned}} \right\} V_{sw}/U_m > \pi \tag{C.10}$$

where, from (C.7),  $\Psi$  is given by

$$\frac{\Psi + \sin(\Psi)}{\sin(\Psi/2)} = \frac{V_{sw}}{U_m} \quad ; \quad \pi < V_{sw}/U_m \leq 4 \quad (C.11)$$

$$\Psi = 0 \quad ; \quad V_{sw}/U_m > 4$$

*Assumption C*

For this case it is assumed that the interplanetary field will merge preferentially with the most nearly antiparallel geomagnetic field available. This assumption, which is the converse of Assumption A, yields

$$u(\psi) = 0 \quad ; \quad \psi < \Psi \quad (C.12)$$

$$= U_m \sin(\psi/2) \quad ; \quad \psi \geq \Psi$$

and (C.7) yields the following definition of  $\Psi$ :

$$\Psi = 2\cos^{-1}\left(\frac{V_{sw}}{4U_m}\right) \quad ; \quad V_{sw}/U_m \leq 4 \quad (C.13)$$

$$\Psi = 0 \quad ; \quad V_{sw}/U_m > 4$$

The solutions for  $\psi$  from (C.9), (C.11), and (C.13) are shown in figure C-4.

*Derivation of Merging Rates -- General*

We will now define the following symbolism:

$U_{ON}$  = merging velocity for open field lines at the northern polar neutral point

$U_{CN}$  = merging velocity for closed field lines at the northern polar neutral point

$U_{OS}$  = merging velocity for open field lines at the southern polar neutral point

$U_{CS}$  = merging velocity for closed field lines at the southern polar neutral point

From the symmetry implied from the assumption that the boundary between open and closed field lines at the neutral point is the plane through the neutral point and perpendicular to the projection of the earth-sun line into the plane of the field interface (see figure C-2), and the assumption that  $U_{ON} + U_{CN} = U_{OS} + U_{CS}$ , we have

$$U_{ON} = U_{CS}$$

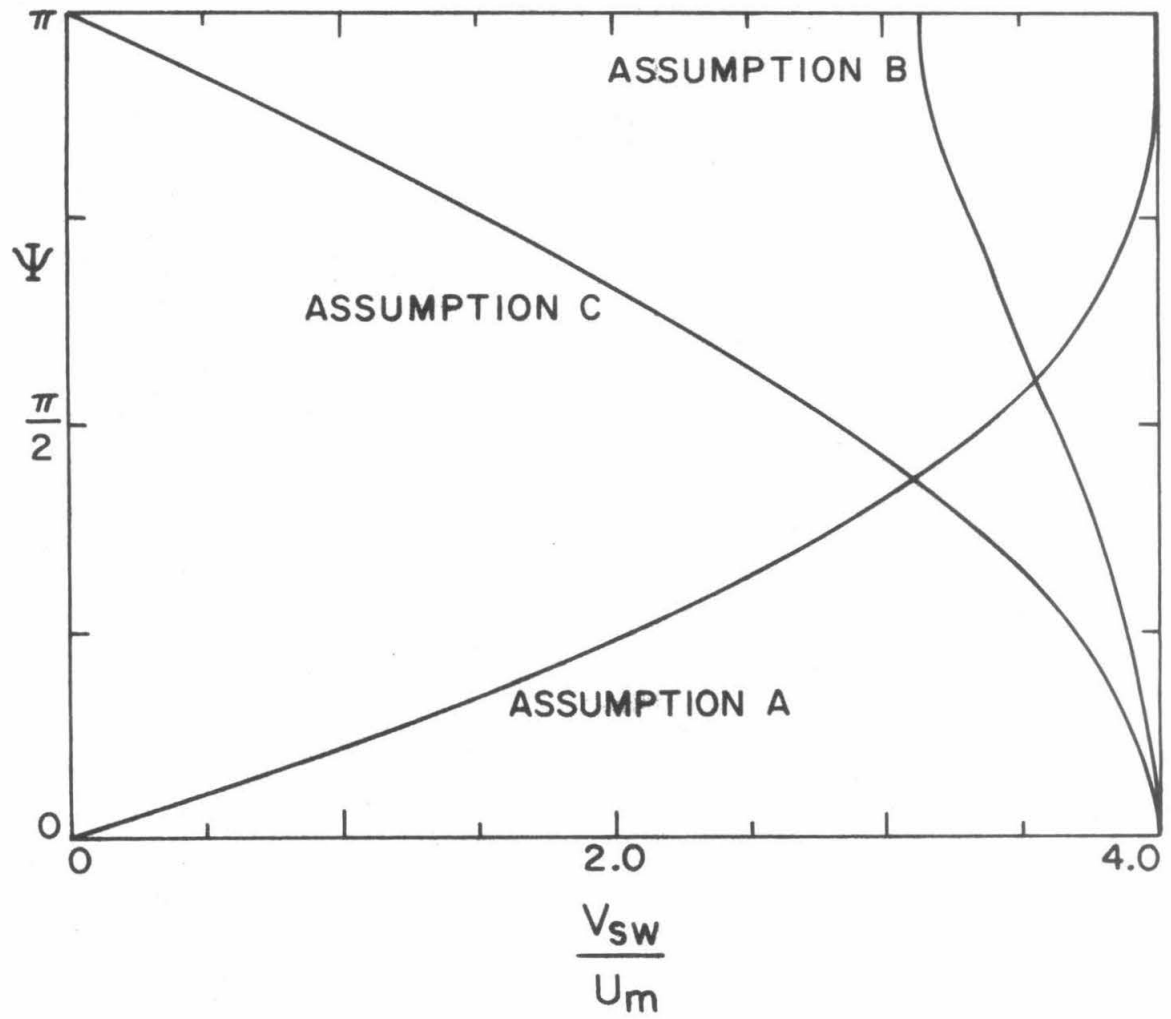
$$U_{OS} = U_{CN}$$

(C.14)

Concentrating our attention on  $U_{ON}$  and  $U_{OS}$ , then, we can write

Figure C-4

Critical angle,  $\psi$ , as a function of  $V_{sw}/U_m$  for each of the three assumptions made in the text.



Case I:  $\Phi \in [-\pi/2, \pi/2]$ :

$$u_{0p}^I(\Phi, \sigma) = \int_{\Phi-\pi}^{-\pi/2} d\phi P(\phi) v_{0p1}(\phi) + \int_{-\pi/2}^{\pi/2} d\phi P(\phi) v_{0p2}(\phi) + \int_{\pi/2}^{\Phi+\pi} d\phi P(\phi) v_{0p3}(\phi) \quad ; \quad p=N, S \quad (C.15)$$

Case II:  $\Phi \in [\pi/2, 3\pi/2]$ :

$$u_{0p}^{II}(\Phi, \sigma) = \int_{\Phi-\pi}^{\pi/2} d\phi P(\phi) v_{0p2}(\phi) + \int_{\pi/2}^{3\pi/2} d\phi P(\phi) v_{0p3}(\phi) + \int_{3\pi/2}^{\Phi+\pi} d\phi P(\phi) v_{0p4}(\phi) \quad ; \quad p=N, S \quad (C.16)$$

where the  $v_{0pi}(\phi)$  are given by

$$v_{0N1}(\phi) = \int_{-\pi}^{-(\phi+3\pi/2)} d\psi |u(\psi)| + \int_{-(\phi+\pi/2)}^{\pi} d\psi |u(\psi)| \quad (C.17)$$

$$v_{0S1}(\phi) = \int_{-(\phi+3\pi/2)}^{-(\phi+\pi/2)} d\psi |u(\psi)| \quad (C.18)$$

$$v_{ON2}(\phi) = \int_{-\phi-\pi/2}^{-\phi+\pi/2} d\psi |u(\psi)| \quad (C.19)$$

$$v_{OS2}(\phi) = \int_{-\pi}^{-\phi-\pi/2} d\psi |u(\psi)| + \int_{-\phi+\pi/2}^{\pi} d\psi |u(\psi)| \quad (C.20)$$

$$v_{ON3}(\phi) = \int_{-\pi}^{-\phi+\pi/2} d\psi |u(\psi)| + \int_{-\phi+3\pi/2}^{\pi} d\psi |u(\psi)| \quad (C.21)$$

$$v_{OS3}(\phi) = \int_{-\phi+\pi/2}^{-\phi+3\pi/2} d\psi |u(\psi)| \quad (C.22)$$

$$v_{ON4}(\phi) = \int_{-\phi+3\pi/2}^{-\phi+5\pi/2} d\psi |u(\psi)| \quad (C.23)$$

$$v_{OS4}(\phi) = \int_{-\pi}^{-\phi+3\pi/2} d\psi |u(\psi)| + \int_{-\phi+5\pi/2}^{\pi} d\psi |u(\psi)| \quad (C.24)$$

In order to be able to expand the  $v_{opi}(\phi)$ , it is useful to at this time introduce the following integrals which will be needed later:

$$\begin{aligned}
I_0(\alpha, \beta) &= \frac{1}{\sigma\sqrt{2\pi}} \int_{\alpha}^{\beta} d\phi \, e^{-(\phi-\Phi)^2/2\sigma^2} \\
&= [\operatorname{erf}(b) - \operatorname{erf}(a)]/2
\end{aligned} \tag{C.25}$$

$$\begin{aligned}
I_1(\alpha, \beta) &= \frac{1}{\sigma\sqrt{2\pi}} \int_{\alpha}^{\beta} d\phi \, \phi \, e^{-(\phi-\Phi)^2/2\sigma^2} \\
&= \frac{\sigma}{\sqrt{2\pi}} \left( e^{-a^2} - e^{-b^2} \right) + \Phi [\operatorname{erf}(b) - \operatorname{erf}(a)]/2
\end{aligned} \tag{C.26}$$

$$\begin{aligned}
I_s(\alpha, \beta) &= \frac{1}{\sigma\sqrt{2\pi}} \int_{\alpha}^{\beta} d\phi \, \sin(\phi/2) \, e^{-(\phi-\Phi)^2/2\sigma^2} \\
&= \frac{e^{-\sigma^2/8}}{\sigma\sqrt{2}} \Im \left\{ e^{i\Phi/2} [\operatorname{erf}(b - i\sigma/\sqrt{8}) - \operatorname{erf}(a - i\sigma/\sqrt{8})] \right\}
\end{aligned} \tag{C.27}$$

$$\begin{aligned}
I_c(\alpha, \beta) &= \frac{1}{\sigma\sqrt{2\pi}} \int_{\alpha}^{\beta} d\phi \, \cos(\phi/2) \, e^{-(\phi-\Phi)^2/2\sigma^2} \\
&= \frac{e^{-\sigma^2/8}}{\sigma\sqrt{2}} \Re \left\{ e^{i\Phi/2} [\operatorname{erf}(b - i\sigma/\sqrt{8}) - \operatorname{erf}(a - i\sigma/\sqrt{8})] \right\}
\end{aligned} \tag{C.28}$$



$$\begin{aligned}
I_{c2}(\alpha, \beta) &= \frac{1}{\sigma\sqrt{2\pi}} \int_{\alpha}^{\beta} d\phi \cos(\phi) e^{-(\phi-\Phi)^2/2\sigma^2} \\
&= \frac{e^{-\sigma^2/2}}{2\sigma} \Re \{ e^{i\Phi} [\operatorname{erf}(b-i\sigma/\sqrt{2}) - \operatorname{erf}(a-i\sigma/\sqrt{2})] \} \quad (C.29)
\end{aligned}$$

where

$$a = \frac{\alpha - \Phi}{\sigma\sqrt{2}} \quad ; \quad b = \frac{\beta - \Phi}{\sigma\sqrt{2}} \quad (C.30)$$

and where

$$\operatorname{erf}(z) = \frac{2}{\sqrt{\pi}} \int_0^z dt e^{-t^2} \quad (C.31)$$

is the standard error function. The approximation used to evaluate  $\operatorname{erf}(x+iy)$  is that given by Saltzer [114]:

$$\begin{aligned}
\operatorname{erf}(x+iy) &= \operatorname{erf}(x) + \frac{e^{-x^2}}{2\pi x} [1 + \cos(2xy) + i \sin(2xy)] \\
&\quad + \frac{2}{\pi} e^{-x^2} \sum_{n=1}^{\infty} \frac{e^{-n^2/4}}{n^2 + 4x^2} [f_n(x, y) + i g_n(x, y)] \quad (C.32)
\end{aligned}$$

$$f_n(x, y) = 2x - 2x \cosh(ny) \cos(2xy) + n \sin(ny) \sin(2xy)$$

$$g_n(x, y) = 2x \cosh(ny) \sin(2xy) + n \sinh(ny) \cos(2xy)$$

The relative error in this approximation is about one part in  $10^{-16}$ .

We must now evaluate these functions ( $v_{0pi}(\phi)$ ) for each of the three assumed forms for  $u(\psi)$ .

*Assumption A -- see (C.8) and (C.9)*

From (C.17),

$$\begin{aligned}
 v_{0N1}^<(\phi) &= \int_{-\pi}^{-(\phi+3\pi/2)} d\psi |u(\psi)| + \int_{-(\phi+\pi/2)}^{\pi} d\psi |u(\psi)| \\
 &= \left| \int_{-\pi}^{-(\phi+3\pi/2)} d\psi u(\psi) \right| + \left| \int_{-(\phi+\pi/2)}^{\pi} d\psi u(\psi) \right| \\
 &= \int_{-\pi}^{-(\phi+3\pi/2)} d\psi u(\psi) + \int_{-(\phi+\pi/2)}^{\pi} d\psi u(\psi)
 \end{aligned} \tag{C.33}$$

This can be combined with (C.8) to give, for  $\Psi \leq \pi/2$ ,

$$\begin{aligned}
\frac{u_{ON1}^{<}(\phi)}{U_m} &= (-\Psi+5\pi/2)\sin(\Psi/2)-2\cos(\Psi/2)+\phi\sin(\Psi/2) \\
&\quad -\sqrt{2}[\sin(\phi/2)+\cos(\phi/2)] \quad \phi \in [-3\pi/2, \Psi-3\pi/2] \\
&= \pi\sin(\Psi/2) \quad \phi \in (\Psi-3\pi/2, -\Psi-\pi/2] \quad (C.34) \\
&= (-\Psi+\pi/2)\sin(\Psi/2)-2\cos(\Psi/2)-\phi\sin(\Psi/2) \\
&\quad +\sqrt{2}[-\sin(\phi/2)+\cos(\phi/2)] \quad \phi \in (-\Psi-\pi/2, -\pi/2]
\end{aligned}$$

and, for  $\Psi > \pi/2$ ,

$$\begin{aligned}
\frac{u_{ON1}^{>}(\phi)}{U_m} &= (-\Psi+5\pi/2)\sin(\Psi/2)-2\cos(\Psi/2)+\phi\sin(\Psi/2) \\
&\quad -\sqrt{2}[\sin(\phi/2)+\cos(\phi/2)] \quad \phi \in [-3\pi/2, -\Psi-\pi/2] \\
&= 2[(\pi-\Psi)\sin(\Psi/2)-2\cos(\Psi/2) \\
&\quad -\sqrt{2}\sin(\phi/2)] \quad \phi \in (-\Psi-\pi/2, \Psi-3\pi/2] \quad (C.35) \\
&= (-\Psi+\pi/2)\sin(\Psi/2)-2\cos(\Psi/2)-\phi\sin(\Psi/2) \\
&\quad +\sqrt{2}[-\sin(\phi/2)+\cos(\phi/2)] \quad \phi \in (\Psi-3\pi/2, -\pi/2]
\end{aligned}$$

Similarly, from (C.18),

$$\begin{aligned}
u_{0S1}^<(\phi) &= \int_{-(\phi+3\pi/2)}^{-(\phi+\pi/2)} d\psi |u(\psi)| \\
&= \int_0^{-(\phi+\pi/2)} d\psi u(\psi) + \int_0^{\phi+3\pi/2} d\psi u(\psi)
\end{aligned} \tag{C.36}$$

which, as before, can be expanded into, for  $\Psi \leq \pi/2$ ,

$$\begin{aligned}
\frac{u_{0S1}^<(\phi)}{u_m} &= 4 - (\Psi + \pi/2) \sin(\Psi/2) - 2 \cos(\Psi/2) - \phi \sin(\Psi/2) \\
&\quad + \sqrt{2} [\cos(\phi/2) + \sin(\phi/2)] \quad \phi \in [-3\pi/2, \Psi - 3\pi/2] \\
&= 4 + (\pi - 2\Psi) \sin(\Psi/2) - 4 \cos(\Psi/2) \quad \phi \in (\Psi - 3\pi/2, -\Psi - \pi/2] \\
&= 4 - (\Psi - 3\pi/2) \sin(\Psi/2) - 2 \cos(\Psi/2) + \phi \sin(\Psi/2) \\
&\quad - \sqrt{2} [\cos(\phi/2) - \sin(\phi/2)] \quad \phi \in \{-\Psi - \pi/2, -\pi/2\}
\end{aligned} \tag{C.37}$$

and, for  $\Psi > \pi/2$ ,

$$\begin{aligned}
\frac{v_{0S1}^{>}}{U_m}(\phi) &= 4 - (\Psi + \pi/2) \sin(\Psi/2) - 2\cos(\Psi/2) - \phi \sin(\Psi/2) \\
&\quad + \sqrt{2}[\cos(\phi/2) + \sin(\phi/2)] \quad \phi \in [-3\pi/2, -\Psi - \pi/2] \\
&= 4 + 2\sqrt{2}\sin(\phi/2) \quad \phi \in (-\Psi - \pi/2, \Psi - 3\pi/2] \quad (C.38) \\
&= 4 - (\Psi - 3\pi/2) \sin(\Psi/2) - 2\cos(\Psi/2) + \phi \sin(\Psi/2) \\
&\quad - \sqrt{2}[\cos(\phi/2) - \sin(\phi/2)] \quad \phi \in (\Psi - 3\pi/2, -\pi/2]
\end{aligned}$$

These rather cumbersome equations can be written in a simplified form if we introduce the following notation (" $<$ " refers to  $\Psi \leq \pi/2$ , while " $>$ " refers to  $\Psi > \pi/2$ ):

$$\begin{aligned}
f_0(\phi) &= 1 \\
f_1(\phi) &= \frac{\pi}{2} \sin(\Psi/2) \\
f_2(\phi) &= 2\cos(\Psi/2) + \sin(\Psi/2) \\
f_3(\phi) &= \phi \sin(\Psi/2) \\
f_4(\phi) &= \sqrt{2}\sin(\phi/2) \\
f_5(\phi) &= \sqrt{2}\cos(\phi/2)
\end{aligned} \tag{C.39}$$

$$\begin{aligned}
\alpha_0^< &= \alpha_0^> = \Phi - \pi \\
\alpha_1^< &= \alpha_2^> = \max[\Phi - \pi, \Psi - 3\pi/2] \\
\alpha_2^< &= \alpha_1^> = \max[\Phi - \pi, -\Psi - \pi/2] \\
\alpha_3^< &= \alpha_3^> = \max[\Phi - \pi, -\pi/2] \\
\alpha_4^< &= \alpha_5^> = \max[\Phi - \pi, \Psi - \pi/2] \\
\alpha_5^< &= \alpha_4^> = \max[\Phi - \pi, -\Psi + \pi/2] \\
\alpha_6^< &= \alpha_6^> = \pi/2 \\
\alpha_7^< &= \alpha_8^> = \min[\Phi + \pi, \Psi + \pi/2] \\
\alpha_8^< &= \alpha_7^> = \min[\Phi + \pi, -\Psi + 3\pi/2] \\
\alpha_9^< &= \alpha_9^> = \min[\Phi + \pi, 3\pi/2] \\
\alpha_{10}^< &= \alpha_{11}^> = \min[\Phi + \pi, \Psi + 3\pi/2] \\
\alpha_{11}^< &= \alpha_{10}^> = \min[\Phi + \pi, -\Psi + 5\pi/2] \\
\alpha_{12}^< &= \alpha_{12}^> = \Phi + \pi
\end{aligned} \tag{C.40}$$

In addition, let  $A_{ijp}^<$  be defined as in table C-1.

With this notation (C.34), (C.35), (C.37), and (C.38) can be expressed as

Table C-1  
Definition of  $A_{ijp}^{<}$

j	p	$\psi^{< \pi/2}$	i											
			1	2	3	4	5	6	7	8	9	10	11	12
0	N	<	0	0	0	4	4	4	0	0	0	4	4	4
		>	0	0	0	4	4	4	0	0	0	4	4	4
	S	<	4	4	4	0	0	0	4	4	4	0	0	0
		>	4	4	4	0	0	0	4	4	4	0	0	0
1	N	<	5	2	1	1	2	1	1	2	5	5	2	-3
		>	5	4	1	1	0	1	1	4	5	5	0	-3
	S	<	-1	2	3	3	2	3	3	2	-1	-1	2	7
		>	-1	0	3	3	4	3	3	0	-1	-1	4	7
2	N	<	-1	0	-1	-1	-2	-1	-1	0	-1	-1	-2	-1
		>	-1	-2	-1	-1	0	-1	-1	-2	-1	-1	0	-1
	S	<	-1	-2	-1	-1	0	-1	-1	-2	-1	-1	0	-1
		>	-1	0	-1	-1	-2	-1	-1	0	-1	-1	-2	-1
3	N	<	1	0	-1	-1	0	1	1	0	-1	-1	0	1
		>	1	0	-1	-1	0	1	1	0	-1	-1	0	1
	S	<	-1	0	1	1	0	-1	-1	0	1	1	0	-1
		>	-1	0	1	1	0	-1	-1	0	1	1	0	-1
4	N	<	-1	0	1	-1	0	-1	1	0	-1	1	0	1
		>	-1	0	1	-1	-2	-1	1	0	-1	1	2	1
	S	<	1	0	-1	1	0	1	-1	0	1	-1	0	-1
		>	1	0	-1	1	2	1	-1	0	1	-1	-2	-1
5	N	<	-1	0	-1	1	0	-1	1	0	1	-1	0	1
		>	-1	-2	-1	1	0	-1	1	2	1	-1	0	1
	S	<	1	0	1	-1	0	1	-1	0	-1	1	0	-1
		>	1	2	1	-1	0	1	-1	-2	-1	1	0	-1

$$\frac{u_{0p1}^{<}}{u_m} = \sum_{j=0}^5 A_{ijp}^{<} f_j(\phi) \quad ; \quad \phi \in [\alpha_{i-1}^{<}, \alpha_i^{<}] \quad ;$$

$$i = 1, 2, 3 \quad ; \quad p = N, S \quad (C.41)$$

The rest of the  $u_{0pi}$  functions can be evaluated in a like manner, and comes as no surprise that they can all be combined and written as

$$\frac{u_{0pk}^{<}}{u_m} = \sum_{j=0}^5 A_{ijp}^{<} f_j(\phi) \quad ; \quad \phi \in [\alpha_{i-1}^{<}, \alpha_i^{<}] \quad ;$$

$$i = 3k-2, \dots, 3k \quad ; \quad p = N, S \quad ; \quad k = 1, \dots, 4 \quad (C.42)$$

We can now combine (C.42) with (C.15) and (C.16) to give an expression for  $u_{0p}$ :

$$\frac{u_{0p}^{<}}{u_m} = \frac{1}{\sigma\sqrt{2\pi}} \sum_{i=1}^{12} \int_{\alpha_{i-1}^{<}}^{\alpha_i^{<}} d\phi e^{-(\phi-\Phi)^2/2\sigma^2} \sum_{j=0}^5 A_{ijp}^{<} f_j(\phi) \quad ; \quad p = N, S \quad (C.43)$$

Using the integral definitions given in (C.25) through (C.30), we now have



$$\frac{U_{0p}^{<}}{U_m}(\phi, \sigma) = \sum_{i=1}^{12} \left\{ \left[ \sum_{j=0}^2 A_{ijp}^{<} f_j(\phi) \right] I_0(\alpha_{i-1}, \alpha_i) + A_{i3p}^{<} \sin(\psi/2) I_1(\alpha_{i-1}, \alpha_i) \right. \\ \left. + \sqrt{2} A_{i4p}^{<} I_c(\alpha_{i-1}, \alpha_i) + \sqrt{2} A_{i5p}^{<} I_s(\alpha_{i-1}, \alpha_i) \right\} ;$$

p = N, S (C.44)

Figure C-5 shows  $U_{ON}/U_m$  as a function of  $\phi$  for a range of values of  $\sigma$  and of  $V_{sw}/U_m$ .  $U_{OS}/U_m$  can be related to these curves by the relationship

$$U_{OS}(\phi, \sigma) = U_{ON}(\pi - \phi, \sigma) \quad (C.45)$$

*Assumption B -- see (C.10) and (C.11)*

$$V_{sw}/U_m \leq \pi$$

In this case the forms of  $U_{ON}$  and  $U_{OS}$  are particularly simple; it can be shown that

$$\frac{U_{ON}}{U_m} = \frac{V_{sw}}{2\pi U_m} [\pi I_0(\phi - \pi, \phi + \pi) - I_{c2}(-\pi, \pi)]$$

$$\frac{U_{OS}}{U_m} = \frac{V_{sw}}{2\pi U_m} [\pi I_0(\phi - \pi, \phi + \pi) + I_{c2}(-\pi, \pi)] \quad (C.46)$$

$$V_{sw}/U_m > \pi$$

The derivation of  $U_{ON}$  and  $U_{OS}$  in this case parallels that given in

Figure C-5

Resultant relative merging rates for open field lines at the northern polar neutral point for Assumption A. Note the changing vertical scale. Since

$$U_{ON}(\phi, \sigma) = U_{OS}(\pi - \phi, \sigma)$$

and

$$U_{ON}(\phi, \sigma) + U_{OS}(\phi, \sigma) = \min[V_{sw}, 4U_m]$$

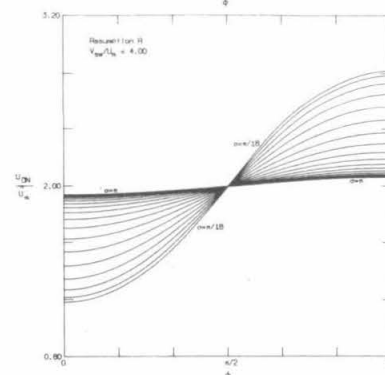
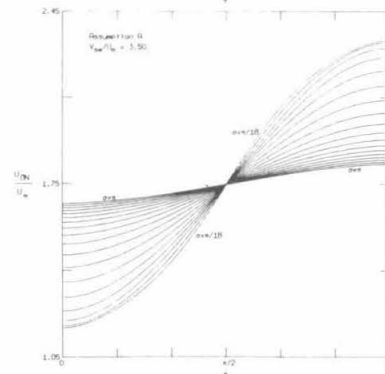
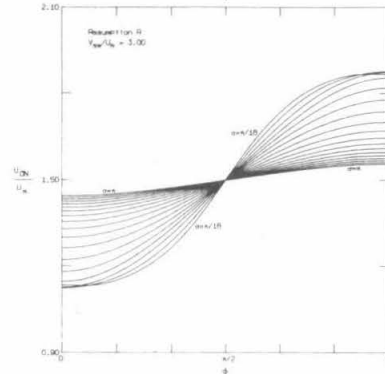
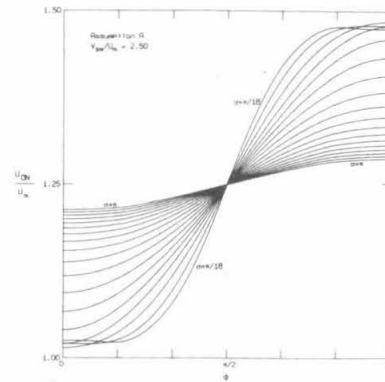
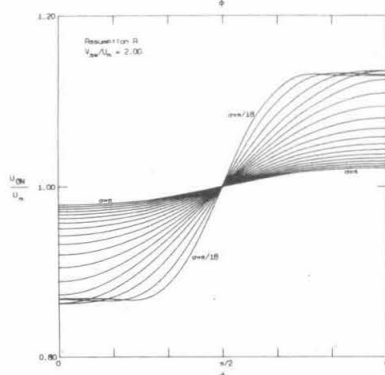
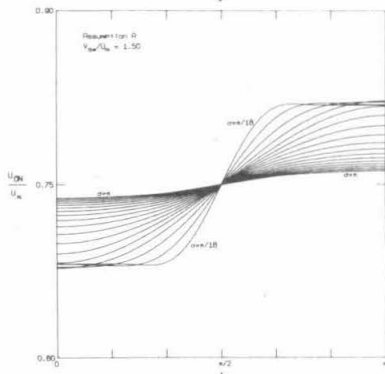
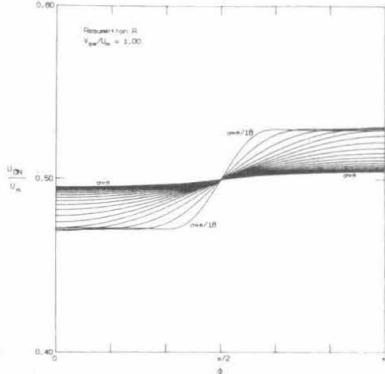
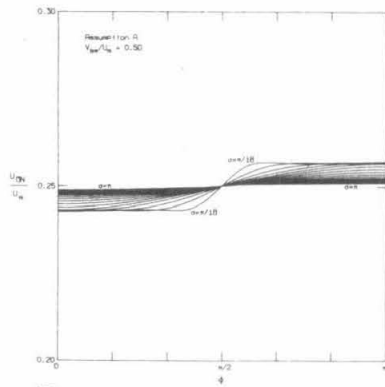
we have

$$U_{ON}(\phi, \sigma) + U_{OS}(\pi - \phi, \sigma) = \min[V_{sw}, 4U_m]$$

and, as a consequence,

$$U_{ON}(\pi/2, \sigma) = \min[V_{sw}/2, 2U_m]$$

In plotting  $U_{ON}/U_m$ , therefore, the vertical scales were chosen so as to reflect these symmetries. On all plots, the midpoint of the vertical scale corresponds to  $V_{sw}/2U_m$ , while the distance between each pair of tick marks on the vertical scale corresponds to  $V_{sw}/10U_m$ .



detail for Assumption A to the extent that it is sufficient to merely specify the results of the derivation. In order to do so concisely, we will use the notation of (C.40) and define  $g_j(\phi)$  as

$$\begin{aligned}
 g_0(\phi) &= V_{sw}/2U_m \\
 g_1(\phi) &= \pi/[4\sin(\psi/2)] \\
 g_2(\phi) &= \phi/[2\sin(\psi/2)] \\
 g_3(\phi) &= \sqrt{2}\cos(\phi/2) \\
 g_4(\phi) &= \sqrt{2}\sin(\phi/2) \\
 g_5(\phi) &= \cos(\phi)/[2\sin(\psi/2)]
 \end{aligned} \tag{C.47}$$

With this notation and the definition of  $B_{ijp}^{\lessgtr}$  given in table C-2, we have (as before, "<" refers to  $\psi \leq \pi/2$ , while ">" refers to  $\psi > \pi/2$ ):

$$\begin{aligned}
 \frac{v_{0pk}^{\lessgtr}}{U_m} &= \sum_{j=0}^5 B_{ijp}^{\lessgtr} g_j(\phi) \quad ; \quad \phi \in [\alpha_{i-1}^{\lessgtr}, \alpha_i^{\lessgtr}] \quad ; \\
 i &= 3k-2, \dots, 3k \quad ; \quad p = N, S \quad ; \quad k = 1, \dots, 4 \tag{C.48}
 \end{aligned}$$

which can be shown to yield

Table C-2  
Definition of  $B_{ijp}^{<}$

j	p	$\psi^{<}$ $\pi/2$	i											
			1	2	3	4	5	6	7	8	9	10	11	12
0	N	<	1	0	1	1	2	1	1	0	1	1	2	1
		>	1	2	1	1	0	1	1	2	1	1	0	1
		<	1	2	1	1	0	1	1	2	1	1	0	1
		>	1	0	1	1	2	1	1	0	1	1	2	1
1	N	<	-3	0	1	1	0	1	1	0	-3	-3	0	5
		>	-3	-2	1	1	2	1	1	-2	-3	-3	2	5
		<	3	0	-1	-1	0	-1	-1	0	3	3	0	-5
		>	3	2	-1	-1	-2	-1	-1	2	3	3	-2	-5
2	N	<	-1	0	1	1	0	-1	-1	0	1	1	0	-1
		>	-1	0	1	1	0	-1	-1	0	1	1	0	-1
		<	1	0	-1	-1	0	1	1	0	-1	-1	0	1
		>	1	0	-1	-1	0	1	1	0	-1	-1	0	1
3	N	<	1	0	-1	-1	-2	-1	-1	0	1	1	2	1
		>	1	0	-1	-1	0	-1	-1	0	1	1	0	1
		<	-1	0	1	1	2	1	1	0	-1	-1	-2	-1
		>	-1	0	1	1	0	1	1	0	-1	-1	0	-1
4	N	<	-1	-2	-1	-1	0	1	1	2	1	1	0	-1
		>	-1	0	-1	-1	0	1	1	0	1	1	0	-1
		<	1	2	1	1	0	-1	-1	-2	-1	-1	0	1
		>	1	0	1	1	0	-1	-1	0	-1	-1	0	1
5	N	<	-1	0	-1	-1	0	-1	-1	0	-1	-1	0	-1
		>	-1	-2	-1	-1	-2	-1	-1	-2	-1	-1	-2	-1
		<	1	0	1	1	0	1	1	0	1	1	0	1
		>	1	2	1	1	2	1	1	2	1	1	2	1

$$\begin{aligned}
\frac{U_{0p}^{\leq}(\phi, \sigma)}{U_m} = \sum_{i=1}^{12} \{ [B_{i0p}^{\leq} g_0(\phi) + B_{i1p}^{\leq} g_1(\phi)] I_0(\alpha_{i-1}, \alpha_i) \\
+ \frac{1}{2} B_{i2p}^{\leq} I_1(\alpha_{i-1}, \alpha_i) + \sqrt{2} B_{i3p}^{\leq} I_c(\alpha_{i-1}, \alpha_i) \\
+ \sqrt{2} B_{i4p}^{\leq} I_s(\alpha_{i-1}, \alpha_i) + \frac{1}{2} B_{i5p}^{\leq} I_{c2}(\alpha_{i-1}, \alpha_i) \} \quad ; \\
p = N, S \quad (C.49)
\end{aligned}$$

Figure C-6 shows  $U_{ON}/U_m$  (and, hence,  $U_{OS}/U_m$  [cf. (C.45)]) as a function of  $\phi$  for a range of values of  $\sigma$  and of  $V_{sw}/U_m$ .

*Assumption C -- see (C.12) and (C.13)*

Here again the derivation of  $U_{ON}$  and  $U_{OS}$  parallels that for Assumption A closely, and we will once again define a convenient notation:

$$\begin{aligned}
h_0(\phi) &= 2\cos(\psi/2) \\
h_1(\phi) &= \sqrt{2}\cos(\phi/2) \\
h_2(\phi) &= \sqrt{2}\sin(\phi/2)
\end{aligned} \quad (C.50)$$

and we will let  $C_{ijp}^{\leq}$  be defined as in table C-3. Then the resultant expression for  $U_{0p}$  can be written as

## Figure C-6

Resultant relative merging rates for open field lines at the northern polar neutral point for Assumption B. The vertical scale convention specified in the caption for figure C-5 is observed here as well.

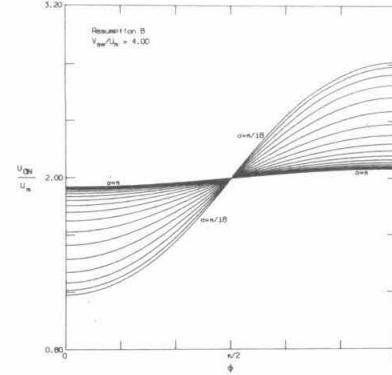
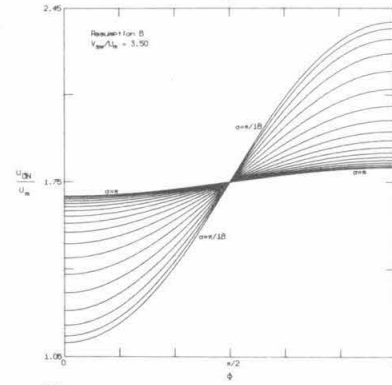
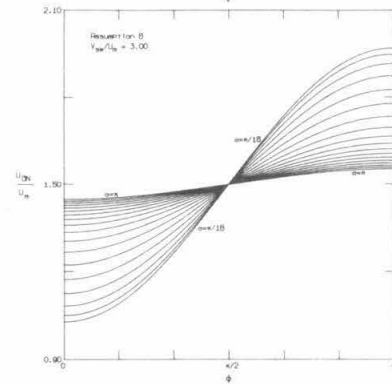
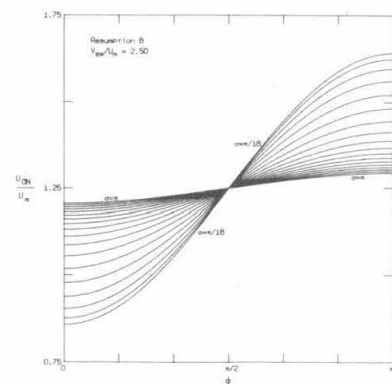
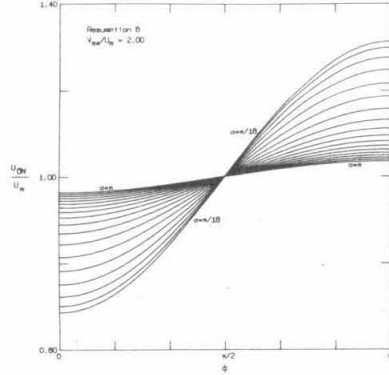
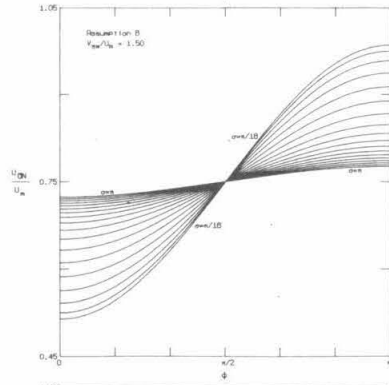
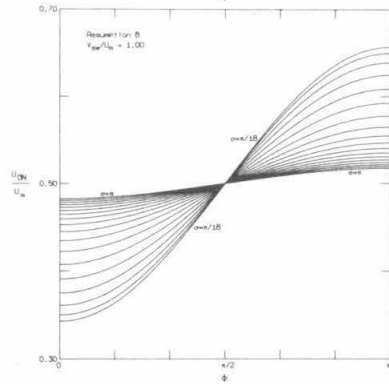
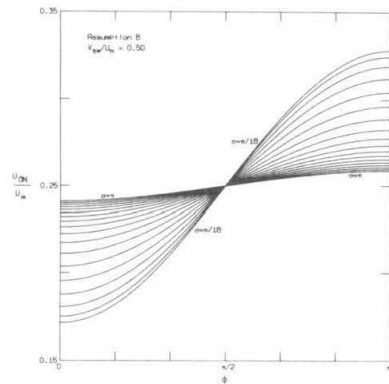




Table C-3  
Definition of  $C_{ijp}^{\leq}$

j	p	$\psi \leq \pi/2$	i											
			1	2	3	4	5	6	7	8	9	10	11	12
0	{ N }	<	1	0	1	1	2	1	1	0	1	1	2	1
		>	1	2	1	1	0	1	1	2	1	1	0	1
		<	1	2	1	1	0	1	1	2	1	1	0	1
		>	1	0	1	1	2	1	1	0	1	1	2	1
1	{ N }	<	1	0	-1	-1	-2	-1	-1	0	1	1	2	1
		>	1	0	-1	-1	0	-1	-1	0	1	1	0	1
		<	-1	0	1	1	2	1	1	0	-1	-1	-2	-1
		>	-1	0	1	1	0	1	1	0	-1	-1	0	-1
2	{ N }	<	-1	-2	-1	-1	0	1	1	2	1	1	0	-1
		>	-1	0	-1	-1	0	1	1	0	1	1	0	-1
		<	1	2	1	1	0	-1	-1	-2	-1	-1	0	1
		>	1	0	1	1	0	-1	-1	0	-1	-1	0	1

$$\frac{U_{0p}^{\leq}(\phi, \sigma)}{U_m} = \sum_{i=1}^{12} \left\{ C_{i0p}^{\leq} h_0(\phi) I_0(\alpha_{i-1}, \alpha_i) + \sqrt{2} C_{i1p}^{\leq} I_C(\alpha_{i-1}, \alpha_i) + \sqrt{2} C_{i2p}^{\leq} I_S(\alpha_{i-1}, \alpha_i) \right\} ; \quad p = N, S \quad (C.51)$$

$U_{ON}/U_m$ , as given by (C.51), is shown in figure C-7.

### Results

Since the uncertainty concerning the proper value of  $U_m$  and the interplanetary plasma and magnetic field parameters at the polar neutral points prevents the determination of *absolute* merging rates, the purpose of this study is to determine whether the *relative* merging rates for open field lines at the two poles is sufficient to yield the relative access window locations observed with the OGO-4 data. Results from the EDP observations (see Sections VII and VIII) indicate that the ratio between the position of the  $\beta$ -high polar latitude access window to the position of the  $\alpha$ -high polar latitude access window is typically  $\sim 5:1$  ( $\sim 1500 R_{\oplus} : \sim 300 R_{\oplus}$  behind the earth). For this field configuration, this ratio would necessitate a similar ratio between the length of the  $\beta$ -geomagnetic tail and the length of the  $\alpha$ -geomagnetic tail. This could be accomplished if the ratio of  $\alpha$ -pole open field merging rate to  $\beta$ -pole open field merging rate were comparable to 5:1.

Figures C-8 to C-10 show the north to south open field line merging rate ratio for each of the three assumptions and for a range of

## Figure C-7

Resultant relative merging rates for open field lines at the northern polar neutral point for Assumption C. The vertical scale convention specified in the caption for figure C-6 is observed here as well.

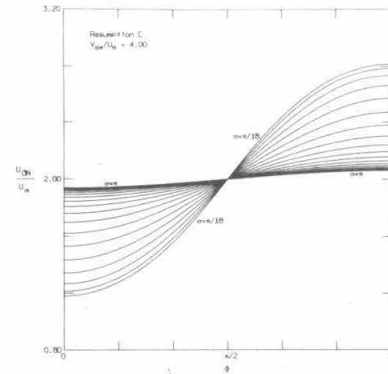
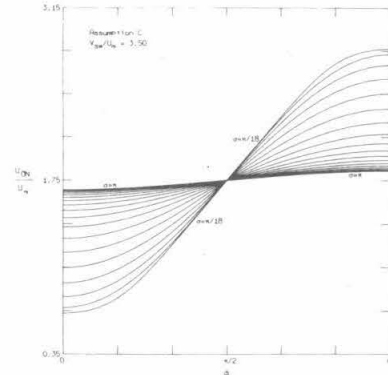
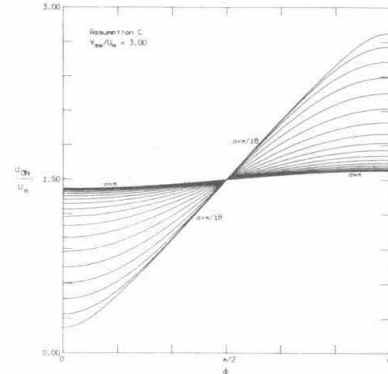
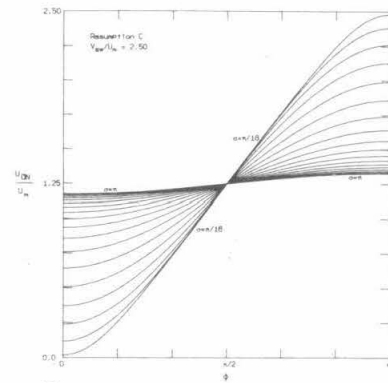
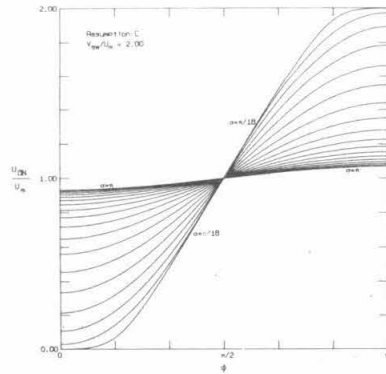
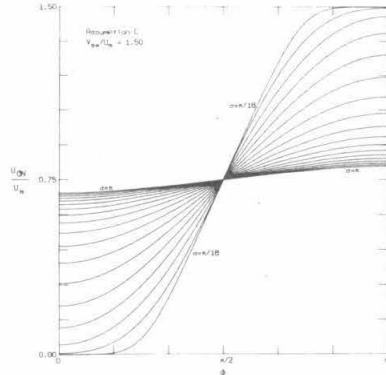
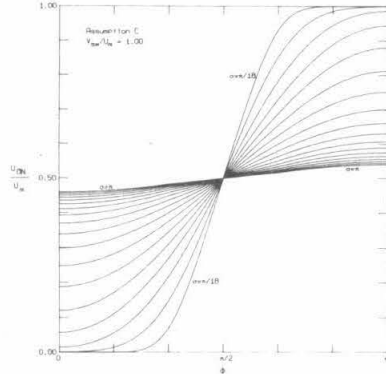
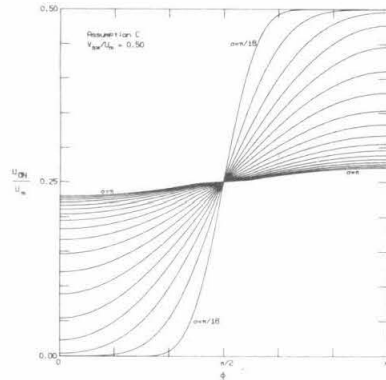


Figure C-8

Ratio between the open field line merging rates at the northern and southern polar neutral points for Assumption A.

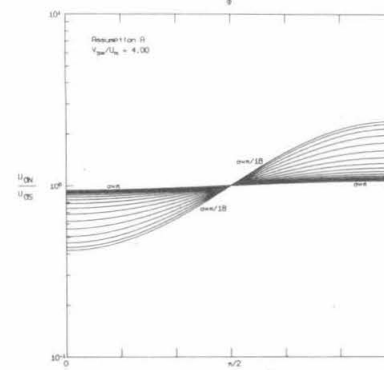
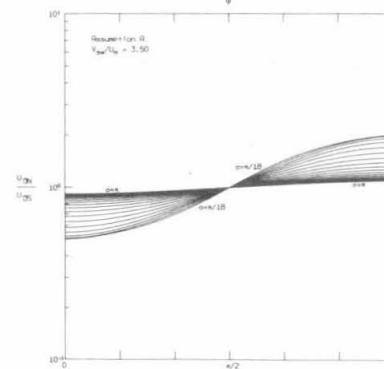
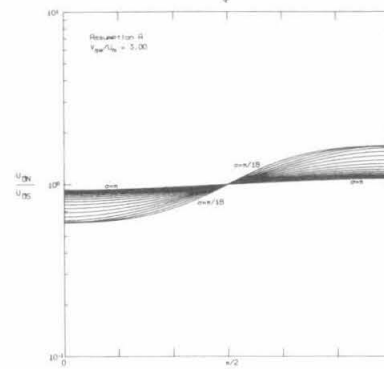
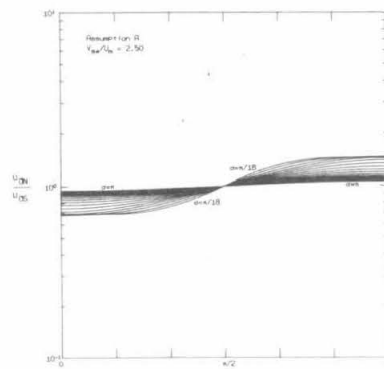
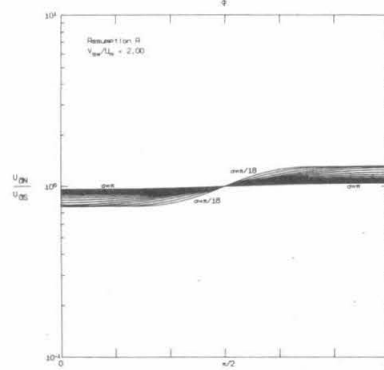
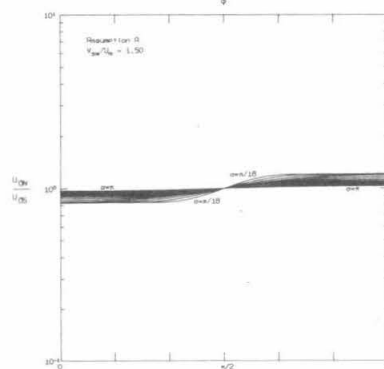
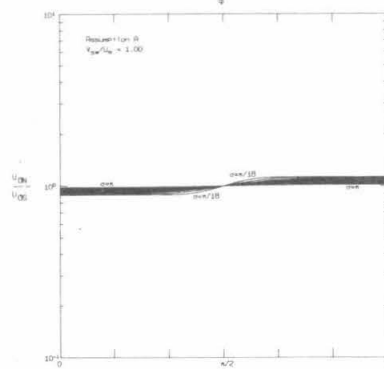
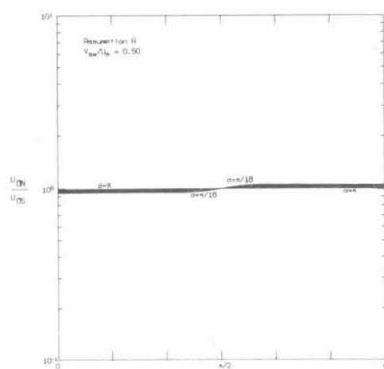


Figure C-9

Ratio between open field line merging rates at the northern and southern polar neutral points for Assumption B.

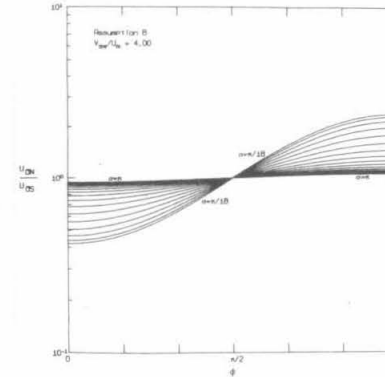
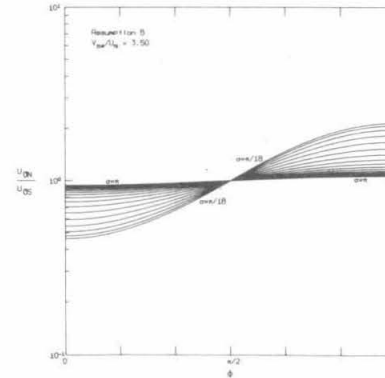
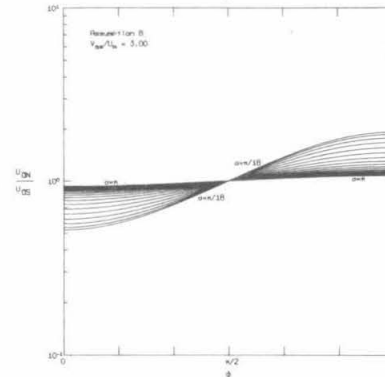
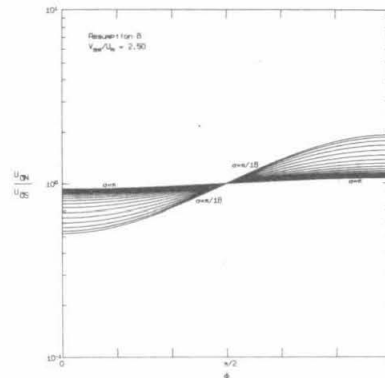
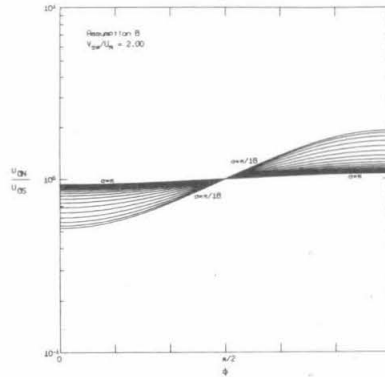
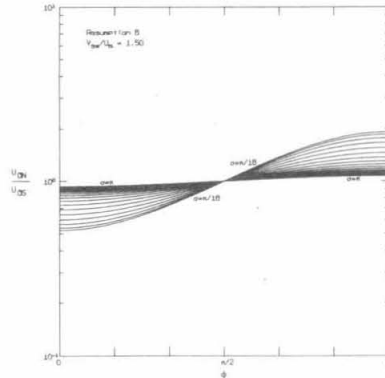
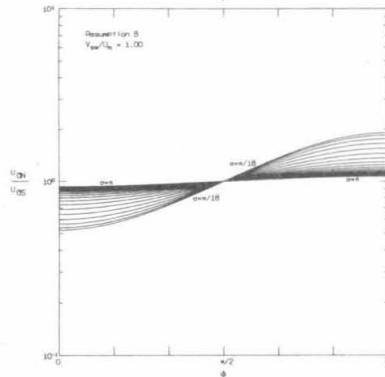
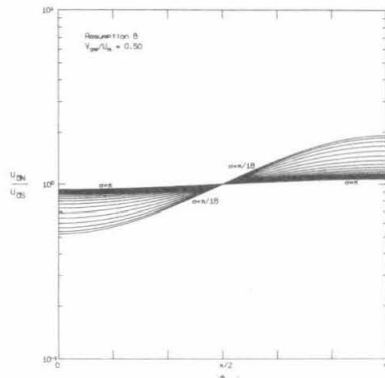
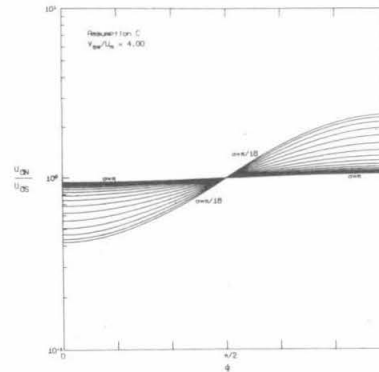
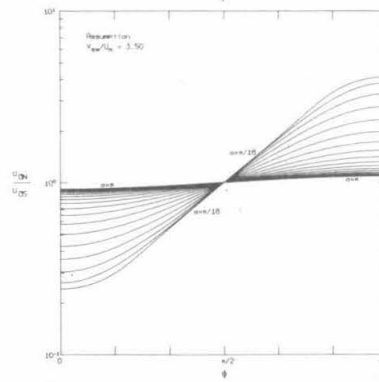
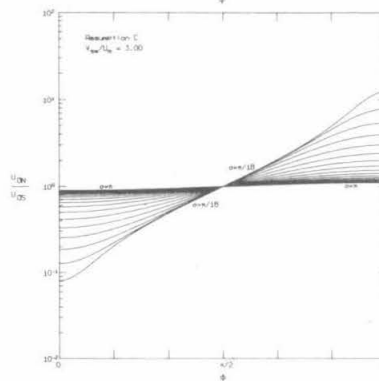
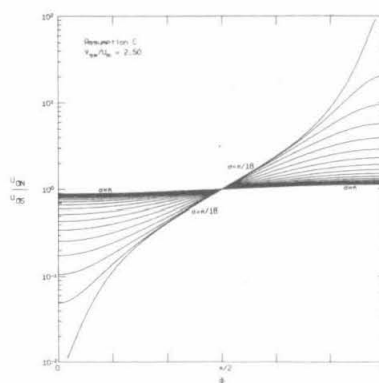
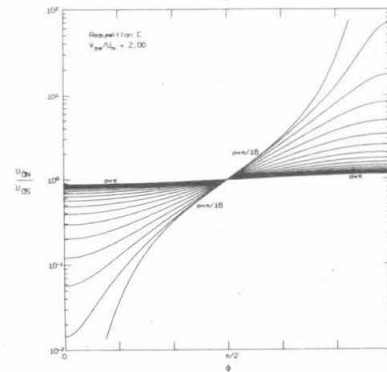
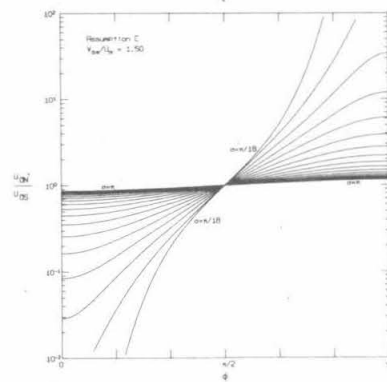
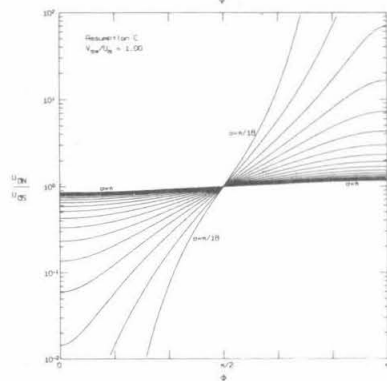
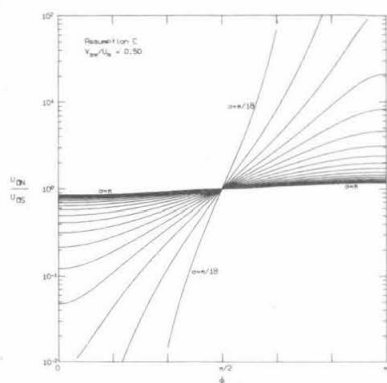




Figure C-10

Ratio between open field line merging rates at the northern and southern polar neutral points for Assumption C. Note the change in vertical scale between the sixth and seventh graphs (i.e., between  $V_{sw}/U_m = 3.00$  and  $V_{sw}/U_m = 3.50$ ).

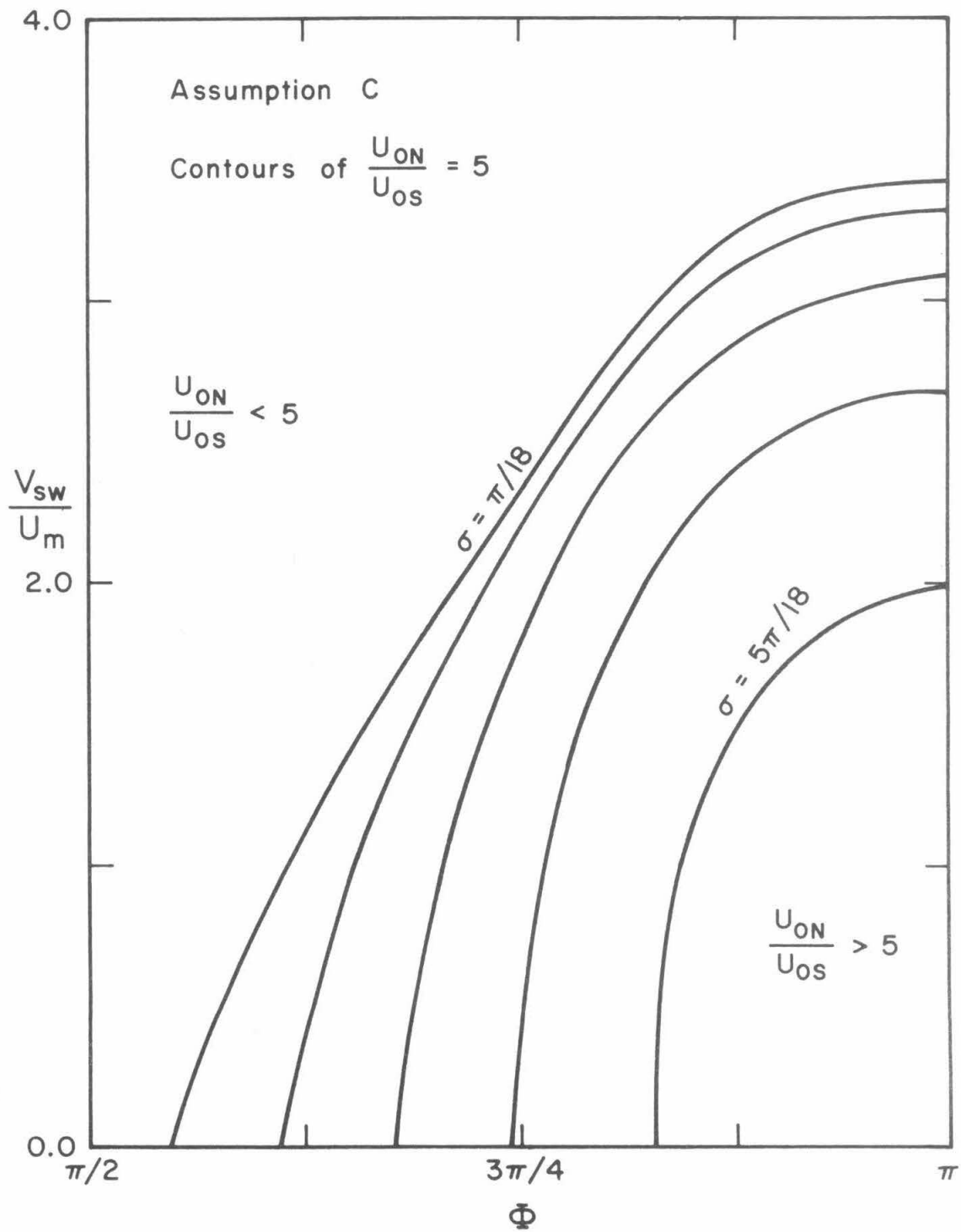


values of  $\sigma$  and of  $V_{sw}/U_m$ . Note that for values of  $V_{sw}/U_m$  greater than 4.0 these ratios will not change. These figures indicate that a 5:1 ratio between the open field merging rates at the two poles is possible only with Assumption C. The maximum value of  $U_{ON}/V_{OS}$  shown is 2.38 for Assumptions A and B ( $\Phi=\pi$ ,  $\sigma=\pi/18$ ,  $V_{sw}/U_m=4.0$ ). Figure C-11 indicates the range of parameters which will give  $U_{ON}/U_{OS} \geq 5$  for Assumption C.

These results are discussed further in Section VII.

Figure C-11

Contours of  $U_{ON}/U_{OS} = 5.0$  in  $\Phi$ -( $V_{sw}/U_m$ ) space for Assumption C. The range of  $\Phi$  and  $V_{sw}/U_m$  corresponding to  $U_{ON}/U_{OS} > 5$  for a given value of  $\sigma$  is represented by that region below and to the right of the appropriate contour.



## REFERENCES

1. L. J. Cahill, Jr., "Preliminary Results of Magnetic Field Measurements in the Tail of the Geomagnetic Cavity," *Transactions of the American Geophysical Union*, 45 (1964), 231.
2. J. W. Dungey, "Interplanetary Magnetic Field and the Auroral Zones," *Physical Review Letters*, 6 (1961), 47.
3. A. J. Dessler, "The Length of the Magnetospheric Tail," *Journal of Geophysical Research*, 69 (1964), 3913.
4. L. A. Frank, "Comments on a Proposed Magnetospheric Model," *Journal of Geophysical Research*, 76 (1971), 2512.
5. H. E. Petschek, "Magnetic Field Annihilation," in *AAS-NASA Symposium on the Physics of Solar Flares*, ed. by W. N. Hess, NASA SP-50 (1964), 425.
6. P. A. Sturrock, "Explosions in Galaxies and Quasars," in *Plasma Instabilities in Astrophysics; Proceedings of the Conference, Monterey, California, October 14-17, 1968*, D. G. Wentzel and D. A. Tidman, eds., Gordon and Breach, Science Publishers, Inc., New York, 1969, p. 297.
7. J. A. Van Allen, "Energetic Particle Phenomena in the Earth's Magnetospheric Tail," in *Particles and Fields in the Magnetosphere; Summer Advanced Study Institute, Symposium, University*

of California, Santa Barbara, California, August 4-15, 1969, B. M. McCormac, ed., Dordrecht, D. Reidel Publishing Co., 1970, p. 111.

8. J. A. Van Allen, "On the Electric Field in the Earth's Distant Magnetotail," *Journal of Geophysical Research*, 75 (1970), 29.
9. K. A. Anderson and R. P. Lin, "Observation of Interplanetary Field Lines in the Magnetotail," *Journal of Geophysical Research*, 74 (1969), 3953.
10. F. C. Michel and A. J. Dessler, "Diffusive Entry of Solar-flare Particles into Geomagnetic Tail," *Journal of Geophysical Research*, 75 (1970), 6061.
11. L. C. Evans and E. C. Stone, "Access of Solar Protons into the Polar Cap -- A Persistent North-South Asymmetry," *Journal of Geophysical Research*, 74 (1969), 5127.
12. Y. Hakura, "Entry of Solar Cosmic Rays Into the Polar Cap Atmosphere," *Journal of Geophysical Research*, 72 (1967), 1461.
13. G. C. Reid and H. H. Sauer, "Evidence for Non uniformity of Solar-proton Precipitation over the Polar Caps," *Journal of Geophysical Research*, 72 (1967), 4383.
14. C. O. Bostrom, J. W. Kohl, and D. J. Williams, "The February 5, 1965, Solar Proton Event, I," *Journal of Geophysical Research*, 72 (1967), 4487.
15. D. J. Williams and C. O. Bostrom, "The February 5, 1965, Solar Proton Event, II," *Journal of Geophysical Research*, 72 (1967),

4497.

16. J. B. Blake, G. A. Paulikas, and S. C. Freden, "Latitude-intensity Structure and Pitch-angle Distributions of Low-energy Solar Cosmic Rays at Low Altitude," *Journal of Geophysical Research*, 73 (1968), 4927.
17. S. M. Krimigis, J. A. Van Allen, and T. P. Armstrong, "Solar Particle Observations inside the Magnetosphere during the 7 July 1966 Proton Flare Event," in *The Proton Flare Project (The July 1966 Event)*, A. C. Stickland, ed., Massachusetts Institute of Technology Press, Cambridge, Mass, 1969, p. 395.
18. J. R. Burrows, I. B. McDiarmid, and M. D. Wilson, "On the High Latitude Limit of Closed Geomagnetic Field Lines," *Proceedings of the IEEE*, 57 (1969), 1051.
19. D. J. Williams and C. O. Bostrom, "Proton Entry into the Magnetosphere on May 26, 1967," *Journal of Geophysical Research*, 74 (1969), 3019.
20. R. D. Sharp, D. L. Carr, and R. G. Johnson, "Satellite Observations of the Average Properties of Auroral Particle Precipitation: Latitudinal Variations," *Journal of Geophysical Research*, 74 (1969), 4618.
21. C. O. Bostrom, "Entry of Low Energy Solar Protons into the Magnetosphere," in *Intercorrelated Satellite Observations Related to Solar Events; European Space Research Organization, Annual ESLAB/ESRIN, Symposium, 3rd, Noordwijk, Netherlands*,



- September 16-19, 1969, *Proceedings*, V. Manno and D. E. Page, eds., Dordrecht, D. Reidel Publishing Co., 1970, p. 229ff.
22. I. B. McDiarmid and J. R. Burrows, "Relation of Solar Proton Latitude Profiles to Outer Radiation Zone Electron Measurements," *Journal of Geophysical Research*, 74 (1969), 6239.
  23. G. A. Paulikas, J. B. Blake, and A. L. Vampola, "Solar Particle Observations over the Polar Caps," in *Particles and Fields in the Magnetosphere; Summer Advanced Study Institute, Symposium, University of California, Santa Barbara, California, August 4-15, 1969, Proceedings*, B. M. McCormac, ed., D. Reidel Publishing Co., Dordrecht, 1970, p. 141ff.
  24. J. Englemann, R. J. Hynds, G. Morfill, F. Axisa, A. Bewick, A. C. Durney, and L. Koch, "Penetration of Solar Protons over the Polar Caps during the February 25th 1969 Event," *Journal of Geophysical Research*, 76 (1971), 4245.
  25. J. A. Van Allen, J. F. Fennell, and N. F. Ness, "Asymmetric Access of Energetic Solar Protons to the Earth's North and South Polar Caps," *Journal of Geophysical Research*, 76 (1971), 4262.
  26. G. E. Morfill and J. J. Quenby, "The Entry of Solar Protons over the Polar Caps," to be published.
  27. A. L. Vampola, "Access of Solar Electrons to Closed Field Lines," *Journal of Geophysical Research*, 76 (1971), 36.
  28. L. C. Evans, J. L. Faselow, and E. C. Stone, "User's Notes

for Experiments C-08 and D-08 Rate Plots," Space Radiation Laboratory Internal Report No. 11, January, 1970.

29. W. E. Althouse, E. C. Stone, R. E. Vogt, and T. H. Harrington, "A Solar and Galactic Cosmic Ray Satellite Experiment," *IEEE Transactions on Nuclear Science*, 15 (1967), 229.
30. J. F. Janni, *Calculations of Energy Loss, Range, Pathlength, Straggling, etc.*, Technical Report AFWL-TR-65-150, 1966.
31. L. C. Evans and E. C. Stone, "OGO-4, Experiment 08, Calibrations," Space Radiation Laboratory Internal Report No. 27, August, 1971.
32. J. E. Lupton and J. W. Brown, private communication, 1971.
33. J. E. Lupton, private communication, 1971.
34. OGO Experiment Bulletin F-143, "OGO Operations Summary Report June, 1969," Report No. 08672-6032-T0-00 (1969), 5.
35. L. C. Evans, "OGO-4 Data Coverage Plots," Space Radiation Laboratory Internal Report No. 25, August, 1971.
36. W. N. Hess, *The Radiation Belt and Magnetosphere*, Blaisdell Publishing Co., Division of Ginn and Co., Waltham, Mass., 1968, p. 57ff.
37. T. A. Fritz and D. A. Gurnett, "Diurnal and Latitudinal Effects Observed for 10 keV Electrons at Low Satellite Altitudes," *Journal of Geophysical Research*, 70 (1965), 2485.
38. Cain, et al., *Computation of the Main Geomagnetic Field from*

- Spherical Harmonic Expansions*, NSSDC 68-11, Goddard Space Flight Center, Greenbelt, Md., 1968.
39. E. A. Aguilar, J. L. Fanselow, and L. C. Evans, "Magnetic Tape Formats for Experiment 08 on OGO II and IV," Space Radiation Laboratory Internal Report No. 22.
  40. I. B. McDiarmid and J. R. Burrows, "Latitude Profiles of Low-energy Solar Electrons, *Journal of Geophysical Research*, 75 (1970), 3910.
  41. H. I. West, Jr. and A. L. Vampola, "Simultaneous Observations of Solar Flare Electron Spectra in Interplanetary Space and within the Earth's Magnetosphere," *Physical Review Letters*, 26 (1971), 458.
  42. D. A. Bryant, T. L. Cline, U. D. Desai, and F. B. McDonald, "Studies of Solar Protons with Explorers XII and XIV," *Astrophysical Journal*, 141 (1965), 478.
  43. D. A. Bryant, T. L. Cline, U. D. Desai, and F. B. McDonald, "Continual Acceleration of Solar Protons in the MeV Range," *Physical Review Letters*, 14 (1965), 481.
  44. U. R. Rao, K. G. McCracken, and R. P. Bukata, "Cosmic-Ray Propagation Processes, II," *Journal of Geophysical Research*, 72 (1967), 4325.
  45. R. P. Lin and K. A. Anderson, "Electrons >40 keV and Protons >500 keV of Solar Origin," *Solar Physics*, 1 (1967), 446.

46. C. Y. Fan, M. Pick, R. Pyle, J. A. Simpson, and D. R. Smith, "Protons Associated with Centers of Solar Activity and Their Propagation in Interplanetary Magnetic Field Regions Corotating with the Sun," *Journal of Geophysical Research*, 73 (1968), 1555.
47. K. A. Anderson, "Electrons and Protons in Long Lived Streams of Energetic Particles," *Solar Physics*, 6 (1969), 111.
48. J. F. Steljes, *Cosmic Ray NM-64 Neutron Monitor Data*, Atomic Energy of Canada Limited, AECL-3064, 1968.
49. J. A. Simpson, private communication, 1971.
50. R. P. Lin, S. W. Kahler, and E. C. Roelof, "Solar Flare Injection and Propagation of Low-energy Protons and Electrons in the Event of 7-9 July, 1966," *Solar Physics*, 4 (1968), 338.
51. E. C. Stone, "Time Dependence of Non-Störmer cutoff for 1.5 MeV Protons in Quiet Geomagnetic Field," *Journal of Geophysical Research*, 69 (1964), 3577.
52. E. N. Parker, "Dynamics of the Interplanetary Gas and Magnetic Field," *Astrophysical Journal*, 128 (1958), 664.
53. D. H. Fairfield, "The Ordered Magnetic Field of the Magnetosheath," *Journal of Geophysical Research*, 72 (1967), 5865.
54. N. F. Ness, C. S. Scarce, and J. B. Seek, "Initial Results of the IMP 1 Magnetic Field Experiment," *Journal of Geophysical Research*, 69 (1964), 3531.

55. P. J. Coleman, Jr., "Variations in the Interplanetary Magnetic Field -- Mariner 2, I," *Journal of Geophysical Research*, 71 (1966), 5509.
56. J. M. Wilcox and N. F. Ness, "Quasi-stationary Corotating Structure in the Interplanetary Medium," *Journal of Geophysical Research*, 70 (1965), 5793.
57. J. M. Wilcox and D. S. Colburn, "Interplanetary Sector Structure in the Rising Portion of the Sunspot Cycle," *Journal of Geophysical Research*, 74 (1969), 2388.
58. J. M. Wilcox and D. S. Colburn, "Interplanetary Sector Structure near the Maximum of the Sunspot Cycle," NASA-CR-110861; AD-707748, 1970.
59. K. G. McCracken and U. R. Rao, "Solar Cosmic Ray Phenomena," *Space Science Reviews*, 11 (1970), 155.
60. J. J. O'Gallagher, "The Heliocentric Longitude Intensity Profile of 15-MeV Protons from the February 5, 1965, Solar Flare," *Journal of Geophysical Research*, 75 (1970), 1163.
61. M. A. Forman, "Convection-Dominated Transport of Solar Cosmic Rays," *Journal of Geophysical Research*, 74 (1971), 759.
62. D. A. Bryant, T. L. Cline, U. D. Desai, and F. B. McDonald, "Explorer 12 Observations of Solar Cosmic Rays and Energetic Storm Particles after the Solar Flare of September 28, 1961," *Journal of Geophysical Research*, 67 (1962), 4983.
63. K. G. McCracken, U. R. Rao, and N. F. Ness, "Interrelationship

- of Cosmic-ray Anisotropies and the Interplanetary Magnetic Field," *Journal of Geophysical Research*, 73 (1968), 4159.
64. U. R. Rao, F. R. Allum, W. C. Bartley, R. A. R. Palmeira, J. A. Harries, and K. G. McCracken, "Measurement of Cosmic Ray Anisotropy of Solar Origin by Explorer 34 Satellite," in *Solar Flares and Space Research; COSPAR, Plenary Meeting, 11th, Symposium, Tokyo, Japan, May 9-11, 1968, Proceedings*, C. de Jager and Z. Švestka, eds., North Holland Publishing Co., Amsterdam, 1969, p. 267ff.
  65. K. G. McCracken, U. R. Rao, R. P. Bukata, and E. P. Keath, "The Decay Phase of Solar Flare Events," *Solar Physics*, 18 (1971), 100.
  66. K. G. McCracken, U. R. Rao, and R. P. Bukata, "Cosmic Ray Propagation Processes, I, A study of the Cosmic-Ray Flare Effect," *Journal of Geophysical Research*, 72 (1967), 4293.
  67. E. N. Parker, "Interaction of the Solar Wind with the Geomagnetic Field," *Physics of Fluids*, 1 (1958), 171.
  68. D. B. Beard, "The Interaction of the Terrestrial Magnetic Field with the Solar Corpuscular Radiation," *Journal of Geophysical Research*, 65 (1960), 3559.
  69. J. R. Spreiter and B. R. Briggs, "Theoretical Determination of the Form of the Boundary of the Solar Corpuscular Stream Produced by the Interaction with the Magnetic Dipole Field of the Earth," *Journal of Geophysical Research*, 67 (1962), 37.

70. J. R. Midgley and L. Davis, "Calculation by a Moment Technique of the Perturbation of the Geomagnetic Field by the Solar Wind," *Journal of Geophysical Research*, 68 (1963), 5111.
71. W. N. Hess, *op. cit.*, p. 293ff.
72. D. H. Fairfield, "The Magnetic Field of the Magnetosphere and Tail," NASA-TM-X-63508; X-616-69-124, 1969.
73. D. H. Fairfield, "The Configuration of the Geomagnetic Field," NASA-TM-X-63891; X-692-70-163, 1970.
74. N. F. Ness, "The Earth's Magnetic Tail," *Journal of Geophysical Research*, 70 (1965), 2989.
75. N. F. Ness, K. W. Behannon, C. S. Scarce, and S. C. Cantarano, "Observations of the Earth's Magnetic Tail and Neutral Sheet at 510,000 Kilometers by Explorer 33," *Journal of Geophysical Research*, 72 (1967), 927.
76. N. F. Ness, "The Geomagnetic Tail," *United States National Academy of Sciences and NASA Goddard Space Flight Center, International Symposium on the Physics of the Magnetosphere, Washington, D. C., September 3-13, 1968, Reviews of Geophysics*, 7 (1969), 97.
77. F. Mariani and N. F. Ness, "Observations of the Geomagnetic Tail at 500 Earth Radii by Pioneer 8," *Journal of Geophysical Research*, 74 (1969), 5633.
78. G. L. Siscoe, F. L. Scarf, D. S. Intriligator, J. H. Wolfe, J. H. Binsack, H. S. Bridge, and V. M. Vasyliunas, "Evidence

- for a Geomagnetic Wake at 500 Earth Radii," *Journal of Geophysical Research*, 75 (1970), 5319.
79. N. F. Ness, C. S. Searce, and S. C. Cantarano, "Probable Observation of the Geomagnetic Tail at  $10^3$  Earth Radii by Pioneer 7," *Journal of Geophysical Research*, 72 (1967), 3769.
  80. D. H. Fairfield, "Simultaneous Measurements on Three Satellites and the Observation of the Geomagnetic Tail at  $1000 R_E$ ," *Journal of Geophysical Research*, 73 (1968), 6179.
  81. D. S. Intriligator, J. H. Wolfe, D. D. McKibbin, and H. R. Collard, "Preliminary Comparison of Solar Wind Plasma Observations in the Geomagnetospheric Wake at 1000 and 500 Earth Radii," *Planetary and Space Science*, 17 (1969), 321.
  82. R. Gall, J. Jiménez, and L. Camacho, "Arrival of Low-energy Cosmic Rays via the Magnetospheric Tail," *Journal of Geophysical Research*, 73 (1968), 1593.
  83. R. Gall, J. Jiménez, and A. Orozco, "Direction of Approach of Cosmic Rays for High Latitude Stations," *Journal of Geophysical Research*, 74 (1969), 3529.
  84. P. A. Sweet, Proceedings of the International Astronomical Union Symposium on Electromagnetic Phenomena in Cosmical Physics, No. 6 (Stockholm, 1956), p. 123 (1958), *Nuovo Cimento*, Supplement 8, Section X (1958), 188.



85. E. N. Parker, "The Solar Flare Phenomena and the Theory of Reconnection and Annihilation of Magnetic Fields," *Astrophysical Journal, Supplement Series* 77, 8 (1963), 177.
86. H. E. Petschek, "Reconnection and Annihilation of Magnetic Fields," in *The Solar Wind; Proceedings of a Conference, California Institute of Technology, Pasadena, California, April 1-4, 1964*, R. J. Mackin, Jr. and M. Neugebauer, eds., Jet Propulsion Laboratory, Pasadena, California, 1966, p. 221ff.
87. B. U. Ö. Sonnerup, "Magnetic-field re-connexion in a highly conducting incompressible fluid," *Journal of Plasma Physics*, 4 (1970), 161.
88. T. Yeh and W. I. Axford, "On the re-connexion of magnetic field lines in conducting fluids," *Journal of Plasma Physics*, 4 (1970), 207.
89. J. A. Van Allen and N. F. Ness, "Particle Shadowing by the Moon," *Journal of Geophysical Research*, 74 (1969), 71.
90. K. A. Anderson, "Entry of Solar Cosmic Rays into the Earth's Magnetosphere," in *Particles and Fields in the Magnetosphere; Summer Advanced Study Institute, Symposium, University of California, Santa Barbara, California, August 4-15, 1969, Proceedings*, B. M. McCormac, ed., D. Reidel Publishing Co., Dordrecht, 1970, p. 3ff.
91. M. Siebert, "Magnetic Activity Differences between the Two Hemispheres following the Sector Structure of the Interplane-

- tary Magnetic Field," *Journal of Geophysical Research*, 73 (1968), 3049.
92. J. M. Wilcox, "Asymmetry in Geomagnetic Response to the Polarity of the Interplanetary Magnetic Field," *Journal of Geophysical Research*, 73 (1968), 6835.
  93. J. K. Hargreaves, "Conjugate and Closely-spaced Observations of Auroral Radio Absorption, III," *Planetary and Space Science*, 17 (1969), 1919.
  94. D. H. Fairfield, private communication, 1971.
  95. R. Gall and A. Orozco, "On the Uneven Illumination of Polar Caps by Solar Cosmic Rays," *Transactions of the American Geophysical Union*, 51 (1970), 800.
  96. A. J. Dessler and R. D. Juday, "Configuration of Auroral Radiation in Space," *Planetary and Space Science*, 13 (1965), 63.
  97. F. C. Michel, "The Effect of Magnetospheric Tail on Cosmic Ray Cutoffs," *Planetary and Space Science*, 13 (1965), 753.
  98. F. C. Michel and A. J. Dessler, "The Physical Significance of Inhomogeneities in PCA Events," *Journal of Geophysical Research*, 70 (1965), 4305.
  99. A. J. Dessler, "Solar Wind Interactions," (*International Association of Geomagnetism and Aeronomy, Birkeland Symposium on Aurora and Magnetic Storms, Sandefjord, Norway, September 18-22, 1967*), *Annales de Géophysique*, 24 (1968), 333.

100. A. J. Dessler, "Formation and Geometry of Geomagnetic Tail,"  
in *Particles and Fields in the Magnetosphere; Summer Advanced Study Institute, Symposium, University of California, Santa Barbara, California, August 4-15, 1969, Proceedings*, B. M. McCormac, ed., D. Reidel Publishing Co., Dordrecht, 1970, p. 18ff.
101. L. C. Evans, "The Cross-sectional Shape of the Distant Geomagnetic Tail," Space Radiation Laboratory Internal Report No. 26, August, 1971.
102. J. W. Dungey, "The Structure of the Exosphere, or Adventures in Velocity Space," in *Geophysics, the Earth's Environment*, C. DeWitt, J. Hieblot, and A. Lebeau, eds., Gordon and Breach, New York, 1963, p. 504ff.
103. R. H. Levy, H. E. Petschek, and G. L. Siscoe, "Aerodynamic Aspects of the Magnetospheric Flow," *American Institute of Aeronautics and Astronautics*, 2 (1964), 2065.
104. W. J. Axford, H. E. Petschek, and G. L. Siscoe, "The Tail of the Magnetosphere," *Journal of Geophysical Research*, 70 (1965), 1231.
105. J. W. Dungey, "The Length of the Magnetospheric Tail," *Journal of Geophysical Research*, 70 (1965), 1753.
106. J. W. Dungey, "The Theory of the Quiet Magnetosphere," in *Solar-Terrestrial Physics*, J. N. King and W. S. Newman, eds., Academic Press, London, 1967, p. 91ff.

107. J. W. Dungey, "The Reconnection Model of the Magnetosphere,"  
in *Earth's Particles and Fields; Proceedings of the NATO  
Advanced Study Institute, Freising, West Germany, July 31-  
August 11, 1967*, B. M. McCormac, ed., Reinhold Book Corp.,  
New York, 1968, p. 385ff.
108. P. D. Hudson and H. R. Anderson, "Non-uniformity of Solar  
Protons over the Polar Caps on March 24, 1966," *Journal of  
Geophysical Research*, 74 (1969), 2881.
109. L. A. Frank, "Plasma in the Earth's Polar Magnetosphere," to  
be published.
110. L. A. Frank and D. A. Gurnett, "On the Distribution of Plasmas  
and Electric Fields over the Auroral Zones and the Polar Caps,"  
to be published.
111. J. R. Spreiter, A. L. Summers, and A. Y. Alksne, "Hydromag-  
netic Flow around the Magnetosphere," *Planetary and Space  
Science*, 14 (1966), 223.
112. J. R. Spreiter and A. L. Summers, "On Conditions near the Neut-  
ral Points on the Magnetosphere Boundary," *Planetary and Space  
Science*, 15 (1967), 787.
113. A. Y. Alksne, "Steady-state Magnetic Field in the Transition  
Region," *Planetary and Space Science*, 15 (1967), 239.
114. H. E. Salzer, "Formulas for Calculating the Error Function of  
a Complex Variable," *Mathematical Tables and Aids to Computa-  
tion*, 5 (1951), 67 in W. Gautschi, "Error Function and Fresnel

Integrals," in *Handbook of Mathematical Functions with Formulas, Graphs, and Mathematical Tables*, M. Abramowitz and I. A. Stegun, eds., National Bureau of Standards, United States Department of Commerce, Washington D. C., 1964, p. 295ff.